

E L E T T R A H I G H L I G H T S > 0 9 - 1 0



2 0 0 9 - 1 0





E L E T T R A H I G H L I G H T S > 0 9 - 1 0

2 0 0 9 - 1 0





ELETTRA HIGHLIGHTS 2009-2010

EDITORIAL COMMITTEE

- > Carlo Callegari
- > Andrea Goldoni
- > Claudio Masciovecchio
- > Adriana Pertosi
- > Maurizio Polentarutti
- > Kevin Prince
- > Paola Storici

Graphic Design:
Studio Link (www.studio-link.it)
Graphart s.r.l.

Print:
Graphart s.r.l.



The Elettra Highlights publication for 2009-2010 reflects both the renewed interest of our international user community in the enhanced capabilities of Elettra and the great strides that were recently made in the development of the novel free-electron laser source FERMI@Elettra.

For the Elettra third-generation light source the strategies we have implemented together with our partners have been aimed at assuring the renewed and extended competitiveness of the source, responding to the competition generated by the completion of various third generation synchrotron radiation laboratories, such as Diamond in the UK and Soleil in France. The introduction of a new full-energy injector capable of bringing Elettra to function in top-up mode, and the actions taken to upgrade the existing beamlines currently underway, are keeping Elettra up to par with the most advanced competition. At the time of this writing, Elettra routinely operates in top-up mode at both 2.0 and 2.4 GeV, and the users are greatly benefitting from the higher stability and the increased average brightness of the source. Thus Elettra has become one of the few synchrotron radiation sources in the world that operate in top-up mode, and the one and only machine in the world that was not designed for top-up, but has been successfully converted to operate in top-up mode.

New international partnerships are also making novel facilities available on the Elettra experimental floor. An agreement with the Indian Institute of Science in Bangalore is now supporting the construction of two new x-ray diffraction beamlines, one for macromolecular structural studies and the other for high pressure/temperature diffraction studies. An agreement with the Institute of Solid State Research, Institut für Festkörperforschung Forschungszentrum Jülich lead to the installation of an aberration-corrected NanoESCA spectro-microscope on the right-hand branch of the Nanospectroscopy beamline. The microscope will be available for studies in the fields of materials science, surface physics and magnetism.

As we are entering the commissioning phase of the new fourth generation source FERMI@Elettra, a free-electron laser (FEL) source designed as a seeded source from the start, we are relaunching our international presence and attracting a number of new highly qualified international partners. More than twentyfive international institutions take part in the scientific programs currently under development at FERMI, in the three areas Low Density Matter (LDM), Elastic and Inelastic Scattering (EIS) and Diffraction and Projection Imaging (DiProl).

The beginning of the commissioning phase was celebrated with a ceremony on November 30, 2009, when the FERMI photoinjector was inaugurated by the Italian Minister of Education, University and Research, the honorable Mariastella Gelmini. All civil construction was completed in the Fall of 2010 with the official delivery of the FERMI experimental building. In parallel, the upgraded linac had been under commission behind a temporary shielding wall, and achieved an operating energy of 1.2 GeV, at which assembly of the FEL-1 undulator chain was started. The single linear polarization modulator and six elliptical polarization radiators produced by the new industrial spin-off company of Sincrotrone Trieste, Kyma S.r.l., were successfully installed and commissioning of FEL-1 started in November 2010.

We project that with the SLED fully optimized and with the two new S-band accelerating sections and the single new X-band accelerating sections still to be installed, the e-beam energy will substantially exceed the



upwardly-revised operating energy of 1.5 GeV. FERMI@Elettra is scheduled to produce gigawatt pulses at wavelength tunable down to 10 nm by the end of 2010 and down to 3-4 nm by the end of 2011.

These developments have been made possible by financial contributions from the Italian Government, the European Commission and the Regional government of Friuli Venezia Giulia, as well as by an 80 million euro loan from the European Investment Bank (EIB), which recognized the importance of our project on a pan-European level. This also allowed us to strengthen the trend towards an internationalization of Sincrotrone Trieste with the perspective of institutional ties with long-term European programs. The beginning of the next European Framework Program in 2013 and the perspective of transforming our laboratory into a European Research Infrastructure Consortium (ERIC), are important targets not to be missed.

FERMI@Elettra is already part of the roadmap of the European Strategy Forum for Research Infrastructure (ESFRI) through the EuroFEL initiative (once IRUVX-FEL, from infrared, ultraviolet, X-ray Free Electron Laser). Our Laboratory has a proven track record in the development of high quality research and technological innovation, as we have seen the successful fulfillment of common initiatives with partner institutions in Austria, the Czech Republic, Slovenia, Croatia, India, France, Germany and other EU and non-EU countries. The transformation of Sincrotrone Trieste, at the moment a shareholders company with the participation of the Italian government, into an ERIC is a realistic possibility that will require the participation of nearby countries.

The new strategic directions opening up for us and for our partners are exemplified by the thematic workshops that will take place as part of the XVIII Elettra Users' Meeting: "SPEM-2010 - 1st International Workshop on Scanning Photoelectron Microscopy", and "SESTRE - Seeded FEL sources and Time-resolved experiments". These will be followed by a workshop on Soft X-ray Science and Instrumentation at the European XFEL, also organized in Trieste by XFEL and Sincrotrone Trieste jointly. Such workshops will serve the purpose of engaging a broader user community, and our partner institutions will have prominent roles in the above events.

We take this opportunity to thank our employees, our Partners and external Users for their enthusiasm and dedication over the years. We trust that with their help we will be able to meet the major challenge of fully exploiting an upgraded Elettra light source while developing the new FERMI@Elettra FEL source.

Alfonso Franciosi
Chief Executive Officer
Sincrotrone Trieste S.C.p.A.

TABLE OF CONTENTS

RESEARCH HIGHLIGHTS

Chemical and Materials Science	10
> X-ray Imaging and Microspectroscopy Study of Metallic Plate Corrosion and Uptake of Corrosion Products by Nafion in PEMFCs	12
> Methane partial oxidation on NiCu-based catalysts	14
> Fabrication of Advanced Functional Devices Combining Sol-Gel with X-ray Lithography	16
> Fractal structure in the spacer layers favours high temperature superconductivity in $\text{La}_2\text{CuO}_{4+y}$	18
> Re-oxidation of reduced ceria as an indicator for CO_2 activation	20
> Bio-inspired Water Oxidation Electrodes Integrating Carbon Nanotubes and polyoxometalates	22
> Probing interlayer relaxation at a metal-oxide interface	24
Graphene	26
> Graphene Synthesis on Cubic SiC/Si Wafers - Perspectives for Mass Production of Graphene-Based Electronic Devices	28
> Graphene-like electronic signature in silicene nano-ribbons	30
> Geodesic carbon nanodomes as precursors to nearly free-standing graphene	32
> Band dispersion in the deep 1s core level of graphene	34
> Corrugation in Exfoliated Graphene	36
Nanostructures and organic films	38
> Relating Energy Level Alignment and Amine-Linked Molecular Junction Conductance	40
> Universality of zwitterionic bonding scheme of amino-acids on surfaces	42
> Contactless Monitoring of Diameter-Dependent Conductivity of GaAs nanowires	44
> Distribution of vacancies in NiO nanoparticle: searching for the origin of magnetic behaviour in antiferromagnetic nanoparticles	46
> Adsorption of dopamine on titania: towards novel biosensors and photovoltaics	48

Magnetism and highly correlated systems 50

- > Experimental Study of the Incoherent Spectral Weight in the Photoemission Spectra of the Misfit Cobaltate $[\text{Bi}_2\text{Ba}_2\text{O}_4][\text{CoO}_2]_2$ 52
- > Correlated Electrons Step-by-Step: Itinerant-to-Localized Transition of Fe Impurities in Free-Electron Metal Hosts 54
- > Domain-wall depinning assisted by pure spin currents 56
- > Ferromagnetic and ordered MnSi(111) epitaxial layers 58
- > Orbital nature of the multiband Fermi surface of $\text{Ba}_2(\text{Fe}_{1-x}\text{Co}_x)_2\text{As}$ 60
- > A microscopic view on the metal-insulator transition in a Mott system 62
- > THz spectroscopy of multi-gap superconductors 64

Atomic and Molecular Physics 66

- > The interplay of inductive and resonance effects in the XPS spectra of halopyrimidines 68
- > Rotational and core level spectroscopies as complementary techniques in tautomeric/conformational studies: 2-mercaptopyridine 70
- > Dissociative double photoionization of CO_2 molecules in the 36–49 eV energy range: angular and energy distribution of ion products 72

Theory@Elettra 74

- > Metallization of the fullerene/Rh interface revealed by valence photoelectron spectroscopy and density functional theory calculations 76
- > Valence electronic properties of porphyrin derivatives 78
- > The GWL project 80

Life Sciences 82

- > Temperature Dependence of Hydrogen-Bond Dynamics in Acetic Acid-Water Solutions 84
- > Toward Multiprotein Nanoarrays Using Nanografting and DNA Directed Immobilization of Proteins 86
- > X-ray microtomography as one of the complementary techniques for microspatial analysis of biominerals 88
- > Structure of Jack bean urease revealed 80 years after it was crystallized - insecticidal property of plant ureases explained 90
- > An aminotransferase branch point connects purine catabolism to amino acid recycling 92
- > Localization of aluminium in tea (*Camellia sinensis*) leaves using low energy X-ray fluorescence spectro-microscopy 94
- > Versatile loops in mycocypins inhibit three protease families 96

Free Electron Laser and other coherent light sources 98

- > Update on FERMI@Elettra, a next-generation free-electron laser user facility 99
- > The FERMI@Elettra free-electron-laser source for coherent X-ray physics 102
- > Ultrafast insulator-to-metal phase transition as a switch to measure the spectrogram of a supercontinuum light pulse 104
- > Bursting coherent THz radiation at Elettra 106
- > The FERMI@Elettra Control System 108
- > A method for estimating the temperature in high energy density free electron laser experiments 110

Instrumentation Development and Software 112

- > Pore3D Software-as-a-Service (SaaS): a tool for quantitative analysis of 3D images 114
- > Elettra operates in top-up mode 116
- > A photoelectron velocity map imaging spectrometer for experiments combining synchrotron and laser radiation 118
- > The Scientific Computing Infrastructure of the Laboratory 120
- > Angle resolved photoemission spectroscopy and imaging with sub- μm probe at Spectromicroscopy-3.2L beamline 122

FACTS & FIGURES

- > The company 126
- > Beamlines and users 128
- > Staff 132
- > Financial figures 133
- > Projects / Sponsored research 134
- > Technology transfer at Elettra 136
- > Insertion device design and manufacturing@KYMA Srl 139

EVENTS

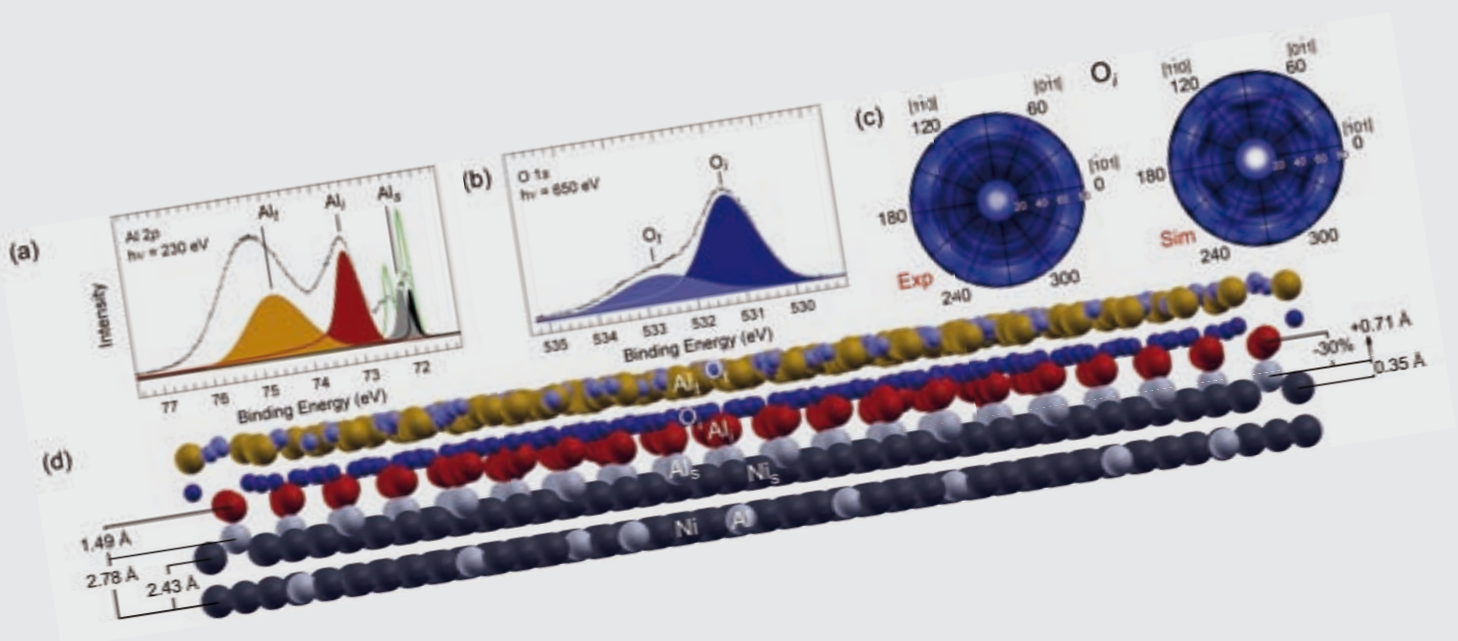
- > Institutional events 142
- > Welcome to Elettra 148
- > Visits 153





RESEARCH HIGHLIGHTS

CHEMICAL AND MATERIALS SCIENCE



X-ray IMAGING AND MICROSPECTROSCOPY STUDY OF METALLIC PLATE CORROSION AND UPTAKE OF CORROSION PRODUCTS BY NAFION IN PEMFCs

B. Bozzini¹, A. Gianoncelli², B. Kaulich², M. Kiskinova², M. Prasciolu³, I. Sgura⁴

¹Dipartimento di Ingegneria dell'Innovazione, Università del Salento, Lecce, Italy

²Sincrotrone Trieste S.C.p.A., Trieste, Italy

³Laboratorio Nazionale TASC IOM-CNR, Trieste, Italy

⁴Dipartimento di Matematica, Università del Salento, Lecce, Italy

E-mail: benedetto.bozzini@unisalento.it



TWINMIC

Polymer Electrolyte Fuel Cells (PEFC) are a hot topic within the realm of sustainable and renewable energetics. Notwithstanding the huge research effort deployed for the development of these devices, state-of-the-art systems are still far from widespread use. The two crucial drawbacks are the excessive weight and the limited durability. Currently, about 80% of the weight and 45% of the cost are due to the use of graphite bipolar plates (BiP) [1]. Thinner, lighter and cheaper BiPs can be fabricated with metals, whose operation is nevertheless impaired by corrosion-related problems - chiefly due to galvanic contact with C-based materials - such as: (i) release of cationic species that will interact with other critical FC materials (chiefly PE and catalysts); (ii) formation of high-resistance layers at the BP/Gas Diffusion Layer interface; (iii) loss of hydraulic tightness across the BPs owing to formation of perforating pinholes. In particular, it has been proven that the presence of trace amounts of some metals, such as Fe^{2+} , ions tends to enhance radical attack of Nafion and to poisons proton hopping sites [2].

In order to develop efficient, stable and long lasting PEFCs, the degradation modes of the different components ought to be understood at a molecular level in working devices. The major obstacle in this respect is that we need appropriate morphologically and chemically sensitive methods with sufficient lateral resolution for monitoring the relevant local processes going on under electrochemical conditions. Recently, this requirement has been in part met by the demonstration of soft X-ray transmission microscopy (SXTM), combined with micro-spot X-ray absorption spectroscopy (μ -XAS) with sub-micrometer resolution, during in-situ electrochemical experiments [3, 4].

In this report, we highlight the corrosion of Fe electrodes in contact with a hydrated Nafion film in a thin-layer cell. The STXM images in Figure 1(a-c), taken using photon energies below and across the Fe L edge, reflect the density distribution and complex morphology resulting from corrosion processes taking place under working conditions, encompassing residues of the solid electrode - exhibiting cracks and localised pits - and corrosion products migrated into the few μm thick electrolyte. The spatial variations in the Fe concentration are confirmed and the oxidation state pinpointed by the μ -XAS Fe L_3 spectra, measured at selected spots (Figure 1 (d)).

Figure 2 shows the XRF maps of C, F, O and Fe, measured in the area corresponding to Figure 1. XRF discloses a strong correlation between C and F, corresponding to the location of the fluorocarbon polymer. The Fe map correlates with that of O, indicating that the residual portion of the oxidised electrode is in fact composed of Fe oxi-hydroxides, coherently with the μ -XAS results. One can also observe that the electrode edges are smeared out, apparently due to corrosion.

The results obtained in this work are relevant to the fabrication and application of metallic BPs for PEMFCs, in particular we have contributed to the understanding of the way Fe films of nanometric thickness are corroded by galvanic coupling to Au in a thin-layer configuration. The obtained morphological and chemical details of the corrosion process and of the fixation of the corrosion products in the Nafion film reveal that corrosion of Fe is characterised by the diffusion of Fe species into the Nafion film, accompanied by changes of the Fe chemical state. This pioneering investigation of an electrochemical system em-

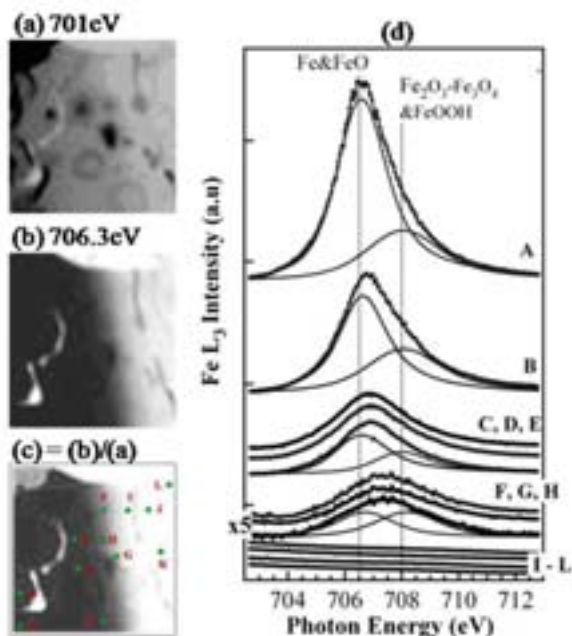


Figure 1. 22x22 μm^2 STXM images taken at photon energy (a) below (b) above the Fe L_3 -edge and (c) the Fe concentration map obtained after dividing the intensity at 706.3 eV by that at 701 eV. (d) μ -XAS Fe L_3 spectra measured in the indicated spots located at different distance from the Fe electrode edge.

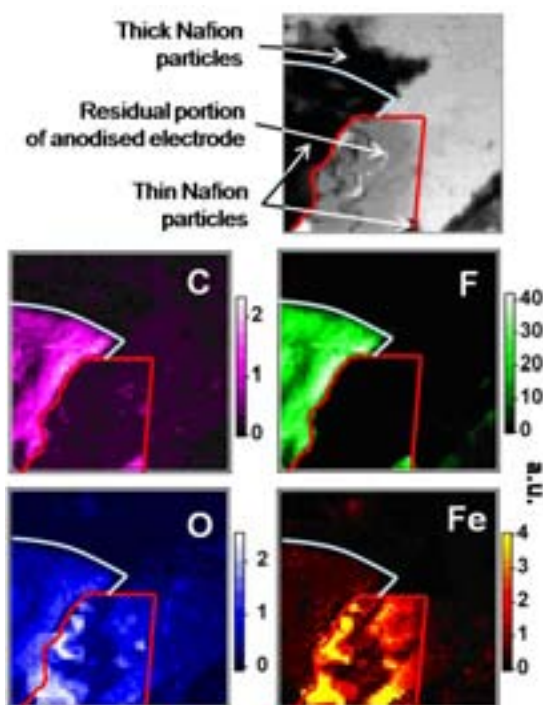


Figure 2. 40x40 μm^2 XRF maps of the Fe electrode acquired at 1014 eV photon energy. The color scales are also shown. The corresponding image with indication of the electrode and Nafion areas are indicated in the STXM image on the top-right.

ploying simultaneously soft X-ray imaging and two space resolved X-ray spectroscopies demonstrates the power of such approach not only for the system investigated - with potential impact in the acquisition of fundamental information relevant to fuel-cell technology - but potentially for all fields of electrochemical materials science and bioelectrochemistry.

References

- [1] Ch. Y. Chung, Sh. K. Chen, P.-J. Chiu, M.-Hs. Chang, T.-Ts. Hung, Ts.-H. Ko, *J. Power Sources* **176**, 276 (2008).
- [2] M. Inaba, M. Sugishita, J. Wada, K. Matsuzawa, H. Yamada, A. Tasaka, *J. Power Sources* **178**, 699 (2008).
- [3] B. Bozzini, L. D'Urzo, A. Gianoncelli, B. Kaulich, M. Kiskinova, M. Prasciolu, A. Tadjeddine, *Electrochem. Comm.* **10**, 1680 (2008).
- [4] B. Bozzini, L. D'Urzo, A. Gianoncelli, B. Kaulich, M. Prasciolu, I. Sgura, E. Tondu and M. Kiskinova, *J. Phys. Chem. C* **113**, 9783 (2009).

METHANE PARTIAL OXIDATION ON NiCu-BASED CATALYSTS

L. De Rogatis¹, T. Montini¹, A. Cognigni², L. Olivi², P. Fornasiero¹

¹Department of Chemical Sciences, University of Trieste, Trieste, Italy

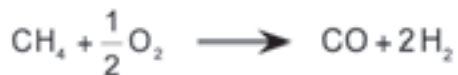
²Sincrotrone Trieste S.C.p.A., Trieste, Italy

E-mail: tmontini@units.it



XAFS

Hydrogen (H₂) demand is increasing worldwide since this is a very important molecule in the chemical industry and it represents a possible energy vector for energy production in the future in combination with fuel cells. Nowadays, H₂ is mainly produced by methane steam reforming, a highly endothermic process [1], but more efficient and less expensive processes must be developed to meet the hydrogen demand in the next decades. In this context, Catalytic Partial Oxidation of Methane (CPOM) is considered an interesting alternative since the process is slightly exothermic (drastically reducing the requirement of external heat) and produces syn-gas with a good composition, important for many applications (H₂ production after purification, methanol synthesis, Fischer-Tropsch synthesis etc.) [2].



For the CPOM process, heterogeneous catalysts comprising both noble metals (Pt, Rh, Ru etc.) and other d metals (essentially Ni) are widely investigated. Concerning the less expensive Ni-based catalysts, the main drawback of these systems is a considerable coke deposition, which easily deactivates the catalysts [3]. In this work, Al₂O₃-supported Ni-based catalysts have been investigated for the CPOM process with the aim to reduce the coke production and increase the stability of these systems by alloying the active phase with Cu.

All the samples possess a high surface area (80 – 100 m² g⁻¹), in agreement with the properties of the commercial support used. Powder XRD evidences the presence of transitional γ -Al₂O₃ and θ -Al₂O₃. Moreover, XRD patterns of samples reduced at 750 °C in H₂ flow indicate the formation of a Ni-Cu alloy in Ni(5%)-Cu(5%)/Al₂O₃ with cubic structure and cell parameter in good agreement with the theo-

retical value calculated by Vegard's law. CO chemisorption allows to estimate an apparent particle size of ~ 25nm for both reduced Ni(10%)/Al₂O₃ and Ni(5%)-Cu(5%)/Al₂O₃.

XANES/EXAFS spectroscopy was employed to analyze the chemical state of Ni and Cu in the samples reduced in H₂ flow at 750 °C and exposed to air. By linear combination of the normalised XANES spectra of the Ni and NiO as well as Cu, CuO and Cu₂O standards, it was possible to reconstruct the normalised spectra of the samples and to find out the weighted fraction of every component in the materials. The analysis of the Ni(10%)/Al₂O₃ evidences the presence of highly dispersed NiO in the calcined sample while the reduced sample is formed by a combination of metallic Ni (65%) and NiO (35%) (see Figure 1). In the case of Ni(5%)-Cu(5%)/Al₂O₃, the quality of the reconstruction of the XANES spectra (both at the Ni and Cu K edges) is lower, suggesting that at least another phase is present (Figure 1). EXAFS analysis evidences very low M – M coordination numbers in all cases, suggesting a high dispersion of the metal phases. In conclusions, the characterization of the reduced samples evidences a high dispersion of the metal phases, an effective formation of Ni-Cu alloy in the bimetallic sample and a easy re-oxidation of the metal nanoparticles after exposure to O₂ (at least as an oxidized superficial layer that passivates the metal nanoparticles).

The CPOM activity of pre-reduced Ni(10%)/Al₂O₃ and Ni(5%)-Cu(5%)/Al₂O₃ is presented in Figure 2. Upon increasing the catalyst temperature, different phenomena are observed. A small O₂ consumption is observed between 150 and 250 °C, indicating that a partial re-oxidation of the metal phases takes place (similarly to the pre-reduced samples exposed to air during XANES/EXAFS analysis). Above 300 °C, significant CH₄ and O₂ conversion is

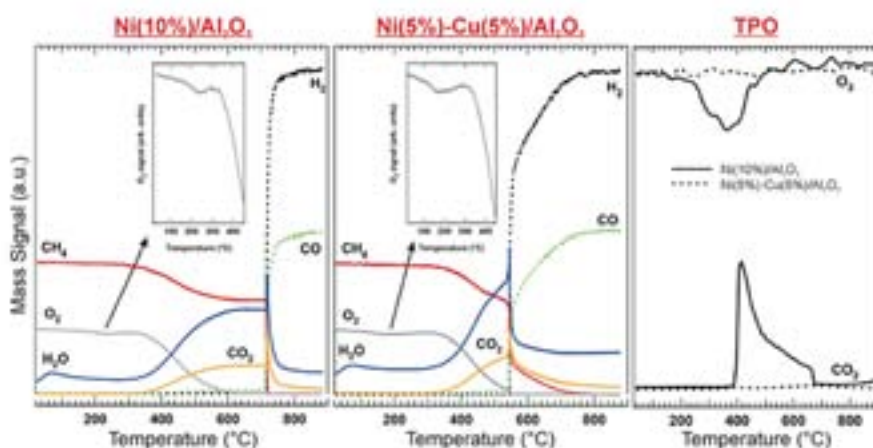


Figure 1. Fitting of the XANES spectra of pre-reduced Ni(10%)/Al₂O₃ and Ni(5%)-Cu(5%)/Al₂O₃.

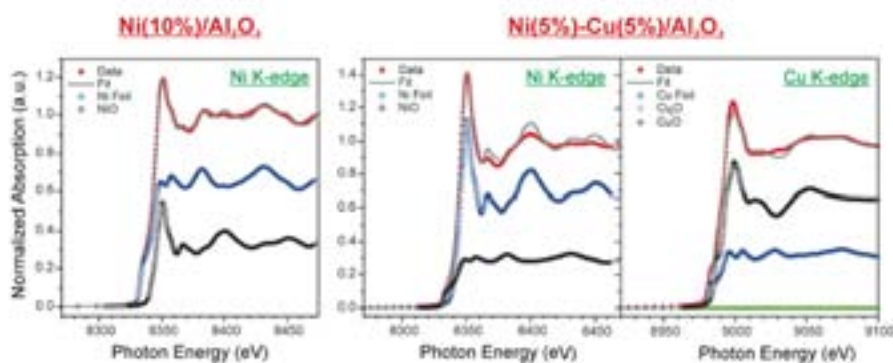


Figure 2. CPOM activity on pre-reduced Ni(10%)/Al₂O₃ and Ni(5%)-Cu(5%)/Al₂O₃. Conditions: CH₄ (2.0%) + O₂ (1.0%) in Ar, GHSV = 50000 mL g⁻¹ h⁻¹. Coke deposition were evaluated by Temperature Programmed Oxidation (TPO) on the aged catalysts.

observed with concomitant production of CO₂ and H₂O, suggesting that the combustion of CH₄ is preferred with respect to CPOM. Above a critical temperature, a sharp increase in the syn-gas production (H₂ and CO) is observed, with the concomitant decrease in the amounts of CH₄, CO₂ and H₂O. This critical temperature is strongly influenced by the composition of the metal phase (710 °C for Ni(10%)/Al₂O₃ and 540 °C for Ni(5%)-Cu(5%)/Al₂O₃), suggesting that the presence of Cu promotes the elimination of the passivating layer. Both the catalysts show stable performances under CPOM conditions at 900 °C for at least 65h. Temperature Programmed Oxidation (TPO) experiments performed on aged catalysts (Figure 2) show the evolution of CO₂ only from aged Ni(10%)/Al₂O₃, suggesting a beneficial effect of Cu in the reduction of the coke deposition of reforming Ni- based catalysts.

References

- [1] M. E. S. Hegarty, A. M. O'Connor, J. R. H. Ross, *Catal. Today* **42**, 225 (1998).
- [2] P. Ferreira-Aparicio, M. J. Benito, J. L. Sanz, *Catal. Rev. Sci. Eng.* **47**, 491 (2005).
- [3] H. S. Benggaard, J. K. Norskov, J. Sehested, B. S. Clausen, L. P. Nielsen, A. M. Molenbroek, J. R. Rostrup-Nielsen, *J. Catal.* **209**, 365 (2002).

FABRICATION OF ADVANCED FUNCTIONAL DEVICES COMBINING Sol-Gel WITH X-ray LITHOGRAPHY

P. Falcaro¹, L. Malfatti², S. Costacurta³, B. Marmiroli⁴, G. Greci⁵, L. Vaccari⁶, H. Amenitsch⁴, P. Innocenzi²

¹CSIRO, Division of Materials Science and Engineering, Victoria 3169, Australia

²Laboratorio di Scienza dei Materiali e Nanotecnologie (LMNT), CR-INSTM. Università di Sassari, Alghero (SS), Italy

³Associazione CIVEN - Nano Fabrication Facility, Venezia, Italy

⁴Institute of Biophysics and Nanosystems Research, Austrian Academy of Sciences, Graz, Austria

⁵Laboratorio Nazionale TASC IOM-CNR, Trieste, Italy

⁶Sincrotrone Trieste S.C.p.A., Trieste, Italy

E-mail: paolo.falcaro@csiro.au, plinio@uniss.it



DXRL

Lithography offers a method by which fine-scale patterns, required for fabrication and integration of component devices, are achieved. Increasing resolution and making the process easier, faster, cheaper or more versatile are the current areas of focus to improve existing micro- and nanofabrication techniques [1]. In our recent discoveries, the Deep X-ray Lithography (DXRL) facility at Elettra has been combined with sol-gel syntheses to efficiently fabricate a wide variety of patterned functional hybrid films. Depending on the coating, a one- or two-step lithographic process (exposure or exposure and developing, respectively) can be performed within a few minutes of irradiation. This approach can exploit the newest sol-gel hybrid materials for applications in microelectronics, organic electronics, biotechnology, microfluidics, or complex smart platforms such as lab-on-a-chip. Here we present how this new approach has been discovered and what are the recent developments of this technique.

In 2006, during an in situ study of the self-assembly process on hafnia, using the Austrian Small Angle X-ray Scattering (SAXS) beam line at the Elettra, an interaction between X-rays and the hybrid matrix has been detected [2]. Briefly, using synchrotron radiation it has been possible to selectively induce the collapse of the mesostructure on the areas exposed to the X-ray beam. Motivated by this preliminary experiment, deep X-ray lithography has been used to pattern mesoporous films using synchrotron radiation. The potential of the technique that uses X-ray lithography to pattern mesostructured sol-gel silica films has been demonstrated in 2008 [3]. The films, synthesized mesoporous using an organic block co-

polymer (Pluronic F-127) as templating agent, have been exposed to hard X-ray. After that, the films have been washed with a mixture of ethanol/ethylene glycol. In few minutes, the unexposed region can be easily etched. This developing process is fast and effective, as proved by optical profilometry measurements and FTIR mapping. The hexagonal 2D mesostructure (p6m space group) in the silica matrix is not affected by the X-ray lithographic process, as confirmed by SAXS.

The FTIR investigation on the films, before and after X-ray exposure, shows that a sharp decrease in intensity of some organic modes occurred (e.g., the CH₂ stretching mode). The surfactant molecules have been decomposed by X-ray radiation. A further study pointed out how DXRL can be used to efficiently pattern hierarchical hybrid organic-inorganic thin films as well [4]. In particular, the patterning process has been performed on a film with different templating agents (supramolecular units obtained by Pluronic F-127 and fluorinated organic nanoparticles). A tetragonal arrangement of micelles has been obtained through a self-assembly process of Pluronic F-127. TEM images on such coatings show 2 different pores size (6 and 60 nm, related to micelles and nanoparticles respectively). A mixture of methyltriethoxysilane (MTES) and triethoxysilane (TEOS) precursors has been used to synthesize the organic-inorganic matrix. The samples were exposed through X-ray masks containing test patterns (of different size and shape from 20 to 500 μm). After the lithography the exposed regions can be easily etched. The measure of the refractive index makes the film interesting for microelectronics applications and the possibility to precisely pattern

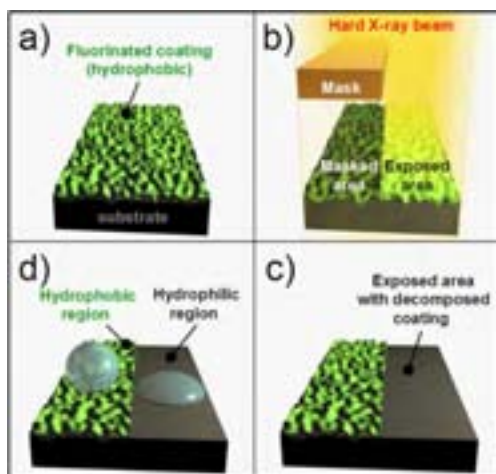


Figure 1.

Procedure involving Deep X-Ray Lithography to pattern fluorinate hydrophobic functionalized surface (a). The exposed regions allow for the interaction between the X-rays and the organic functionality of the film, while the masked regions are protected from radiation damage (b). Under the proper conditions, X-rays completely decompose the hydrophobic coating (c). In the exposed and masked regions, different contact angles are detected (d).

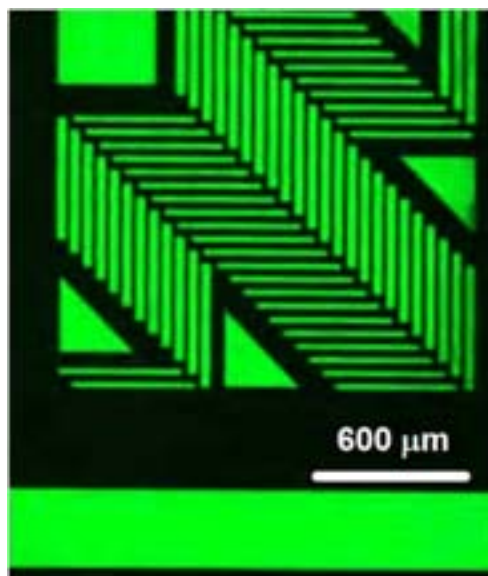


Figure 2.

Aminosilane coating lithographed with hard X-rays. A laser scanner measurement reveals the dye molecules (green regions) selectively bonded to the aminosilanes in the unexposed regions (areas with the undamaged molecule functionalities).

such coating with X-rays might open new prospective for device fabrication. The SAXS measurements confirm that X-ray lithography does not affect the mesostructure on silica films. The hierarchically porous film exhibited a lower refractive index compared to the film prepared using TEOS only.

The capability of DXRL to induce local changes in chemical groups with specific properties has been investigated in non porous films as well [1]. Colloidal silica nanoparticles solution has been used for coating depositions. The film of nanoparticles has been decorated with a fluorosilane (1H,1H,1H,2H,2H-perfluoro-octyltriethoxysilane). The contact angle measured on the fluorinated film (around 140°) highlights the high hydrophobicity of the coating. Few minutes' exposure to hard X-ray is enough to decrease the angle down to 10° (high hydrophilicity). Therefore, a contact angle change around 130° has been induced with an external source (one-step process, Figure 1). The capability to master the hydrophobic/hydrophilic properties is an important issue to develop surfaces suitable for microfluidic devices.

A solution containing a mixture of TEOS, MTES and 3-aminopropyltriethoxysilane (APTES) has been dip-coated on silicon and silica substrates. Using DXRL, 5 min of expo-

sure are enough to decompose the amino functionalities on the unmasked regions. A dye has been used to highlight the ability of the amino functionalized surface to bind biomolecules, as required by microarray technology. The resulting laser scan images are presented in Figure 2. The strong difference observed in the fluorescence intensity reproduces exactly the mask shape. Dye molecules bind to the amino groups only on unexposed areas. With this approach and by using a proper mask, different patterned functionalized surfaces can be prepared for selective molecule recognition.

References

- [1] P. Falcaro, L. Malfatti, L. Vaccari, H. Amenitsch, B. Marmiroli, G. Greci, P. Innocenzi *Adv. Mater.* **21**, 4936 (2009).
- [2] P. Falcaro, S. Costacurta, L. Malfatti, M. Takahashi, T. Kidchob, M. Casula, M. Piccinini, A. Marcelli, B. Marmiroli, H. Amenitsch, P. Schiavuta, P. Innocenzi, *Adv. Mater.* **20**, 1864 (2008).
- [3] L. Malfatti, T. Kidchob, S. Costacurta, P. Falcaro, P. Schiavuta, H. Amenitsch, P. Innocenzi, *Chem. Mater.* **18**, 4553 (2006).
- [4] P. Falcaro, L. Malfatti, T. Kidchob, G. Giannini, A. Falqui, M. F. Casula, H. Amenitsch, B. Marmiroli, G. Greci, P. Innocenzi *Chem. Mater.* **21**, 2055 (2009).

FRACTAL STRUCTURE IN THE SPACER LAYERS FAVOURS HIGH TEMPERATURE SUPERCONDUCTIVITY IN $\text{La}_2\text{CuO}_{4+y}$

G. Campi¹, M. Fratini^{2*}, N. Poccia², A. Ricci², A. Bianconi²

¹Institute of Crystallography, CNR, Monterotondo-Roma, Italy

²Department of Physics, Sapienza University of Rome, Roma, Italy

*Present address: Institute for Photonic and Nanotechnologies, CNR, Roma, Italy

E-mail: antonio.bianconi@roma1.infn.it



XRD1

The discovery of oxygen «superstructures» in cuprates has shed new light on the origins of high-temperature superconductivity, which has been a major theme in the physics of the last 20 years. All high-temperature superconductors consist of parallel planes of copper oxide sandwiched between rock-salt layers. The metallic quasi two-dimensional phase is due to itinerant “holes” moving in the planar oxygen orbitals, while charge neutrality is assured by chemical dopants that provide the static negative localized charges in the spacer layers. The motivation of this research is based on the idea that the distribution of chemical dopants in the spacer layers is relevant to understand the complexity of these systems driven by interplay between superconducting and magnetic phases in copper-oxide based superconductors. Complexity emerged as a paradigm for understanding the high temperature superconductivity when, investigating the local structure of the Cu oxide plane by a fast and local probe such as EXFAS, it was found that the statistical distribution of the instantaneous local lattice conformations of the Cu sites was quite different from the structure averaged in time and space [1]. The interest soon shifted toward a special system $\text{La}_2\text{CuO}_{4+y}$ [2] where the chemical dopants in the spacer layers are oxygen interstitial ions inserted in the rocksalt $[\text{La}_2\text{O}_{2+y}]^{2-\delta}$ intercalated by $[\text{CuO}_2]^{2-\delta}$ layers. Due to the interstitial oxygen mobility, this compound exhibits a rich phase diagram with:

(i) a phase separation between a low doped anti-ferromagnetic phase ($y=0.01$) and a superconductivity phase ($y=0.05$);

(ii) a second phase separation at $y>0.06$ between a magnetic commensurate striped crystal ($y=0.06$) and a superconductor at optimum doping ($y=0.1$) with $T_c=40$ K [3].

In this framework, our idea has been that the mobility of the intercalated oxygen ions, i-O is expected to track the phase separation in these materials in some way since the chemical potential in the spacer layers and in the superconducting layers should be the same at equilibrium. The search for the ordering of i-O has been carried out for about ten years on the XRD1 beamline at the Elettra synchrotron in Trieste; we have identified the weak diffraction superstructure spots, shown in Fig. 1B, due to the ordering of i-O and how they depend on the thermal treatment in the $\text{La}_2\text{CuO}_{4.1}$ ($T_c=40\text{K}$) sample. Our single-crystals show the main Bragg reflections of orthorhombic $Fmmm$ space group surrounded by the known satellite peaks with wavevector $q_2 = (0.087\pm 0.004)a^* + (0.247\pm 0.003)b^* + (0.497\pm 0.005)c^*$ where a^* , b^* and c^* are the reciprocal lattice units. These superstructures [4] are associated with the three-dimensional ordered i-O dopants. In fact, they get disordered at higher temperatures, as shown by the behavior of integrated intensity, $\langle I \rangle$, of the q_2 superstructure peak in Fig. 2a: we heated the sample at a slow rate observing a continuous order-to-disorder phase transition in the [300–350] K range. Subsequently, starting from this disordered phase, the sample was rapidly quenched below 200K, producing so, a stable disordered arrangement of frozen randomly distributed i-O. This was followed by a very slow heating that leads the i-O to move and rearrange themselves; as a result, a disorder-to-order transition in the [180–200] K range is observed. Further increasing of the temperature, in combination with annealing processes, affects and controls the i-O ordering; in particular, annealing the sample for a long time at constant temperature in the [200–

300] K range allows the i-O ordering to reach the maximum allowed intensity of the q_2 superstructure (Fig. 2a).

Using different annealing times in the [200–300] K range followed by quenching produces samples with different i-O domain order. In Fig. 2a we show two *annealing/quenching* processes indicated by A and B: the higher degree of the i-O ordering obtained in A leads to higher T_c , as shown in Fig. 2b by measurements of the superconducting diamagnetic response. We used a single-coil inductance method recording $(\omega_0/\omega(T))^2$, where $\omega(T)$ is the resonance frequency of an LC circuit, L is the inductance of the submillimetre coil placed near the surface of the superconducting sample and ω_0 is the reference resonance frequency for a non-superconducting sample. The green curve is for the $T_c=40$ K phase where $\langle I \rangle$ is larger (annealing process A), while the red curve is for the two $T_c=16+32$ K phase, where $T_{c1}=16$ K, $32 < T_{c2} < 36$ K and $\langle I \rangle$ is small (annealing process B).

The i-O ordered domains in these phases show an intriguing spatial distribution; indeed, using space resolved X ray diffraction measurements, performed at the ID13 beamline at ESRF, we find that the arrangement of these atoms changes from point to point (Fig. 1C), and the ordered patterns draw fractal networks [4]; moreover, larger extent of spatial correlations in these networks is related to higher critical temperature for superconductivity. These results open new avenues in the double-sided issue of superconductivity, which pertains to both technology, as related to controlled fabrication of superconducting devices, and to basic physics, as related to the formation and evolution of quantum coherence in matter.

References

- [1] A. Bianconi et al. *Phys. Rev. Lett* **76**, 3412–3415 (1996).
- [2] A. Lanzara, et al. *Phys. Rev. B* **55**, 9120–9124 (1997).
- [3] H. E. Mohottala et al. *Nature Mater.* **5**, 377 (2006).
- [4] M. Fratini, N. Poccia, A. Ricci, G. Campi, M. Burghammer, G. Aeppli & A. Bianconi, *Nature*, **466**, 841 (2010).

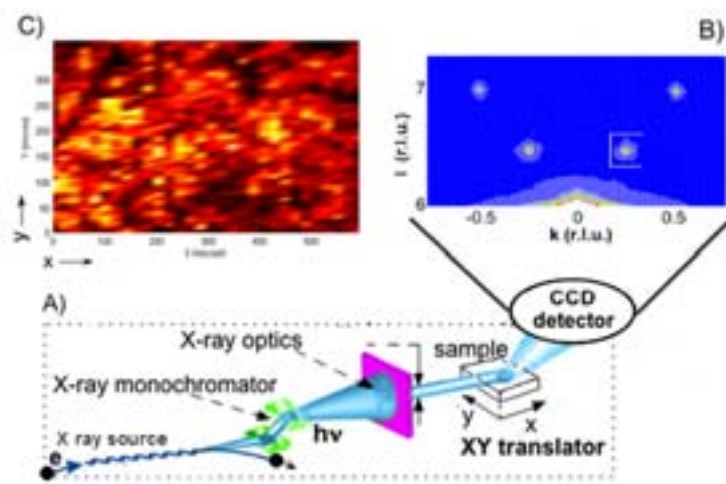


Figure 1.

A) Experimental setup for X ray micro-diffraction measurements. B) X ray diffraction image with satellite reflections q_2 surrounding the main 006 Bragg peak. C) Mapping of the $\langle I \rangle$ intensity of the q_2 superstructure with a beam size of $1\mu\text{m} \times 1\mu\text{m}$ in a $600 \times 400\mu\text{m}$ region of the surface of the sample.

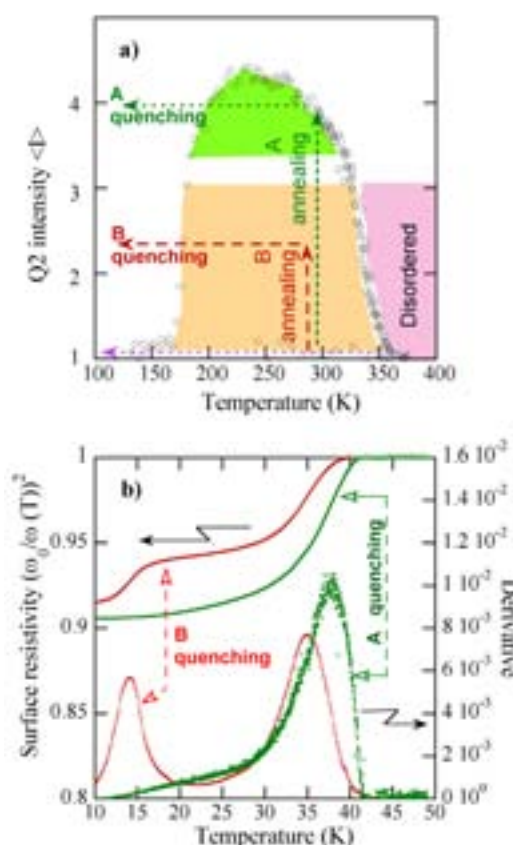


Figure 2.

a) The integrated intensity of the q_2 superstructure satellite reflections as a function of the temperature. The A and B *annealing/quenching* processes are indicated. b) Complex conductivity $(\omega_0/\omega(T))^2$ measured in the A and B case; the derivatives of $(\omega_0/\omega(T))^2$ are also shown in the lower part of the figure.

RE-OXIDATION OF REDUCED CERIA AS AN INDICATOR FOR CO₂ ACTIVATION

T. Staudt¹, Y. Lykhach¹, N. Tsud², T. Skála³, K.C. Prince³, V. Matolín^{2,3}, J. Libuda^{1,4}

¹Lehrstuhl für Physikalische Chemie II, Friedrich-Alexander-Universität Erlangen-Nürnberg, Erlangen, Germany

²Department of Surface and Plasma Science, Charles University, Prague, Czech Republic

³Sincrotrone Trieste S.C.p.A., Trieste, Italy

⁴Erlangen Catalysis Resource Center, Erlangen, Germany

E-mail: Yaroslava.Lykhach@chemie.uni-erlangen.de



MATERIALS SCIENCE

Activation of CO₂, e.g. its splitting into CO and oxygen, is the most critical step with respect to its utilization in chemical processes. Effective CO₂ activation is crucial, for example, for dry reforming of methane [1, 2]. The reaction is usually carried out over a surface of a solid oxide catalyst loaded with finely dispersed transition or noble metal particles. The two gases, methane and CO₂, interact with the surface of the catalyst in a very different fashion. Whereas methane decomposes mainly on the surface of the noble metal, CO₂ is initially anchored on the oxide surface. Mechanistic details of this important reaction are only poorly understood, however. CO₂ may initially be adsorbed in the form of carbonates or carboxylates. In the next step, part of the hydrogen released upon methane decomposition, reacts with these species, yielding CO and water.

Ceria (CeO₂) based materials are considered to be effective catalysts for CO₂ activation. In its reduced form (Ce₂O₃), Ce³⁺ ions serve as active sites for carbonate/carboxylate formation. Direct dissociation of CO₂ into CO and oxygen was reported on metal-loaded ceria. In presence of supported Pt or Pd metals, CO is released into the gas phase and oxygen is consumed by the ceria support. The uptake of oxygen by reduced ceria upon CO₂ dissociation finally causes its re-oxidation. The reaction mechanism on the oxide and the role of the noble metal has been debated and contradicting experimental results have been published.

In our study we demonstrated [3] that the dissociation of CO₂ and the following re-oxidation of ceria does not require a noble metal component nor the presence of surface hydroxyl groups. In fact, the atomically clean and strongly reduced ceria surface exhibits a high intrinsic activity towards CO₂, causing its

partial re-oxidation even at room temperature.

These conclusions were obtained from studies on ceria model catalyst surfaces under ultrahigh vacuum (UHV) conditions. The adsorption of CO₂ was tested at 300 K on strongly pre-reduced ultra-clean ceria films. These films were prepared by the methanol mediated reduction of well-ordered epitaxial CeO₂ thin films grown on a Cu(111) single crystal surface under UHV conditions.

The most important property of ceria is the facile release and uptake of lattice oxygen [4]. During this process, cerium ions change their oxidation state between Ce³⁺ and Ce⁴⁺. We take advantage of these changes of oxidation state and use them as an indicator for CO₂ dissociation. To monitor the effect, we employed resonant photoelectron spectroscopy (RPES) at the Materials Science Beamline. The method is based on measuring the valence bands at photon energies corresponding to the 4d→4f resonance, either in Ce³⁺ or Ce⁴⁺ ions. The ratio of the resonant enhancements of the corresponding features D(Ce³⁺)/D(Ce⁴⁺), denoted as the resonant enhancement ratio (RER, see Fig. 1), is a direct measure for Ce³⁺/Ce⁴⁺ ratio at the ceria surface.

The loss of lattice oxygen during methanol reduction is accompanied by a significant increase of D(Ce³⁺) and a corresponding decrease of D(Ce⁴⁺) resonant features (Fig. 1a and Fig. 1b). On the contrary, recovery of lattice oxygen upon CO₂ dissociation leads to a decrease of D(Ce³⁺) and increase of D(Ce⁴⁺) (Fig. 1b and Fig. 1c). The evolution of the RER is displayed in Figure 2 as a function of CO₂ exposure. A detailed analysis reveals a dependency of the reaction probability on the degree of reduction: The reaction probability is large for a strongly reduced surface, but decreases

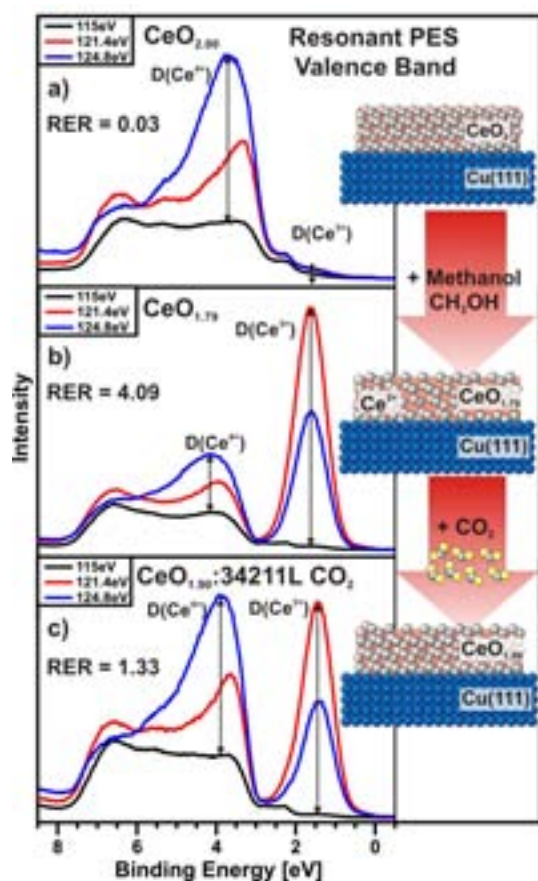


Figure 1. Valence band spectra obtained at photon energies corresponding to resonant enhancement in Ce^{3+} (121.4 eV), Ce^{4+} (124.8 eV) and off resonance (115 eV): a) stoichiometric CeO_2 film, b) reduced ceria film, c) ceria film after re-oxidation by CO_2 at 300 K (CO_2 dose: 34200 L).

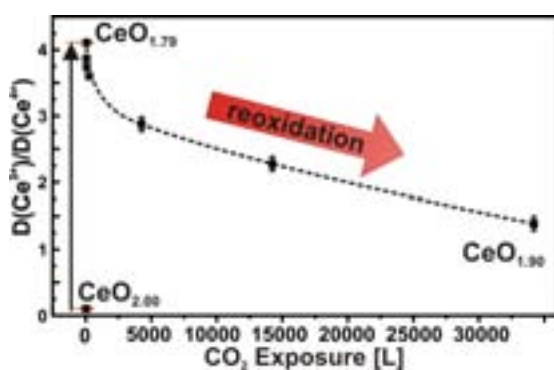


Figure 2. Evolution of RER during stepwise exposure of reduced ceria to CO_2 at 300 K.

rapidly as the reaction proceeds. The detailed mechanism of CO_2 dissociation remains unclear, yet. Planned theoretical calculations and vibrational spectroscopy measurements may help to identify potential pathways and intermediates. Yet, it remains noteworthy that (i) no noble metal component and (ii) no water or OH groups are required for CO_2 dissociation on highly reduced ceria. CO_2 is activated on intrinsic defect sites of the ceria surface if the concentration of Ce^{3+} centers is sufficiently high. This intrinsic pathway for the decomposition of CO_2 is characterized by a remarkable low activation barrier, which allows efficient re-oxidation even at room temperatures.

References

- [1] Y. H. Hu, E. Ruckenstein, *Advances in Catalysis* **48**, 297 (2004).
- [2] M. C. J. Bradford, M. A. Vannice, *Catal. Rev.*, **41**, (1), 1 (1999).
- [3] T. Staudt, Y. Lykhach, N. Tsud, T. Skála, K. C. Prince, V. Matolín, J. Libuda, *J. Catal.* **275**, 181 (2010).
- [4] A. Trovarelli, *Catalysis by Ceria and Related Metals*, Imperial College Press (2002).

BIO-INSPIRED WATER OXIDATION ELECTRODES INTEGRATING CARBON NANOTUBES AND OLYOXOMETALATES

F.M. Toma^{1,2}, P. Parisse³, M. Carraro⁴, A. Sartorel⁴, T. Da Ros¹, L. Casalis³, A. Goldoni³, H. Amenitsch⁵, F. Bondino⁶, G. Scoles³, M. Prato¹, M. Bonchio⁴

¹Chemistry Department, University of Trieste, Trieste, Italy

²International School for Advanced Studies (S.I.S.S.A.), Trieste, Italy

³Sincrotrone Trieste S.C.p.A., Trieste, Italy

⁴Chemistry Department, University of Padova, Padova, Italy

⁵Austrian Academy of Sciences, Wien, Austria

⁶Laboratorio Nazionale TASC IOM-CNR, Trieste, Italy

E-mail: pietro.parisse@elettra.trieste.it



BACH
SAXS
Nanostructure Lab (SENIL)

Obtaining clean energy is one of the major challenges of present day research and mimicking what nature does, may be a suitable way to succeed. Nonetheless, artificial photosynthesis is still not within our reach because, due to the large endothermicity ($\Delta G = 113.38$ kcal (4.92 eV)) of the water oxidation reaction, the process that plants continuously use to obtain sugars and oxygen from the basic ingredients, light and water, is far from being fully understood and efficiently reproduced.

A multi-center multi-discipline collaboration involving researchers at UNITS, UNIPd and Elettra, has achieved the implementation of a very efficient water-oxidation catalyst onto a conductive solid support, whose catalytic activity was finally tested via electrochemistry by a group at UniBo. The chosen catalyst is a Ruthenium substituted polyoxometalate [di- γ -decatungstosilicate embedding a tetra-ruthenium(IV)-oxo, hereafter RuPOM]. It was previously proven that this polyoxometalate, in solution, is a unique molecular catalyst for water oxidation, due to the synergistic action of the four ruthenium sites that mimic, in an unprecedented way, the natural system of the Photosystem II enzyme [1]. Typically catalytic molecules, however, lose some of their properties when placed on a solid support to realize, for instance, a photo-active electrode.

The Trieste/Padova team has realized and characterized an oxygen evolving anode that combines the excellent catalytic properties of POMs with a solid conductive device that is needed to guide and transport the electrons released after water splitting, without changing the properties of the catalyst. To fulfill those requirements, we use multiwalled carbon nan-

otubes (MWCNT), decorated with positively charged polyamidoamine (PAMAM) dendrimers (MWCNT-dend). The characterization of this hybrid material by means of electrochemical studies attests the achievement of an impressive performance. The turn over frequency (TOF) measured is the highest reported: at pH 7.0, TOF was 36 h^{-1} at a low overpotential ($\eta=0.35\text{V}$), till 306 h^{-1} at $\eta=0.60\text{V}$.

The composite has been thoroughly characterized by means of a variety of complementary spectroscopy and microscopy techniques in solution and after deposition, by drop casting, into indium tin oxide (ITO) electrodes [2]. Here, we focus our attention on the measurements obtained by using small angle X-ray scattering (SAXS) and the X-Ray Photoelectron spectroscopy (XPS). The first technique provides information about the aggregation state of the RuPOM composite, whereas the chemical analysis provided by XPS is useful to gain insights on the oxidative states of the Ru in the complex and on the electron transfer between the RuPOM cage and the MWCNTs.

In Figure 1 we report the SAXS diffraction patterns obtained and analysed for both MWCNT-dend (dark cyan trace) and RuPOM@MWCNT (blue trace), both at pH 5.5, 0.5 mg/mL, and compared with the solution behaviour of Li10RuPOM in water (pH 5.5, 1 mg/mL red trace and 50 mg/mL black trace). The scattering pattern observed in solution for Li10RuPOM and the simulated curve are consistent with the geometry of the isolated molecule. The study on the solution gave a nearest-neighbour distance of 6 nm at 50 mg/mL and no indication of aggregation phenomena. The comparison of the experimental curves reg-

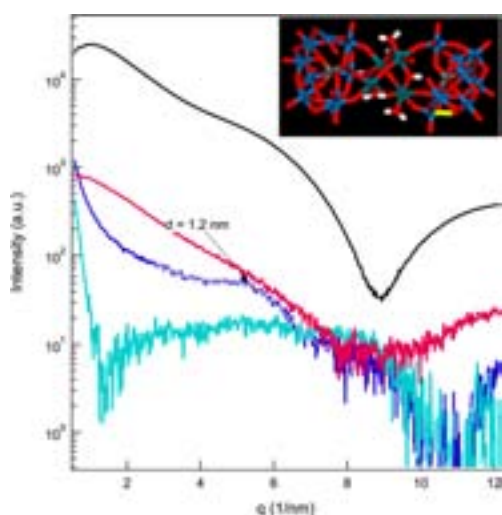


Figure 1. SAXS measurements (H_2O , pH 5.5) of RuPOM@MWCNT (blue curve, 1 mg/mL) and fitting of the correlation peak (grey curve) with a d -spacing of about 1.2 nm, of MWCNT-dend (dark cyan curve, 1 mg/mL) and of (1 blue curve, 0.5 mg/mL). q =scattering vector; a.u.=arbitrary units.

istered for RuPOM@MWCNT (Fig. 1, blue trace) and MWCNT-dend (Fig. 1, dark cyan trace) showed that, in the observed regime, the scattering from RuPOM is dominating over that from the MWCNT walls. Accordingly, the inorganic oxoclusters appear to be deposited on the MWCNT surface mainly as a single entity (nearest-neighbour distance was $d=1.2$ nm), with a compact distribution driven by the positively charged terminal functions of the dendron moiety. This is a key point to access single-site catalysis that approaches homogeneous behaviour.

In Figure 2, we report the XPS spectra of the C1s-Ru3d region for a RuPOM/ITO sample (Fig. 2a) and for a RuPOM@MWCNT-dend/ITO (Fig.2b). We can observe the presence of several features related to the C 1s and Ru 3d core levels. The C 1s shows peaks due to the unavoidable contamination during sample preparation (a) and to MWCNT-dend presence (b). We were able to separate the carbon components and then we resolved the Ru peak in two distinct components centered at 280.9 and 281.7 eV binding energy. The Ru3d peaks are due to Ru $^{4+}$ state [3] and to Ru with higher oxidation states [4], respectively. The ratio

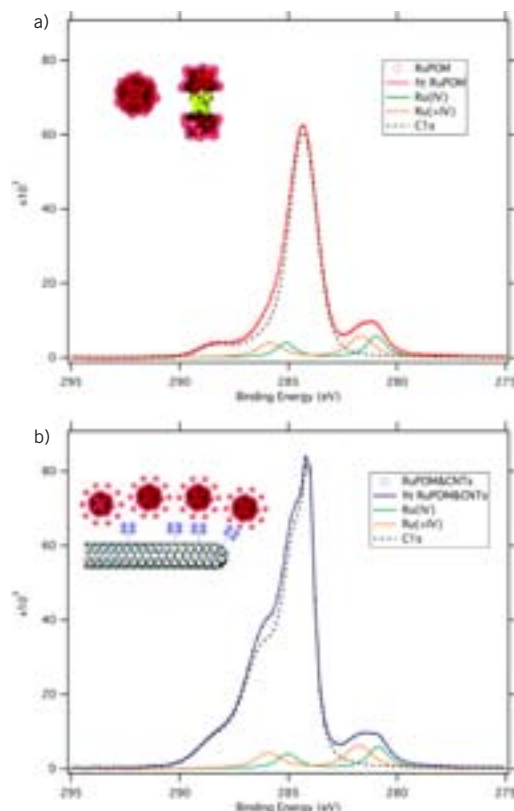


Figure 2. a) X-ray photoemission spectrum of the Ru3d-C1s region on a RuPOM/ITO sample with the side and top view sketch of the molecule. b) X-ray photoemission spectrum of the Ru3d-C1s region on a RuPOM-MWCNTS-dend/ITO sample with a sketch of the complex.

between the two components changes going from the pristine RuPOM to the RuPOM/MWCNT-dend. The presence of MWNTs induces a 30% increase of the component at higher binding energy and therefore of the Ru in an higher oxidation state, thus indicating a charge transfer between the RuPOM entities and the functionalized MWNTs.

These measurements helped in understanding the mechanism behind the impressive performance of the RuPOM/MWCNT-dend composite as water-oxidation catalyst. In particular, SAXS and XPS results have evidenced the fact that the formation of a nanostructured heterogeneous interface, between single entities of POMs and MWCNTs-dend, is responsible for the very efficient electron-transfer events under controlled conditions.

References

- [1] A. Sartorel et al., *J. Am. Chem. Soc.* **131**, 16051–16053 (2009).
- [2] F. M. Toma et al., *Nat. Chem.*, **2**, 826-831 (2010).
- [3] Pylypenko et al., *ACS Appl. Mater. & Inter* **1**, 604 (2009).
- [4] Li et al., *Appl. Phys. Lett.* **85**, 6157 (2004).

PROBING INTERLAYER RELAXATION AT A METAL-OXIDE INTERFACE

E. Vesselli^{1,3}, A. Baraldi^{1,3}, S. Lizzit², G. Comelli^{1,3}

¹Physics Department and CENMAT, University of Trieste, Trieste, Italy

²Sincrotrone Trieste S.C.p.A., Trieste, Italy

³Laboratorio Nazionale TASC IOM-CNR, Trieste, Italy

E-mail: alessandro.baraldi@elettra.trieste.it



SURFACE SCIENCE LABORATORY
SUPERESCA

Knowledge of the atomic positions at metal-oxide junctions is a prerequisite for the rational design of ultrathin oxide films interfaces with tailored properties. However, the breaking of the translational symmetry and the abrupt discontinuity often result in a large atomic rearrangement, confined within few Ångstrom from the interface, which is extremely difficult to characterize experimentally. Because of the large lattice mismatch, in general, the periodic structural modifications of the crystalline lattice extend laterally over a few nanometers. This strongly limits the applicability of diffraction techniques based on long-range order due to the large dimensions of the unit cells that may include up to thousands of atoms.

These problems are particularly relevant for ultrathin epitaxial oxide films grown on metals. Indeed, recent studies have shown that these systems cannot be considered in general as simple analogues of the corresponding thicker films, because of significant variations in the atomic structure at the interface that largely modify the electronic properties [1].

In this contest, ultrathin alumina films are considered of great interest, not only as supports in heterogeneous catalysis, but also for their application in the development of new high-K gate nanocapacitors, protective coatings against corrosion, and templates for nanopatterning. Despite the structural investigations of alumina films grown on Ni_xAl ($x=1, 3$) alloys, the morphology of this important metal-oxide interface still remains largely unsolved.

The possibility to separate nonequivalent atomic species in chemical state-specific x-ray photoelectron diffraction measurements, allowed us to unveil a large modification of the $\text{Ni}_3\text{Al}(111)$ ultrathin oxide film interface morphology [2].

The measurements, carried out at the Super-ESCA beamline and in a dedicated ultrahigh vacuum chamber of the Surface Science Laboratory, were performed at photon energies ranging from 150 to 1486 eV to collect Al 2*p* and O 1*s* core level spectra.

Upon formation of a well ordered alumina thin film, new components grow in the Al 2*p* core level spectrum (see Fig. 1a) with respect to the clean $\text{Ni}_3\text{Al}(111)$ surface (green curve). In addition to the bulk component (black), three distinct features appear, accompanied by their spin orbit split replicas (not shown in the Figure). With reference to the bulk feature, a peak (gray, Al_1) grows, which is attributed to the surface Al atoms at the metal-oxide interface. Additionally, two progressively larger features appear at higher binding energies, which can be associated to the oxide interface layer in contact with the substrate (red, Al_2), and to the oxide termination (orange, Al_3), respectively. The O 1*s* spectrum presents two components due to oxygen atoms at the metal-oxide interface (dark blue, O_1), and at the oxide terminal layer (blue, O_2), respectively (Fig. 1b).

In order to determine the structure of the alumina film we have compared the experimental photoelectron diffraction modulation functions of chemically nonequivalent aluminum and oxygen species with multiple-scattering simulations. An example of 2D diffraction pattern is reported in Fig. 1c for the O 1*s* core level corresponding to oxygen atoms at the interface. The structural optimization was performed using both Al 2*p* and O 1*s* signals, with an overall angular span of about 22000° and a unit cell consisting of more than 2300 atoms. Satisfactory agreement with the experimental modulation function was obtained only when full relaxation of the alumina and metal interlayer distances was allowed.

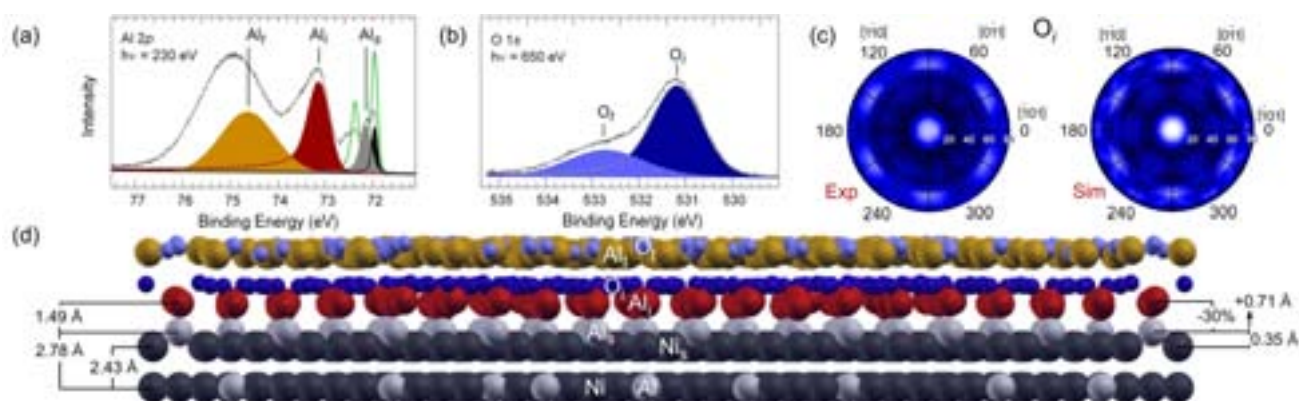


Figure 1.

(a) Al $2p$ and (b) O $1s$ core level spectra of the alumina/ $\text{Ni}_3\text{Al}(111)$ ultrathin film. Best fit and decomposition components are also shown, together with the Al $2p$ spectrum corresponding to the clean surface.

(c) O $1s$ experimental and simulated half-solid angle modulation function distributions in the forward-scattering regime. (d) Structural model of the relaxed oxide layers, including two Ni_3Al surface layers.

The remarkable outcome of this structural determination is the ejection of the alloy first-layer Al_s atoms towards the ultrathin oxide layer (see Fig. 1d). Al_s atoms are lifted by more than 0.7 \AA , yielding a first-to-second metal layer distance relaxation of +35%.

Our findings provide evidence for the formation of a new, low density, aluminum intermediate metallic layer at the metal-oxide interface and provide the first experimental support to the interface model recently proposed on the basis of theoretical *ab initio* thermodynamics calculations [3]. The formation of this new interface structure is crucial for the explanation of several properties of the aluminum

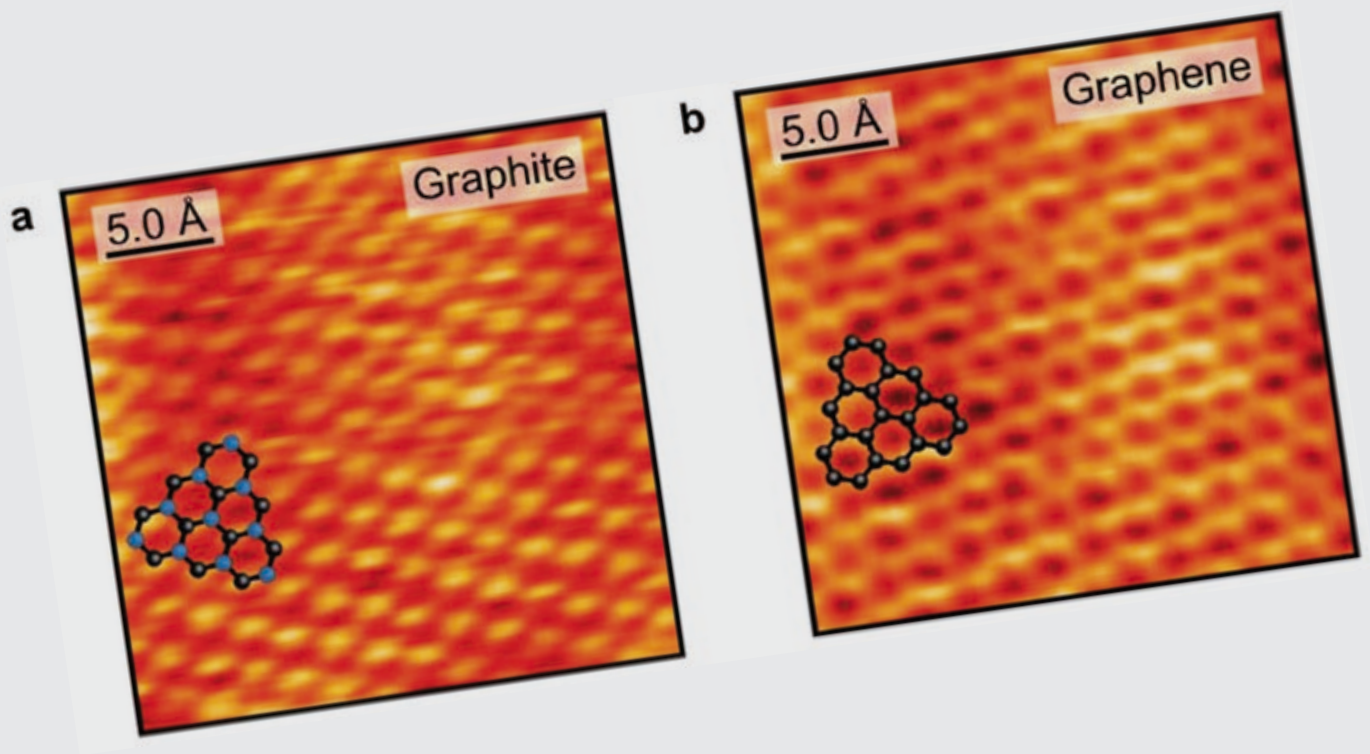
oxide films. For example, the geometrical arrangement of the Al atoms at the interface is a key feature for the use of alumina coatings as protective layers and for tuning the electronic properties of alumina supported active metal clusters, which is an important issue in the engineering of new catalytic materials.

References

- [1] C. Freysoldt, P. Rinke and M. Scheffler, *Phys. Rev. Lett.* **99**, 086101 (2007).
- [2] E. Vesselli, A. Baraldi, S. Lizzit, G. Comelli, *Phys. Rev. Lett.* **105**, 046102 (2010).
- [3] J. Feng, W. Zhang, W. Jiang, H. Gu, *Phys. Rev. Lett.* **97**, 246102 (2006).



GRAPHENE



a

5.0 Å

Graphite

b

5.0 Å

Graphene

GRAPHENE SYNTHESIS ON CUBIC SiC/Si WAFERS - PERSPECTIVES FOR MASS PRODUCTION OF GRAPHENE-BASED ELECTRONIC DEVICES

V. Yu. Aristov,^{1,2} G. Urbanik,¹ K. Kummer,³ D. V. Vylikh,³ O. V. Molodtsova,¹ A. B. Preobrajenski,⁴ A. A. Zakharov,⁴ C. Hess,¹ T. Hänke,¹ B. Büchner,¹ I. Vobornik,⁵ J. Fujii,⁵ G. Panaccione,⁵ Y. A. Ossipyan,³ and M. Knupfer²

¹Leibniz Institute for Solid State and Materials Research, Dresden, Germany

²Institute of Solid State Physics, Russian Academy of Sciences, Chernogolovka, Moscow District, Russia

³Institute of Solid State Physics, Dresden University of Technology, Dresden, Germany

⁴MAX-lab, Lund University, Lund, Sweden

⁵Laboratorio Nazionale TASC IOM-CNR, Trieste, Italy

E-mail: ivana.vobornik@elettra.trieste.it



The outstanding properties of graphene - a single graphite layer, render it a top candidate for substituting silicon in future electronic devices [1]. The so far exploited synthesis approaches, however, require conditions typically achieved in specialized laboratories, and result in graphene sheets whose electronic properties are often altered by interactions with substrate materials. The development of graphene-based technologies requires an economical fabrication method compatible with mass-production. Here we demonstrate the feasibility of graphene synthesis on cubic, commercially available β -SiC substrates, which result in macroscopic graphene flakes electronically decoupled from the substrate [2]. After optimization of preparation procedures, the proposed synthesis method can represent a big step towards graphene-based electronic technologies.

Current graphene production, although resulting in high quality graphene layers, does not meet the requirements of industrial mass-production because it involves processes performed by hand, such as mechanical exfoliation, or results in strong graphene-substrate interaction, altering the film properties.

Although α -SiC initially seemed promising for industrial graphene production (graphene is formed as an outcome of repeated annealing cycles), the considerable interaction between the fabrication costs of the α -SiC wafers, have precluded possible technological applications. On the other hand, cubic 3C-SiC (β -SiC) is readily grown onto large size commercially available Si wafers. Due to its cubic lattice, β -SiC would not appear suitable for graphene growth. Contrary to common belief, we succeeded in growing high quality graphene on cubic β -SiC and

found that the interaction with the substrate is almost negligible when compared to α -SiC, rendering this system a perfect candidate for future graphene-based electronics.

In order to understand which type of carbon overlayer is actually formed - graphite, graphene or both, we used scanning tunneling microscopy (STM). The topographic STM scans on a large micrometer scale show atomically flat terraces, whose size strongly depends on annealing time and temperature. We obtained two types of atomically resolved STM images (Fig. 1). The atomic pattern in Fig. 1A points to a graphite structure, where stacking of the monoatomic layers gives rise to two non-equivalent atomic sites. Due to the shift between neighboring layers half of the atoms of the upper layer are located directly above atoms of the lower layer (site A) while the other half is located above the hexagon centers in the lower layer (site B). Accordingly, A sites appear as minima and B sites as maxima in STM images, as demonstrated earlier. Fig. 1B shows the honeycomb array, characteristic for graphene. Here the stacking-induced asymmetry is absent and consequently all atomic sites are equivalent.

The electronic band structure of the occupied electronic states was examined by angle-resolved photoelectron spectroscopy (ARPES). A typically observed energy-momentum map is shown in Figure 2. The measured dispersion of the π and σ bands is characteristic of graphene. The additional, non-dispersive feature at about 3 eV binding energy is very likely caused by the presence of amorphous carbon, not included in the graphene flakes. The vertex of the π band at the Γ point lies at about 7.9 eV bind-

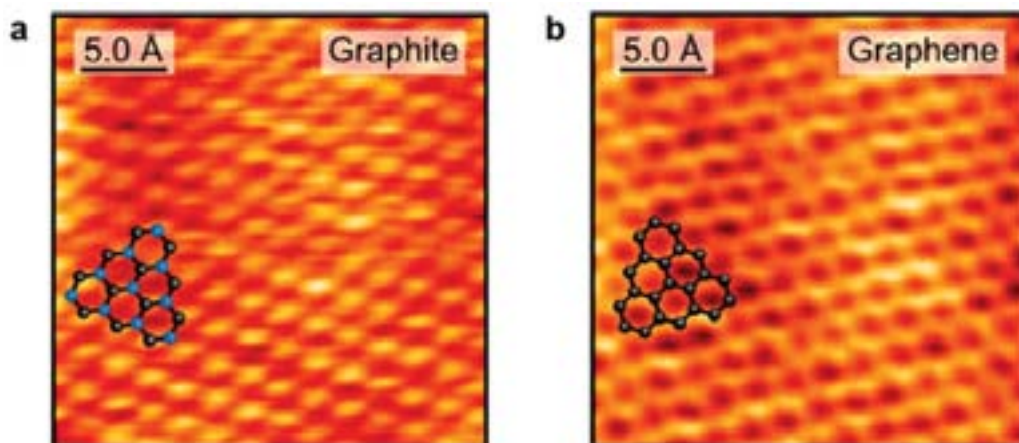


Figure 1. Scanning tunneling microscopy. (a) Graphite structure, (b) Graphene structure: All carbon atom sites are equivalent. Hence the characteristic honeycomb pattern shows up.

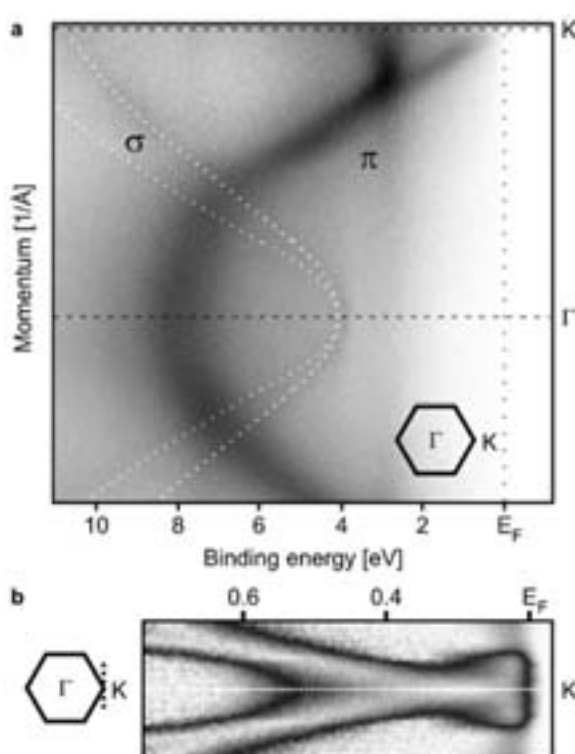


Figure 2. Electronic states in graphene on the β -SiC(001) surface. (a) Overview ARPES intensity map taken along the Γ K direction. (b) ARPES intensity map taken at K along the black dotted line.

ing energy. This position is correlated with the strength of the graphene-substrate interaction and it is much lower than the one reported for the graphene/ α -SiC system (8.5 eV), indicating that the hybridization between graphene and β -SiC is significantly decreased by virtue of the strong lattice mismatch. A close inspection of the dispersion relation around the K point at $T = 40$ K reveals that, similar to graphene on α -SiC, the Dirac point (E_D) is pushed below the Fermi level to 0.25 eV binding energy. It was demonstrated previously that with growing number of graphene layers E_D gradually

shifts back to the Fermi level. For graphene on α -SiC an E_D value similar to ours was detected when three layers were reached. Hence, given the weaker hybridization strength, we anticipate that the number of graphene layers in our case does not exceed three and generally varies between one and three. This conclusion is supported also by our STM results.

References

- [1] A. K. Geim, *Science* **324**, 1530 (2009).
- [2] Victor Yu. Aristov *et al.*, *Nano Letters*, **10**, 992–995 (2010), and references therein.

GRAPHENE-LIKE ELECTRONIC SIGNATURE IN SILICENE NANO-RIBBONS

P. De Padova¹, C. Quaresima¹, C. Ottaviani¹, P. M. Sheverdyaeva², P. Moras³, C. Carbone³, D. Topwal⁴, B. Olivieri⁵, A. Kara⁶, H. Oughaddou⁷, B. Aufray⁸, G. Le Lay⁸

¹CNR-ISM, Roma, Italy

²Sincrotrone Trieste S.C.p.A., Trieste, Italy

³CNR-ISM, Trieste, Italy

⁴ICTP, Trieste, Italy

⁵CNR-ISAC, Roma, Italy

⁶Department of Physics, University of Central Florida, Orlando, USA

⁷DSM/IRAMIS/SPCSI, CEA, Gif sur Yvette, France

⁸CRMCN-CNRS, Marseille, France

E-mail: paola.depadova@ism.cnr.it



VUV PHOTOEMISSION

Silicene, one-atom thick silicon sheet arranged in a honeycomb lattice [1-3], is a new allotropic form of silicon. Theory predicts that free-standing silicene sheets and ribbons are stable in a flat or in a low puckered configuration. In both cases basically this gives the same electronic properties of graphene [1-3]. The predicted electronic structure of silicene presents π and π^* bands, which form the so-called Dirac cones at the Brillouin zone corners. This means that, as in graphene, the charge carriers in silicene should behave as massless relativistic particles. Therefore, all graphene expectations [4], such as high-speed electronic nanometric devices based on ballistic transport at room temperature, could be transferred to this innovative material, with the crucial advantage of easily fitting into the silicon-based electronics industry.

We synthesized high aspect ratio silicon nano-ribbons (SiNRs) by depositing in situ Si on Ag(110) surface, under ultra-high vacuum conditions [5]. These NRs are several nanometers in lengths, share a common width of 1.6 nm and are just 0.2 nm in height. They grow epitaxially in a parallel manner over the sample surface. At monolayer completion, they form a grating with a pitch of just 2 nm [5-6]. High-resolution STM showed that these SiNRs display a honeycomb, silicene-like, arrangement [5,7-10]. These observations confirm the atomic structure of the SiNRs lying on the Ag(110) substrate predicted through Density Functional Theory calculations in the General Gradient Approximation (DFT-GGA) [8-10]. Namely, these calculations yield a ground state geometry comprising a honeycomb silicon architecture arched on the substrate, in-

dicating a silicene-like structure, mediated by the silver substrate [8-10].

The angle-resolved photoelectron spectroscopy measurements of SiNRs arranged in a one-giving (1D) grating, were carried out at the Elettra VUV beamline in Trieste. The electronic states deriving from the silicene structure displayed a quasi-1D character [5]. We identified bands crossing the Fermi level, at the zone boundary, which are like the Dirac cones in graphene [5].

Figure 1 displays the photoemission data for k_x in the vicinity of the X' point and for k_y integrated from 0.55 to 0.70 \AA^{-1} . In this momentum range there is little overlap with the more intense Ag bands. One can observe two branches of highly dispersive Si bands, separated by a gap of about 0.5 eV and centered at 0.6 eV below E_F . This is reminiscent of the π^* (upper branch) and π (lower branch) bands of silicene predicted by theory [3], although shifted below E_F and separated by a gap. We attribute this downward shift and the opening of the gap to the interaction with the Ag(110) substrate. This behavior is very similar to that of the π^* and π band dispersions near the K point of graphene grown on different surfaces, where charge transfer pulls down the π^* branch and the interaction with the substrate opens a gap [11, 12]. Following this analogy, we identified the observed bands as the π^* (upper branch) and the π (lower branch) of our SiNRs. This interpretation is consistent with the STM images showing that the internal hexagonal atomic structure of the nano-ribbons is oriented as in zig-zag cut honeycomb sheets with apexes aligned along their lengths.

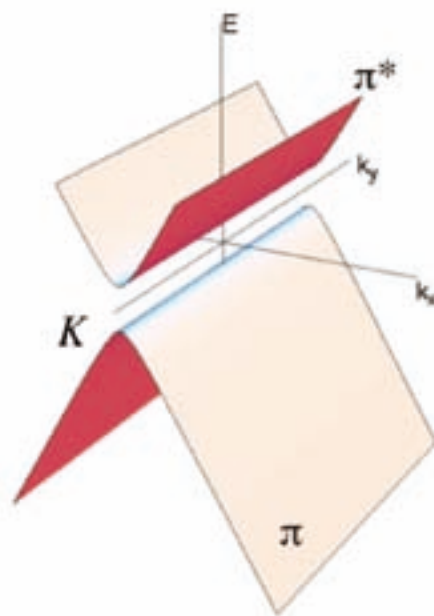
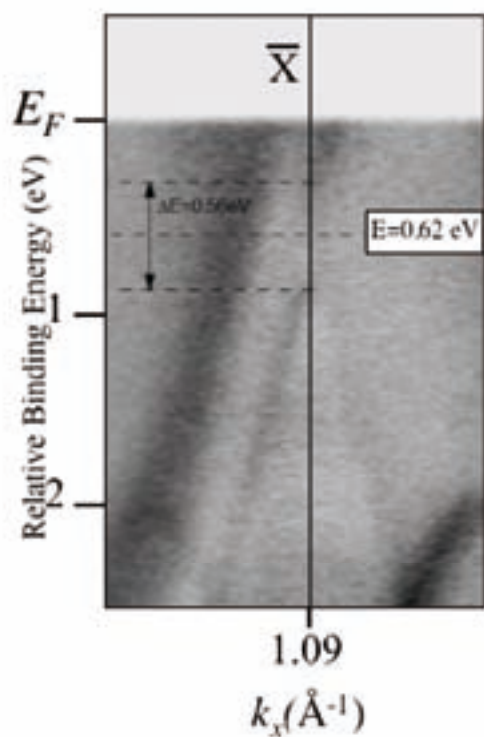


Fig. 1. Horizontal slice $I(E, k_x)$ along the $[-110]$ Ag direction integrated on k_y from 0.55 to 0.7 \AA^{-1} for SiNRs on Ag(110). The 1D projection of the π and π^* cones around the Dirac points is shown on the right side of the figure.

References

- [1] G. G. Guzman-Verri and L.C. Lew Yan Voon, *Phys. Rev. B* **76**, 075131 (2007).
- [2] S. Lebègue and O. Eriksson, *Phys. Rev. B* **79**, 115409 (2009).
- [3] S. Cahangirov, M. Topsakal, E. Aktuerk, H. Sahin and S. Ciraci, *Phys. Rev. Lett.* **102**, 236804 (2009).
- [4] A. K. Geim and K. S. Novoselov, *Nat. Mat.* **6**, 183 (2007).
- [5] P. De Padova, C. Quaresima, C. Ottaviani, P. M. Sheverdyayeva, P. C. Carbone, D. Topwal, B. Olivieri, A. Kara, H. Oughaddou, B. Aufray, and G. Le Lay, *Appl. Phys. Lett.*, **96**, 261905 (2010).
- [6] H. Sahaf, L. Masson, C. Léandri, B. Aufray, G. Le Lay and F. Ronci, *Appl. Phys. Lett.*, **90**, 263110 (2007).
- [7] G. Le Lay, B. Aufray, C. Léandri, H. Oughaddou, J. P. Biberian, P. De Padova, M. E. Davila, B. Ealet and A. Kara, *Appl. Surf. Sci.*, **256**, 524 (2009).
- [8] B. Aufray, A. Kara, S. Vizzini, H. Oughaddou, C. Léandri, B. Ealet and G. Le Lay, *Appl. Phys. Lett.*, **96**, 183102 (2010).
- [9] A. Kara, C. Léandri, M. E. Davila, P. De Padova, B. Ealet, B. Aufray and G. Le Lay *J. Supercond. Nov. Magn.* **22**, 259 (2009).
- [10] A. Kara, S. Vizzini, C. Léandri, B. Ealet, H. Oughaddou, B. Aufray and G. Le Lay, *Phys. Condens. Matter*, **22**, 045004 (2010).
- [11] J. Winterlin and M.-L. Bocquet, *Surface Sci.* **603**, 1841 (2009).
- [12] A. Grüneis, K. Kummer and D. V. Vyalikh, *New J. Phys.* **11**, 073050 (2009).

GEODESIC CARBON NANODOMES AS PRECURSORS TO NEARLY FREE-STANDING GRAPHENE

P. Lacovig^{1,2}, M. Pozzo³, D. Alfè³, P. Vilmercati^{2,4}, A. Baraldi^{2,5}, S. Lizzit¹

¹Sincrotrone Trieste S.C.p.A., Trieste, Italy

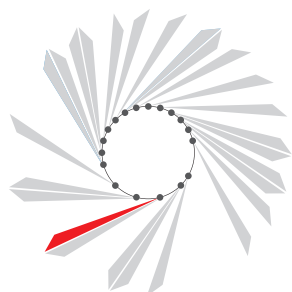
²Physics Department and CENMAT, University of Trieste, Trieste, Italy

³University College London, London, United Kingdom

⁴University of Tennessee, Knoxville, Tennessee, USA

⁵Laboratorio Nazionale TASC, IOM-CNR, Trieste, Italy

E-mail: alessandro.baraldi@elettra.trieste.it



SUPERESCA

The growth of graphene has been attracting tremendous attention ever since its discovery in 2004. Various methods have been employed to fabricate graphene films, such as epitaxial growth on SiC samples, self-assembly procedures, where graphene oxide films are transferred to a substrate and reduced to graphene by chemical reaction or heating, and chemical vapor deposition of hydrocarbons on a hot metal substrate. The latter method allows to produce large, high-quality graphene films on metal surfaces, which can then be transferred intact to other substrates [1,2].

By combining *in-situ* high-resolution photoelectron spectroscopy and *ab initio* calculations, we have shown that carbon nanoislands formed during the growth of a long-range ordered graphene layer on Ir(111), assume a peculiar domelike shape [3], thus producing at the nanometer length scale a morphology that recalls the Eden Project in Cornwall, UK (see Figure 1). The growth mechanism is completely different from all those previously observed for two-dimensional islands on metals.

The temperature programmed growth involved the adsorption of ethylene at room temperature, followed by sequential heating to higher temperatures. For temperatures below 1000 K (see Figure 2(a)), the single C 1s peak at 284.12 eV, corresponding to a perfect graphene layer, is split into three components. After heating to higher temperatures, two of the components (C_A and C_C) gradually shift and disappear, while the third one (C_B) grows and, after heating to 1270 K, only one peak remains. At the same time, an additional peak appears in the Ir $4f_{7/2}$ spectrum for the low-temperature anneals, but gradually disappears as the temperature is increased. After heating

to high temperature, the Ir $4f_{7/2}$ spectrum corresponding to a well ordered graphene layer is practically unchanged with respect to that of the clean Ir(111) surface, a direct indication that the quasi-free standing graphene layer is weakly interacting with the iridium surface.

These results were interpreted with the help of density functional theory (DFT) calculations on the morphology of graphene clusters of different sizes on iridium, and by making calculations on the C 1s and Ir $4f_{7/2}$ core levels. The DFT show that the carbon species resulting in C 1s core level components at lower and higher binding energy with respect to the main peak are due to atoms at the periphery of cluster region (C_C) bonded to two carbon atoms, and to carbon atoms (C_A) bonded with three carbon atoms and directly bonded to the periphery atoms. The main component (C_B) is due to the atoms at the center of the cluster.

Moreover calculations show that the interaction of the carbon atoms with the iridium substrate is much larger at the edges of the island than in the center. As the islands grow larger, the central carbons detach and move away from the substrate, thus creating a dome-shaped island. For very large islands, almost all of the carbon atoms are in this nearly free-standing state, and only those at the perimeter of the islands are strongly bound to the surface as a result of the C 2p hybridization with the first-layer Ir d band.

Further support to our interpretation arises from the evolution of the calculated binding energy/atom in the cluster as a function of N_p/N_T (N_p is the number of atoms at the periphery, N_T is the total number of atoms in the cluster) for different cluster sizes. The graph, shown in Figure 2(b), displays a remarkably

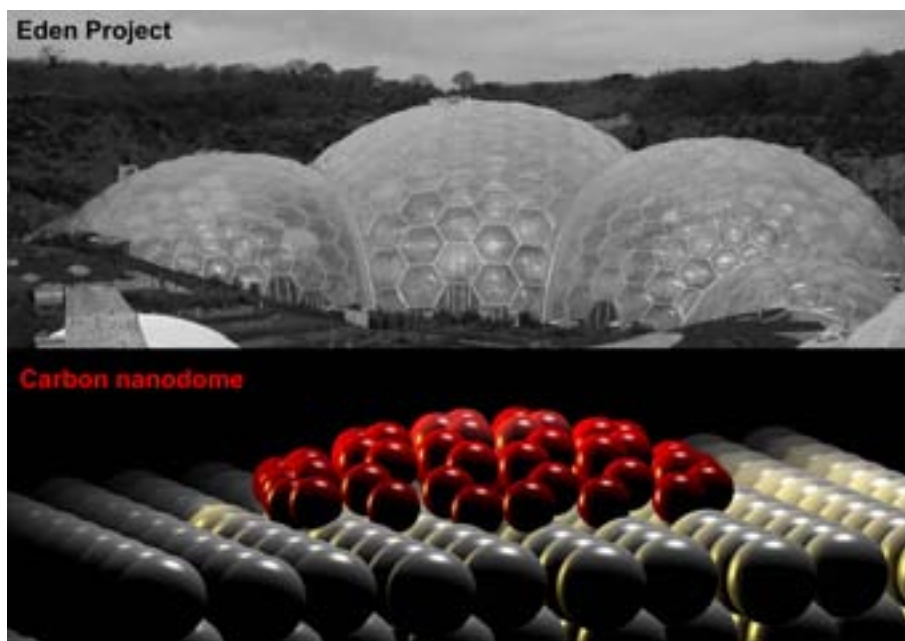


Figure 1. The modern architectural structures of the Eden Project in Cornwall (top) compared to the morphology of the carbon nanodomains grown on Ir(111) (bottom).

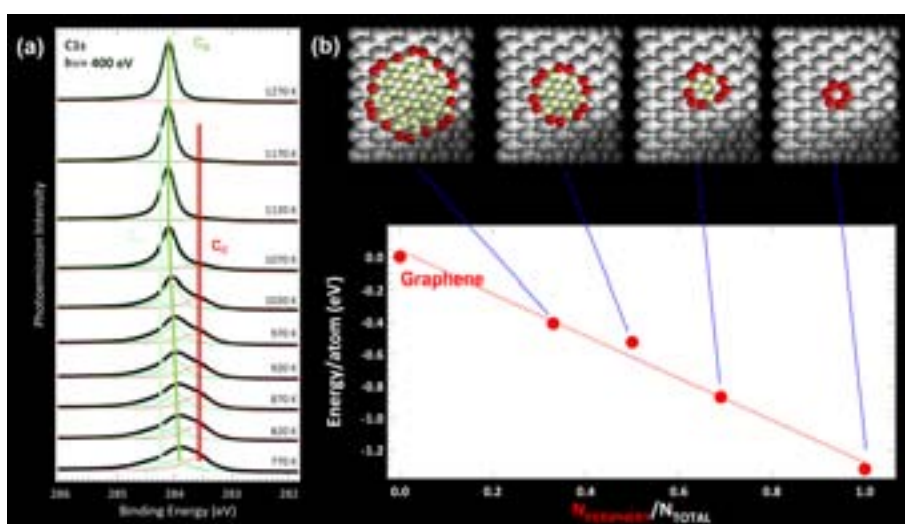


Figure 2. (a) C 1s spectra after annealing at different temperatures of the Ir(111) surface saturated with C_2H_4 at 300 K. The spectra were measured at 300 K. The different components represent nonequivalent C and Ir atoms, as explained in the text. (b) Evolution of the binding energy per atom as a function of the ratio of C atoms at the periphery N_p and the total number N_T in each C cluster.

linear behavior and indicates that the islands are bonded to the substrate mainly with the C atoms at the edges.

This scenario matches the experimental findings, indicating an evolution, as a function of the heating temperature, from small graphene islands in which carbon atoms have several different chemical environments, to very large islands that approach free-standing graphene. These results show that the size of these geodesic carbon nanodomains depends on the temperature of the metallic substrate, suggesting a number of possible ways to control the size of graphene sheets at the nanoscale.

References

- [1] K. S. Kim, Y. Zhao, S. Y. Lee, J. M. Kim, K. S. Kim, J. H. Ahn, P. Kim, J. Y. Choi, and B. H. Hong, *Nature* **457**, 406 (2009).
- [2] X. Li, W. Cai, J. An, S. Kim, J. Nah, D. Yang, R. Piner, A. Velamakanni, I. Jung, E. Tutuc, S. K. Banerjee, L. Colombo, and R. Ruoff, *Science* **324**, 1312 (2009).
- [3] P. Lacovig, M. Pozzo, D. Alfè, P. Vilmercati, A. Baraldi, S. Lizzit, *Phys. Rev. Lett.* **103**, 166101 (2009), selected as ViewPoint, J. O. Sofo and R. D. Diehl, *Physics* **2**, 84 (2009) and described by L. Donaldson, *MaterialsToday* **12**, 12 (2009).

BAND DISPERSION IN THE DEEP 1s CORE LEVEL OF GRAPHENE

S. Lizzit¹, G. Zampieri², L. Petaccia¹, R. Larciprete³, P. Lacovig^{1,4}, E. D. L. Rienks⁵, G. Bihlmayer⁶, A. Baraldi^{4,7}, Ph. Hofmann⁵

¹Sincrotrone Trieste S.C.p.A., Trieste, Italy

²Centro Atómico Bariloche, Bariloche, Argentina

³CNR-Institute for Complex Systems, Roma, Italy

⁴Physics Department and CENMAT, University of Trieste, Trieste, Italy

⁵Institute for Storage Ring Facilities and iNANO, University of Aarhus, Aarhus, Denmark

⁶Institute für Festkörperforschung and Institute for Advanced Simulation, Jülich, Germany

⁷Laboratorio Nazionale TASC IOM-CNR, Trieste, Italy

E-mail: silvano.lizzit@elettra.trieste.it; philip@phys.au.dk



SUPERESCA

The assumption that electrons in deep core states do not participate in the bonding of solids, and thus do not show band-like dispersion, is at the base of our understanding of the solid state. It is also of essential practical significance for many experiments, such as X-ray Photoelectron Spectroscopy. This technique derives its power from the fact that the precise value of the core level binding energy depends on the chemical environment of the emitting atoms, but it is tacitly assumed that it has a single, well-defined energy, i.e. it does

not show any dispersion. Violations of this assumption have only been found for small molecules in the gas phase such as C_2H_2 or N_2 with much stronger bonding and shorter bonding distances than present in solids [1, 2]. Here we report the observation of a sizable band-like dispersion (up to 60 meV) of the deep C 1s core level in graphene. The dispersion is observed as an emission-angle dependent binding energy modulation. Due to a Young's double slit-like interference effect, a situation arises in which only the bonding or only the anti-bonding state is observed for a given photoemission geometry [3].

Angle-resolved C1s photoemission spectra were measured at the SuperESCA beamline, on a graphene layer grown on Ir(111), over many polar θ and azimuthal angles ϕ and at different photon energies, as depicted in Fig. 1(a). A good fit to all the spectra can be obtained using one component with constant lineshape, letting its intensity and binding energy position to vary (Fig. 1(b)). Fig. 1(c) shows the C 1s intensity modulation function at different photon energies, compared to the multiple scattering simulations for a flat, free-standing layer of graphene. The excellent agreement between experiments and simulations confirms that the C 1s intensity variations are indeed well understood in terms of photoelectron diffraction effects.

Fig. 2(a) shows the binding energy modulation of the C 1s peak measured at 700 eV photon energy, represented as a function of k_{\parallel} , the wavevector component parallel to the surface. A periodic pattern emerges, with the same periodicity at all photon energies, which does not coincide with that of the reciprocal

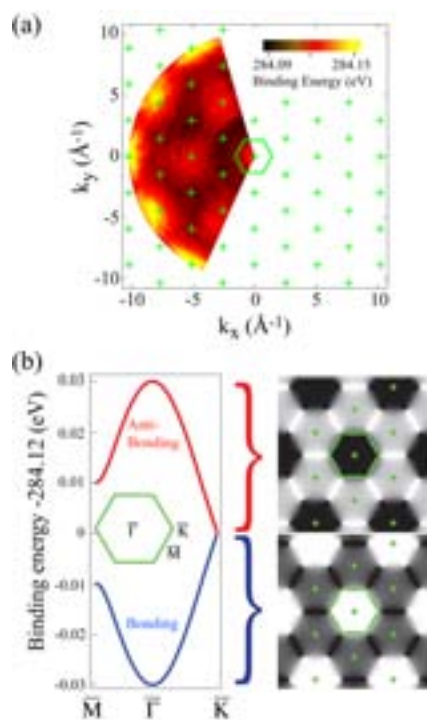


Figure 1.

(a) Binding energy modulation as a function of k . Crosses are reciprocal lattice points. The hexagon is the first Brillouin zone. (b) (left) Tight-binding calculation for a σ -type band formed from the C 1s core states in graphene. (right) Calculated photoemission intensity from all of the antibonding (top) and bonding (bottom) states. Bright corresponds to high intensity.

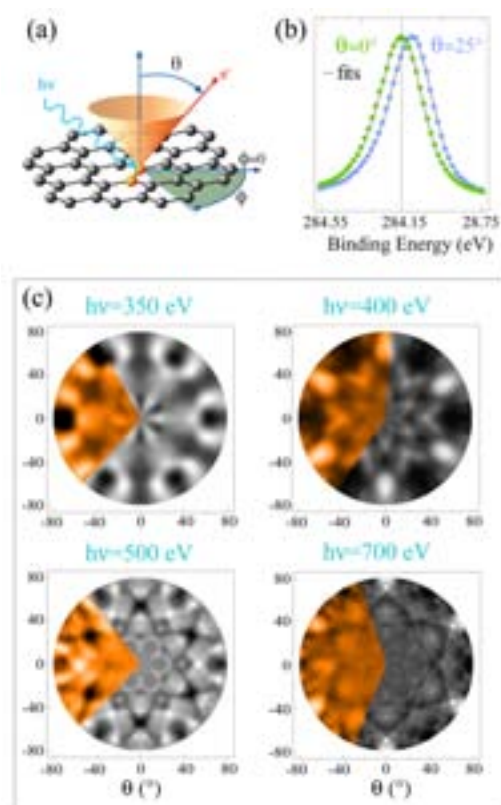


Figure 2. (a) Schematic of the graphene lattice and the experimental geometry. (b) C 1s photoemission spectra taken at a photon energy of 400 eV and at different polar angles. (c) stereographic projection of the integrated photoemission intensity modulation $(I-I_0)/I_0$ (experiment in colour, simulation in grey scale) as a function of emission angle for scans taken at different photon energies $h\nu$.

lattice mesh. At a first sight this observation appears to invalidate a band dispersion hypothesis.

Among the different mechanisms that could lead to the observed binding energy variations, such as the existence of several unresolved components from carbon atoms in a chemically different environment, or a recoil effect in which some of the photoelectron's energy is used to excite lattice vibrations, band-like dispersion of the initial state remains the most plausible one.

The simplest conceivable picture for this is the formation of a σ -type band between the 1s states of the two atoms in the unit cell of graphene. A tight-binding calculation of such a band is shown in Fig. 2(b). The dispersion shows a bonding and antibonding band with the highest energy separation at Γ and degeneracy at the K point of the two-dimensional Brillouin zone. This dispersion would imply the presence of two C 1s components at Γ and a narrow one at K, which is not observed experimentally. However, the band dispersion hypothesis and the experimental results can be reconciled by taking into account a curious interference effect that is caused by the presence

of two atoms in the unit cell of graphene. The effect of the interference is evident in Fig. 2(b) where the expected photoemission intensities for all of the antibonding and all of the bonding states are displayed: the two bands behave in opposite ways, so that only one state is ever observable, causing the seemingly wrong periodicity in the reciprocal space.

Our results are of fundamental importance for the localization of deep core levels in solids and can have important implications for the interpretation of high resolution core-level data from graphene, graphite and carbon related materials.

References

- [1] B. Kempgens, H. Köppel, A. Kivimäki, M. Neeb, L. S. Cederbaum, and A. M. Bradshaw, *Phys. Rev. Lett.* **79**, 3617 (1997).
- [2] U. Hergenbahn, O. Kugeler, A. Rudel, E. E. Rennie, and A. M. Bradshaw, *J. Phys. Chem. A* **105**, 5704 (2001).
- [3] S. Lizzit, G. Zampieri, L. Petaccia, R. Larciprete, P. Lacovig, E. D. L. Rienks, G. Bihlmayer, A. Baraldi and Ph. Hofmann, *Nature Phys.* **6**, 345 (2010), also on the cover page of the same issue.

CORRUGATION IN EXFOLIATED GRAPHENE

A. Locatelli¹, K.R. Knox^{2,3}, D. Cvetko^{4,5}, T.O. Montes¹, M.Á. Niño¹, S. Wang⁶, M.B. Yilmaz⁷, P. Kim³, R.M. Osgood Jr.³, A. Morgante^{4,8}

¹Sincrotrone Trieste S.C.p.A., Trieste, Italy

²Department of Physics and ³Department of Applied Physics, Columbia University, New York, USA

⁴Laboratorio Nazionale TASC, IOM-CNR, Trieste, Italy

⁵University of Ljubljana, Ljubljana, Slovenia

⁶Department of Physics, Renmin University of China, Beijing, China

⁷Department of Physics, Fatih University, Buyukcekmece, Istanbul, Turkey

⁸Department of Physics, Trieste University, Trieste, Italy

E-mail: andrea.locatelli@elettra.trieste.it



NANOSPECTROSCOPY

The transport properties of graphene, a single monolayer of carbon atoms arranged in a honeycomb lattice, depend strongly on the quality of its crystalline lattice, on the presence of defects and dopants, and on the charge transfer from adsorbed or bound species. In fact, crystal deformations, due to either intrinsic thermal fluctuations or interactions with the substrate, largely contribute to electron scattering and any attendant decrease in conductivity and carrier mobility. This has motivated considerable experimental and theoretical efforts, dedicated to issues related to the morphology of graphene, addressing in particular the origin of any intrinsic corrugation. In this work, we investigate the corrugation in both freely suspended and SiO₂-supported exfoliated graphene layers, at length scales from interatomic distances to several hundred nm [1]. Our approach takes full advantage of the multi-technique capabilities offered by a low energy electron microscope (LEEM): real space imaging of the sample morphology over large surface areas (up to several tens of micron), with lateral resolution of 10 nm and atomic depth sensitivity (see Figure 1), and micro-probe low energy electron diffraction (μ -LEED). Due to the intrinsic sensitivity of the line shape of diffracted electron beams to local height variations, μ -LEED guarantees access to lattice distortions at length scales well below the horizontal correlation length (few tens of nm in single- and double-layer graphene).

The most prominent feature that we observed in all graphene samples was the broadening of the diffraction profile upon increasing the perpendicular electron momentum

transfer. Diffraction line-shape analysis, based on a kinematic approach [2], revealed quantitative differences in surface morphology, depending on film thickness and interaction with the substrate, allowing us to estimate the roughness exponent, an important parameter that describes the short range behavior of the height-height correlation function of the surface (see Figure 2). Our results show clearly that the corrugation observed on supported graphene samples is quantitatively different from that observed on suspended samples. While the former is largely determined by the morphology of the substrate, the latter is influenced by intrinsic and extrinsic factors. Supported graphene samples display a rough morphology at short wavelengths, up to a thickness of several layers. This corrugation decreases with increasing film thickness, as the stiffer multi-layer film becomes effectively suspended on the hills of the SiO₂ substrate. Suspended samples appear significantly smoother in the short-range than those supported on SiO₂. For instance, bi-layer suspended graphene shows very narrow diffraction peaks, comparable to those measured on thick supported graphite films. The smooth short-range texture of suspended bi-layer is confirmed by the high value of the roughness exponent (0.8), typical of a smooth short-range morphology. Suspended single-layer graphene films are sensibly more corrugated. The roughness exponent, 0.55 at room temperature, indicates a jagged morphology. The reduced corrugation of suspended graphene reported here correlates well with the significantly improved transport properties of suspended-graphene devices [3].

Figure 1.

(A) LEEM image at 4.2 eV of suspended disks and SiO₂-supported graphene (disk diameter is 5 μm). The local thickness, in units of graphitic layers (indicated by labels), was determined by measuring the electron reflectivity curves in the energy interval of 1 to 8 eV; (B) LEEM image of the same region at electron kinetic energy of 38 eV; (C) LEEM image of the suspended portion of the single-layer region at electron kinetic energy of 10 eV. The disks (suspended graphene) appear bright because of their lower corrugation. (Bottom) Zero-order diffraction LEED IV curves of SiO₂-supported and suspended trilayer graphene (reproduced with copyright permission).

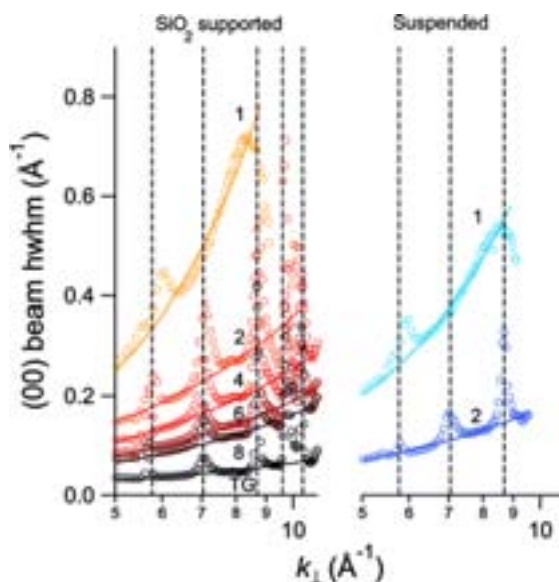
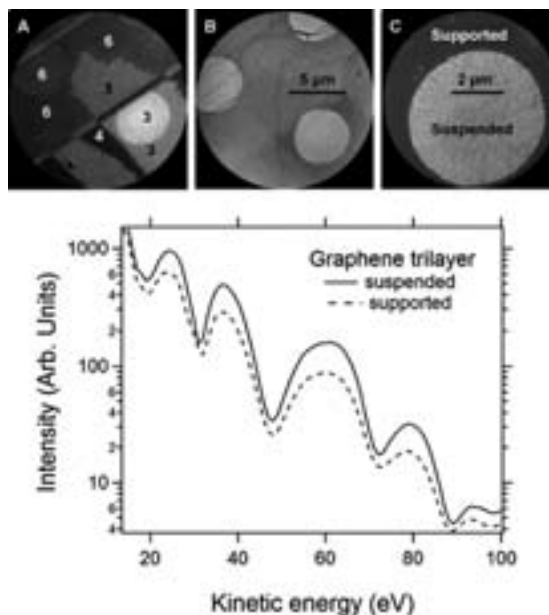


Figure 2.

Variation of the primary diffraction beam half-width at high medium (hwhm) for different graphene films as a function of the electron momentum transfer k , measured at room temperature. The hwhm curves for SiO₂-supported and suspended graphene are shown in the left and right panels, respectively. The dashed vertical lines indicate resonances corresponding to out-of-phase diffraction conditions in multilayers. The continuous lines represent best fits using a power law. According to the model in ref. [2], the exponent identifies the roughness exponent. The film thickness is indicated by the numeric labels; TG refers to thick graphite film on SiO₂ (reproduced with copyright permission).

Most relevantly, our experiments provide evidence that the corrugation in single layer suspended graphene is sensitive to adsorbate load and temperature variations. This behaviour, which is characteristic of single layer graphene, is determined by the very high flexibility of the crystal at this thickness. The weak temperature dependence of the diffraction line shape observed in single layer disks points to a line broadening mechanism that is only in part phonon-induced, and thus intrinsic in nature, which supports the picture that thermal fluctuations produce deviations from planarity [4]. However, we underline that the most important contributions to corrugation in single layer exfoliated graphene are extrinsic. Our results, in fact, suggest that interactions with physisorbed or chemisorbed species can cause significant changes in the surface morphology. We envisage that the ability to modi-

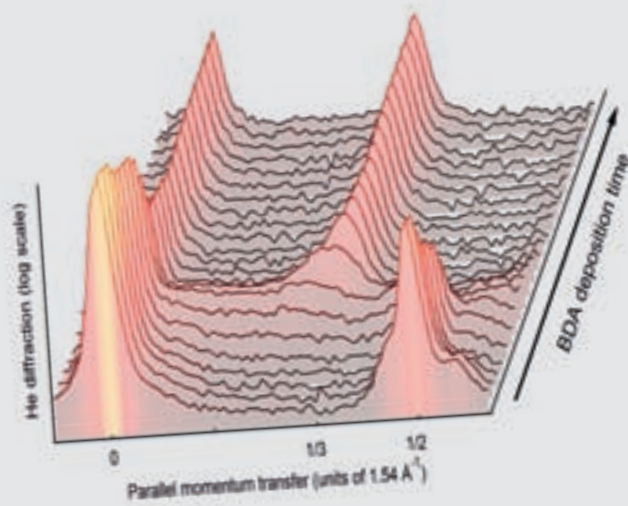
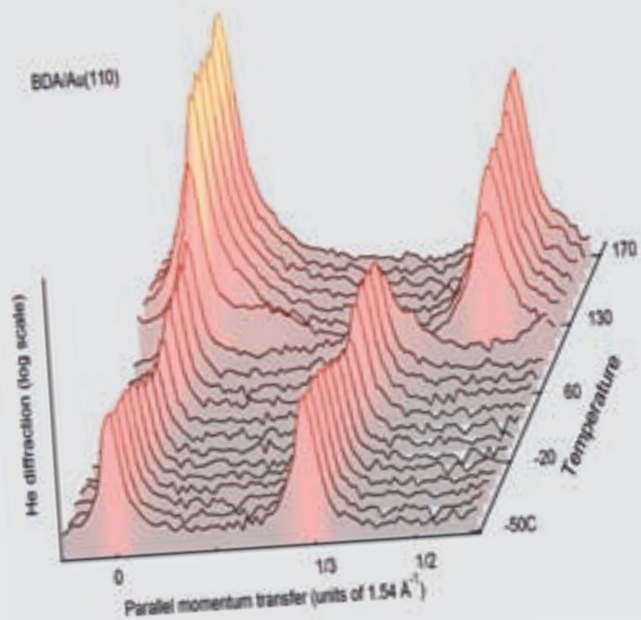
fy such corrugation, by means of temperature, boundary conditions, deposition or removal of host adatoms and molecules etc., will be crucial in assuming further control of the transport properties of graphene, with important implications to their future exploitation in practical devices.

References

- [1] A. Locatelli et al, *ACS Nano*, **4**, 4879 (2010).
- [2] H.-N. Yang, G.-C. Wang, T.-M. Lu, *Diffraction from Rough Surfaces and Dynamic Growth Fronts*, World Scientific Publishing, Singapore (1993).
- [3] K.I. Bolotin, K.J. Sikes, Z. Jiang, G. Fudenberg, J. Hone, P. Kim, H.L. Stormer, *Solid State Commun.* **146**, 351 (2008).
- [4] A. Fasolino, J.H. Los, M.I Katsnelson, *Nat. Mater.* **6**, 858 (2008).



NANOSTRUCTURES AND ORGANIC FILMS



RELATING ENERGY LEVEL ALIGNMENT AND AMINE-LINKED MOLECULAR JUNCTION CONDUCTANCE

M. Dell'Angela^{1,6}, G. Kladnik³, A. Cossaro¹, A. Verdini¹, M. Kamenetska⁴, I. Tambljn⁵, S.Y. Quek⁵, J.B. Neaton⁵, D. Cvetko³, A. Morgante^{1,2}, L. Venkataraman⁴

¹Laboratorio Nazionale TASC IOM-CNR, Trieste, Italy

²Department of Physics, University of Trieste, Trieste, Italy

³Department of Physics, Faculty for Mathematics and Physics, University of Ljubljana, Slovenia

⁴Department of Applied Physics and Applied Mathematics, Columbia University, New York, USA

⁵Molecular Foundry, Lawrence Berkeley National Laboratory, Berkeley, USA

⁶Institut für Experimentalphysik, Universität Hamburg, Hamburg, Germany

E-mail: Dean.Cvetko@fmf.uni-lj.si



ALOISA

We use resonant X-ray photoemission (ResXPS) to determine molecular level alignment for three Benzene Diamine (BDA) derivatives on Au(111) and Au(110). Comparing the results to STM break-junction based single molecule conductance measurements and first-principles density functional theory, we find that the HOMO shift from the Fermi level (E_F) for the 3 molecules correlates well with changes in their conductance values. Our results agree quantitatively with DFT calculations incorporating self-energy corrections. Additionally, our results for the BDA/Au(110) are consistent with theoretically predicted preferential adsorption of BDA at uncoordinated Au sites.

Understanding transport properties of single molecules bonded between metal electrodes is critical to progress in molecular electronics. Transport characteristics are typically determined from the low-bias conductance of molecular junctions [2]. However, transport measurements are at best indirect probes of the molecular orbital alignment relative to E_F . The ionization potential and the electron affinity of molecules can often be characterized in the gas-phase, but physical effects such as charge transfer, hybridization, and electrode polarization are expected to drastically alter the electron removal/addition energies in the molecular junctions. In fact, it is well known that for interfaces of organic semiconductors and metals the vacuum level alignment rule breaks down, so spectroscopic measurements on molecular interface systems are required to probe the junction level alignments.

We focus on 3 amine-terminated molecules: tetramethyl 1,4-diaminobenzene (TMBDA)

which has 4 electron donating methyl substituents, 1,4-diaminobenzene (BDA) and tetrafluoro-1,4-diaminobenzene (TFBDA) which has 4 electron withdrawing fluorine substituents. These molecules have been shown to bind to under-coordinated Au atoms through an N-Au donor-acceptor bond with a binding energy of about 0.5-1 eV and on atop site on Au(111) with binding energy of 0.1-0.3 eV [3]. We have characterized the molecular adsorption on Au(111) and Au(110) by means of Helium Atom Scattering (HAS). Fig. 1a shows a series of HAS diffraction scans along the [001] direction, taken during BDA/Au(110) deposition. Starting from (1x2)Au(110) held at 270K, which displays $\frac{1}{2}$ -order diffraction peaks, the adsorption of BDA molecules initially causes a steep drop of HAS signal consistent with BDA molecules gradually covering the Au substrate. At higher BDA coverage the Au(110) substrate undergoes a structural transformation from 2-fold “missing row” to a higher symmetry 3-fold reconstruction, which is also the symmetry of the BDA/Au(110) monolayer. The upper panel shows a series of HAS scans as a function of annealing temperature of the monolayer BDA/Au(110). We note that as BDA desorbs at ~ 410 K, the zero-order peak increases steeply, and simultaneously the 3-fold periodicity transforms to the original 2-fold of the bare Au(110). We identify the steep increase of the 0-order HAS as a fingerprint of molecular desorption, uncovering the Au beneath. In Fig. 1b we report the evolution of the 0-order HAS as a function of temperature for all considered systems. We find desorption temperatures of 297, 327 and 415 K for TFBDA, BDA and TMBDA respec-

Molecule	measured adsorption energy [eV]		calculated adsorption energy [eV]		Energy of HOMO level from E_F [eV]			Exp. conductance $10^{-3} G_0$	
					Au(111)				Au(110)
					UPS	Resonant XPS	Theory		Resonant XPS
TMBDA	Au(111) 1.2		Au(111) 0.44	-1.0 ± 0.1	-1.3 ± 0.2	-1.2	-1.6 ± 0.2	8.2 ± 0.2	
BDA	Au(111) 1.0	Au(110) 1.1	Au(111) 0.36	-1.4 ± 0.1	-1.6 ± 0.2	-1.6	-1.8 ± 0.2	6.4 ± 0.2	
TFBDA	Au(111) 0.9		Au(111) 0.26	-1.5 ± 0.1	-1.65 ± 0.2	-1.8		5.5 ± 0.2	

Table 1. Adsorption energies on Au(111) determined from T-ramp HAS and from DFT- Σ calculation [1,3]. HOMO energy levels relative to E_F from UPS and ResXPS on Au(111) and Au(110) and determined from DFT- Σ [1,3]. STM break junction conductance values from [2].

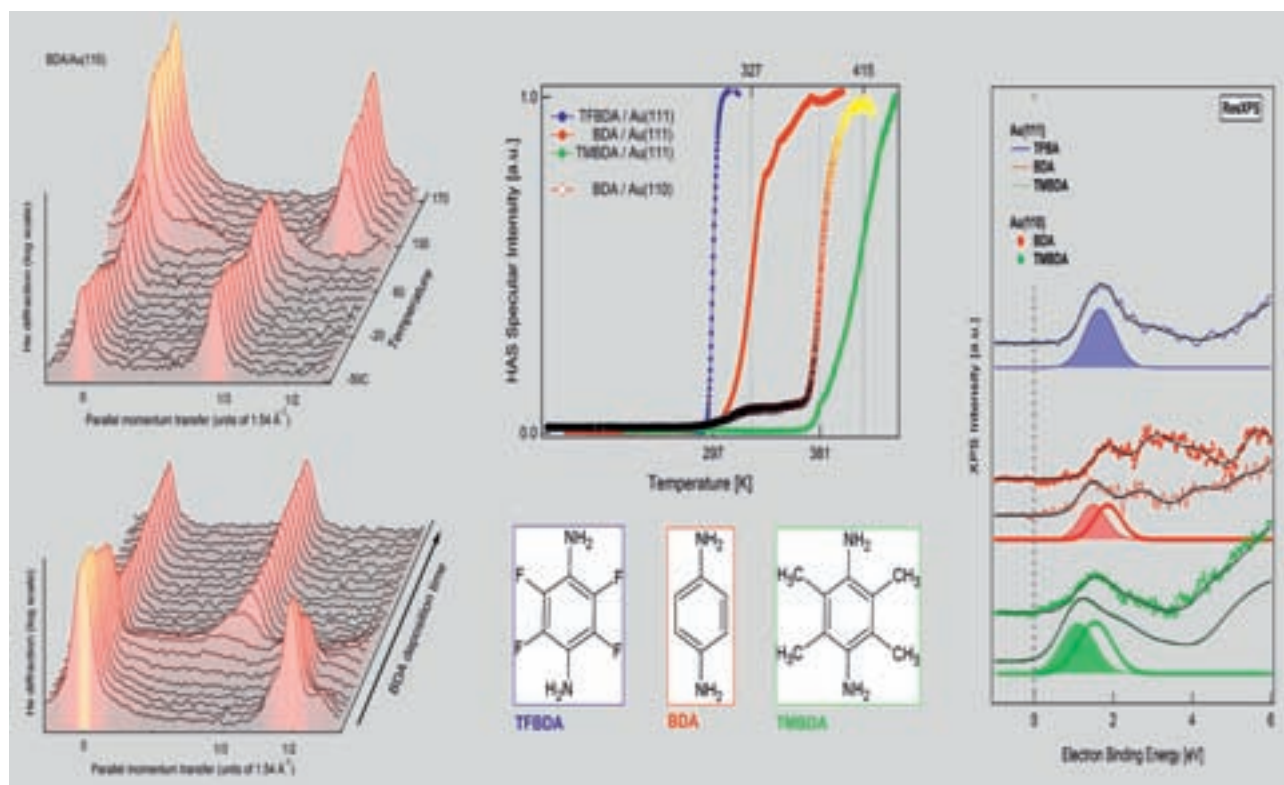


Figure 1. Left: Series of real-time HAS scans during BDA/Au(110) deposition (bottom) and during thermal desorption of 1 ML BDA/Au(110) (top). Middle: 0-order HAS peak for TFBDA/BDA/TMBDA desorption on Au(111) and Au(110). The respective desorption temperatures are indicated. Right: VB spectra of molecular films on Au(111) and Au(110) with ResXPS ($h\nu = 286.6$ eV for BDA and TMBDA and $h\nu = 287$ eV for TFBDA). Fitted HOMO peaks are also shown. See also Table 1.

tively, and estimate their desorption barriers E_B . The observed trend is consistent with the calculated molecular bonding energies in Table 1.

We use ResXPS to study the electronic properties of molecular layers on Au(111) and Au(110). In particular, VB photoemission has been measured in resonant conditions for autoionization across the C K-edge (fig. 1c). At selected photon energies, the HOMO intensities are enhanced due to resonant X-ray absorption and subsequent core-hole decay via autoionization. Compared with BDA, we find that the HOMO shifts closer to E_F by ~ 0.4 eV for TMBDA, but shifts away from E_F by ~ 0.1 eV for TFBDA. Relating this trend in the level alignment across the 3 molecules with the break-junction conductance measurements, where the molecules are bound to Au at both amine end-groups, shows that a Deeper HOMO correlates with Smaller Conductance. In Table 1 we compare our experimental results to the first-principles DFT calculations. The HOMO level alignments have been calculated within a self-energy corrected DFT-GGA

framework, implemented in SIESTA [1]. The values are -1.2, -1.6, and -1.8 eV for TMBDA, BDA and TFBDA, respectively which agrees well with the experiment.

In conclusion, we have determined the HOMO energy levels for 3 different 1,4-diaminobenzene derivatives on Au(111) using resonant XPS, and found excellent quantitative agreement with self-energy corrected DFT calculations. We find a direct correlation between position of molecular HOMOs and break junction conductance values, which provides the first direct comparison between spectroscopic energy level alignment at hybrid interface with molecular junction transport properties.

References

- [1] M. Dell'Angela et al., *Nano Lett.* **10**, 2470 (2010).
- [2] L. Venkataraman et al., *Nature* **442**, 904 (2010); *Nano Lett.* **7**, 502 (2007).
- [3] S. Y. Quek et al., *Nano Lett.* **7**, 3477 (2007), L. Venkataraman et al. *Nano Lett.* **6**, 458 (2006).

UNIVERSALITY OF ZWITTERIONIC BONDING SCHEME OF AMINO-ACIDS ON SURFACES

J. Reichert^{2,3}, A. Schiffrin¹, W. Auwärter³, A. Weber-Bargioni², M. Marschall³, M. Dell'Angela^{4,5}, D. Cvetko^{4,6}, G. Bavdek^{4,6}, A. Cossaro⁴, A. Morgante^{4,5}, J. V. Barth³

¹Max-Planck-Institut für Quantenoptik (MPQ), Garching, Germany

²Department of Physics & Astronomy, The University of British Columbia, Vancouver, Canada

³Physik Department E20, Technische Universität München, Garching, Germany

⁴Laboratorio Nazionale TASC IOM-CNR, Trieste, Italy

⁵Dipartimento di Fisica, Università di Trieste, Trieste, Italy

⁶Physics Department, University of Ljubljana, Ljubljana, Slovenia

E-mail: cossaro@tasc.infm.it



ALOISA

The study of self-assembly of simple bio-molecules (amino-acids or small peptides) on surfaces can give new insights into life-science fundamental processes and at the same time is a promising approach toward the design of new nanoscale architectures.

The supramolecular noncovalent interactions driving the growth of these thin films are the same that are involved in the formation of secondary and tertiary structure of proteins. The folding process of polypeptides is in fact guided by the hydrogen-bonding or by aromatic–aromatic interactions between the side chains of the amino acid units. Therefore, a better understanding of order phenomena at the molecular level can provide insight in the global characterization of more complex biologically relevant systems.

Furthermore, the control of the assembly processes of these molecules defines a promising approach for the design of one-dimensional (1D) and two-dimensional (2D) functional nanostructures. As revealed by STM imaging on different systems [1-3], the interplay between molecule-molecule and molecule-substrate forces leads to the formation of long-range ordered structures on the surfaces.

In order to understand the mechanism driving the formation of the architectures, we combined the STM with X-Ray spectroscopy (XPS and NEXAFS). to study the morphology and chemical properties of the self-assembly of the L-tyrosine amino acid ($\text{COOH-CH}(\text{NH}_2)\text{-CH}_2\text{-C}_6\text{H}_4\text{-OH}$) on the close-packed noble-metal surface Ag(111) under ultrahigh vacuum (UHV) conditions [1].

The low temperature STM images revealed that at submonolayer coverages, molecular dimers are the building blocks of 1-D arrays extending along the high symmetry directions of the substrate. Upon increasing the molecular coverage, merging of these structures takes place, with the formation of 2-D architectures. In fact, when the molecules are deposited onto the Ag(111) surface held at 170 K the molecules diffuse to the step edges and show no particular ordering pattern. A subsequent annealing at a temperature of 320 K leads to the molecular ribbons formation (Fig.1). This demonstrates that the proper balancing between the inter-molecular forces and the substrate reactivity rules the structures formation process.

XPS and NEXAFS spectroscopies have been used to characterize the chemistry and the geometry of the intermolecular interaction. The position of N1s and carboxylic O1s components (Fig. 2) indicates that the molecules are in their zwitterionic state, as observed for the ordered structures found in similar systems. Amino-acids are known to form zwitterions in their crystalline form, where the intermolecular interaction takes place through hydrogen bonds between their amino- and carboxylic functional groups. NEXAFS show a tilted adsorption of the L-tyrosine phenol ring with respect to the substrate plane, allowing interdigitation and parallel-displaced $\pi\text{-}\pi$ stacking between the side chains of adjacent molecules.

By combining these results with STM imaging a model has been derived for the amino acid nanostructure formation where the zwitterions dimerize through hydrogen bonds between

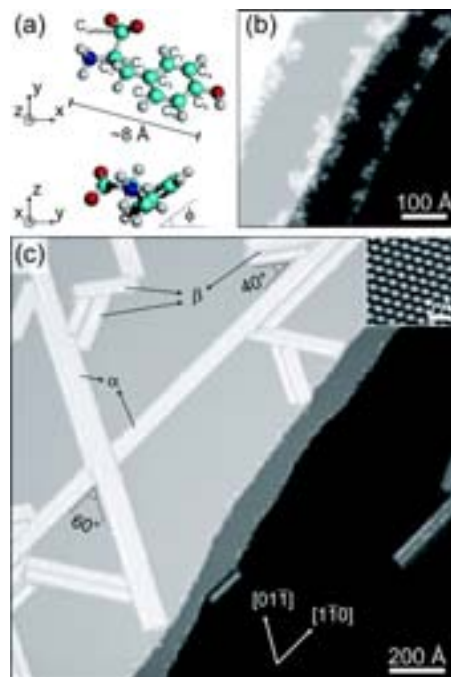


Figure 1. (a) Structure model of the l-tyrosine amino acid zwitterion. (b) Amino acid molecules deposited at 170 K: molecules diffuse and form clusters decorating the substrate step edges. (c) System annealed at 320 K: supramolecular self-assembled domains extend under the influence of the underlying substrate symmetry. From Ref. [1].

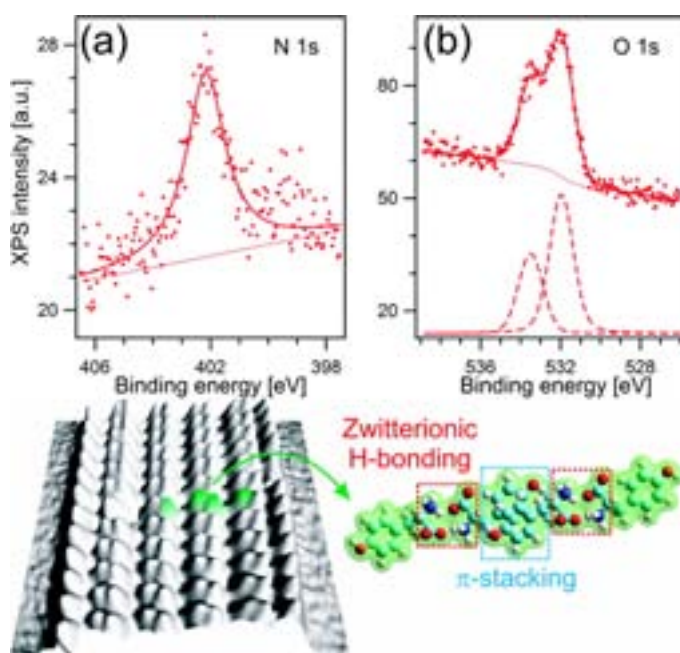


Figure 2. Top: N1s and O1s XPS spectra on the annealed submonolayer of l-tyrosine on Ag(111). The nitrogen and low energy oxygen components can be related to zwitterionic molecules. The high energy O1s component is related to the hydroxyl group oxygen. Bottom: Schematic of the intermolecular bonding mechanism within the wider amino acid nanostructure as can be deduced from the combination of X-ray spectroscopies and STM imaging. From Ref. [1].

carboxylate and ammonium, and 1-D ribbons merge *via* parallel-displaced π - π interactions between the phenol side chains (Fig.2). From the similarities with cited systems [2-3], we propose the zwitterionic pairing of amino-acids as universal scheme for the architectures growth on poorly reactive surfaces.

References

- [1] J. Reichert, A. Schiffrin, W. Auwärter, A. Weber-Bargioni, M. Marschall, M. Dell'Angela, D. Cvetko, G. Bavdek, A. Cossaro, A. Morgante, J.V. Barth, *ACS Nano*, **4** (2), 1218 (2010).
- [2] A. Schiffrin, A. Riemann, W. Auwärter, Y. Pennec, A. Weber-Bargioni, D. Cvetko, A. Cossaro, A. Morgante, J.V. Barth, *PNAS*, **104** (13), 5279 (2007).
- [3] A. Kuhnle, T. R. Linderoth, B. Hammer, F. Besenbacher, *Nature*, **415**, 891 (2002).

CONTACTLESS MONITORING OF DIAMETER-DEPENDENT CONDUCTIVITY OF GaAs NANOWIRES

F. Jabeen^{1,2}, S. Rubini², F. Martelli², A. Franciosi^{1,2}, A. Kolmakov³, L. Gregoratti¹, M. Amati¹, A. Barinov¹, A. Goldoni¹, M. Kiskinova¹

¹Sincrotrone Trieste S.C.p.A., Trieste, Italy

²Laboratorio Nazionale TASC IOM-CNR, Trieste, Italy

³Department of Physics, Southern Illinois University Carbondale, Carbondale, IL, USA

E-mail: kiskinova@elettra.trieste.it; rubini@tasc.infm.it



ESCAMICROSCOPY

Semiconductor nanowires (NWs) are promising building blocks for future nanodevices. The NW conductivity, one of the most important properties exploited in numerous applications, is expected to undergo substantial changes with decreasing width, but can hardly be characterized by conventional transport measurements, especially in undoped or low-doped NWs. The present study of undoped GaAs NWs demonstrates that using the potential of scanning photoelectron microscopy (SPEM) it is possible to examine the interplay between NW diameter and conductance by contactless monitoring of the changes in the conductivity along the axis of the NWs.

GaAs NWs oriented along the [111] substrate direction were grown by Au-catalysed molecular beam epitaxy (MBE) on n-type GaAs (111)B substrates [1]. To protect the NWs surface from oxidation a thick amorphous As cap was deposited in the MBE chamber after the NW growth, and removed by heating at 450 °C after the transfer of the sample into the ultra-high-vacuum SPEM station. The NWs consist of a cylindrical base (a few μm long, with diameter in the 120 nm range) followed by a region with a monotonically decreasing width (see Fig 1a). The low spatial density of the NWs allowed us to collect spectra from different spots along individual NWs, selected from the Ga 3d SPEM images of the NW array in a cross-sectional geometry, see Fig. 1b.

Measuring the conductance changes through XPS in low-conductivity nanostructures is in principle straightforward: the ineffective screening of the electron holes created by photoemission results in the build-up of a positive surface potential, V_s . V_s grows until the photoelectron current I_{ph} becomes equal

to the neutralization current flowing between the irradiated spot and ground. As a result, all photoelectrons emitted from the probed area undergo a rigid kinetic energy shift relative to the ground potential, $\Delta E_k = V_s$, which reflects the potential drop between the irradiated spot and ground, and therefore the conductance of that portion of wire. A scheme of the contactless set-up used to monitor V_s by collecting spectra from different spots is sketched in Fig. 1c. The As 3d spectra in Fig. 2a, measured at spots along the NW from the base towards the tip, clearly show energy shifts, ΔE_k which increase upon moving from the substrate toward the tip. The Ga 3d spectra showed very similar evolution, as evidenced by the As 3d and Ga 3d ΔE_k reported as a function of the distance x from the substrate in Fig. 2b. The shifts are almost identical for the two investigated samples. No changes in line shape and width were observed, which excludes changes in the chemical state of the surface, band bending and related surface photovoltage effects. Measurements performed at 225 °C display a considerably smaller ΔE_k (Fig. 2b). This is a clear indication of the charging-related origin of ΔE_k , that is reduced when conductivity increases.

The linear increase of ΔE_k with x in the cylindrical part of the NW is well reproduced assuming ohmic behavior of the wire. Given the parameters of the experiment, we estimate a value of $\sigma_0 = 0.15$ S/m for the NW conductivity. This value is much lower than that measured on undoped GaAs epitaxial layers grown by the same system ($\sigma = 30\text{--}140$ S/m). Possible reasons can be that the incorporation of impurities during the NWs growth is different from standard epitaxial growth, and/or that the electron and hole relaxation times for the

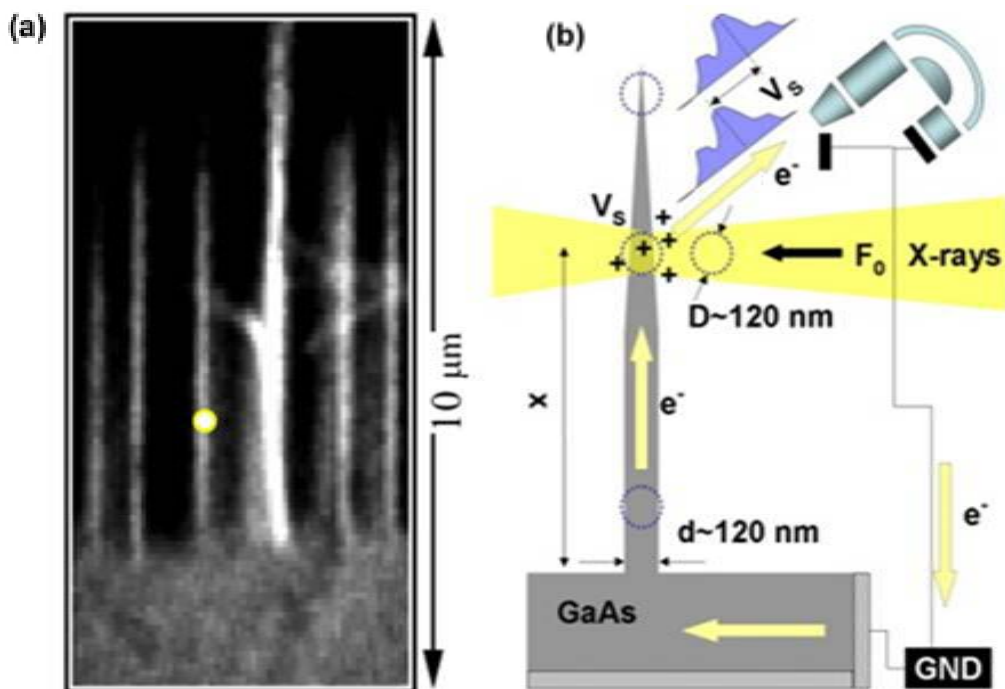
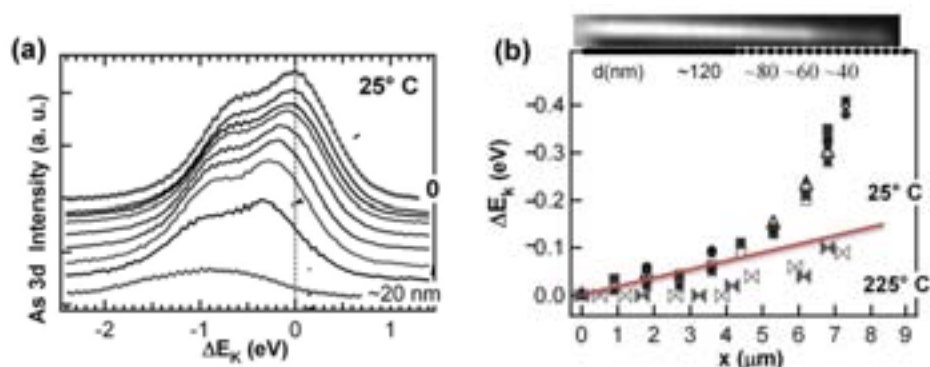


Figure 1. (a) Ga 3d SPEM image of a NW array in cross section used for selecting individual NWs for analysis. The yellow spot indicates the photon microprobe. (b) Scheme of the contactless set-up to monitor the evolution of V_s by collecting spectra from different spots along the NW. Courtesy of Nano Research – Springer.

Figure 2.

(a) As 3d spectra recorded at different positions along a NW from the base toward the tip. (b) E_K shift, ΔE_K , vs the position x from the substrate (at 0) constructed using four sets of Ga 3d (open symbols) and As 3d spectra (solid symbols) at room temperature, and at 225°C. Red line: calculated V_s values as a function of x assuming ohmic behaviour with constant $\sigma_0 = 0.15$ S/m for cylindrical NW with diameter $d_0 = 120$ nm. The NW diameter as a function of x , as determined by high resolution SEM images is also reported at the top of the figure. A representative SPEM Ga 3d image is shown above the plot panel on the same scale of the x axis. Courtesy of Nano Research – Springer.



NWs are much lower compared to bulk GaAs due to surface scattering or the presence of structural defects. The ΔE_K data measured in the conical part of the wire show a rather steep increase, that could not be reproduced by simply taking into account the diameter change of the wire and assuming ohmic conductance. This indicates a size dependent conductivity with a fivefold drop in the conductivity on reducing the diameter from 120 to ~ 20 nm.

References

- [1] M. Piccin, G. Bais, V. Grillo, F. Jabeen, S. De Franceschi, E. Carlino, M. Lazzarino, F. Romanato, L. Businaro, S. Rubini, F. Martelli and A. Franciosi, *Physica E* **37**, 134 (2007).
- [2] F. Jabeen, S. Rubini, F. Martelli, A. Franciosi, A. Kolmakov, L. Gregoratti, M. Amati, A. Barinov, A. Goldoni and M. Kiskinova, *Nano Res.* **3**, 706 (2010).

DISTRIBUTION OF VACANCIES IN NiO NANOPARTICLE: SEARCHING FOR THE ORIGIN OF MAGNETIC BEHAVIOUR IN ANTIFERROMAGNETIC NANOPARTICLES

S. Mandal¹, S. Banerjee¹, K. S. R. Menon¹

¹Surface Physics Division, Saha Institute of Nuclear Physics, Kolkata, India

E-mail: krishna.menon@saha.ac.in



Nickel Oxide (NiO) is a fascinating material not only for condensed matter physicists, but for a very large community comprising material scientists, solid state chemists, technologists and others. It has been studied extensively for many decades, with many different experimental techniques and has found extensive applications, used in catalysis, battery cathodes, gas sensors, electro-chromic films, and magnetic materials. The performance of these devices strongly depends on the stoichiometry or preparation condition of the material. In particular, the vacancy distribution has a strong effect on the overall electrical, electronic (such as oxidation state of Ni in defective NiO) and magnetic properties of the material. For the case of nanoparticles, the defect chemistry is expected to be considerably different from that of the bulk under similar preparation conditions due to the very large surface contribution and can have interesting material properties compared to bulk NiO. Here, we have specifically considered the magnetic properties [1, 3] of NiO nanoparticles demonstrating the general importance of the vacancy distribution over the particle volume.

To correlate the structure and magnetism, we have performed a detailed local characterization of the structure by EXAFS and of the electronic structure by XANES at the Ni K edge. We have prepared the nanoparticles by decomposing chemically precipitated nickel hydroxide at various temperatures, because this method has been widely used in relevant studies [1]. The magnetic properties have been characterized by SQUID magnetometer measurements and we observed a glassy behaviour, with a loop shift upon field cooling, as in other work. From the XRD data, we see the formation of different single phase NiO nanoparticles with different preparation temperatures. The average particle sizes, as estimated from

the line broadenings, are 9.8 nm (prepared at 300 °C), 12.5 nm (360 °C), and 17.3 nm (420 °C). The sample prepared at 800 °C with large grain size (greater than 100 nm, estimated from TEM images) is chosen as a standard. From the XANES measurements, and by comparing the spectral shape at the Ni K-edge with the Ni L₂-edge [2] (see Fig. 1a), we conclude that the Ni ions in NiO remain in a 2+ state and in a high spin electronic configuration. Thus we exclude the possibility that Ni³⁺ ions cause the observed large magnetic moment.

In Fig. 1b, we show the spectra in R space (real space) for different nanoparticles in both TRANS (transmission) and CEY (conversion electron yield) modes [3]. A careful inspection reveals that the FT (Fourier Transformed) intensity decreases for the higher Ni co-ordination shells (indicated by an arrow) as the particle size decreases. Since this intensity gives an estimation of the population (N) and disorder parameter (σ) of the corresponding shell, we have an indication of the enhancement of Ni deficiency as well as of static disorder, as we make particle size smaller. The data acquired in TRANS mode, give very small variations as shown in the inset of Fig. 1b in comparison to CEY mode. One has to remember that TRANS mode gives the variation of overall (surface + bulk) parameters, while CEY mode gives mostly near-surface region information. It does not give only surface information, because our particle sizes are less than typical information depth of CEY mode, but we get most of the surface information because of the exponential decaying nature of the signal. So the variations observed in TRANS mode can actually be attributed to near-surface region. These observations strongly suggest different behaviour of Ni vacancies and static disorder parameters near the surface and inside the bulk of the particles.

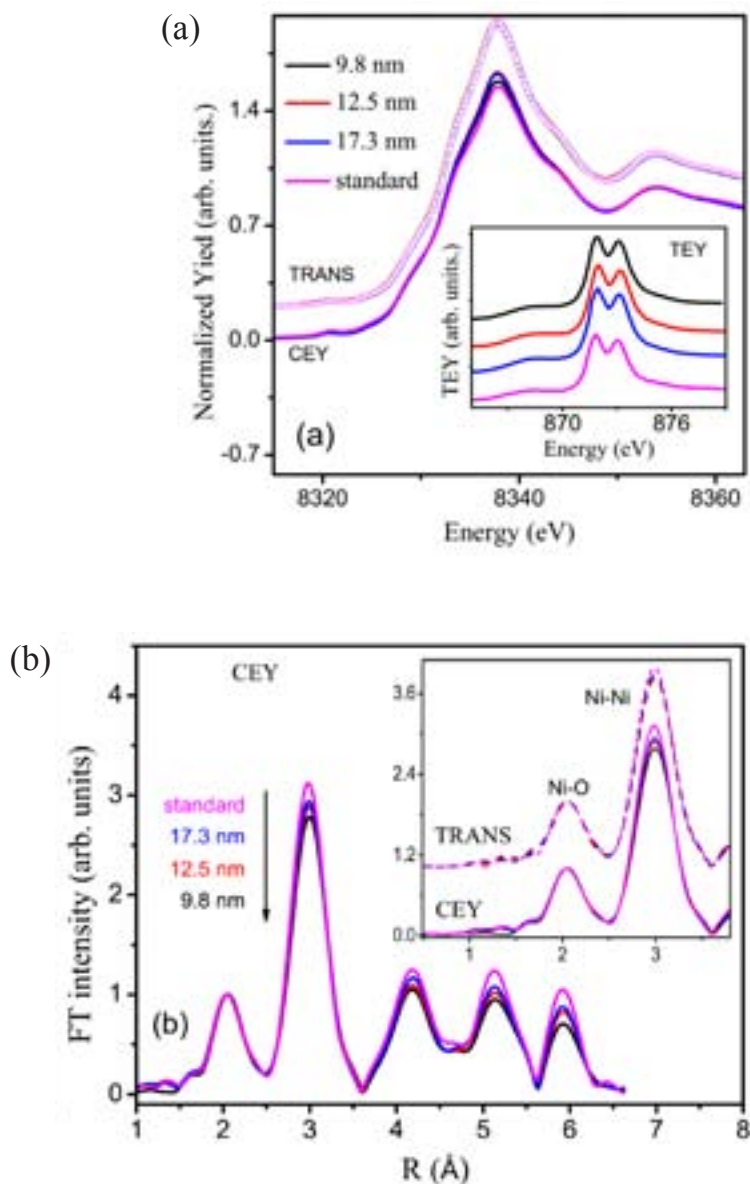


Figure 1. a) Ni K-edge XANES spectra for different nanoparticles (main panel), Ni L_2 edge (inset) showing the absence of any Ni^{3+} . b) The particle size dependence of FT intensity in CEY mode (main panel). Comparison of the data of CEY mode with TRANS mode (inset).

We have performed a detailed structural refinement to quantify these results, and the details can be found in Ref. [3]. The maximum vacancy concentration was found to be 10.3% (CEY) for the smallest (9.8 nm) particle. The corresponding value with TRANS mode is 5.2% (the overall vacancy concentration). From these observations, we can conclude that there exists a definite vacancy distribution pattern over whole particle volume. The near surface region of particles contains a larger amount of vacancies, compared to the bulk of the particles. These findings show that overall vacancy concentration is dominated by a high surface contribution of the nanoparticles. From these observations, we hypothesise an explanation for the long standing problem of

the observed magnetic behaviour of antiferromagnetic nanoparticles. The observed magnetic moment is attributed to the interacting vacancies inside the antiferromagnetic host and the distribution of vacancies over the particle volume determines the behaviour, such as size-dependent nature of spin-glass freezing and exchange bias [3].

References

- [1] R. H. Kodama, S. A. Makhlof and A. E. Berkowitz, *Phys. Rev. Lett.* **79**, 1393 (1997).
- [2] L. Soriano, M. Abbate, J. Vogel *et al.*, *Chem. Phys. Lett.* **208**, 460 (1993).
- [3] S. Mandal, S. Banerjee, and K. S. R. Me non, *Phys. Rev. B* **80**, 214420 (2009).

ADSORPTION OF DOPAMINE ON TITANIA: TOWARDS NOVEL BIOSENSORS AND PHOTOVOLTAICS

A. G. Thomas¹, K. L. Syres¹, F. Bondino², M. Malvestuto², M. Grätzel³

¹School of Physics and Astronomy and Photon Science Institute, The University of Manchester, Manchester, UK

²Sincrotrone Trieste S.C.p.A., Trieste, Italy

³EPFL, Lausanne, Switzerland

E-mail: a.g.thomas@manchester.ac.uk



BACH

Titania (Titanium dioxide, TiO_2) has been used in a number of technological applications, ranging from a white pigment to biosensors, for a number of years. Since the discovery by Fujishima and Honda [1] in 1971 that water can be split photocatalytically by TiO_2 , there has been vigorous research into understanding the photoactive properties of TiO_2 , culminating, most notably, with the development of the photoelectrochemical dye-sensitised solar cell by Grätzel and co-workers [2]. The cost of making such cells is much lower than for conventional cells but the efficiency is currently limited to about 10 % compared with around 30 % for the best semiconductor based cells. In part this efficiency limit is thought to be due to charge trapping at vacancy sites in the TiO_2 . The cells consist of nanoparticulate TiO_2 coated with a photoactive dye which is excited by absorption of sunlight. The photogenerated electron is then transferred to the conduction band of the oxide as shown schematically in figure 1. The hole left on the dye is “mopped up” by a liquid electrolyte though there is currently much research into replacing the electrolyte with a solid state p-type material. Catechols such as dopamine adsorbed on TiO_2 are of some interest in photovoltaics since they shift the optical absorption band from the ultra-violet into the visible region. In the case of catechol adsorbed on TiO_2 it is thought that the photogenerated electron transfers directly from the molecule to the TiO_2 , without involving an excited state in the dye, as shown in figure 1 [3].

Titania is also well known as a bio-compatible material, indeed in titanium based medical implants it is the surface layer of oxide which contributes to their success. As a result there have been attempts to use functionalised nanoparticulate TiO_2 based devices both as in vitro analytical tools [4] and in vivo functional bio-

materials [5]. Dopamine is a particularly useful functional molecule since the amine side chain allows it to be attached to a range of biological or other organic molecules such as polyethylene glycol (PEG). Dopamine mediated charge transfer between DNA and TiO_2 has shown promise as a photactivated system capable of identifying particular base pairs in DNA [4]. Functionalisation of TiO_2 nanoparticles with dopamine-PEG is currently being investigated as a targeted biomaterial system, possibly capable of detecting the location of cancerous tissue [5].

In both the photovoltaic and biomaterial applications, clearly the stability of the molecule/surface bond is crucial in the success of the devices. In addition the orientation of the adsorbed molecules and the strength of bonding play important roles. It is thought that the orientation of dye molecules in dye sensitised solar cells is important in control of efficient charge transfer for example. In many of the photoactive applications of TiO_2 it is used in a nanoparticulate form which has the anatase structure. To date the rutile form of TiO_2 has been the most widely studied phase due to the ready availability of high quality single crystals. Recently we have managed to obtain high quality synthetic anatase single crystals and are beginning to understand the differences in electronic structure and adsorption between the anatase and rutile polymorphs.

In this work we have used a combination of photoelectron spectroscopy, Near Edge X-Ray Absorption Fine Structure (NEXAFS) spectroscopy and DFT calculations to understand the dopamine/ TiO_2 surface [6]. Photoelectron spectroscopy results show that the molecule binds to the surface through both hydroxyl groups following loss of the protons. Using the NEXAFS searchlight effect, we have been

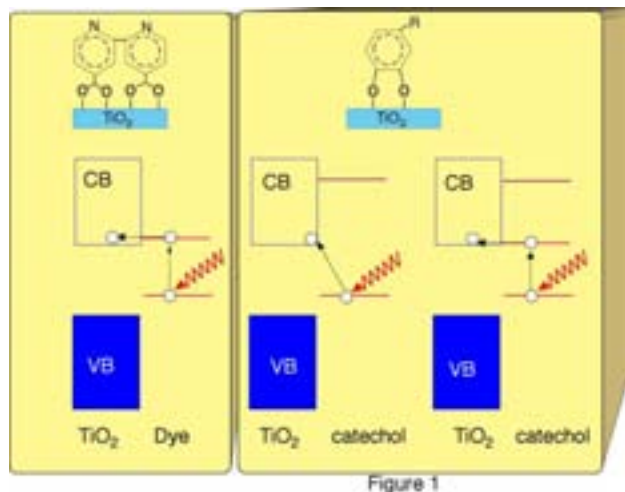


Figure 1

Figure 1. Left panel: excitation of the N3-dye molecule followed by transfer of the electron from the excited state of the dye to the conduction band (CB) of the TiO_2 substrate. Right panel: the direct transfer mechanism proposed by Persson et al [3] which was used to explain the fact that the HOMO-LUMO separation in catechol is larger than the TiO_2 band gap. On the right we show the location of the new states observed in the NEXAFS spectra, which may allow a transfer mechanism similar to that seen in the N3-dye.

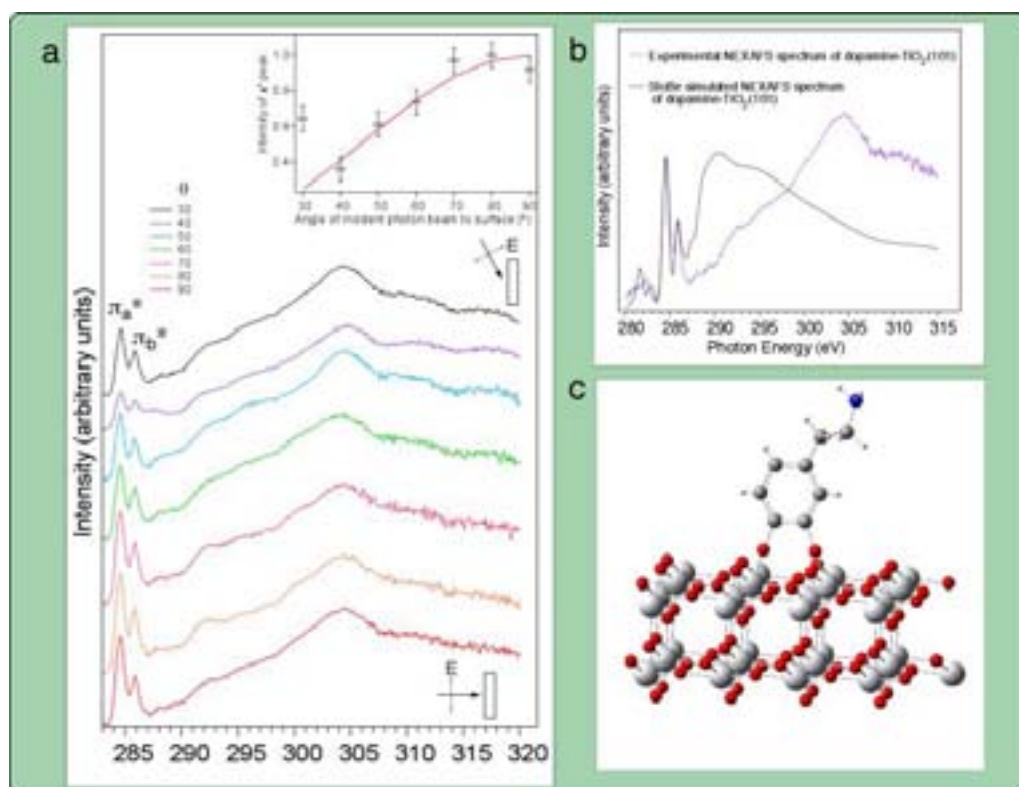


Figure 2.

a) Angle resolved C K-edge NEXAFS spectra of dopamine adsorbed on anatase TiO_2 (101). The inset shows a fit to the intensity of the π_a^* peak which indicates the molecule stands upright with the plane of the ring normal to the surface. b) A comparison of experimental data and DFT calculated NEXAFS spectrum. The peak around 282 eV does not appear in the spectrum of the isolated molecule. c) A schematic diagram of the dopamine molecule adsorbed on an anatase TiO_2 (101) surface.

able to determine that the plane of the ring in dopamine lies normal to the surface (see figure 2) and forms an ordered monolayer. Pyrocatechol which has no side groups, on the other hand is found to tilt around 25° off normal. The differences are thought to lie in steric effects due to the amine side chain. DFT calculations and NEXAFS spectra show the appearance of new unoccupied states thought to be due to hybridisation between the molecule and the surface which may support the direct transfer mechanism. These states appear to be less strong following adsorption on rutile. Furthermore analysis of the separation of π^* derived peaks in the NEXAFS spectra suggest that the bonding strength is greater on anatase although our recent work suggests that the bonding geometry is similar. The reasons for this are not yet fully understood but it is clear

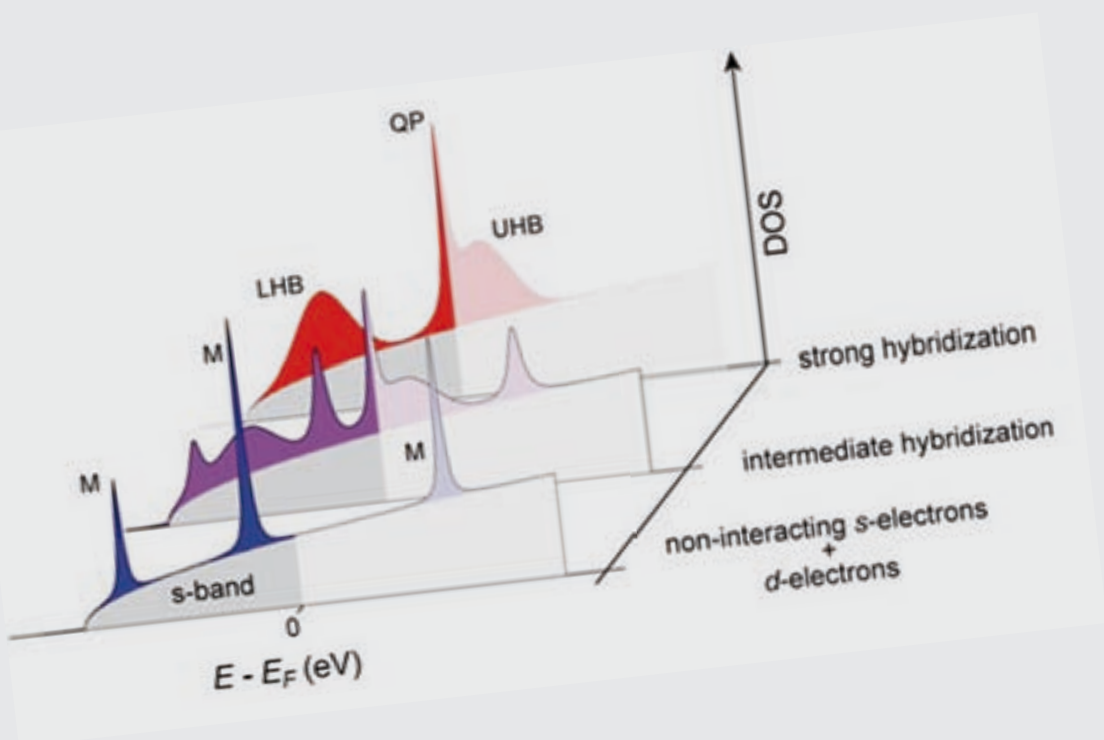
that differences in reactivity between anatase and rutile surfaces are significant.

References

- [1] A. Fujishima and K Honda, *Nature* **238**, 37 (1972).
- [2] B. O'Regan and M. Grätzel, *Nature* **353**, 737 (1991).
- [3] P. Persson, R. Bergström and S. Lunell, *J. Phys. Chem. B* **104**, 10348 (2000).
- [4] T. Kotsoskechagia, F. Cellési, A. Thomas, M. Niederberger and N. Tirelli, *Langmuir* **24**, 6988 (2008).
- [5] J. Q. Liu, L. de la Garza, L. G. Zhang, N. M. Dimitrijevic, X. B. Zuo, D. M. Tiede, and T. Rajh, *Chem. Phys.* **339**, 154 (2007).
- [6] K. L. Syres, A. G. Thomas, F. Bondino and M. Malvestuto and M. Grätzel, *Langmuir* **26**, 14548 (2010).



**MAGNETISM
AND HIGHLY CORRELATED SYSTEMS**



EXPERIMENTAL STUDY OF THE INCOHERENT SPECTRAL WEIGHT IN THE PHOTOEMISSION SPECTRA OF THE MISFIT COBALTATE $[\text{Bi}_2\text{Ba}_2\text{O}_4][\text{CoO}_2]_2$

A. Nicolaou^{1,2}, V. Brouet¹, M. Zacchigna³, I. Vobornik³, A. Tejada^{2,4}, A. Taleb-Ibrahimi², P. Le Fèvre², F. Bertran², S. Hébert⁵, H. Muguerra⁵, D. Grebille⁵

¹Laboratoire de Physique des Solides, Université Paris-Sud, Orsay, France

²Synchrotron SOLEIL, L'Orme des Merisiers, Gif-sur-Yvette, France

³Laboratorio Nazionale TASC IOM-CNR, Trieste, Italy

⁴Institut Jean Lamour, CNRS-Nancy-Université-UPV-Metz, Vandoeuvre-les-Nancy, France

⁵Laboratoire CRISMAT, UMR 6508 CNRS et Ensicaen, Caen, France

E-mail: ivana.vobornik@elettra.trieste.it



In a Fermi liquid, elementary excitations can be described as quasiparticles (QP) with a weight Z that decreases as correlations increase, the remaining weight being transferred to incoherent excitations. Angle-resolved photoemission (ARPES) is a unique tool to observe both coherent and incoherent excitations. This often leads to a characteristic “peak-dip-hump” (PDH) structure of the spectra, where the peak corresponds to the QP and the hump (HP) to the incoherent excitations. The PDH is then a direct “image” of the correlation strength, but its interpretation is not always straightforward. In a strongly correlated metal, the QP band is typically renormalized by a factor Z^{-1} , and the HP corresponds to the residual lower Hubbard band [1]. Another type of PDH can be observed, even in a weakly correlated metal, due to the coupling between electrons and a collective mode of energy ω_0 , most frequently phonons [2]. The PDH occurs in the vicinity of ω_0 , and, for moderate couplings, the dominant effect is a “kink” in the dispersion at ω_0 [3]. The amplitude of the kink is directly related to the strength of the coupling, but ω_0 is an independent energy scale.

Here we describe an intermediate situation, where a PDH structure (see Fig. 1) is found with a dip at an energy $\omega_0=0.2$ eV, larger than typical phonon frequencies, but smaller than the 1.2 eV bandwidth predicted by LDA calculations [4]. This structure is observed in the misfit cobaltate $[\text{Bi}_2\text{Ba}_2\text{O}_4][\text{CoO}_2]_2$ (BiBaCoO). The question arises whether ω_0 indicates the QP bandwidth or a “kink” energy.

We show that Z can change from 0.1 to 0.7, depending on this interpretation [5]. Such an

uncertainty in the value of Z is clearly inconclusive. We solve this problem by using the redistribution of spectral weight between QP and HP as an indicator of the interaction strength. This establishes that the PDH corresponds to strong many-body effects, characterized by $Z = 0.15 \pm 0.05$.

In Fig. 1, we show ARPES measurements taken at the APE beamline of Elettra. The beam was linearly polarized, either in the plane of incidence [Linear Horizontal (LH)] or perpendicularly [Linear Vertical (LV)] (the plane of incidence is defined by the incoming beam and the sample's surface normal). Fig. 1 shows that the spectra are very different for LH and LV polarizations. In LH, a sharp peak (QP) crosses the Fermi level (E_F) and a broad shoulder (HP) disperses to higher binding energies, eventually merging with a nearly nondispersive peak (NDP) centered at ~ -0.8 eV. For LV, the sharp peak and the shoulder are totally suppressed and only the NDP remains. In Figs. 1(c) and 1(d), the PDH structure is emphasized at different k by subtracting the LV from LH spectra, after normalizing at -1.5 eV.

In our experimental configuration, we expect to detect even/odd orbitals with respect to the scattering plane with LH (a_{1g} and one e_g [4]) / LV (the other e_g). We overlay on our measurements in Figs. 1(a) and 1(b) the calculated LDA bands. Clearly, the slope of both the QP and the HP dispersions correspond to that of the a_{1g} band. The question arises as to why there is a “break” in the a_{1g} dispersion, giving rise to the QP and HP parts. Along ΓM , a large hybridization gap is predicted between a_{1g} and e_g , which seems to be

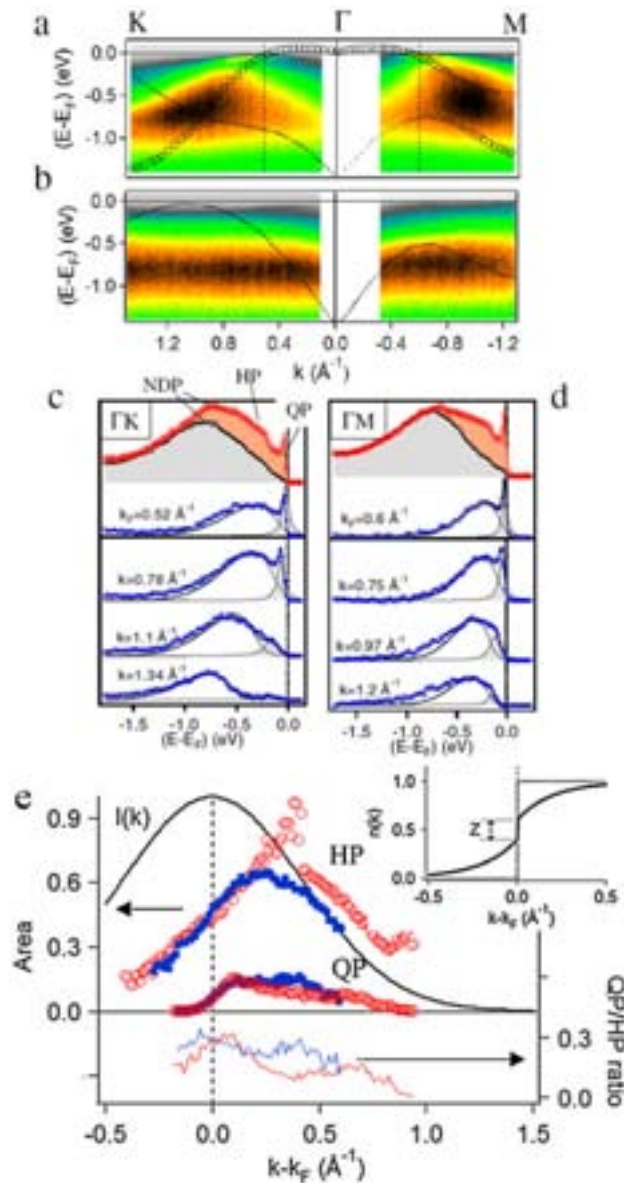


Figure 1. ARPES intensity plots along ΓK (left) and ΓM (right) with LH (a) and LV (b) polarizations. The LDA dispersion of even/odd bands is superimposed on the LH/LV image [4].

The a_{1g} character is indicated by the size of the markers. (c), (d) Top: Spectra at k_F in LH (large circles, light gray/red) and LV (small circles, black). Bottom: Difference spectra (LH-LV, blue), at the indicated k values, fitted with a Lorentzian cut by the Fermi function for the QP and an asymmetric function for the HP. (e) Top: Area of QP and HP along ΓK (open red circles) and ΓM (solid blue squares) obtained with the EDC fit of Fig. 1. Bottom: ratio of QP and HP area as a function of k . Inset: Sketch of the theoretical variations of $n(k)$ for $Z = 0.2$.

able to produce such a situation, as proposed before [5]. The main problem with this explanation is that no hybridization gap should occur along ΓK , whereas we measure almost the same PDH in the two directions. Therefore, we propose an alternative explanation: the PDH is an intrinsic structure of a_{1g} due to correlation effects [5]. The similarity between the two directions is then natural, as the bandwidth is quite similar.

An estimation of Z can be obtained through direct observation of the spectral weight redistribution. The QP weight at k_F is reduced, half the incoherent weight is transferred to the HP and the other half to previously unoccupied states at $k < k_F$, yielding $QP/HP = 2Z(1-Z)$. As shown in Fig. 1(e), the HP is much stronger at k_F than the QP and remains strong at $k < k_F$ as expected for small Z . In the bottom part of Fig. 1(e), the ratio of areas of QP and HP

is shown to be about 0.3 near k_F for both ΓM and ΓK , yielding $Z = 0.15 \pm 0.05$. This value is well defined and significantly smaller than the usual estimation from the effective mass [5]. Remarkably, this new estimation of Z is consistent with the ratio of the QP and LDA bandwidth $\sim 0.2/1.2 = 0.17$. This gives a self-consistent view of the correlations, where 200 meV directly indicates the QP energy scale.

References

- [1] A. Georges, et al., *Rev. Mod. Phys.* **68**, 13 (1996).
- [2] S. LaShell, E. Jensen, and T. Balasubramanian, *Phys. Rev. B* **61**, 2371 (2000).
- [3] A. Damascelli, Z. Hussein, and Z.-X. Shen, *Rev. Mod. Phys.* **75**, 473 (2003).
- [4] D. J. Singh, *Phys. Rev. B* **61**, 13397 (2000).
- [5] A. Nicolaou et al., *Phys. Rev. Lett.* **104**, 056403 (2010), and references therein.

CORRELATED ELECTRONS STEP-BY-STEP: ITINERANT-TO-LOCALIZED TRANSITION OF Fe IMPURITIES IN FREE-ELECTRON METAL HOSTS

C. Carbone¹, M. Veronese¹, P. Moras¹, S. Gardonio¹, C. Grazioli¹, P. H. Zhou², O. Rader³, A. Varykhalov³, C. Krull⁴, T. Balashov⁴, A. Mugarza⁴, P. Gambardella^{4,5}, S. Lebegue⁶, O. Eriksson⁷, M. I. Katsnelson⁸, A. I. Lichtenstein⁹

¹Istituto di Struttura della Materia, Consiglio Nazionale delle Ricerche, Trieste, Italy

²International Center for Theoretical Physics, Trieste, Italy

³BESSY GmbH, Berlin, Germany

⁴Centre d'Investigacions en Nanociència i Nanotecnologia, Barcelona, Spain

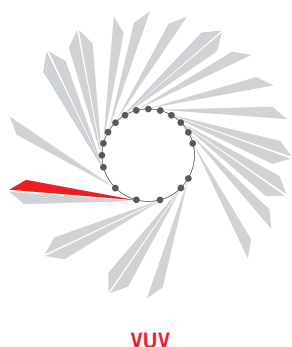
⁵Institució Catalana de Recerca i Estudis Avançats, Barcelona, Spain

⁶Institut Jean Barriol, Nancy Université, Vandoeuvre-lès-Nancy, France

⁷Department of Physics and Materials Science, Uppsala University, Uppsala, Sweden

⁸Institute for Molecules and Materials, Radboud University of Nijmegen, Nijmegen, The Netherlands

⁹Institute for Theoretical Physics, University of Hamburg, Hamburg, Germany



Magnetic atoms on surfaces represent the ultimate limit of monodisperse magnetic particles. Although individual atoms generally present paramagnetic behavior, their investigation provides insights into fundamental and practical issues in magnetism, such as the survival of local moments in nanoparticles and thin films deposited on nonmagnetic supports, the onset of magnetic anisotropy and the tendency to display either classical or quantum behavior.

The description of the electronic excitations of magnetic atoms is highly nontrivial and may be considered as a benchmark for understanding electron correlation in *d*-metal systems. The established theory of atomic multiplet structure describes with great accuracy the magnetic moments of transition-metal ions. The main mechanism of energy level formation in this case is related to the strong Coulomb interaction among *3d*-electrons. On a surface, the factor determining whether an atomic multiplet structure should form, or if energy bands are to be expected, is the competition between the Coulomb energy and the kinetic energy associated with electrons hopping from site to site in the lattice (Fig. 1). When neither of these two terms dominates, one often observes complicated electron states that are manifestations of electron correlation. For moderate hybridization between impurity and host electron states, the Anderson model describes well the formation of a magnetic moment and the many-body spin-flip processes may lead to the Kondo effect [1].

To study the onset and progression of *d-sp* hybridization for magnetic impurities on metal substrates we have employed STM and high-resolution photoemission spectroscopy of Fe atoms deposited on alkali metal films [2]. Depending on the atomic volume of the alkali ions, the surface electron density can be decreased or increased by moving towards heavier and lighter alkali species, respectively. We find the hybridization of the Fe *d*-states to change drastically from very weak for Cs to much stronger for Li. Fig. 2a shows photoemission spectra for 0.01 ML Fe atoms on Cs, K, Na, and Li hosts after subtraction of the surface background. From Cs to K only a reduction of intensity of the multiplet features is observed, accompanied by a moderate energy broadening. On Na and Li, however, the spectra change qualitatively, indicating the onset and progression of *d-sp* electron hybridization. For Fe on Li the spectrum presents a renormalized quasi-particle resonance near E_F and lower Hubbard bands around -2 eV. In the Anderson model, the quasi-particle resonance peak near E_F is identified with the Kondo effect, representing low-energy excitations that involve the spin degrees of freedom of the impurity and conduction electrons. In this case, STM conductance spectra reveal an electronic resonance centered about E_F that is the signature of a many-body Kondo state with characteristic temperature $T_K = 96$ K (Fig. 2b,c). Moreover, an interesting and unique feature is found for the Fe-Na system: the photoemission spectrum in this case is a mixture of an

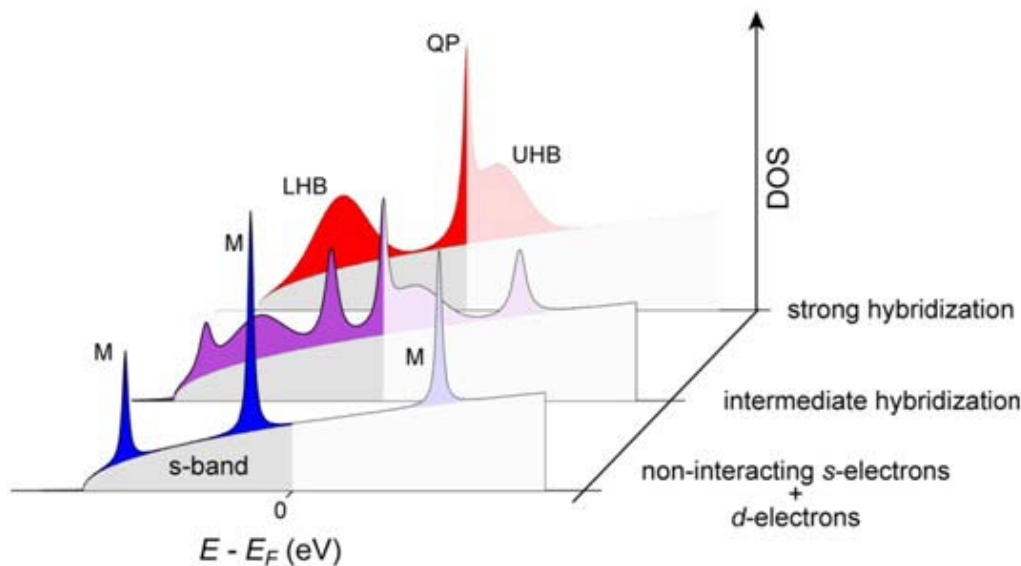


Figure 1. Spectral function of a many-body d-electron impurity and host conduction electrons. Depending on the local Coulomb interaction and hybridization strength different behaviors are expected: localized impurity limit (bottom); intermediate coupling (middle); strong hybridization limit (top). Letters indicate multiplet (M), quasi-particle resonance (QP), lower and upper Hubbard bands (LHB, UHB) spectral features.

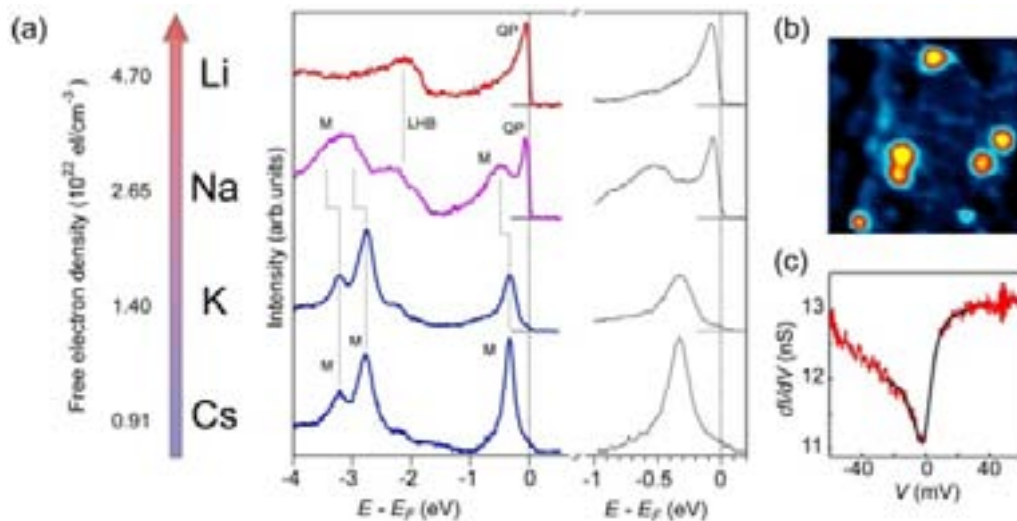


Figure 2. (a) Host-dependent Fe impurity photoemission spectra on free-electron like substrates. The data represent the impurity photoemission intensity after subtraction of the alkali background. (b) Spatially-resolved Kondo resonances measured by STM corresponding to individual Fe impurities deposited on a 3.8 monolayer-thick Li film on Cu(100). (c) Conductance spectrum measured on top of a Fe adatom.

atomic multiplet structure, quasi-particle bands near E_F , and the low lying Hubbard bands around -2 eV. Such features mark the transition between the localized and hybridized extremes of Fig. 1.

These data show that the interplay between delocalization, mediated by the free-electron environment, and Coulomb interaction among d -electrons gives rise to complex electronic configurations. The multiplet structure of a single Fe atom evolves and gradually dissolves into a quasi-particle peak near E_F with increasing host electron density. Metal adatoms thus provide a model system to characterize the “resilience” of electron correlation at surfaces in sub-nanometer structures. Moreover, general ab-initio theories of localized-to-itinerant electron behavior that go beyond DFT, such as the recently developed first-principles Dynamical Mean Field Theory [1,3], can be put

to the test in order to improve our description of magnetism in solid state systems [2].

References

- [1] G. Kotliar, S. Y. Savrasov, K. Haule, V. S. Oudovenko, O. Parcollet, C. A. Marianetti, *Rev. Mod. Phys.* **78**, 865 (2006).
- [2] C. Carbone, M. Veronese, P. Moras, S. Gardonio, C. Grazioli, P. H. Zhou, O. Rader, A. Varykhalov, C. Krull, T. Balashov, A. Mugarza, P. Gambardella, S. Lebeque, O. Eriksson, M. I. Katsnelson, and A. I. Lichtenstein, *Phys. Rev. Lett.* **104**, 117601 (2010).
- [3] M. I. Katsnelson, V. Yu. Irkhin, L. Chioncel, A. I. Lichtenstein, R. A. de Groot, *Rev. Mod. Phys.* **80**, 315 (2008); E. Gorelov, T. O. Wehling, A. N. Rubtsov, M. I. Katsnelson, and A. I. Lichtenstein, *Phys. Rev. B* **80**, 155132 (2009).

DOMAIN-WALL DEPINNING ASSISTED BY PURE SPIN CURRENTS

E. Tafr¹, D. Ilgaz,² J. Nievendick², L. Heyne², D. Backes^{2,3}, J. Rhensius^{1,2,3}, T. A. Moore², M.A. Nino⁴, A. Locatelli⁴, T. O. Menten⁴, A. v. Schmidfeld², A. V. Bieren^{1,2}, S. Krzyk², J. Heidler¹, L. J. Heyderman³, M. Kläui^{1,2}

¹SwissFEL, Paul Scherrer Institut, Villigen, Switzerland and Laboratory for Nanomagnetism and Spin Dynamics, Ecole Polytechnique Fédérale de Lausanne, Lausanne, Switzerland

²Fachbereich Physik, Universität Konstanz, Konstanz, Germany

³Laboratory for Micro- and Nanotechnology, Paul Scherrer Institut, Villigen, Switzerland

⁴Sincrotrone Trieste S.C.p.A., Trieste, Italy

E-mail: mathias.klaui@epfl.ch



NANOSPECTROSCOPY

Today's Information and Communication Technology devices are based on semiconductor technology, which faces severe limitations in the near future, due to the continuous trend towards miniaturisation. These limitations call for alternative approaches. Furthermore, today's drive towards green technology necessitates replacing volatile with non-volatile random access memories (RAM). One of the newly devised non-volatile memories is the so-called racetrack memory which is based on magnetic domain wall (DW) motion [1]. For DW motion various approaches have been put forward such as moving them by spin polarized charge currents, which has been probed previously at Elettra [2]. However, these currents generate strong heating and entail further problems (see [3]). Using pure diffusive spin currents, where the electrons diffuse without an associated net charge current, is a possible alternative approach. Its main advantage is that the generation of spin currents, that involves energy dissipation, can occur at a distant location from the device, which can thus be kept cool and still manipulated by the absorbed diffusive spin currents. In line with this approach, nonlocal spin valve (NLSV) geometries have been developed, where pure spin currents are generated across ferromagnetic (FM) – non-magnetic (NM) contacts. Recently, the reversal of the magnetic state of a permalloy ($\text{Ni}_{80}\text{Fe}_{20}$, Py) disc in a NLSV geometry was observed [4].

At Elettra we recently achieved the first observation of DW depinning assisted by pure spin currents [3]. A scanning electron microscope (SEM) image of one of the samples is shown in Fig. 1(a). We inject a spin-polarized current I as shown in Fig. 2(b) and measure

the non-local voltage U originating from the spin current diffusing from the top to the bottom permalloy element. This allows us to deduce important parameters such as the spin polarization in Py and spin diffusion length in the non-magnetic Cu wire. This, in turn, enables us to determine the pure spin current density that arrives at the bottom Py half-ring element.

In the next step we used the pure spin current to manipulate magnetization. For that purpose, a transverse DW (TDW) was positioned in the Py half-ring, below the central Cu wire (NM in Fig. 2b). In Fig. 1b, we show an X-ray Magnetic Circular Dichroism Photoemission Electron Microscopy (XMCD-PEEM) image of the magnetization configuration with a DW taken at the Nanospectroscopy beamline at Elettra. A corresponding micromagnetic simulation is presented (Fig. 1c). The pure spin current is generated by spin-polarized charge current I at the top as shown in Figs. 2b and 2c. It diffuses down (green spins in b, red spins in c) in the central Cu wire NM and is absorbed by the bottom permalloy half ring with the domain wall. These absorbed spins exert a torque on the domain wall and move it as shown schematically in Fig. 2d. The measured dependence of the depinning magnetic field as a function of the current amplitude is shown in Fig. 2a. For negative currents, the depinning field decreases with increasing current amplitude, and we obtain a depinning efficiency of $\varepsilon = (6 \pm 1) \cdot 10^{-14} \text{ T m}^2/\text{A}$, and by extrapolation a spin current density of $(7 \pm 2) \cdot 10^{10} \text{ A/m}^2$ at which the DW would depin without any external field. Compared to the case where the combined spin and charge current flows in the ferromagnet [2], we obtain an efficiency that

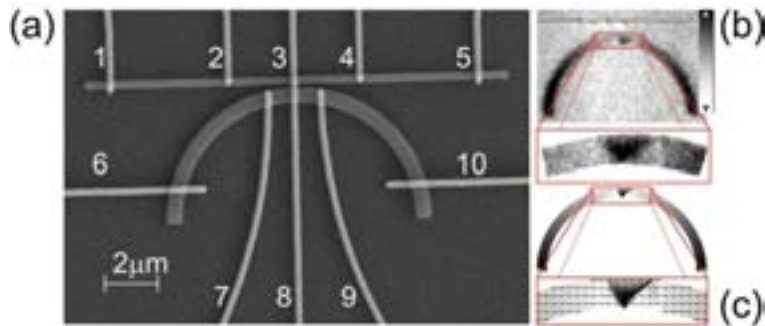


Figure 1. (a) Scanning electron microscopy image of the NLSV geometry of the samples used in the experiment with the contacts numbered 1–10. The bright stripes are the Cu contacts, while the darker stripes are the Py wire and half-ring. (b) XMCD PEEM image of the spin configuration and enlarged image of the transverse domain wall in the half-ring prior to contacting. The shades of gray correspond to the vertical component of the magnetization configurations, which is in agreement with the micromagnetic simulation shown in (c). (Reprinted from ref. [3], Copyright American Physical Society).

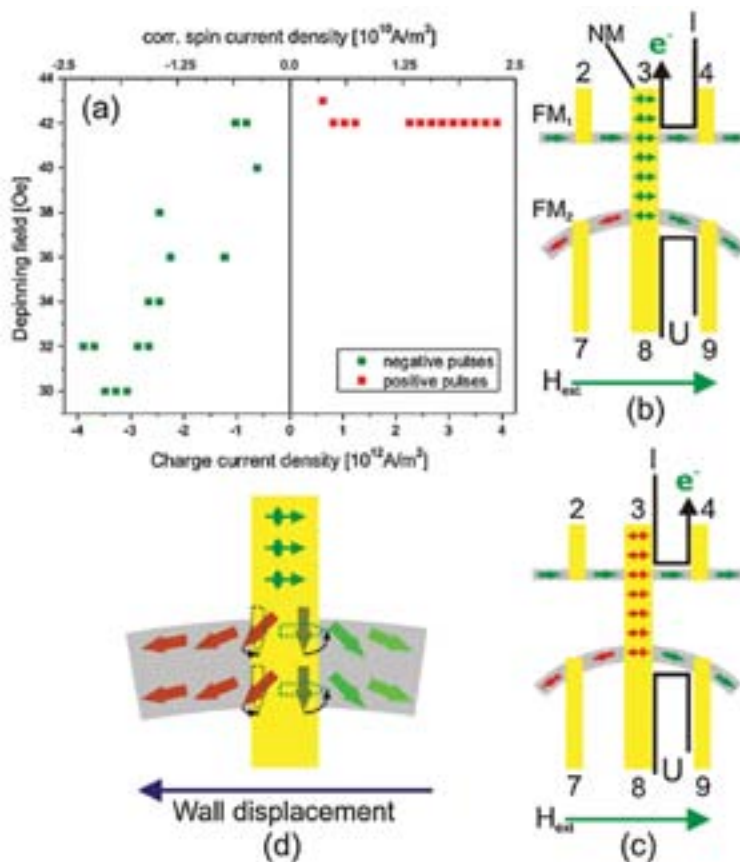


Figure 2. (a) Depinning field as a function of the applied charge currents and the resulting corresponding spin current density (top x-axis). The situation for negative and positive charge current pulses is shown in (b) and (c), where arrows with circles represent the spins in the pure spin current. In (d) the torque exerted by the spin current on the DW leading to DW motion is shown for negative pulses. (Reprinted from ref. [3], Copyright American Physical Society).

is larger by an order of magnitude and the extrapolated zero-field depinning current density is about 30 times smaller. The observed high efficiency can be explained theoretically as a consequence of large torque acting on the surface layers of the FM, where the DW pinning originates (see [3] for details).

In conclusion, we have shown that the depinning of DWs can be efficiently assisted by pure diffusive spin currents, which opens new possibilities for future low-power spintronic devices.

References

- [1] S.S.P. Parkin, *et al.*, *Science* **320**, 190 (2008).
- [2] L. Heyne, *et al.*, *Phys. Rev. Lett.* **100**, 066603 (2008).
- [3] D. Ilgaz, *et al.*, *Phys. Rev. Lett.* **105**, 076601 (2010).
- [4] T. Yang, *et al.*, *Nature Phys.* **4**, 851 (2008).

FERROMAGNETIC AND ORDERED MnSi(111) EPITAXIAL LAYERS

E. Magnano¹, F. Bondino¹, C. Cepek¹, M. C. Mozzati², F. Parmigiani^{1,3}

¹Laboratorio Nazionale TASC IOM-CNR, Trieste, Italy

²Dipartimento di Fisica "A. Volta," CNISM, Università di Pavia, Pavia, Italy

³Dipartimento di Fisica, Università degli Studi di Trieste, Trieste, Italy

E-mail: magnano@tasc.infm.it



BACH

The possibility of growing layers on semiconductors which are ferromagnetic at room temperature is of paramount importance for non-volatile memories and spintronic devices based on the injection of spin-polarized current from a ferromagnetic metal into a semiconductor. In this perspective MnSi films grown on Si substrates represent an interesting case study. MnSi is an intermetallic compound crystallizing in the cubic crystal structure B20 with four Mn ions and four Si ions per unit cell. At temperatures below ~ 30 K, MnSi has a helical magnetic structure with a spiral period of ~ 180 Å. When a magnetic field of ~ 650 Oe is applied in this temperature range, a phase transition from the helical structure to a conical spin-structure is observed, while for magnetic field larger than 6 kOe the system becomes a conventional ferromagnet [1]. It is rather interesting to note that the lattice parameter of a MnSi(111) film matches epitaxially the Si(111) surface. The (1x1) surface unit cell of MnSi(111) has a mismatch of 3.2% with respect to the $(\sqrt{3}\times\sqrt{3})$ unit cell of Si(111). For ultrathin films, a ferromagnetic metallic ground state with a high

degree of spin polarization at the Fermi level is expected [2]. Therefore, highly-ordered MnSi films on silicon, having the same magnetic and electronic properties of the bulk compound, will address the possibility of integrating ferromagnetic materials with silicon.

In figure 1 the formation of the ordered MnSi film on the Si(111)-(7x7) surface is tracked by collecting at normal emission the valence-band spectra from clean Si, from the non-reacted interface after deposition of a Mn film of ~ 10 nm thickness, and from the MnSi film after annealing at ~ 620 K. Two features are clearly observed in the non-reacted interface, one very close to the Fermi edge (A) and the other at ~ 2.5 eV below the Fermi edge (B), which are characteristic of the Mn 3d density of states. After annealing, the valence-band spectrum shows a new spectral feature (C) at ~ 1.7 eV below E_F , a clear sign of the hybridization of Mn 3d with Si sp states. A non/zero density of states at the Fermi edge is still detected, indicating metallic character for these MnSi films. The LEED pattern observed for the MnSi thick film is $(\sqrt{3}\times\sqrt{3})R30^\circ$, compatible with the (1x1) surface unit cell of MnSi(111). The Si 2p core level presents the characteristic lineshape already observed for thin MnSi films. XAS spectra at the Mn 2p edge show a lineshape with a typical high-energy shoulder already observed for thin MnSi films and bulk MnSi single crystals, originating from the hybridization of the Mn 3d states with the Si sp states [3].

Figure 2(a) shows the ZFC (Zero Field Cooling) and FC (Field Cooling) temperature dependence of the volume magnetization (M) for the MnSi/Si(111) sample at 100 Oe. The peak observed at ~ 30 K in the ZFC curve matches well with that commonly reported for MnSi single-crystal and polycrystalline samples but,

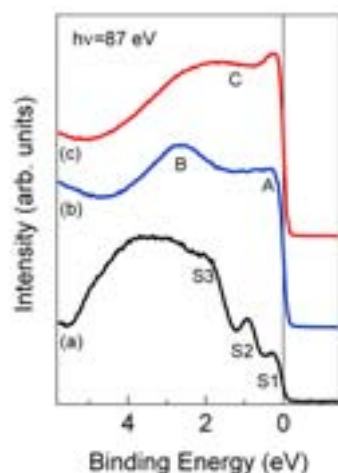


Figure 1. Valence-band photoemission spectra from the clean (7x7) reconstructed Si(111) surface (a), from the Mn/Si(111) interface after Mn deposition (b), and after the annealing at 620 K (c). The spectra have been measured at RT with photon energy $h\nu=87$ eV.

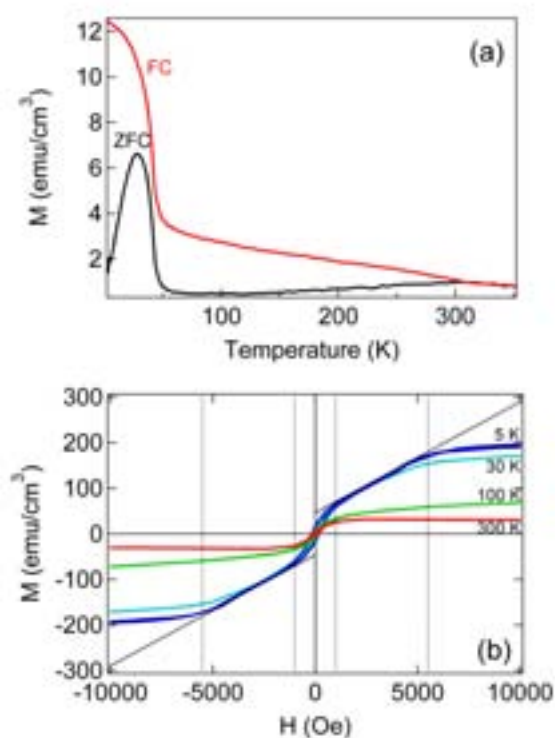


Figure 2. (a) Temperature dependence of MnSi/Si(111) volume magnetization at 100 Oe, in ZFC and FC regimes, with magnetic field applied parallel to the thin film plane. (b) Hysteresis loops collected for the same sample (H parallel to the sample plane) at 5 K and 30 K (corresponding to the ordered phase of bulk MnSi), and at 100 K and 300 K (in the paramagnetic range for bulk MnSi, blue line).

in addition, a distinct thermomagnetic history effect occurs in the whole temperature region below 300 K, suggesting the presence of a second ferromagnetic-like contribution. In figure 2(b) the M vs. H behaviour of MnSi/Si(111) at 5 K, 30 K, 100 K and 300 K is reported. The characteristic features of the MnSi hysteresis cycle [4] are clearly detectable in our results at 5 K, at least for field $|H| > 1$ kOe. An unusual behaviour is instead observed in the low fields region (corresponding to the helical state of MnSi), where an open hysteresis cycle ($H_C \sim 180$ Oe) appears to overlap the closed cycle expected for MnSi. We confidently consider this ferromagnetic open cycle to be connected to the “second magnetic phase”, which is also responsible for the different behaviour, from RT downwards, of the ZFC and FC M vs. T curves.

Recently Hortamani and coworkers [2] calculated that Mn atoms at the surface and at the interface with silicon possess larger spin polarization at the Fermi level and larger magnetic moments ($2.3 \mu_B$ and $3.4 \mu_B$ at the surface and interface respectively) than Mn atoms in bulk MnSi ($0.4 \mu_B$). These calculations further predict a strong increase of the Curie temperature in ultrathin MnSi films compared to the transition temperature of bulk

MnSi. Therefore, a more focused study of the magnetic properties of MnSi/Si(111) ultrathin film seems to be important for the fabrication of spintronic devices based on the injection of spin-polarized current from a ferromagnetic metal into a semiconductor.

In conclusion, we have shown the possibility of growing MnSi layers on Si(111) with the same bulk MnSi main physical properties, so closing a long-standing question. Moreover, the observed ferromagnetic transition at ~ 300 K is very interesting in relation to recent calculations and it could be promising for the above mentioned applications in the field of spintronics.

References

- [1] Y. Ishikawa, K. Tajima, D. Bloch and M. Roth, *Solid State Commun.* **19**, 525 (1976).
- [2] M. Hortamani, L. Sandratskii, P. Kratzer, I. Mertig, and M. Scheffler, *Phys. Rev. B* **78**, 104402 (2008).
- [3] E. Magnano, F. Bondino, C. Cepek, M. C. Mozzati, and F. Parmigiani, *Appl. Phys. Lett.* **96**, 152503 (2010) and reference therein.
- [4] S. B. Roy and M. K. Chattopadhyay, *European Phys. Lett.* **79**, 47007 (2007).

ORBITAL NATURE OF THE MULTIBAND FERMI SURFACE OF $\text{Ba}_2(\text{Fe}_{1-x}\text{Co}_x)_2\text{As}$

B. Mansart¹, V. Brouet¹, E. Papalazarou¹, M. Fuglsang Jensen¹, L. Petaccia², S. Gorovikov², A.N. Grum-Grzhimailo³, F. Rullier-Albenque⁴, A. Forget⁴, D. Colson⁴, M. Marsi¹

¹Laboratoire de Physique des Solides, CNRS-UMR 8502, Université Paris-Sud, Orsay, France

²Sincrotrone Trieste S.C.p.A., Trieste, Italy

³Institut of Nuclear Physics, Moscow State University, Moscow, Russia

⁴Service de Physique de l'Etat Condense, CEA Saclay, Gif-sur-Yvette, France

E-mail: mansart@lps.u-psud.fr



BAD ELPH

Understanding the secrets of high temperature superconductivity is one of the main open questions in condensed matter physics, since its discovery in 1986 in copper oxide compounds. The discovery in 2008 of high temperature superconductivity in the completely different family of FeAs compounds – the iron pnictides – caused a lot of excitement, opened new perspectives and raised more questions. The highest critical temperature T_c found so far in an iron pnictide is 55 K, and while a lot of effort is devoted to searching other compounds with even higher T_c , a few points already emerged from the studies of these materials [1], in particular when they are compared with cuprates. While, like in cuprates, the superconductivity takes place onto the quasi two-dimensional planes (FeAs rather than CuO: in Fig. 1a the structure of the pnictides of the $\text{Ba}_2\text{Fe}_2\text{As}$ family can be seen), it is clear that the overall electronic structure of iron pnictides is markedly more three-dimensional [2]; while the normal state in cuprates is a Mott insulator, in iron pnictides it is a metallic state characterized by the presence of a spin density wave; while in cuprates superconductivity and magnetism are mutually exclusive, in the FeAs phase diagram, regions can be found where the two properties exist simultaneously [1]; finally, while copper oxides are essentially one-band systems, where the Fermi surface is determined by Cu $3d_{x^2-y^2}$ electrons that are responsible for the opening of the superconducting gap, iron pnictides are multiband systems: their Fermi surface is composed by five different Fe $3d$ orbitals. These five orbitals have different orientations in space, as represented in Fig. 1c: d_{xy} and $d_{x^2-y^2}$ are essentially in the xy plane (i.e. in the Fe-As plane), while d_{xz} and

d_{yz} are perpendicular to it; finally, d_{z^2} is also perpendicular to it and essentially directed along the z axis. The band structure and the Fermi surface of FeAs are thus a complicated mixture of these 5 orbitals and they can be predicted by advanced theoretical methods, like those shown in Fig. 1d for $\text{Ba}_2\text{Fe}_2\text{As}$. Since the opening of the superconducting gap takes place at the Fermi surface, a knowledge of the detailed nature of the orbitals that contribute to electron and hole pockets is essential to understand and attempt to model the high temperature superconductivity in these materials.

Angle Resolved PhotoElectron Spectroscopy (ARPES) can be a very powerful tool to get insight into the orbital nature of the Fermi surface of multiband materials like FeAs compounds. By changing the polarization of the incoming photon, not only can one get information on the dispersion of the bands in the reciprocal space (Fig. 1b and 2a), but also on the symmetry of the involved orbitals. We used this approach to study in detail the electronic structure of superconducting $\text{Ba}_2(\text{Fe}_{1-x}\text{Co}_x)_2\text{As}$ ($x=0.08$, $T_c=24$ K) [3], exploiting the variable polarization available on the BadElPh beamline [4]: examples of ARPES band dispersion measured along the ΓX directions are shown in Fig. 2b and 2c. The asymmetry in the band dispersion, dependent on the light polarization (Fig. 2d and 2e), can be used to understand the nature of the orbitals composing the bands: thanks to this kind of approach, we were able to shine new light on the orbital nature of the hole pockets around the Γ point in the Brillouin zone. In particular, high angular resolution available on BadElPh at low photon energy made it possible to distinguish clearly, for the first time, two separate

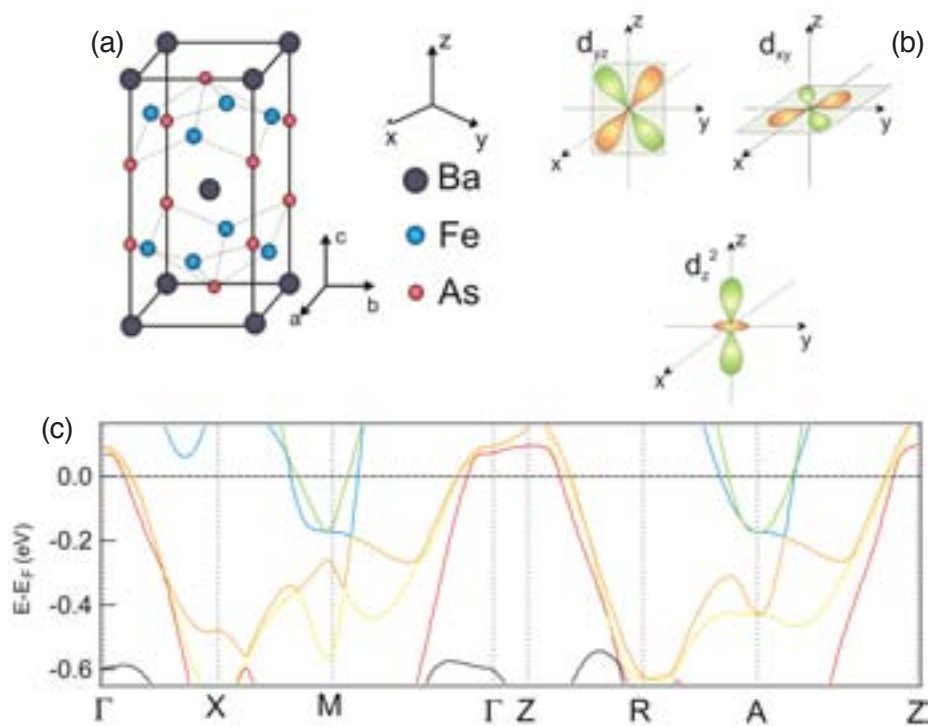


Figure 1. Structure of the $\text{Ba}_2\text{Fe}_2\text{As}$ high temperature superconductors (a) and schematic representation of the spatial distribution of the main Fe orbitals contributing to the electronic structure close to the Fermi level (b). On the basis of this available information, the electronic band structure of this novel family of high temperature superconductors can be computed, as shown in (c) (courtesy of M. Aichorn, S. Biermann et al.), giving a complex structure with several bands that are here represented by different colours.

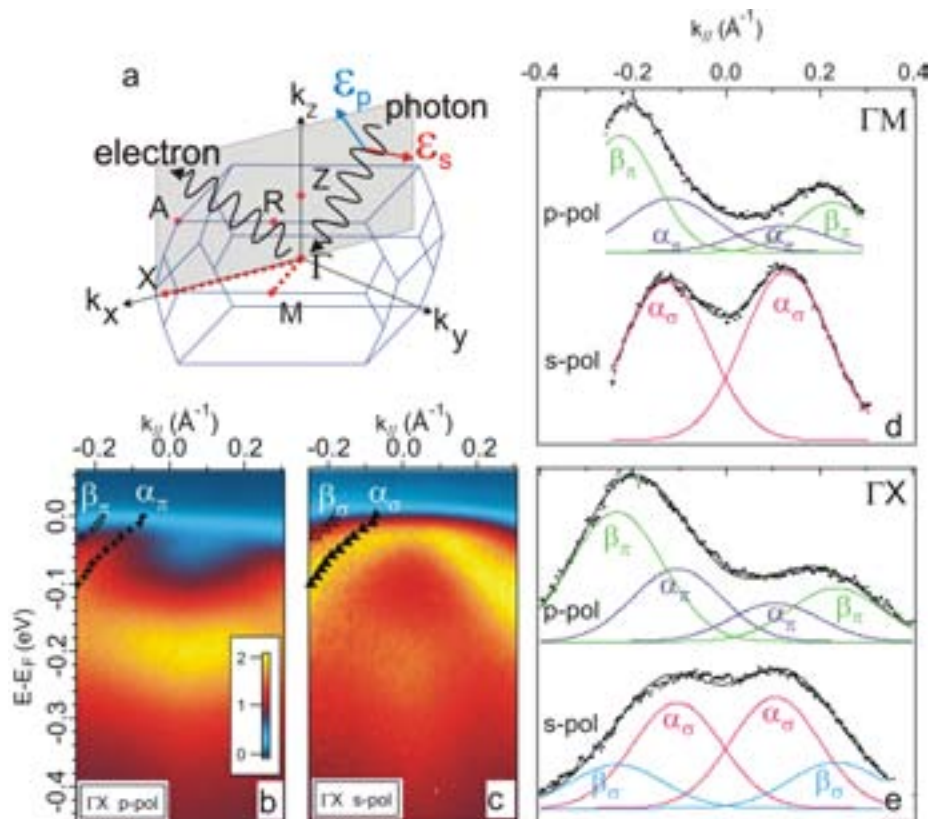


Figure 2. In an ARPES experiment the electronic band structure in the reciprocal space (a) can be directly measured. With synchrotron radiation sources the light polarization can be easily changed, probing the orbital nature of the bands along high symmetry directions (ΓX and ΓM). In (b) and (c) the band structure of superconducting $\text{Ba}_2(\text{Fe}_{1-x}\text{Co}_x)_2\text{As}$ ($x=0.08$) along the ΓX directions was measured with p and s polarization, respectively: the relative momentum distribution curves (sections at binding energy of -30 meV from the Fermi level) are shown in (e), and can be compared with the similar curves taken along ΓM (d). The comparison between ΓX and ΓM , and between s and p polarization can be used to determine the nature of the orbitals forming the Fermi surface.

inner hole pockets (α in Fig. 2), while symmetry considerations allowed us to conclude that the outer pocket (β in Fig. 2) has essentially a d_{z^2} character: furthermore, we were able to conclude that electron correlations play an important role in determining its position with respect to the other bands. This spectroscopic approach appears promising to clarify the nature of the Fermi surface also for other multi-band complex materials, contributing to the

worldwide research efforts aiming at understanding high temperature superconductivity.

References

- [1] I. I. Mazin, *Nature* **464**, 183 (2010).
- [2] P. Vilmercati et al., *Phys. Rev. B* **79**, 220503 (2009).
- [3] B. Mansart et al., *Phys. Rev. B*, (2010) in press.
- [4] L. Petaccia et al., *NIM A* **606**, 780 (2009).

A MICROSCOPIC VIEW ON THE METAL-INSULATOR TRANSITION IN A MOTT SYSTEM

S. Lupi¹, L. Baldassarre², B. Mansart³, A. Perucchi², A. Barinov², P. Dudin², E. Papalazarou³, F. Rodolakis^{3,4}, J.-P. Rueff⁴, J.-P. Itié⁴, S. Ravy⁴, D. Nicoletti⁵, P. Postorino¹, P. Hansmann⁶, N. Parragh⁶, A. Toschi⁶, T. Saha-Dasgupta⁷, O.K. Andersen⁸, G. Sangiovanni⁶, K. Held⁶, M. Marsi³

¹CNR-IOM and Dipartimento di Fisica, Università di Roma «La Sapienza», Roma, Italy

²Sincrotrone Trieste S.C.p.A., Trieste, Italy

³Laboratoire de Physique des Solides, CNRS-UMR 8502, Université Paris-Sud, Orsay, France

⁴Synchrotron SOLEIL, Gif-sur-Yvette, France

⁵Dipartimento di Fisica, Università di Roma «La Sapienza», Roma, Italy

⁶Institute of Solid State Physics, Vienna University of Technology, Vienna, Austria

⁷S. N. Bose Center for Basic Sciences, Kolkata, India

⁸Max-Planck-Institut für Festkörperforschung, Stuttgart, Germany

Email: stefano.lupi@roma1.infn.it; marino.marsi@u-psud.fr



SPETTRO MICROSCOPY
SISSI

Some materials present the fascinating and technologically attractive property of a sudden change in their macroscopic characteristics, in particular, their conductivity, when the interactions between their electrons are modified by thermodynamic parameters such as temperature. Chromium doped vanadium sesquioxide, $(V_{1-x}Cr_x)_2O_3$, is the prototype system to study the properties of this fundamental phenomenon of electronic correlation, called Mott transition: temperature, doping or pressure induce a metal-to-insulator transition (MIT) between a paramagnetic metal (PM) and a paramagnetic insulator (PI) [1]. This or related MITs have a high technological potential, among others, for intelligent windows and field effect transistors. However the spatial scale on which such transitions develop is not known, in spite of their importance for research and applications.

A study performed combining different experimental techniques with different spatial scale sensitivity allowed us to shine new light on this problem, showing for the first time direct evidence of the coexistence of metallic and insulating microscopic regions at a Mott transition induced by temperature [2]. We found that this phase separation can be associated with a thermodynamic instability near the transition, and that this instability is reduced when the phase transition is induced by pressure, that promotes a genuine Mott transition to a more homogeneous metallic state.

In the phase diagram of $(V_{1-x}Cr_x)_2O_3$, a Cr concentration of $x=0.011$ makes it possible to cross

the transition between the PI and PM phases only by changing the temperature between 320 and 200 K. This transition was repeatedly explored with submicron spatial resolution on the Spectromicroscopy photoemission microscope [3]: by measuring the photoemission yield at the Fermi energy, and detecting its lateral variation while scanning the specimen, it was possible to obtain metallicity maps while crossing the phase transition. An example, taken at 220 K, of these metallicity maps is shown in Fig. 1: the red regions correspond to the PM phase, while the blue regions are PI. The sample becomes uniformly insulating when warmed up to 320 K, as expected from the established phase diagram of vanadium sesquioxide [1], mostly determined with spatially averaging transport measurements. When cooling down again towards the PM phase, the metallic regions are found again in the same positions, strongly suggesting that structural defects play an important role in nucleating the phase transition. Further insight into the mechanisms of the PI-PM transition can be obtained by comparing this temperature induced PM-PI transition with the pressure induced transition at 300 K, as well with the PM phase corresponding to the undoped compound [4], thanks to the optical spectroscopy measurements performed on the SISSI beamline and shown in Fig. 2. These results show that during the phase transition induced by pressure, the strain due to the different lattice parameters between PM and PI seems to be accommodated in a more homogeneous way then to the temperature induced

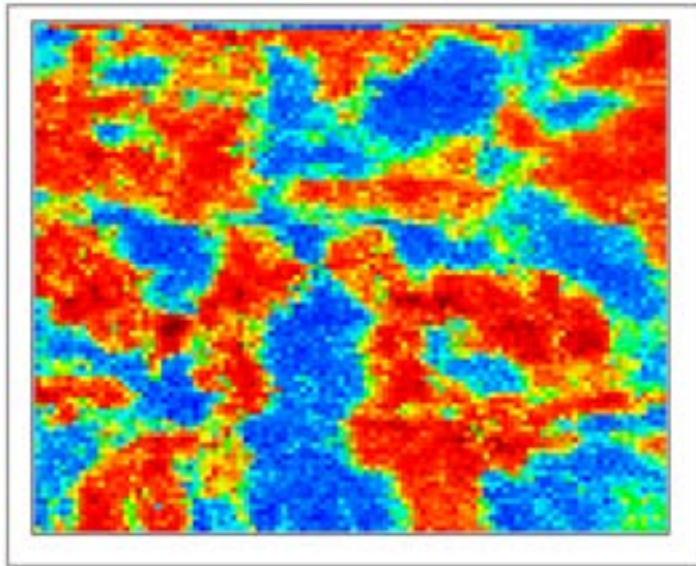


Figure 1. Photoelectron map taken with 27 eV photons and submicron spatial resolution on $(V_{1-x}Cr_x)_2O_3$, $x=0.011$, at 220 K. The field of view is of $50 \times 50 \mu m^2$, and the color scale is the photoemission yield at the Fermi energy of the system, after subtraction of topographic effects and secondary background: blue corresponds to the insulating phase, while red is the metallic state.

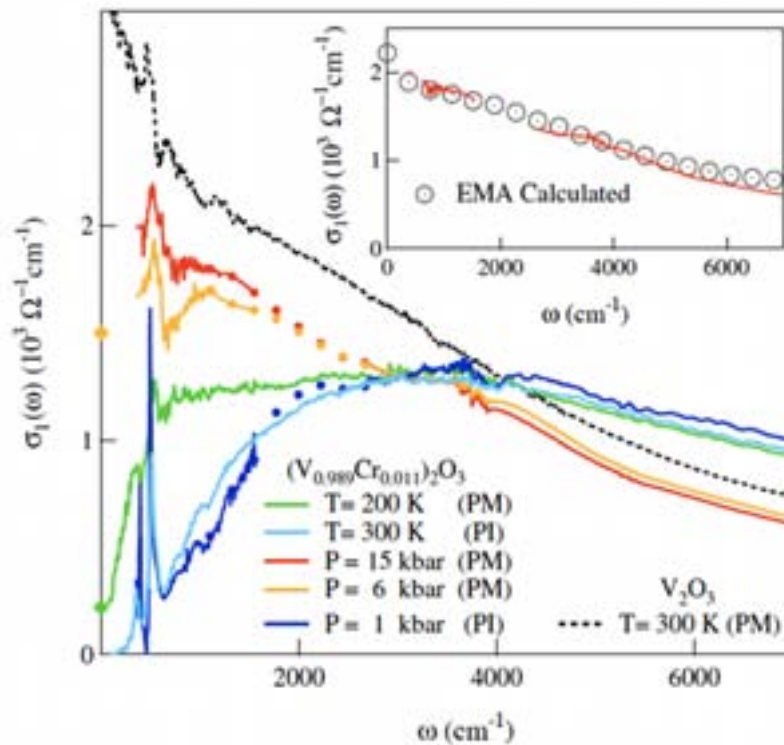


Figure 2. Optical conductivity of $(V_{1-x}Cr_x)_2O_3$, $x=0.011$ under pressure (data between 1600 and 2700 cm^{-1} are replaced by markers due to the strong diamond phonon absorption). In the inset, EMA calculations in good agreement with the experimental optical conductivity of the PM phase. The curves at 1, 6 and 15 kbar are compared to the PM state of undoped V_2O_3 at 300 K and of $(V_{1-x}Cr_x)_2O_3$, $x=0.011$ at 220 K.

transition, which can explain why pressure can give a more homogeneous PM phase and a phase transition more similar to the ideal Mott transition.

Our investigation, performed combining different experimental methods and different ways of inducing the metal-insulator transition, shows that the phase diagram of V_2O_3 , celebrated for its essential simplicity, reveals on a microscopic scale a much richer phenomenology that has to be taken into account in

the physical description of this model Mott-Hubbard system.

References

- [1] D.B. McWhan and J.P. Remeika, *Phys. Rev. B* **2**, 3734 (1970).
- [2] S. Lupi et al., *Nat. Commun.* **1**:105 (2010).
- [3] P. Dudin et al., *J. Synchr. Rad.* **17**, 445 (2010).
- [4] L. Baldassarre et al., *Phys. Rev. B* **75**, 245108 (2007).

THz SPECTROSCOPY OF MULTI-GAP SUPERCONDUCTORS

A. Perucchi¹, L. Baldassarre¹, S. Lupi², D. Nicoletti², M. Putti³, C. Ferdeghini³, P. Dore³

¹Sincrotrone Trieste S.C.p.A., Trieste, Italy

²CNR-IOM and Dipartimento di Fisica, Università di Roma "La Sapienza", Roma, Italy

³CNR-SPIN and Università di Genova, Genoa, Italy

⁴CNR-SPIN and Dipartimento di Fisica, Università di Roma "La Sapienza", Roma, Italy

E-mail: andrea.perucchi@elettra.trieste.it



SISSI

Multigap superconductivity is a very old topic dating back to 1959, when Suhl, Matthias and Walker [1] theoretically predicted the possibility of such a state of matter. However it was only after 2001 that clear-cut experimental evidence for multigap superconductivity was found in magnesium diboride (MgB_2). Today, MgB_2 is considered as the prototype multi-gap superconductor, while less established signatures of multi-gap superconductivity have been found in several systems, including A-15 compounds, copper oxides and heavy fermion compounds. The recent discovery of pnictide superconductors has renewed interest in this topic. Pnictides display multiple bands crossing the Fermi level, thus forming semi-metallic electron and hole pockets. Theoretical arguments suggest the opening of three distinct superconducting gaps over various zones of the Fermi surface [2]. THz spectroscopy is an ideal tool for studying superconducting gaps, since it provides a bulk and contact-less probe of the superconducting gaps, with excellent energy resolution (~ 0.1 meV). As a drawback, optical spectroscopy is not a momentum-resolved technique, thus complicating the interpretation of multiple-gap features.

Our synchrotron-based THz reflectivity measurements [3] on a $\text{BaFe}_{1.84}\text{Co}_{0.16}\text{As}_2$ film (Fig. 1) have been analyzed within a multigap BCS model. A good quality fit of our 6 K data can be achieved by considering two superconducting gaps ($2\Delta_A=31$ and $2\Delta_B=110$ cm^{-1}) opening, while a single-gap model completely fails. We then attempted to use the same double-gap parameters, to model experimental data at higher temperatures (12 and 18 K). The poor agreement between the fit and the temperature-dependent data may indicate that the two-band model used here

still provides an oversimplified description of the superconducting gap structure. Thus the possible presence of nodes in the gap or of a third gap of very low energy cannot be ruled out.

A comparison of our results with recent THz results from other groups shows that the reported values for the low energy optical gap substantially agree with our data. However, because of uncertainties in the data analysis, a large disparity is found in the literature on the value of the large gaps, and also on the overall number of gaps. In order to settle this issue we have addressed the THz properties of multi-gap superconductors in a much simpler material: the BCS superconductor V_3Si [4].

We have measured the ratio of the reflectivity (R_s/R_n) and transmission (T_s/T_n) of V_3Si in the superconducting and normal states, at THz frequencies, for a 180 nm and a 33 nm thick film. In both cases two distinct energy gaps turned out to be necessary in order to reproduce our THz data, within the same multiband model as outlined above for the pnictides. Interestingly, in the reflectivity measurement the value of the smaller of the two gaps was easily identified (Fig. 2a), since it corresponds to the value at which R_s/R_n saturates ($2\Delta_A=20$ cm^{-1}). On the other hand the larger gap value is not defined by any distinct feature in R_s/R_n and can be determined only through modeling ($2\Delta_B=38$ cm^{-1}). The opposite applies to transmission measurements. In this case a peak in T_s/T_n is observed at about 40 cm^{-1} , corresponding to the large gap (Fig. 2b). The small gap feature, which is again required for fitting, is however poorly defined, and ranges from $2\Delta_A=22$ to 32 cm^{-1} .

Our study on V_3Si shows that by using samples of different thicknesses, and combining

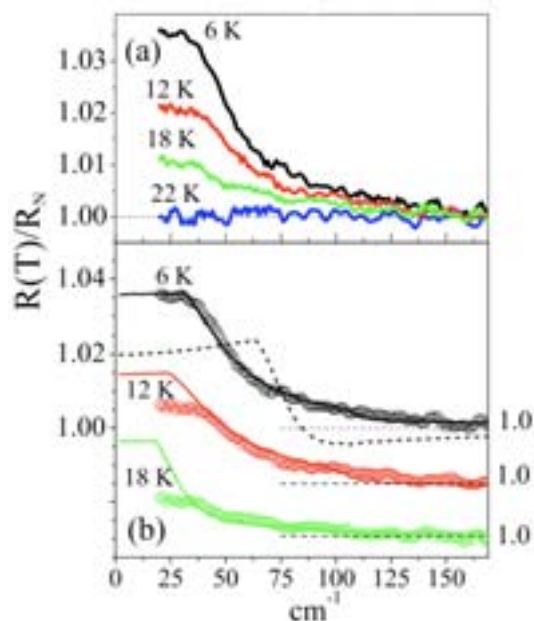


Figure 1. (a) $R(T)/R_n$ spectra of the $\text{BaFe}_{1.84}\text{Co}_{0.16}\text{As}_2$ film in the THz region. (b) The 6, 12, 18 K spectra are compared with the two-band (full line) best fit. In the 6 K case, also the one-band fit (dotted line) is shown. From Ref. [3].

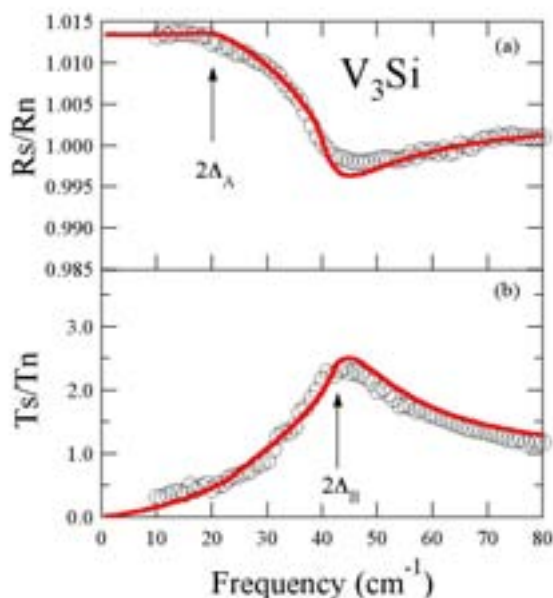
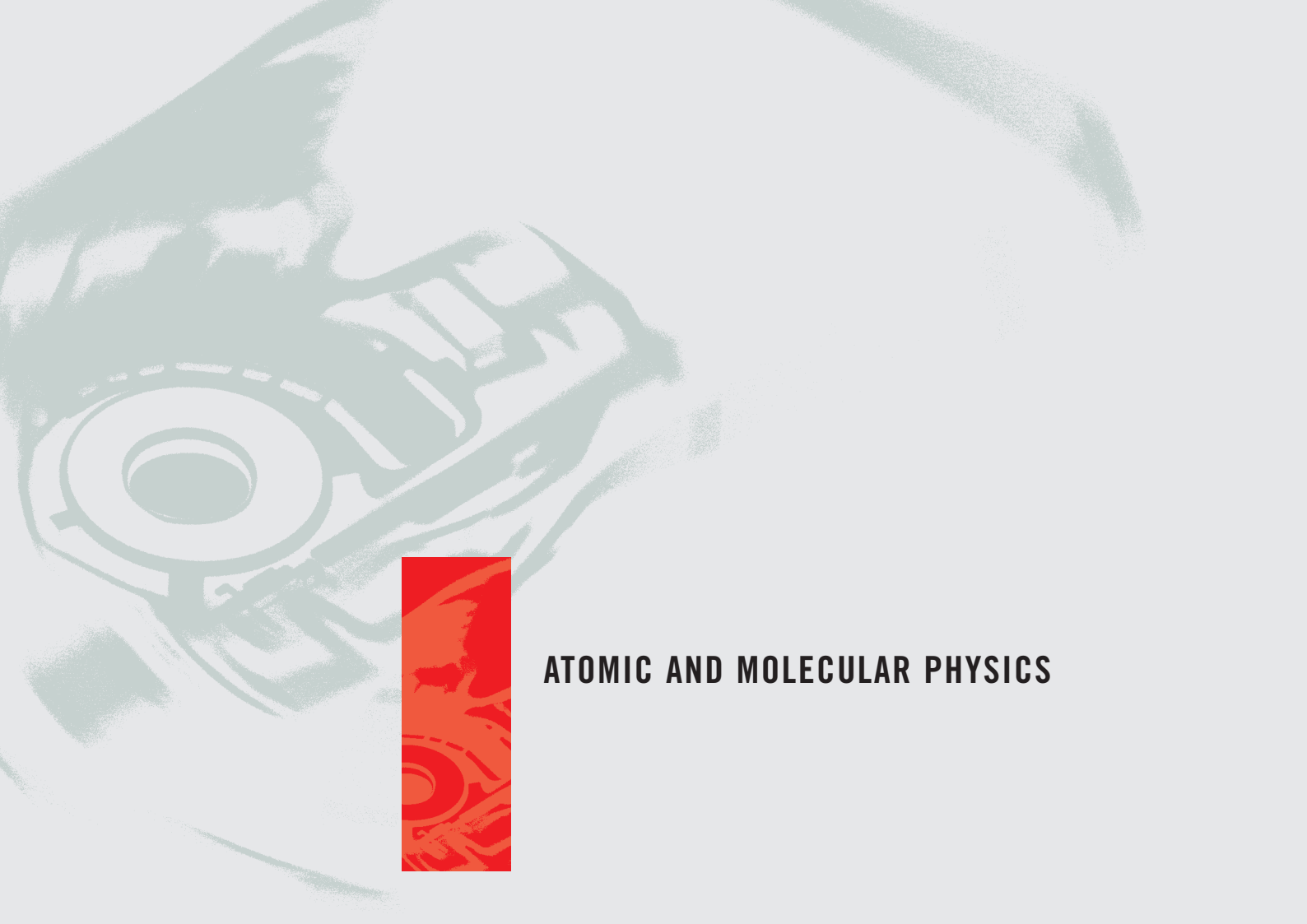


Figure 2. $R(6\text{K})/R_n$ (a) and $T(6\text{K})/T_n$ (b) spectra (black circles) and fit (red curve) for V_3Si , within a double-gap BCS model. In the $R(6\text{K})/R_n$ curve one can easily determine the value of the small gap $2\Delta_A$, while the opposite is true for $T(6\text{K})/T_n$, where $2\Delta_B$ is more defined (see text). From Ref. [4].

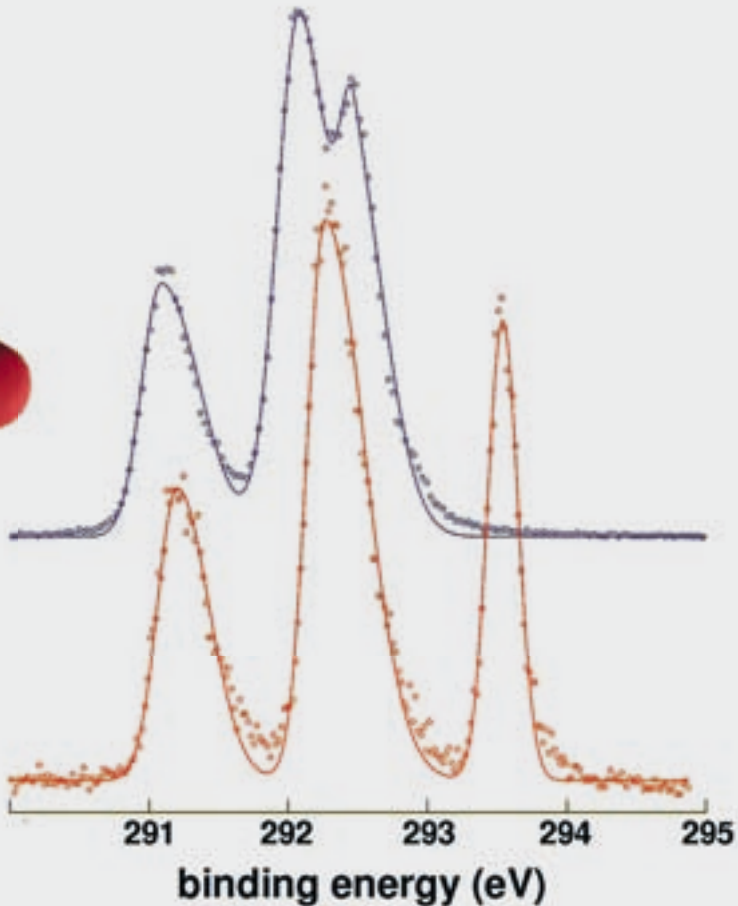
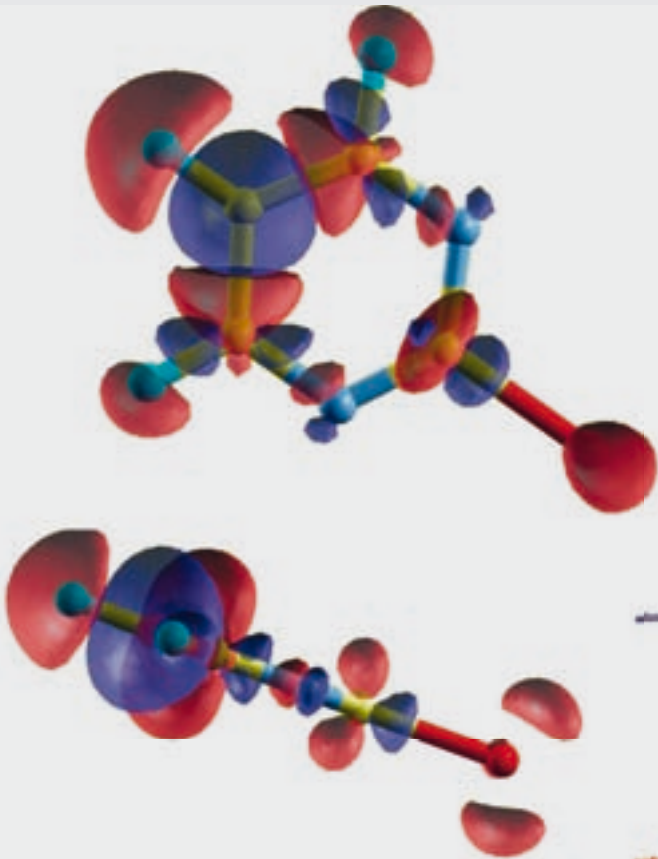
transmission and reflection results, it is indeed possible to better highlight the different superconducting gaps separately. THz transmission measurements on $\text{BaFe}_{1.84}\text{Co}_{0.16}\text{As}_2$ thin films are already planned, in order to determine with better accuracy the values and numbers of this pnictide's superconducting gaps.

References

- [1] H. Suhl, B.T. Matthias, and L.R. Walker, *Phys. Rev. Lett.* **3**, 552 (1959).
- [2] M. Norman *et al.*, *Physics* **1**, 21 (2008).
- [3] A. Perucchi *et al.*, *Eur. Phys. J. B* **77**, 25 (2010).
- [4] A. Perucchi *et al.*, *Phys. Rev. B* **81**, 092509 (2010).



ATOMIC AND MOLECULAR PHYSICS



THE INTERPLAY OF INDUCTIVE AND RESONANCE EFFECTS IN THE XPS SPECTRA OF HALOPYRIMIDINES

P. Bolognesi¹, G. Mattioli², P. O’Keeffe¹, V. Feyer³, O. Plekan³, Y. Ovcharenko^{1,4}, K.C. Prince^{3,5}, M. Coreno^{1,5}, A. Amore Bonapasta², L. Avaldi¹

¹CNR-IMIP, Area della Ricerca di Roma 1, Monterotondo Scalo, Italy

²CNR-ISM, Area della Ricerca di Roma 1, Monterotondo Scalo, Italy

³Sincrotrone Trieste S.C.p.A., Trieste, Italy

⁴Institute of Electron Physics, Uzghorod, Ukraine

⁵CNR-IOM, Gasphase beamline@Elettra, Trieste, Italy

E-mail: Paola.Bolognesi@imip.cnr.it



GASPHASE

When several atoms of the same species are present in a molecule, the chemical shift of their core level binding energies measured by X-ray photoelectron spectroscopy, XPS, provides information on molecular properties, such as proton affinities, chemical equilibrium and reactivity parameters. Thus, inner-shell ionization energies are a local probe of the chemical environment of an atom and make it possible to establish relationships between the chemical shift and chemical properties with ‘site dependence’. The application of XPS to molecules of biological interest has proved that this technique can provide information on the electronic structure, partial atomic charge and electronegativity as well as on the conformation in space of these molecules [1]. In this work XPS has been applied to the study of the C(1s) and N(1s) ionization of pyrimidine and halogenated pyrimidines (fig. 1). Pyrimidines are an important class of organic molecules, forming the base structure of three nucleic acids, i.e., uracil, cytosine and thymine. Halogenated pyrimidine bases have been proposed as potential radiosensitisers in radiotherapy. For example, 5-bromodeoxyuridine (an analogue of thymidine) enhances radiotherapeutic effects, most likely via the Auger cascade induced by the decay of the ionized halogen atom.

The selected set of halopyrimidines allows the effects of the halogenation on different molecular sites or the effects of changing the halogen atom on the same molecular site to be investigated. Each C(1s) spectrum is composed of three main features (fig. 2), corresponding to the ionization of the C atoms in the three non equivalent sites of the molecule: C2, C4/C6 and C5 (fig.1).

The general effect of the halogenation is to shift all the C(1s) and N(1s) binding energies towards higher values (table 1). The shift is more pronounced for the carbon site directly involved in the halogenation, and slightly larger effects have been observed in the case of Cl substitution, due to the higher electronegativity of the Cl with respect to the Br atom. The binding energies of all the samples have also been studied theoretically via a pseudopotential DFT method with the B3LYP exchange-correlation functional. Good agreement between theory and experiment has been found (table 1). The present study shows that the chemical shifts result from the interplay of an isotropic inductive effect, which involves the atoms nearest to the substituent, and a weaker anisotropic resonance effect running along the π -conjugated bonds. This is clearly shown in the difference map of the valence electronic density for a neutral molecule and a molecule with an inner shell hole, shown in figure 2 for the case of the 2-Br-pyrimidine with a 1s hole in the C5 atom. The core hole is screened by an almost spherical charge distribution (blue area in figure 2). This screening charge is drained from the rest of the molecule (red areas) via the inductive effect, which mainly involves the nearest neighbors, producing the red areas in positions C4/C6, symmetrically oriented towards the core hole position, and the resonance effect, which comes from the para position with respect to the core hole and shows an evident π character (red lobes out of the molecular plane in C2).

These combined experimental and theoretical inner shell ionization studies of halopyrimidines provide a detailed description

	Chemical Shift (eV)									
	pyrimidine	2-Cl pyrimidine		2-Br pyrimidine		5-Br pyrimidine		5-Br-2Cl pyrimidine		
		Expt.	Th.	Expt.	Th.	Expt.	Th.	Expt.	Th.	
C2	0	+1.40	+1.25	+1.06	+0.96	+0.05	0	+1.41	+1.33	
C4/C6	0	+0.19	+0.15	+0.18	+0.17	+0.11	+0.07	+0.25	+0.25	
C5	0	+0.09	-0.03	+0.11	+0.01	+1.04	+1.01	+1.02	+1.02	

Table 1. The C(1s) experimental and theoretical chemical shifts of the C2, C4/C6, C5 sites of halogenated pyrimidines reported with respect to the same atoms in the pyrimidine molecule.



Figure 1. Chemical structure of the pyrimidine and halogenated pyrimidine molecules studied in this work.

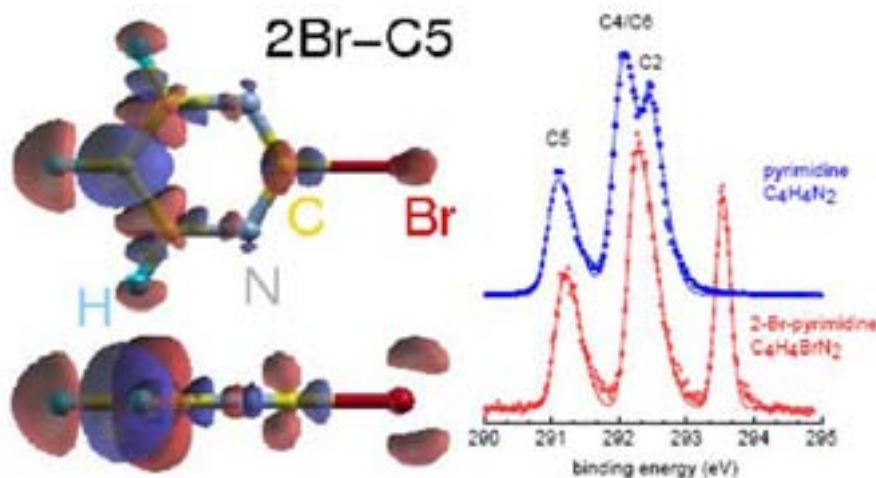


Figure 2. Right panel: C(1s) XPS spectra of pyrimidine and 2-Br-pyrimidine. Left panel: difference electron density map (top and side view) obtained by subtracting the valence electronic density of a ground state calculation from the valence electronic density of the corresponding core hole state calculation. The case of the hole in the C5 of the 2-Br-pyrimidine is reported as an example. The blue colour represents positive zones where some charge density is accumulated in order to screen the core hole, while the red colour shows negative zones where the electron density has been reduced.

of the effects of the halogen substitutions in the pyrimidine ring on the screening of the C(1s) hole located at different positions of the aromatic ring, thus contributing to the determination of the energetics of these molecules which are needed for modeling photoinduced processes and damage in DNA/RNA bases and several pharmaceutical compounds.

References

- [1] O. Plekan et al., *Chem. Phys. Lett.* **442**, 429 (2007); *J. Phys. Chem. A* **111**, 7806 (2007); *J. Chem. Phys.* **347**, 360 (2008).
- [2] P. Bolognesi, G. Mattioli, P.O. Keeffe, V. Feyer, O. Plekan, Y. Ovcharenko, K.C. Prince, M. Coreno, A. Amore Bonapasta and L. Avaldi, *J. Phys. Chem. A* **113**, 13593 (2009).

ROTATIONAL AND CORE LEVEL SPECTROSCOPIES AS COMPLEMENTARY TECHNIQUES IN TAUTOMERIC/ CONFORMATIONAL STUDIES: 2-MERCAPTOPYRIDINE

S. Melandri¹, L. Evangelisti¹, A. Maris¹, W. Caminati¹, B. M. Giuliano², V. Feyer³, K. C. Prince³, M. Coreno⁴

¹Dipartimento di Chimica "G. Ciamician" dell'Università, Bologna, Italy

²Departamento de Química da Universidade de Coimbra, Coimbra, Portugal

³Sincrotrone Trieste S.C.p.A., Trieste, Italy

⁴CNR-IMIP, Montelibretti, Roma, Italy

E-mail: walther.caminati@unibo.it



GASPHASE

Conformers and tautomers are different stable structural arrangements of the same molecule which can interconvert through an internal motion or an intramolecular reaction respectively. Most commonly this internal reaction is the transfer of a proton. Impressive progress has been achieved in the last few years in gas phase investigations of conformational/tautomeric properties of isolated molecules, thanks to the development and application of several spectroscopic techniques. Among them, rotational spectroscopy, in the form of Free Jet Millimetre Wave absorption or Fourier Transform Microwave spectroscopy [1,2] are well established experimental methods. More recently, also synchrotron radiation photoemission (PE) techniques have demonstrated their value in addressing such structural problems [3, 4]. Here we present the combined use of the two techniques (MW and core level PE) applied to solving a single problem [5].

The tautomerism of 2-pyridinone and 2-hydroxypyridine represents a model for intramolecular proton transfer and has been of interest to chemists for a very long time, while the substitution of the oxygen atom with a sulfur atom is likely to change the tautomeric equilibrium. 2-hydroxypyridine (2HP) and 2-mercaptopyridine (2MP) can each exist in three forms, the two conformers due to the internal rotation of the hydroxyl or mercapto group around the C-O or C-S bond, and the tautomeric keto or thione isomer, as shown in Figure 1. The labels "s" or "a" indicate the *syn* or *anti* orientation of the enol or thio hydrogen with respect to the ring nitrogen. While 2HP has been investigated with many spectroscopic techniques, no spectroscopic investigations have been reported of the related molecule

2MP, which also represents a tautomeric problem of biological interest.

We performed preliminary quantum chemical calculations which suggest that the SHa species is the global minimum, but is close in energy to SHs, and that the C=S form is much higher in energy, ca 850 cm⁻¹. From the optimized geometries we also obtained the relative energies and the relevant spectroscopic constants of the three species. The theoretical data also show that the energy difference between the CSH and C=S forms increases even more when we include the ZPE (Zero Point Energy) corrections, or the thermal contributions (Gibbs free energy).

MW experiments were performed first, since they allow conformational/tautomeric assignments directly from the experimentally determined moments of inertia. We observed the rotational spectra of three conformational/tautomeric species and their monodeuterated compounds (easily obtainable by direct exchange with D₂O). The comparison of the experimental rotational constants and the coordinates of the substituted H atom with the theoretical ones confirmed that the two most abundant species are the SHa and SHs followed by the thione species.

The core level photoemission experiment on 2MP, measured at the gas-phase photoemission beamline (Elettra, Trieste), confirmed the observation of the less abundant thione tautomer. The C 1s, N 1s and S 2p core photoemission spectra were taken at 382, 495 and 260 eV photon energy, respectively, and the binding energies were calibrated while the temperature of the sample was 339 K.

As expected, the peaks of the two mercapto conformers could not be distinguished, since

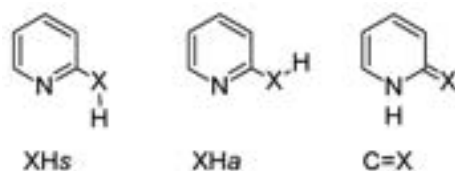


Figure 1. Tautomeric/conformational species of 2-hydroxy (X=oxygen) and 2-mercapto (X=sulphur) pyridine. *s* and *a* stand for *syn* and *anti*.

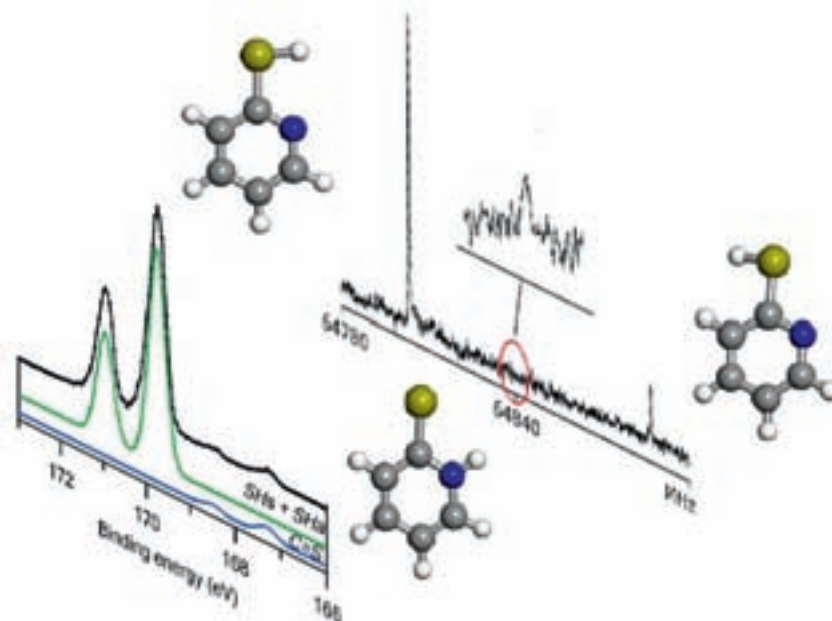


Figure 2. The complementary and precise information on the conformational/tautomeric equilibrium of 2-mercaptopyridine given by millimeter wave free jet absorption and core level photoemission spectroscopy.

they have almost the same electronic structure. A statistical analysis gave the relative populations, with the thione form being 5.3(5)%. From this datum we estimated the free energy differences among the various species, $\Delta(\Delta G)$ between the mercapto (SHs+SHa) and the thione forms (8.6 kJmol⁻¹). In the case of the MW data, we can determine three $\Delta(\Delta G)$ values, but we need to assume that all vibrational states relax to the ground vibrational state upon supersonic expansion. Moreover we assume no conformational or tautomeric interconversion because of the high barriers for these processes. With these assumptions we obtained $\Delta(\Delta G)=8.6$ kJmol⁻¹ between the two thiol forms and $\Delta(\Delta G)=11.4$ kJmol⁻¹ between the lowest energy thiol form and the thione one.

It is interesting to note how the tautomeric/conformational behaviour of 2-OH-pyridine changes dramatically when replacing the oxygen with a sulfur atom. The *anti* conformer, not detectable for 2-OH-pyridine, was easily observed in the case of 2MP. In contrast, the C=S form of 2MP is less stable than the C=O form of 2HP (3.2 kJmol⁻¹ reported in ref. 1). However, the theoretical calculations give relative energies of this C=S tautomer much higher than the value obtained from these experimental measurements. The thione ΔG

values in particular are overestimated by these calculations. In conclusion, the combination of the high quantitative accuracy of XPS with the precise detailed structural information of MW spectroscopy has allowed us to give a detailed description of the structure and energetics of the tautomers of 2MP.

References

- [1] L. D. Hatherley, R. D. Brown, P. D. Godfrey, A. P. Pierlot, W. Caminati, D. Damiani, L. B. Favero and S. Melandri, *J. Phys. Chem.* **97**, 46 (1993).
- [2] J. L. Alonso, I. Peña, J. C. López, V. Vaqueiro, *Angew. Chem. Int. Ed.* **48**, 6141 (2009).
- [3] V. Feyer, O. Plekan, R. Richter, M. Coreno, G. Vall-Ilosera, K. C. Prince, A. B. Trofimov, I. L. Zaytseva, T. E. Moskovskaya, E. V. Gromov, J. Schirmer, *J. Phys. Chem. A* **113**, 5736 (2009).
- [4] O. Plekan, V. Feyer, R. Richter, M. Coreno, G. Vall-Ilosera, K. C. Prince, A. B. Trofimov, I. L. Zaytseva, T. E. Moskovskaya, E. V. Gromov, J. Schirmer, *J. Phys. Chem. A.* **113**, 9376 (2009).
- [5] S. Melandri, L. Evangelisti, A. Maris, W. Caminati, B. M. Giuliano, V. Feyer, K. C. Prince, M. Coreno, *J. Am. Chem. Soc.* **132**, 10269 (2010).

DISSOCIATIVE DOUBLE PHOTOIONIZATION OF CO₂ MOLECULES IN THE 36–49 eV ENERGY RANGE: ANGULAR AND ENERGY DISTRIBUTION OF ION PRODUCTS

M. Alagia^{1,2}, P. Candori³, S. Falcinelli³, M. Lavollée⁴, F. Pirani⁵, R. Richter⁶, S. Stranges^{2,7}, F. Vecchiocattivi³

¹CNR-ISMN Sez. Roma1, Rome, Italy.

²Laboratorio Nazionale TASC IOM-CNR, Trieste, Italy

³Dipartimento d'Ingegneria Civile ed Ambientale, University of Perugia, Perugia, Italy.

⁴CNRS, Université Paris-Sud, Orsay, France.

⁵Dipartimento di Chimica, University of Perugia, Perugia, Italy.

⁶Sincrotrone Trieste S.C.p.A., Trieste, Italy

⁷Dipartimento di Chimica, University of Rome "La Sapienza", Rome, Italy.

E-mail: vecchio@dyn.unipg.it



GASPHASE

We have recently reported some results on the double photoionization of carbon dioxide, in the 34–50 eV photon energy range, by the use of synchrotron radiation [1]. Those results, together with other experimental data which recently appeared in the literature [2], allowed us to assert that the molecular CO₂²⁺ dication is mostly unstable and dissociates to give rise to CO⁺ and O⁺ ions,



with a wide range of lifetimes. Although the vertical threshold for the formation of the molecular CO₂²⁺ dication is 37.3 eV, it has been found that the above reaction starts at around 35.6 eV [2], indicating the presence, in this lower energy range, of an indirect mechanism

leading to the production of a CO⁺ ion together with an autoionizing state of the oxygen atom [1,3]. However, many features of the possible mechanisms promoting this reaction are still not well characterized.

In this paper we report the angular and energy distribution of ion products for the above reaction in the 36–49 eV photon energy range. The experiments have been carried out using synchrotron radiation and a time of flight mass spectrometer equipped with a position sensitive ion detector. The data have been analyzed in order to obtain, as a function of the photon energy and with respect to the linearly polarized light direction, the anisotropy of the ionic product angular distribution and the kinetic energy released into the ion fragments.

Fig. 1 shows the typical angular distribution detected at 49.0 eV for the two ion products CO⁺ and O⁺. In the whole investigated energy range the angular distribution has been found to be similar to that reported in Fig. 1. In particular, we have found that the ratio between the perpendicular and parallel cross section ranges from a minimum of 0.4 up to 0.9. This means that the parallel cross section is always larger than the perpendicular one, except at 36 eV photon energy, where the distribution appears isotropic.

The kinetic energy distributions of CO⁺ and O⁺ products provide further interesting information about the dissociative reaction [3]. As reported in Fig. 2, a simple analysis of the total kinetic energy distributions in terms of Gaussian functions indicates the presence of

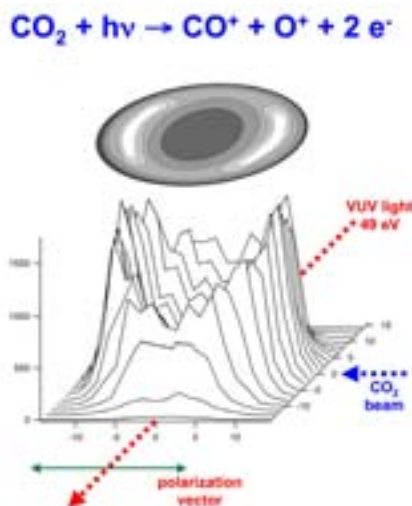


Figure 1. Typical 3D representation of the angular distribution of products at photon energy of 49 eV, with respect to the linearly polarized light direction.

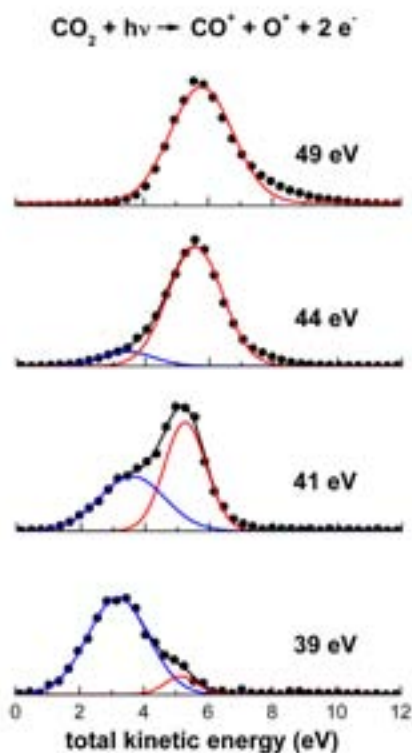
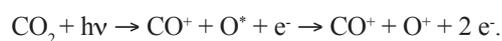


Figure 2. Total kinetic energy of ion products in the 39–49 eV photon energy range. The lines represent the Gaussian functions used for the analysis. Blue line represents mechanism A, red line represents mechanism B.

two mechanisms in the photon energy range between 39 and 49 eV, one producing ions with a total kinetic energy between 3 and 4 eV (mechanism A) the other with energy between 5 and 6 eV (mechanism B). These energy features are of interest for understanding the role of states involved in the dissociation process. Some low lying electronic energy levels of the CO_2^{2+} dication have been studied by Slattery *et al.* [2] on the basis of the photoelectron coincidence spectrum. Some previous calculations [2] have shown that all electronic states of the dissociation products are connected with those of the molecular dication through potential barriers. In particular, the ground state $\text{CO}_2^{2+}(X^3\Sigma_g^-)$ dication is connected, along the collinear CO^+-O^+ separation coordinate, with the ground state ion products, $\text{CO}^+(X^2\Sigma)$ and $\text{O}^+(^4S_0)$, through a barrier that is about 1.4 eV above the bottom of the potential well. For the electronic states immediately above, the potential barriers, correlating with the ion products, are even higher.

Below the vertical threshold of 37.34 eV, the dissociation occurs through the formation of a CO^+ ion and an autoionizing state oxygen atom that ionizes later on [1]:



In the case when the double photoionization happens at the energies around the vertical threshold, and the dissociation leads to

CO^+ and O^+ in their ground electronic and vibro-rotational states (33.15 eV), then one expects an energy release of the product ions of 4.2 eV. Values of the kinetic energy released lower than 4.2 eV should indicate the involvement of some excited internal modes of the final diatom. This seems to be the case of the mechanism A indicated above. The second mechanism, labeled as B, which dominates in the higher energy range and leads to a kinetic energy release larger by about 2 eV, with respect to the other mechanism A, must be due to the population of an electronically or vibro-rotationally (or both) excited state of the CO_2^{2+} dication, and possibly leading to an excited electronic state of ion products. However, it is difficult to assign unequivocally the involved electronic states in this second mechanism.

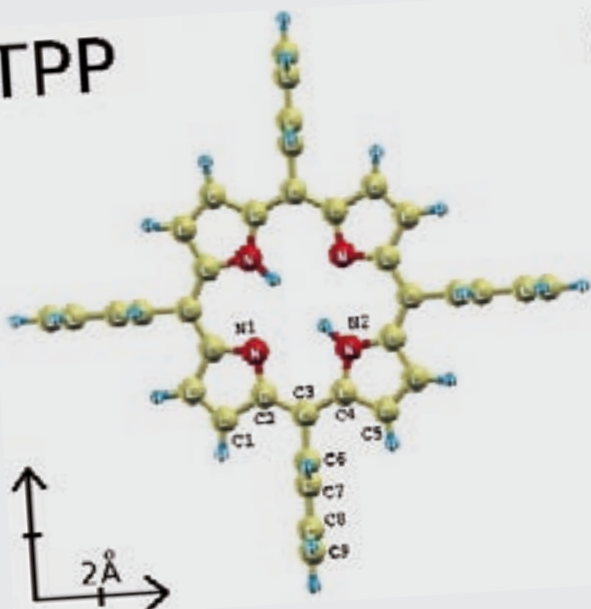
References

- [1] M. Alagia, P. Candori, S. Falcinelli, M. Lavollée, F. Pirani, R. Richter, S. Stranges, F. Vecchiocattivi, *J. Phys. Chem. A* **113**, 14755 (2009).
- [2] A.E. Slattery, T.A. Field, M. Ahmad, R.I. Hall, J. Lambourne, F. Penent, P. Lablanquie, J.H.D. Eland, *J. Chem. Phys.* **122**, 084317 (2005).
- [3] M. Alagia, P. Candori, S. Falcinelli, M. Lavollée, F. Pirani, R. Richter, S. Stranges, F. Vecchiocattivi, *Phys. Chem. Chem. Phys.* **12**, 5389 (2010).

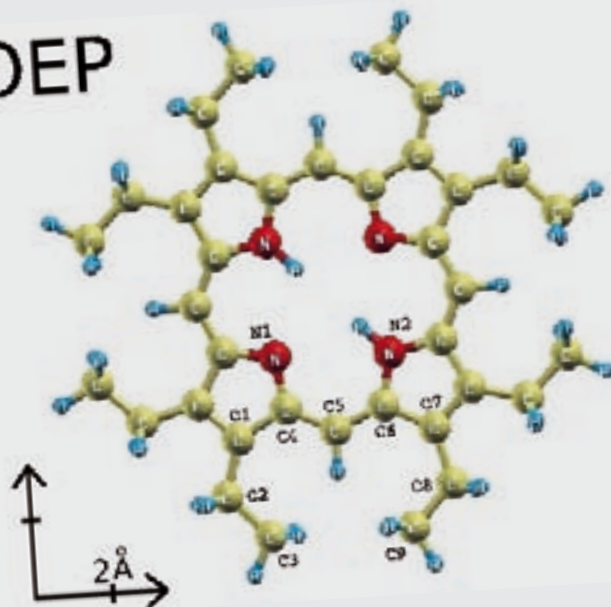


THEORY@ELETTRA

TPP



OEP



TPP

OEP

METALLIZATION OF THE FULLERENE/Rh INTERFACE REVEALED BY VALENCE PHOTOELECTRON SPECTROSCOPY AND DENSITY FUNCTIONAL THEORY CALCULATIONS

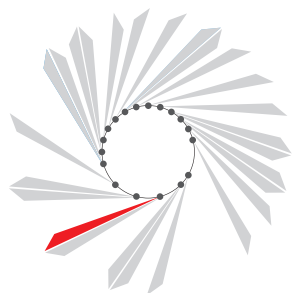
A.-C. Wade^{1,2}, S. Lizzit¹, L. Petaccia¹, A. Goldoni¹, D. Diop², H. Üstünel³, S. Fabris³, S. Baroni³

¹Sincrotrone Trieste S.C.p.A., Trieste, Italy

²Physics Department, Cheik Anta Diop University, Dakar, Senegal

³CNR-IOM DEMOCRITOS, Theory@Elettra and SISSA, Trieste, Italy

E-mail: fabris@sissa.it



SuperESCA

Fullerenes are strong electron acceptors. Therefore, the electron-doping of C_{60} solids is easily achieved, for example, by intercalation of alkali metals, which leads to new systems having distinct properties, such as superconducting phases with an excess charge of almost 3 electrons per molecule. However, intercalation is not the only way to form metallic C_{60} systems. Chemisorption of single fullerene layers on metal surfaces may result in a net charge transfer, from the metal into the C_{60} LUMO. In the case of the fullerene/Rh(100) system studied in this work [1], the binding of the fullerene monolayer to the metal surface, yields the appearance of a new state in the valence band spectrum that crosses the Fermi level. The origin of this state was revealed by combining photoemission spectroscopy with density functional theory (DFT) calculations. The measurements were performed in the ultrahigh vacuum experimental chamber (base pressure about 10^{-10} mbar) of the SuperESCA beamline. The formation of the monolayer (ML) is carried out either by Thermal Desorption of the deposited multilayer annealed at 550 K, or by depositing C_{60} with the substrate kept at 600 K. The DFT calculations were performed in the local Theory group (Theory@Elettra) with the Perdew-Burke-Ernzerhof exchange-correlation functional in a plane-wave pseudopotential framework. All calculations were carried out with the Quantum ESPRESSO suite of codes developed at SISSA and CNR-IOM DEMOCRITOS [2]. Further details can be found in Ref.[1].

The C 1s core level photoemission spectroscopy was used to follow, control, and characterize the layer-by-layer fullerene growth on the metal surface. Indeed, the C 1s spectrum of the first monolayer (Fig. 1a) shows a distinct

difference with respect to the two-layer system (a binding energy shift to lower energies). The valence band photoemission spectrum for the 1ML- C_{60} /Rh(100) is displayed in Fig. 1b, and compared to the spectrum of the clean Rh(100) surface and of a C_{60} multilayer film. The monolayer spectrum is dominated by the characteristic C_{60} molecular orbitals for binding energies higher than 4 eV, while at lower binding energy, i.e. from the HOMO-1 down to the Fermi level, the major contribution is due to emission from Rh 4d states. There is a non-rigid shift of the C_{60} -related peaks towards lower binding energies with respect to the multilayer, but the lineshape of these peaks is only slightly modified compared to the multilayer.

Most importantly, the spectral intensity of the band edge near the Fermi level is higher for the monolayer than for the clean Rh(100). This is a clear sign of the presence of new states near E_F . The difference spectrum (Fig. 1b) clearly shows the peak at E_F . Moreover the HOMO and HOMO-1 states are broader than the corresponding ones in the multilayer case, indicating a strong interaction with the substrate. The electronic structure calculations provide evidence that the peak at the Fermi level originates from a charge transfer from the metal into the LUMO molecular states, leading to a metallization of the interface.

The resulting lowest-energy adsorption geometry for the 1ML C_{60} /Rh(100) system predicted by the DFT calculations is displayed in Fig. 2a. The electronic structure analysis of this adsorption configuration (total and projected density of electronic states) is shown in Fig. 2b. The comparison, between the C PDOS of the isolated and supported fullerenes, shows that the interaction with the metal surface strongly

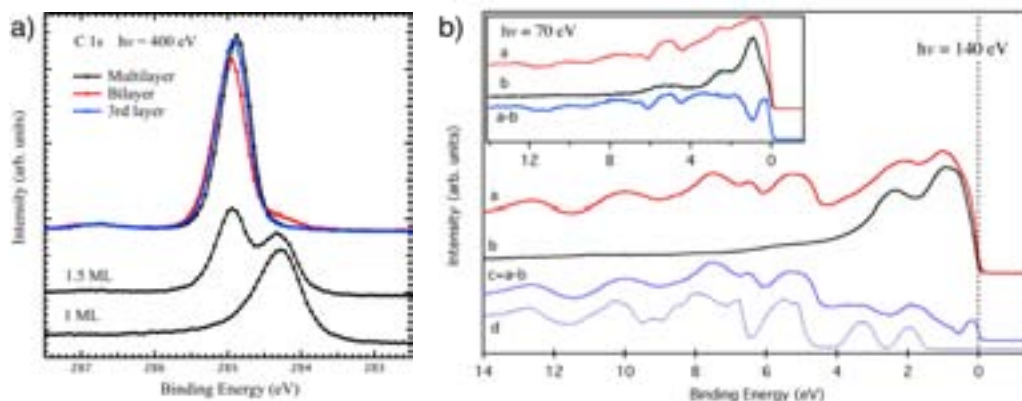


Figure 1. a) C 1s core level spectra obtained during the deposition of a C_{60} multilayer on the Rh(100) surface; b) Valence band photoemission spectra of 1ML C_{60} (a), a clean Rh(100) surface (b) and a C_{60} multilayer (d).

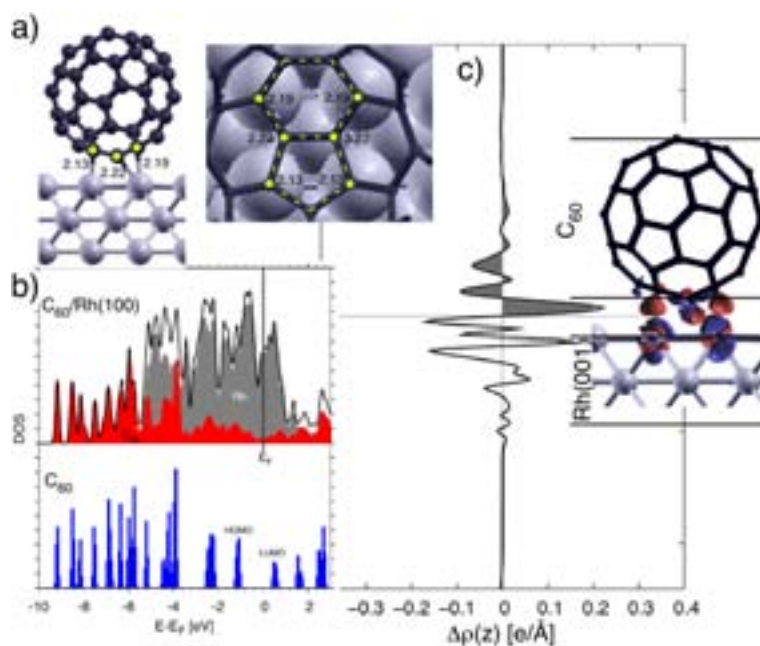


Figure 2. a) Minimum-energy adsorption geometry predicted by the DFT calculations; b) Total density of electronic states (DOS, black line) and projections on Rh (gray area) and on C (red and blue areas) atomic orbitals; c) Differential charge density integrated in the xy planes parallel to the C_{60} /Rh interfaces and spatial representation of the charge density redistribution. Positive and negative values are represented by red and blue isosurfaces, respectively.

modifies the occupied HOMO and HOMO-1 as well as the LUMO and LUMO+1, while the remaining states are weakly perturbed upon adsorption. The C-PDOS of the supported C_{60} monolayer (red area) clearly shows the presence of a continuum of states between the HOMO and LUMO, with a clear peak at E_F as observed in the experimental spectra, hence proving the metallization of the metal/molecule interface. The corresponding molecular states are shown in Fig. 2c). These states are strongly hybridized with the underlying Rh metal states, and can be directly correlated to the strong molecular binding to the metal surface discussed above.

In summary, the calculated electronic structure allows us to correlate the measured interface state with a strong hybridization between the Rh metal states and the molecular HOMO and LUMO. This results in a net charge trans-

fer of ~ 0.5 - $0.6e$ from the metal to the p states of the interfacial C atoms. The charge transfer (Fig. 2c) is shown to be very short range, involving only the C atoms bound to the metal. The electronic structure of the second C_{60} layer is already insulating and resembles the one measured for C_{60} multilayers (supported by the same substrate or calculated for fullerenes isolated in vacuum). These results highlight the distinctive electronic properties of the fullerene/metal interface conferred by the Rh support.

References

- [1] A.-C. Wade, S. Lizzit, L. Petaccia, A. Goldoni, D. Diop, H. Üstünel, S. Fabris, and S. Baroni, *J. Chem. Phys.* **132**, 234710 (2010).
- [2] P. Giannozzi *et al.*, *J. Phys.: Condens. Matter* **21**, 395502 (2009).

TPP

OEP

VALENCE ELECTRONIC PROPERTIES OF PORPHYRIN DERIVATIVES

G. Stenuit¹, C. Castellarin-Cudia², O. Plekan², V. Feyer², K.C. Prince², A. Goldoni², P. Umari¹

¹CNR-IOM Democritos, Theory@Elettra group, Trieste, Italy

²Sincrotrone Trieste S.C.p.A., Trieste, Italy

E-mail: pumari@sissa.it



GAS PHASE

Organic electronics is a very promising branch of nanotechnology. A large number of functional organic molecules can be synthesized for a variety of purposes. Electronic structure calculations play an important role in the characterization of these molecules, as they can predict the behavior of candidate organic devices. For this reason, it is important to use appropriate electronic structure methods in order to obtain reliable results. In the case of large molecules and nanostructured systems, the density functional theory (DFT) method is very popular due to its low computational cost, although the results, in particular when compared with spectroscopic data, are only partially satisfactory. On the contrary, first-principles methods based on many-body perturbation theory, such as those resulting from the so-called GW approximation, in which the self-energy operator is expressed as the frequency convolution of the dynamically screened Coulomb interaction (W) and the Green's function (G), give excellent results for the energy, and the electronic structure of crystals and small molecules. However, until recently, their high computational cost has prevented their use in large molecular and nanostructured systems.

As our recent progress [1] made it possible to significantly reduce the cost of these methods, we wanted to determine the performance of the GW method to reproduce the properties of the electronic structure of some large organic molecules. For this purpose, we performed a study combining experiment and theory parts, to determine the valence electronic structure of isolated free-base porphyrins with different substituents: Tetraphenyl-porphyrin (TPP) and octaethyl-porphyrin (OEP) (see Fig. 1). Based on the results obtained we can conclude [2] that the GW method is appropriate for the study of

electronic properties in organic molecules, while the simple DFT schemes can fail even in the metal-free molecules.

The measurements were carried out at the Gas Phase photoemission beamline, using a 150 mm hemispherical electron energy analyser with 6-channels, mounted at 54.7 degrees with respect to the linear electric vector of the light. The spectra of molecular valence states were recorded with an incident photon energy of 90 and 126 eV and a total energy resolution (photons + analyzer) of 0.25 eV. During the experiment, the quality of the sample was monitored using the valence band and core level photoemission. No signs of thermal decomposition were observed. The calculations were performed within DFT and GW frameworks with the Quantum-Espresso (www.quantum-espresso.org). The DFT method with the PBE approximation was used to obtain the structural configurations of the TPP and OEP isolated molecules. We calculated the density of electronic states and valence vertical ionization energies directly from the eigenenergies PBE and through many-body GW method. We used the GW scheme introduced in ref. [1]. This scheme allows for accurate calculations in large model structures. The frequency dependent polarizability matrices were represented on the optimal basis, which spans the space of products in a real space of the valence and conduction (empty) states.

From our calculations, we found that the GW vertical ionization energy is 6.05 eV and 5.7 eV for the TPP and OEP respectively, which are in good agreement with measured values of 6.42 eV for the TPP and 6.27 eV in OEP. Consequently, the GW method allows to correct the large underestimation of the PBE approximation. These corrections are 4.8 eV and 4.5 eV for the TPP and OEP, respectively. In Fig. 2, the measured photoelectron spectrum

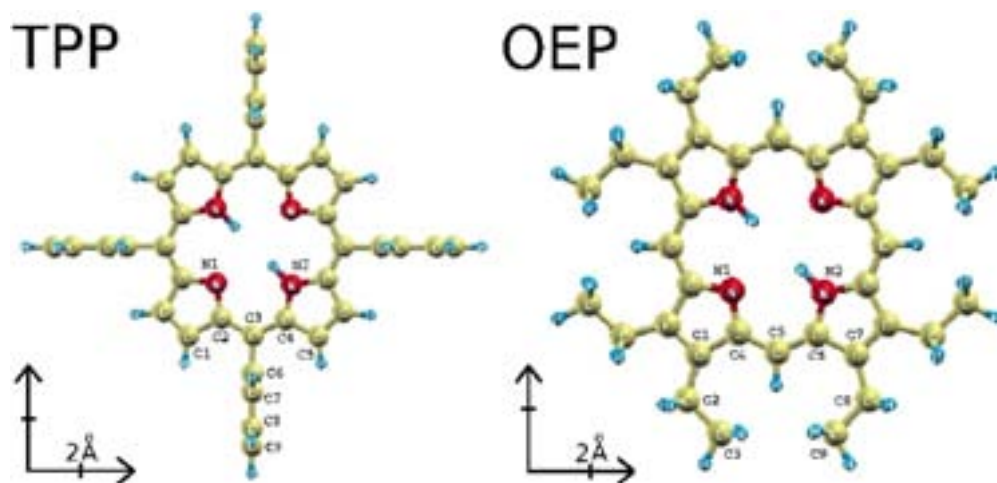


Figure 1. Molecular structure of the tetraphenylporphyrin and octaethylporphyrin. The numbering refers to the set of non-equivalent C and N atoms. Atoms are indicated by their corresponding symbols.

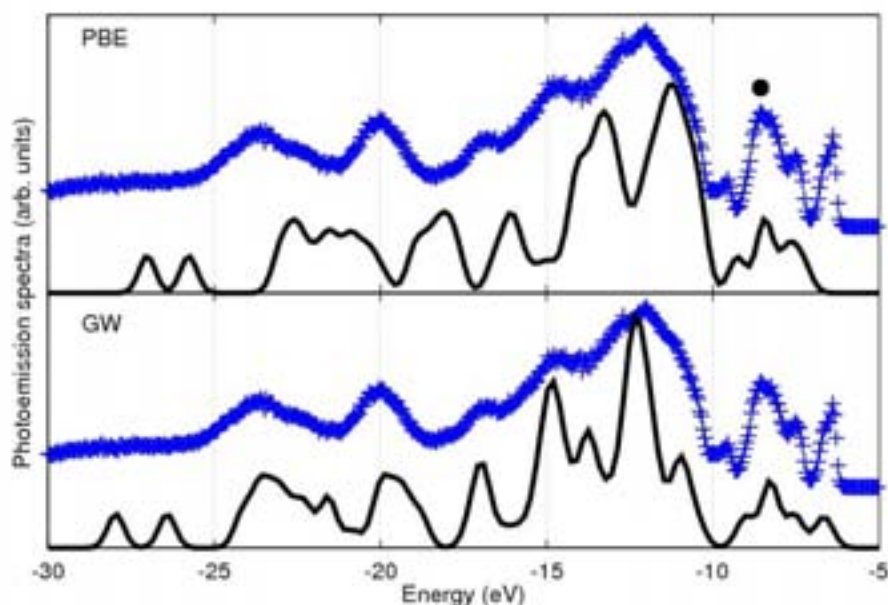


Figure 2. Experiment: photoemission spectra ('+' signs) of the OEP molecule. Theory: PBE and GW density of states (solid lines).

of OEP is reported together with the density of states (DOS) calculated with PBE and GW. A disagreement between the DFT-PBE DOS and the experimental valence band; is observed. Moreover, we note that any approximation, such as an artificial stretching of the energy axis, when applied to the PBE-DOS, can not reproduce the experimental spectrum, especially close to the HOMO level. When the DOS is calculated by the more accurate GW method, these differences disappear. The positions and relative intensities of main peaks visible in the

photoemission spectrum, are well reproduced over the whole energy range, in particular for the peaks near the HOMO level. Similar results are found for the TPP molecule.

References

- [1] P. Umari, G. Stenuit, and S. Baroni, *Phys. Rev. B*, **79**, 201104R (2009).
- [2] G. Stenuit, C. Castellarin-Cudia, O. Plekan, V. Feyer, K. C. Prince, A. Goldoni, and P. Umari, *Phys. Chem. Chem Phys.* **12**, 10812 (2010).

TPP

OEP

THE GWL PROJECT

P. Umari

CNR-IOM Democritos, Theory@Elettra group, Trieste, Italy

E-mail: pumari@sissa.it



GAS PHASE

In the last years, Density-functional theory (DFT) has grown into a powerful tool for the numerical simulation of matter at the nanoscale, allowing one to study the structure and dynamics of realistic material models, consisting of up to a few thousand atoms. The scope of standard DFT, however, is limited to those dynamical processes that do not involve electronic excitations. Moreover, its time-dependent extension, which has been conceived to cope with such processes, still displays conceptual and practical difficulties. The most elementary excitation is the removal or the addition of an electron from a system originally in its ground state. These processes are accessible through the direct / inverse photoemission spectroscopies and can be described in terms of quasi-particles spectra. In insulators, the energy difference between the lowest-lying quasi-electron state and the highest-lying quasi-hole state, is the quasi-particle gap, a quantity that is severely (and to some extent incorrectly) underestimated by DFT.

Many-body perturbation theory (MBPT) provides a general, though unwieldy, framework for calculating quasi-particle properties and other excitations (e.g. optical). A numerically viable approach to quasi-particle energy levels, known as the GW approximation, was introduced in the 60s, but it took two decades to have a realistic application, and even today the numerical effort required by MBPT is such that its scope is usually limited to systems of a handful of inequivalent atoms. The two main difficulties are the necessity to calculate and manipulate large matrices representing the charge response of the system (electron polarizabilities or polarization propagators), on the one hand, and that of expressing such response functions in terms of slowly converging sums over empty one-electron states, on the other hand. Recently, we addressed both problems. In a first work [1] we introduced a method to significantly reduce the computational and

memory loads of GW calculations through the introduction of optimal basis sets for representing polarizability operators built upon Wannier-like orbitals. Then, we proposed an approach [2] to obtain fully converged GW calculations, avoiding at the same time any sum over empty states. In the same work [2], we also explained how also optimal polarizability basis sets can be constructed without explicitly evaluating empty states.

We implemented this approach, which we refer to as GWL, in the Quantum-Espresso density functional theory package (www.quantum-espresso.org), which is released through the GNU public license. The code uses a mixed OPENMP/MPI parallelization strategy. This permitted us to run simulations of model structures containing more than five hundred atoms using over two thousand computational cores.

Although the code is particularly suitable for performing calculations on very large systems, taking advantage of the latest massively parallel computational facilities, it also makes it possible to obtain full converged GW calculations for smaller model systems using much more limited computational resources, such as desktop workstations. We report now on an example of a calculation of this kind: the study of the valence electronic structure properties of the indene molecule (C_9H_8) using GW calculations and experimental photoelectron measurements.

Indene is one of the simplest polycyclic aromatic hydrocarbons, which are important combustion-generated pollutants, both because of their role as potential soot precursors and because of their inherent biological activity. Moreover, they are also of fundamental interest in the fields of nanotechnology and molecular electronics. The measurements were carried out at the Gas Phase photoemission beamline, using a 150 mm hemispherical electron energy analyser with 6-channels, mounted at 54.78 with respect to the electric

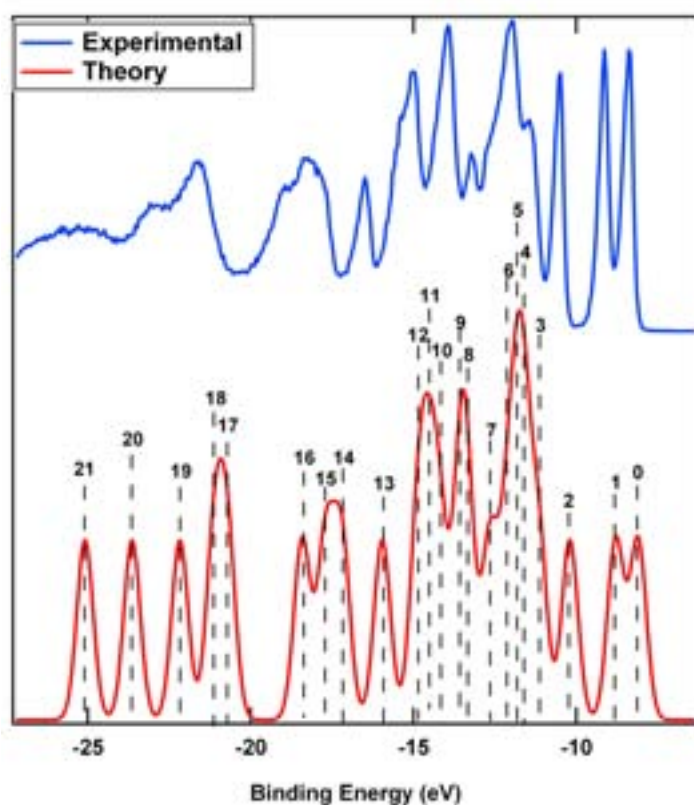


Figure 1. Experimental electron photoemission spectrum (blue) and theoretical valence DOS calculated with the GW method (red). The vertical dashed lines mark the positions of the calculated GW energy levels.

vector of the light. The valence spectrum of the studied molecule was recorded using an incident photon energy of 90 eV with a total energy resolution of 0.25 eV. The calculated GW vertical ionisation energy is 8.11 eV in excellent agreement with the measured photoemission value of 8.37 eV. In Fig. 1, we compare the calculated GW valence density of states with the measured electron photoemission spectrum. Although we neglected any oscillator strength effect, the agreement with the experiment is very good over the entire energy range. In particular, the structure of the peaks appearing at lower binding energy such as the HOMO, the HOMO-1, and the HOMO-2 are nicely reproduced by our calculation.

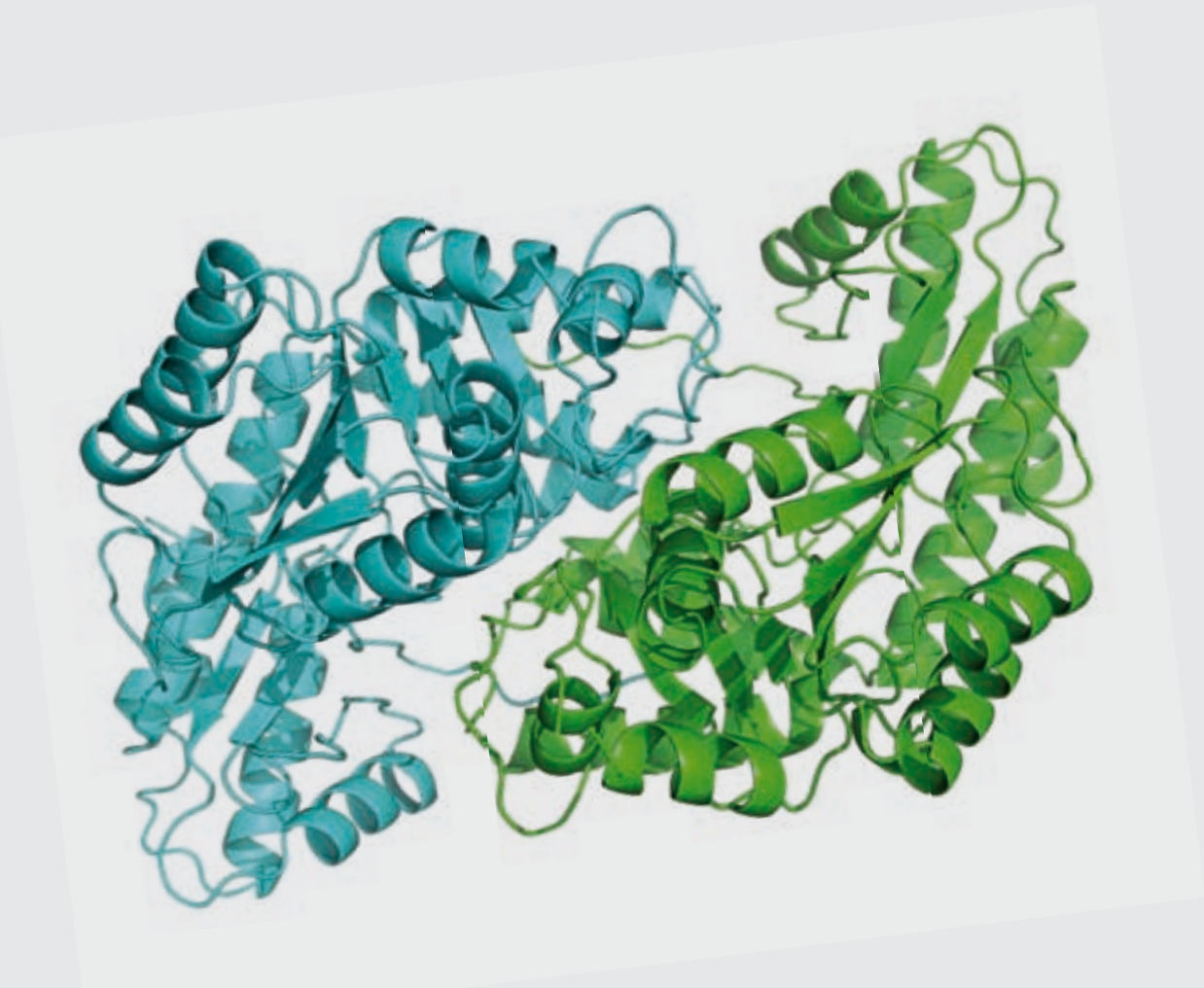
In conclusion, the GWL package is a versatile GW code which permits to address realistic model structures in order to calculate direct and inverse photoelectron spectra. The extension to spin polarised and metallic systems is on the way.

References

- [1] P. Umari, G. Stenuit, and S. Baroni, *Phys. Rev. B*, **79**, 201104R (2009).
- [2] P. Umari, G. Stenuit, and S. Baroni, *Phys. Rev. B*, **81**, 115104 (2010).
- [3] P. Umari, C. Castellarin-Cudia, V. Feyer, G. Di Santo, P. Borghetti, L. Sangaletti, G. Stenuit, and A. Goldoni, *Phys. Status Solidi B*, available online (2010).



LIFE SCIENCES

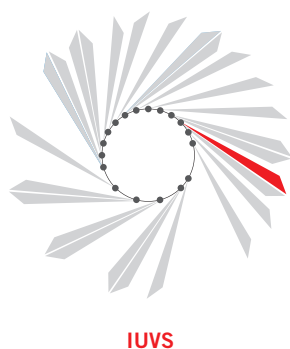


TEMPERATURE DEPENDENCE OF HYDROGEN-BOND DYNAMICS IN ACETIC ACID-WATER SOLUTIONS

F. D'Amico, F. Bencivenga, A. Gessini, C. Masciovecchio

Sincrotrone Trieste S.C.p.A., Trieste, Italy

E-mail: francesco.damico@elettra.trieste.it



The role of water for stability and functionality of a protein is very important. The hydration of proteins provides the right flexibility and the correct three-dimensional structure capable of accomplishing biological processes. It was also demonstrated how the loss of the biological functioning of the protein can be formed in a process of dehydration. The main causes of these effects may be sought in the role played by water in the strength of hydrogen bonds (HB) and in the bond dynamics. Several studies have evidenced an increase of the HB strength in the proteins β -sheet structures in absence of water and a strong temperature dependence of HB dynamics. In folded proteins, the main HB species present on the secondary structure are the NH and the C=O groups of the peptide unit. Therefore the whole comprehension of this HB species behaviour from the energetic point of view is fundamental to a complete understanding of the folding protein dynamic. However, despite the huge number of experiments, the coexistence of different HB species in the same system makes it very difficult to extract information from a single HB. One possible way to overcome this problem is to study a simple model, where only few HB species are present. We chose an aqueous system containing a C=O group, where one can investigate how the force depends on the temperature HB: acetic acid (CH₃COOH) in aqueous solution [1].

It is well known how Brillouin scattering allows the estimation of the HB activation energy through the analysis of the inelastic spectra collected as function of temperature. This can be performed following the Arrhenius law

$$\tau = \tau_0 \exp\left(\frac{E_B}{k_B T}\right)$$

where E_B is the HB activation energy and τ the structural relaxation time. The activation energy, obtained using this method, has been

proved to be strictly correlated to the HB free energy [2]. The τ dependence can be extrapolated from the inelastic spectra through the viscous approximation in the viscoelastic model. In such approximation it is possible to fit the inelastic Brillouin peaks with a damped harmonic oscillator (DHO) function. Moreover, the aforementioned relaxation time τ is found to be proportional to Γ/Q^2 , where Γ is the DHO Lorentzian half width half maximum and Q is the exchanged momentum. Examples of Brillouin spectra performed on acetic acid - water solutions have been reported, with the corresponding curves fit, in Fig. 1, panels A and B. In Fig. 1, panels E and F, also is reported the activation energy derived from the Γ/Q^2 behaviour as a function of temperature, obtained by fitting 5 consecutive points with an Arrhenius law function (panels C and D). In all the panels, n represents the number of water molecules per acetic acid molecules. The analysis of activation energy behavior indicates the presence of a crossover temperature ($T_c = 325 \pm 10$ K). Below T_c , the presence of a stiff HB between water and the acetic acid carboxylic groups causes a strong increase of the average activation energy. Instead, above T_c , the energy of hydrogen bonds responsible for water-acetic acid and acetic acid-acetic acid interactions turns out to be strongly reduced. This behavior can be mainly ascribed to a temperature change in the activation energy of carboxylic groups in acetic acid. Above T_c it is reasonable to suppose that, on thermodynamic grounds, the water-water HB may become almost equally favored with respect to the acetic acid-acetic acid HB, because of the large entropy increase of the former. Although this experiment represents only a model system, it is interesting to point out how the water-acetic acid T_c value is fairly close to the unfolding temperature of some protein systems such as, for example, lysozyme (340–370 K). There-

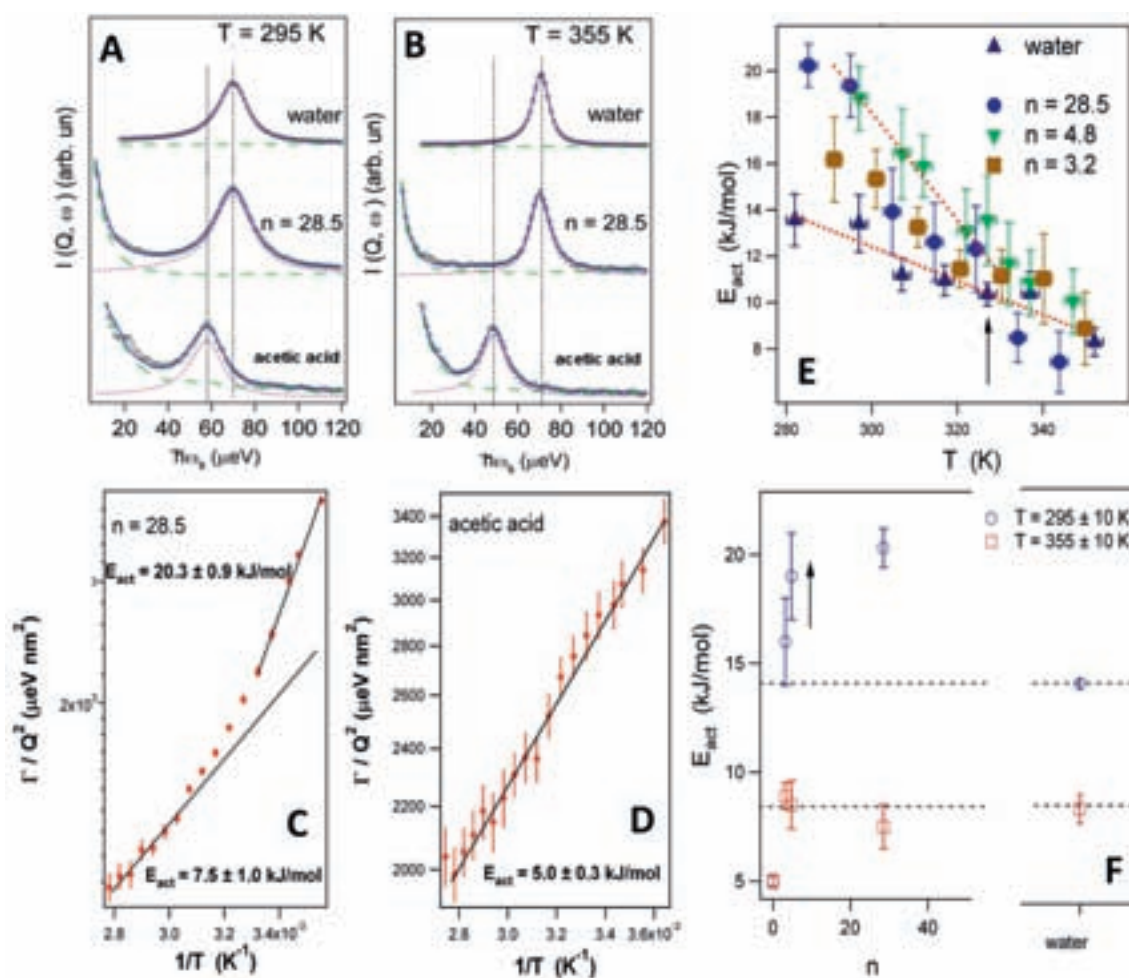


Figure 1. Panels A e B. Selection of IUVS spectra from water, acetic acid, and acetic acid-water solutions at different n and T . Panel C and D: Values of the parameter Γ/Q^2 in pure acetic acid and in acetic acid-water solution reported as a function of the inverse temperature. The straight lines show the Arrhenius trend. Panel E: Activation energy as a function of temperature at the different indicated n -values. The arrow indicates the T_c position. Panel F: Activation energies as a function of n for the lowest and highest investigated temperatures. The dotted lines show the water activation energies for both the temperatures.

fore, although we are far from establishing a real similarity, we can speculate on how the behavior of the activation energy observed in our experiment also occurs in HB involved in protein folding, opening the way for further investigations on biological systems.

References

- [1] F. D'Amico, F. Bencivenga, A. Gessini, C. Masciovecchio *J. Phys. Chem. B* **114**, 10628–10633 (2010).
- [2] C. Masciovecchio, F. Bencivenga, A. Gessini *Condens. Matter Phys.* **11**, 47–56 (2008).

TOWARD MULTIPROTEIN NANOARRAYS USING NANOGRAFTING AND DNA DIRECTED IMMOBILIZATION OF PROTEINS

L. Casalis¹, F. Bano², L. Fruk³, B. Sanavio^{1,2}, P. Parisse², M. Glettemberg³, C. M. Niemeyer³, G. Scoles^{1,2}

¹Sincrotrone Trieste S.C.p.A., Trieste, Italy

²International School of Advanced Studies (SISSA), Trieste, Italy

³Fakultät Chemie, Biologisch-Chemische Mikrostrukturtechnik, Technische Universität Dortmund, Dortmund, Germany

E-mail: loredana.casalis@elettra.trieste.it

Nanostructure LAB (SENIL)

Controlled immobilization of proteins at the micro/nano scale on solid surfaces holds great promise for applications in the field of biomedical diagnostics and, more generally, in the life sciences. Detecting the protein fingerprint in healthy and diseased biosamples, in fact, could provide unique information about diseases at the molecular level and, in turn, novel information useful for therapeutics. Technologically speaking, the major challenge in the field of protein arrays is in the capability for miniaturization^[1]: high-throughput analysis requires that thousands of different proteins/antibodies are harbored on the chip (a cell or a tissue lysate is in fact composed of >100.000 proteins) at high probe density, in order to keep the total dimensions of the device small (mm² scale), allowing the use of a low amount of the sample to be analysed. Towards this end, novel nanotechnology routes must be adopted.

The SISSA/ELETTRA NanoInnovation Lab at Elettra is exploiting nanotechnology for the fabrication of nanoarrays of biomolecules and for the detection of biorecognition events, by means of atomic force microscopy (AFM). We have tried different approaches for immobilizing proteins at the nano scale and, provided that protein activity is retained upon immobilization, we have proved their validity through immunological assays.

Among the different nanofabrication routes, the combination of DNA-directed immobilization (DDI) of Semi-Synthetic Protein (SSP)-DNA conjugates, on complementary ssDNA sequences, is one of the most promising, especially with respect to multiplexing^[2]. We have, for the first time, shown the viability of the DDI approach on the nanoscale by producing nanoarrays of ssDNA sequences complementary to the SSP-DNA conjugates by

AFM tip-assisted nanografting (NG). In this novel approach, different single stranded DNA (ssDNA) sequences are grafted on selected areas of a gold surface, previously passivated by a self-assembled monolayer (SAM) of bio-repellent molecules, by the AFM tip operated at high pressure (about few tens of nN) in a buffer solution containing thiol functionalized DNA molecules. During the nanografting process, the tip favours the exchange between the molecules of the previously formed SAM and the ones in solution (which are also functionalized with thiols, as seen in fig.1). At selected locations on the surface, the DNA molecules from the solution can therefore be arranged to form nanoscale confined monolayers, named NAMs, which are more ordered than spontaneously formed SAMs, due to the “combing” action of the AFM-tip. Once the DNA nanoarray has been created, DDI is used to decorate the DNA nanopatches with SSP-DNA conjugates (see fig. 2). The integrity and biochemical functionality of the resulting protein arrays are demonstrated by AFM topography measurements and immunological assays, respectively.

We investigated the validity of the nanografting/topography platform towards the detection of target proteins in the complex matrix of standardized human serum (BISEKO). Towards this end, a patch array was grafted, containing a control ssDNA patch, a sequence complementary to a DNA-streptavidin (STV) conjugate and another one complementary to a DNA-glucose oxydase (GOx) conjugate. Two specific antibodies, anti-STV IgG and anti-GOx IgG dissolved in BISEKO matrix, were allowed to bind to this array, and each binding was monitored sequentially by topography measurements. As a result, both antibodies could be detected and no indica-

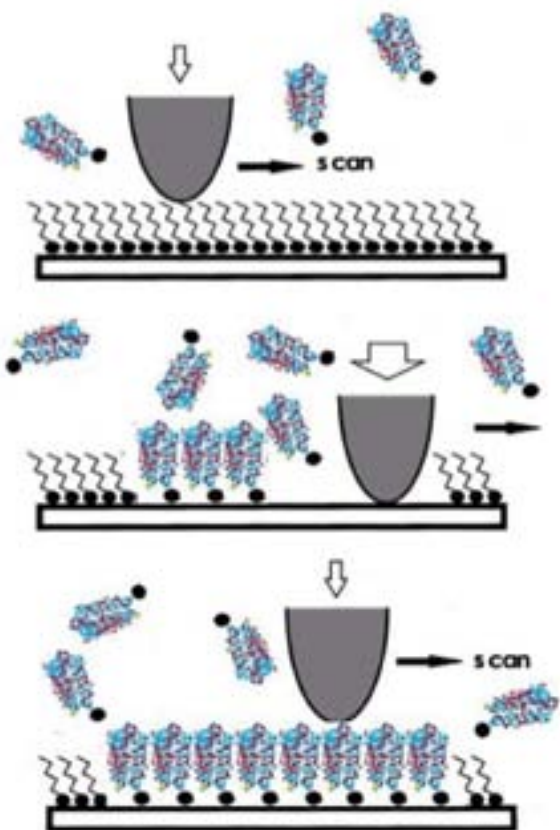


Figure 1. Schematic of the nanografting process. The AFM tip is operated at high load (few tens of nN) over a selected nano-scale area within a SAM of protein-repellent molecules formed on the surface of a gold film. The molecules present in solution, having the same functionality as those of the SAM, substitute the ones removed by the tip.

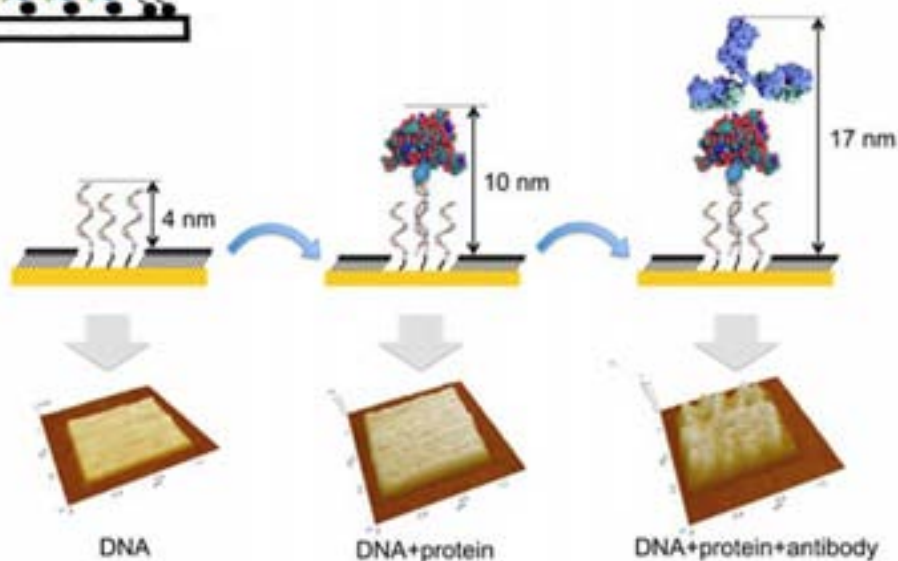


Figure 2. NG-based protein arrays: schematic representation and resulting AFM topographic images obtained for a single-patch DNA (left) directed sensor, generated from a covalent DNA-protein (center), which was then used for the binding of the corresponding antibody (right).

tion of nonspecific binding of either matrix components or target proteins disturbed these analyses. The minimum amount of protein detectable by this method is in the fg range, proving that the specific detection platform has a high sensitivity level.

The observed specificity of biomolecular recognition and the lack of nonspecific binding clearly illustrates that nanografted patch arrays are well suited for applications in label-free biosensing. For further development, we plan to scale-up the DDI/NG platform to

fabricate multifeature protein nanoarrays, for multiplexed proteome analysis, parallelizing the nanografting method by using a matrix of independently actuated cantilever, both for fabrication and read-out purposes.

References

- [1] C. Wingren, C. A. K. Borrebaek, *Drug Discovery Today* **12**, 813 (2007).
- [2] F. Bano, L. Fruk, B. Sanavio, M. Glettemberg, L. Casalis, C.M. Niemeyer, G. Scoles, *Nanoletters* **9**, 2614 (2009).

X-RAY MICROTOMOGRAPHY AS ONE OF THE COMPLEMENTARY TECHNIQUES FOR MICROSPATIAL ANALYSIS OF BIOMINERALS

J. Kaiser^{1,2}, M. Nývltová Fišáková³, M. Galiová⁴, M. Ivanov⁵, K. Novotný⁴, M. Holá⁴, R. Malina², L. Mancini¹, G. Tromba¹, N. Sodini¹, D. Dreossi¹, T. Kořístková⁶, K. Proksová⁴, V. Kanický⁴

¹Sincrotrone Trieste S.C.p.A., Trieste, Italy

²Institute of Physical Engineering, Faculty of Mechanical Engineering, Brno University of Technology, Brno, Czech Republic

³Institute of Archaeology, Academy of Science of the Czech Republic, Brno, Czech Republic

⁴Department of Chemistry, Faculty of Science, Masaryk University, Brno, Czech Republic

⁵Department of Geological Sciences, Faculty of Science, Masaryk University, Brno, Czech Republic

⁶Laboratory Specializing in Urinary Stones Analyses, Calculi®, Brno, Czech Republic

E-mail: kaiser@fme.vutbr.cz



SYRMEP

Mineralized tissues and bio-mineral structures i.e. bones, teeth, shell, fish scale, cockles or urinary calculi have been found to be excellent “archives” related to living habits, nutrition and exposure to changing environmental conditions [1], [2]. Bones and teeth maintain much of the “biological signature” from the living phase over a long time, revealing potentially a wealth of information about the chronology, diet and palaeoenvironment of past populations. As an example, deviations in the Sr/Ca, Sr/Zn and Sr/Ba ratios can indicate population mobility or a social status in the childhood [3]. The Sr/Ca, Sr/Zn and Ba/Ca ratios denote the character of the nutrition, especially the proportion of foodstuffs of animal and vegetable origin in the diet. These ratios may be different in geographical regions with different Sr, Zn, Ba and Ca contents in the environment. Sr/Ba ratio in calcified tissues reflects the Sr/Ba ratio in the environment and some deviations of this ratio in tooth increments indicates the population mobility [3].

Another of the numerous applications is e.g. the study of the development of different diseases on the basis of elemental ratio changes in bone tissue [4]. A degenerative bone disease, *osteitis deformans*, has a complicated aetiology characterized by increased bone remodelling and abnormal bone architecture associated with morphological functional abnormalities of osteoclasts. The latter are abnormal in number, size, and activity, and dig multiple cavities in bone matrix. This phase is followed by a second phase usually characterized by the simultaneous occurrence of both osteoclastic and osteoblastic activity or formation of

a new highly vascular bone of “woven” type. More specifically, the aim of the microspatial analysis could be the determination of different Ca/P ratio in newly formed pathological bone, both in fossil and recent samples [4]. The complex analysis could help to find the causes of *osteitis deformans*, which is quite a difficult task even in osteological material of recent specimens.

Analytical methods that can measure elemental concentrations at appropriate spatial resolution, similar to that of above mentioned bio-minerals structures, are e.g. laser induced breakdown spectroscopy (LIBS) [3, 4] and laser-ablation inductively coupled mass spectrometry/optical emission spectrometry LA-ICP-MS/OES [3]. However, an analysis of such specimens could be difficult due to the low concentration of the elements of interest in comparison to the high concentration of the matrix element (matrix effect) [3], contamination or loss of elements upon handling, and detection limits [4]. In order to apply these techniques effectively, it is advantageous to know the structure of the entire investigated sample before performing the LIBS or LA-ICP-MS/OES analysis, and/or to investigate the parameters of the laser-ablation crater or laser-ablation pattern after the chemical composition mapping.

Synchrotron radiation X-ray microtomography (μ CT) can be utilized to visualize non-destructively the microstructure of biominerals. The SYRMEP beamline is well suited for μ CT experiments, due to the energy range available, the large cross-sectional area, and the small divergence of the beam [4]. Moreover, the

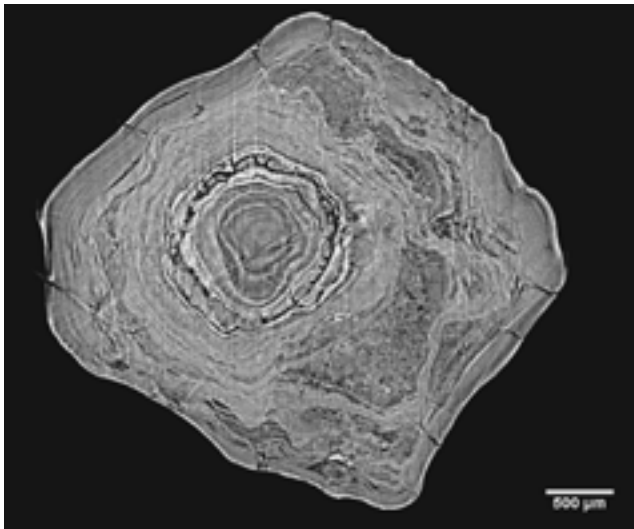


Figure 1.
μCT axial slice of urinary calculi fragment.

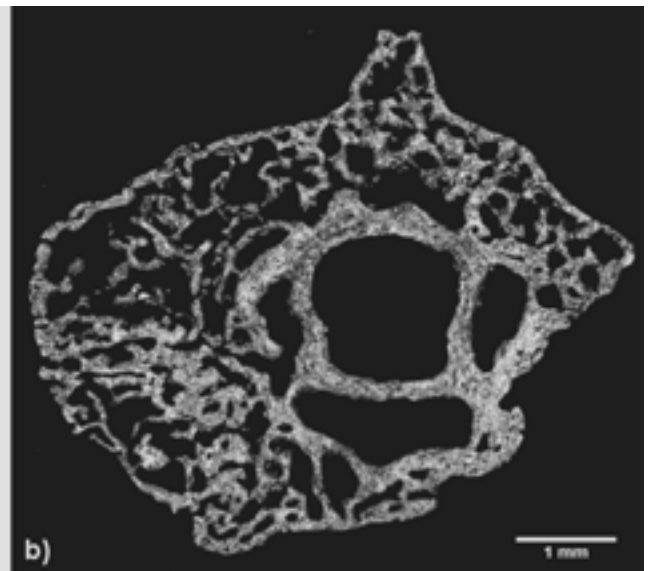
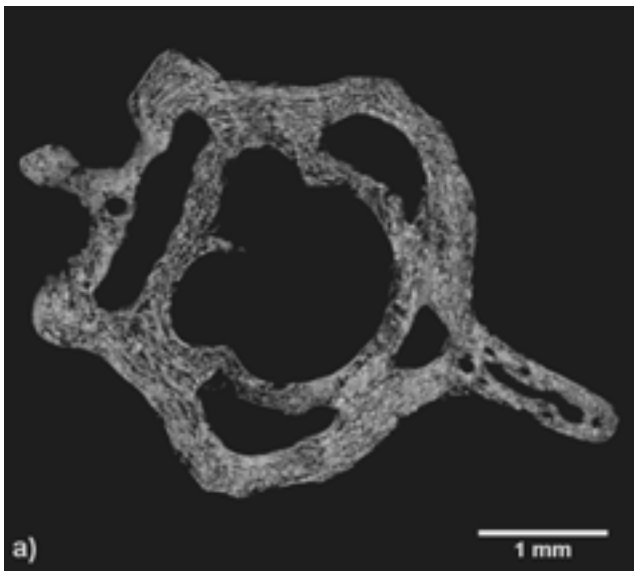


Figure 2.
μCT axial slices of a) healthy and b) pathological fossil snake (*N. natrix*) vertebra.

SYRMEP apparatus allows the analysis of the 3D sample structure utilizing absorption and phase-contrast μCT techniques - with high-resolution and with a high dynamic range. Our earlier study showed the capabilities of this beamline for visualization and the subsequent analysis of e.g. urinary calculi samples (Fig.1). The μCT measurements of snake vertebrae samples (Fig.2) [4] or the microspatial analysis of prehistoric bear (*Ursus arctos*) tooth section [3] also clearly demonstrate the advantages of using the μCT setup available at SYRMEP. In most cases the microstructure of biominerals was investigated prior to the chemical mapping and the proper cut across

the samples was realized on the basis of these measurements. Moreover, the μCT of the calcified tissues provided us with the necessary information about the sample structure in order to validate the outcome of LIBS or LA-ICP-MS/OES analysis.

References

- [1] M. Holá *et al.*, *Environ. Geol.* **58**, 141 (2009).
- [2] K. E. Limburg *et al.*, *X-ray Spectrom.* **36**, 336 (2007).
- [3] M. Galiová *et al.*, *Appl. Opt.* **49**, C191 (2010).
- [4] M. Galiová *et al.*, *Anal. Bioanal. Chem.* **398**, 1095 (2010).

STRUCTURE OF JACK BEAN UREASE REVEALED 80 YEARS AFTER IT WAS CRYSTALLIZED - INSECTICIDAL PROPERTY OF PLANT UREASES EXPLAINED

K. Ponnuraj

Centre of Advanced Study in Crystallography & Biophysics, University of Madras, Guindy Campus, Chennai, India

E-mail: karthe@unom.ac.in, pkarthe@hotmail.com



XRD1

The three dimensional structure of the historic enzyme, the Jack bean urease (JBU) has recently been unraveled. JBU was not only the first enzyme isolated as a crystalline protein by Sumner in 1926, which fetched him the Nobel Prize, but also the first example of a nickel metalloenzyme and the first protein which showed the presence of sulfhydryl groups. Surprisingly, JBU had to wait more than 80 years for its structural revelation!

Ureases are nickel metalloenzymes synthesized by plants, some bacteria and fungi. They provide the ammonia required for growth by catalyzing the hydrolysis of urea into ammonia and carbon dioxide. Although the amino acid sequences of plant and bacterial ureases are closely related, some biological activities differ significantly. Plant ureases, but not bacterial ureases, possess insecticidal properties independent of their ureolytic activity.

Till date, although crystal structures of some microbial ureases were known, very little was known from X-ray analysis of JBU as far as plant ureases are concerned. Multiple isoforms and insolubility of JBU seemingly were the impediments for preventing the X-ray structure determination for so long and we successfully overcome these shortcomings. The reported structure of JBU (Fig.1) is similar to its bacterial counterparts, including the active-site architecture, suggesting a conserved catalytic mechanism.

One of the biological functions that distinguish plant and bacterial ureases concerns the former's ability to act as an insecticide. It was previously determined that in canatoxin (isoform of JBU), an internal 10 kDa peptide was released by hydrolysis of canatoxin by the enzyme cathepsin in the digestive system of susceptible insects, and this was found to be responsible for the entomotoxic effect. Lack of this entomotoxic peptide in microbial ure-

ases is attributed to their ineffectiveness as insecticides. By virtue of the makeup or composition of bacterial ureases (they consist of two or three different chains; α , β , γ) as opposed to a single polypeptide chain in plant ureases, the linker peptide is missing in the former. We propose that this is probably responsible for lack of insecticidal property in bacterial ureases. In fact, mapping the 10 kDa insecticidal region of canatoxin onto the bacterial ureases has shown that a region consisting of the C-terminus of the β -chain, and the N-terminus of the α -chain (Fig.2), corresponding to the region responsible for insecticidal activity, were not linked in bacterial ureases.

In the crystal structure of JBU, the 10 kDa insecticidal region (Gly 230–Val 320) is formed by an α helix, a long loop, another short helix and a β -hairpin motif. It is believed that the pore-forming toxins (PFTs) insert either an amphipathic α -helix or β -hairpin to produce well-defined pores in the plasma membrane of the attacked cells. A subgroup of PFTs known as β -PFTs was predicted to form β -barrels which insert into membranes to create pores. In β -PFT the individual β -hairpin from one monomer pairs up with the neighboring β -hairpin of the other monomer to generate a β -barrel structure that spans the membrane.

In plant ureases, the putative membrane-disruptive β -hairpin motif located in the 10 kDa entomotoxic peptide region, is highly conserved and exhibits an amphipathic character. It has been shown that the recombinant form of the 10 kDa entomotoxic peptide region of JBU possesses membrane-disruptive ability on acidic lipid bilayers and it also forms aggregates. These observations and the structural features revealed in JBU, prompted us to propose that the amphipathic β hairpin located in the C-terminal region of the 10 kDa entomotoxic peptide of plant ureases might form

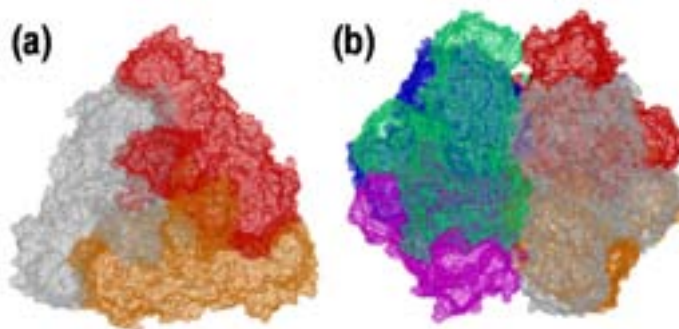


Figure 1. Surface representation of JBU trimer and hexamer. (a) The JBU monomers associated to form a trimer and (b) two trimers pack against one another and form a functional hexamer.

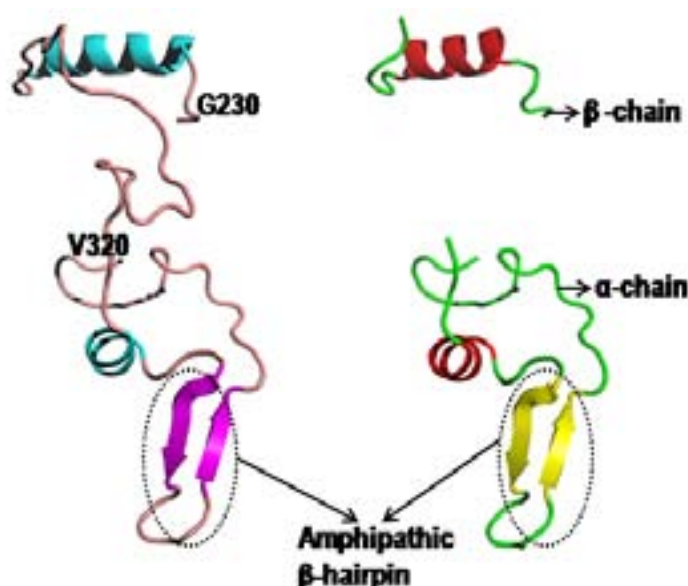


Figure 2. Folding of the 10-kDa entomotoxic peptide region of JBU (Left) and the corresponding region in *B. pasteurii* bacterial urease (Right). The insecticidal region in bacterial urease is not intact and consists of two chains.

a membrane insertion β -barrel as in β -PFTs. This provides a clear explanation for bacterial urease (*B. pasteurii*) not being lethal to insects. From the structure, we understand that although bacterial ureases contain this critical β -hairpin motif, they lack most of the N-terminal part of the β -hairpin motif. This is because in bacterial ureases the 10 kDa region is not intact but instead made up of two chains (α and β). As a consequence, the β -hairpin motif is formed by the α -chain, while the N-terminal part is formed by the β -chain (Fig.2). Therefore it is likely that the N-terminal part of the β -hairpin motif might be required for the overall stability of the putative transmembrane β -barrel and

since this region is not attached to the β -hairpin motif, the overall stability of the β -barrel may be compromised in bacterial ureases.

It is noteworthy that Elettra has also its major impact in this work. The data for JBU crystals was collected at the XRD1 beamline of Elettra (at home source the crystals were diffracting very weakly to 4 Å) and this has contributed significantly to this historic journey of JBU from the first crystal obtained in 1926 to the structure solved till date.

Reference

- [1] A. Balasubramanian and K. Ponnuraj, *J. Mol. Biol.* **400**, 274 (2010).

AN AMINOTRANSFERASE BRANCH POINT CONNECTS PURINE CATABOLISM TO AMINO ACID RECYCLING

I. Ramazzina¹, R. Costa¹, L. Cendron², R. Berni¹, A. Peracchi¹, G. Zanotti², R. Percudani¹

¹Department of Biochemistry and molecular Biology, University of Parma, Parma, Italy

²Department of Biochemistry, University of Padua, Padua, Italy

E-mail: riccardo.percudani@unipr.it, giuseppe.zanotti@unipd.it



XRD1

Whilst the synthesis of purine bases is accomplished through a series of reactions requiring amino acid precursors and the investment of ATP molecules, most organisms are not able to produce energy or useful compounds from purine catabolism. The products of purine catabolism are often discarded as waste material [1]. In fact, the catabolic intermediate, uric acid, can cause gout in humans, and end product glyoxylate can be dangerous, too. Metazoa have a glyoxylate detoxification system in which alanine glyoxylate aminotransferase (AGXT) converts glyoxylate to glycine at the expense of alanine. We have shown that a bacterial gene related to alanine:glyoxylate aminotransferases, present in the purine degradation cluster of *Bacillus subtilis* and named *pucG*, codes for an enzyme with structural similarity to human AGXT1. By combining genetic and biochemical information with genome comparison, logic analysis and experimental evidences, we have demonstrated the function of the protein encoded by the *pucG* gene [2]. We have shown by NMR spectroscopy that the PucG protein from *Bacillus subtilis* catalyses the transamination of an unstable intermediate and the end-product of purine catabolism, S-ureidoglycine and glyoxylate, to oxalurate and glycine. This activity enables soil and gut bacteria to use the animal purine waste as a source of carbon and nitrogen. The reaction catalyzed by (S)-ureidoglycine–glyoxylate aminotransferase (UGXT) illustrates a transamination sequence in which the same substrate provides both the amino group donor and, via its spontaneous decay, the amino group acceptor. The UGXT-catalyzed reaction does not require addition of a keto-acid in the reaction mixture, representing a unique example of a transamination in which the same substrate ((S)-ureidoglycine) provides both the amino group donor and, via

its spontaneous decay, the keto group acceptor.

The crystal structure of *B. subtilis* UGXT provided insights into the function and evolution of the enzyme. The asymmetric unit of the crystal revealed a UGXT homo-dimer, with the two monomers related to each other by a two-fold non-crystallographic axis (Fig. 1). Two UGXT monomers are assembled as an intimate dimer. The N-terminal segment of one monomer wraps around the other monomer, and a large flat surface formed by two α -helices and three loops of the main domain packs against the equivalent region from the other monomer. The overall structure of UGXT is similar to that of PLP-dependent enzymes belonging to the so-called “fold-type” I. The PLP cofactor of UGXT binds in a pocket at the dimer interface (Fig. 2). Its electron density is continuous with that of Lys200, suggesting formation of a Schiff base via covalent attachment of the ϵ -amino group of the lysine side-chain and C4A of the PLP. Structural comparison and mutational analysis suggested a molecular rationale for the functional divergence between UGXT and AGXT1, and allowed the identification of active site residues involved in the enzyme specificity.

The glycine produced by the UGXT reaction can have a variety of metabolic fates in the cell. A possibility is the *de novo* synthesis of purines. Glycine contributes the two central carbon atoms of the purine ring, the same atoms that are recovered as glycine in the catabolic pathway. Why are UGXT enzymes present only in some bacteria? The answer is possibly linked to evolution: according with phylogenetic reconstructions this enzyme originated after the split of eukaryotic kingdom. Nevertheless, this pathway is not relevant only for prokaryotes: in humans, one-third of the uric acid is secreted

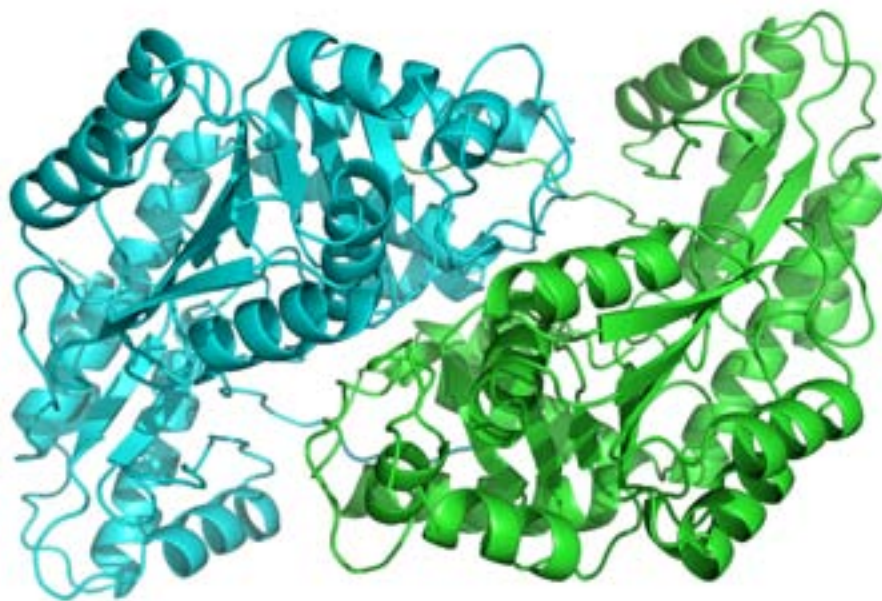


Figure 1.
Cartoon view of the
homo-dimer of UGXT
enzyme.

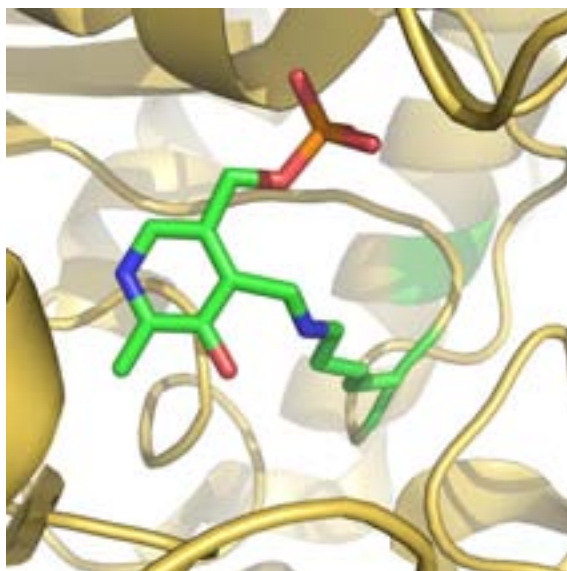


Figure 2.
Detail of the pyridoxal
5'-phosphate (PLP)
cofactor at the active
site. Carbon atoms of
the PLP cofactor and
the covalently bound
Lys200 are in green.

in the gastrointestinal tract, where it can constitute an abundant nutrient source for microorganisms. Through the UGXT protein, *Bacilli* can use discarded uric acid as a source of carbon, nitrogen, and energy, illustrating a perfect example of one species producing waste that another species can use as food.

References

- [1] P. A. Tipton, *Nature chemical biology* **2**, 124-125 (2006).
- [2] I. Ramazzina, R. Costa, L. Cendron, R. Berni, A. Peracchi, G. Zanotti, R. Percudani. *Nature Chemical Biology* **6**, 801 (2010).

LOCALIZATION OF ALUMINIUM IN TEA (*Camellia sinensis*) LEAVES USING LOW ENERGY X-RAY FLUORESCENCE SPECTRO-MICROSCOPY

Roser Tolrà¹, Katarina Vogel-Mikuš², Roghieh Hajiboland^{1,3}, Peter Kump⁴, Paula Pongrac^{2,4}, Burkhard Kaulich⁵, Alessandra Gianoncelli⁵, Vladimir Babin⁵, Juan Barceló¹, Marjana Regvar², Charlotte Poschenrieder¹

¹Laboratorio de Fisiología Vegetal, Facultad de Ciencias, Universidad Autónoma de Barcelona, Bellaterra, Spain

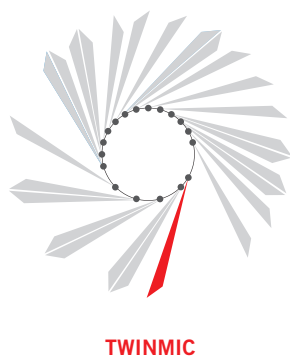
²Department of Biology, Biotechnical Faculty, University of Ljubljana, Ljubljana, Slovenia

³Plant Science Department, University of Tabriz, Tabriz, Iran

⁴Jozef Stefan Institute, Ljubljana, Slovenia

⁵Sincrotrone Trieste S.C.p.A., Trieste, Italy

E-mail: katarina.vogel@bf.uni-lj.si



Aluminum (Al) is an ubiquitous element without any known specific biological function. As one of the most abundant metals in the Earth crust, after Si and O, it is present in the daily life of all organisms. Generally, Al occurs as a component of a variety of crystalline aluminosilicate, oxy-hydroxide and non-silicate-containing minerals, and is thus usually regarded as unavailable for chemical and biological reactions [1]. However, under acidic conditions (pH<4.5) Al is solubilized into a toxic trivalent cation Al³⁺, which is more active in biochemical processes. Al³⁺ has a high affinity for O₂-donor compounds, such as Pi, nucleotides, RNA, DNA, proteins, carboxylic acids, phospholipids, polygalacturonic acid, heteropolysaccharides, lipopolysaccharides, flavonoids, antocyanins, etc. In plant cell cytoplasm even very low concentrations of free Al³⁺ are potentially toxic [2]. Because already micro-molar concentrations of Al³⁺ can drastically affect root growth and development in many agriculturally important plant species, Al toxicity has been recognized as a major factor limiting plant performance in acidic soils [2]. Nevertheless, some plant species have adapted to this high Al³⁺ availability in acidic soils, especially in tropical regions, by developing resistance or tolerance mechanisms. Among them the tea plant (*Camellia sinensis* (L.) O. Kuntze, Theaceae) is the subject of intense research. In tea plants, Al has been reported to be mainly accumulated in old and mature leaves in extremely high concentrations of up to 30,000 µg g⁻¹. Since Al is accumulated in plant parts that are readily consumed by humans, studies of the localization and specia-

tion of Al in tea leaves are especially important not only in the light of revealing plant Al tolerance mechanisms, but also in the light of fate and risks of dietary Al intake in humans, who consume tea-based beverages. Al can act as a neuron-toxicant causing Fe-mediated oxidative stress and cell injury. Although this is still under debate, Al has also been linked to Alzheimer's disease [3].

The aim of the present study was to investigate the spatial distribution of Al and other low-Z elements in optimally developed leaves of tea plants in order to better understand the mechanisms of tolerance to high concentrations of this toxic metal. Localization of the elements in cryo-fixed freeze-dried tea-leaf cross-sections was performed using low-energy X-ray fluorescence (LEXRF) spectro-microscopy (TwinMic beamline) that is highly sensitive for detecting low Z elements such as Al. The results showed that Al was mainly localized in the cell walls of epidermal cells (Figure 1) [4]. On the other hand, in mesophyll cells of the examined tea leaves only a weak Al signal was observed from the cell walls while, in the selected leaf regions, no Al signal was detected from the inner living part (symplast) of the cell. Al distribution pattern didn't show any correlation with other elements such as, for example, silicon or phosphorus, but there was a strong co-localization with oxygen. This indicates that Al is probably bound to free hydroxylic and carboxylic groups that are abundant in the cell walls. Since epidermal cells do not participate directly in photosynthesis, accumulation of toxic metals in less metabolically active epidermal tissues is a common

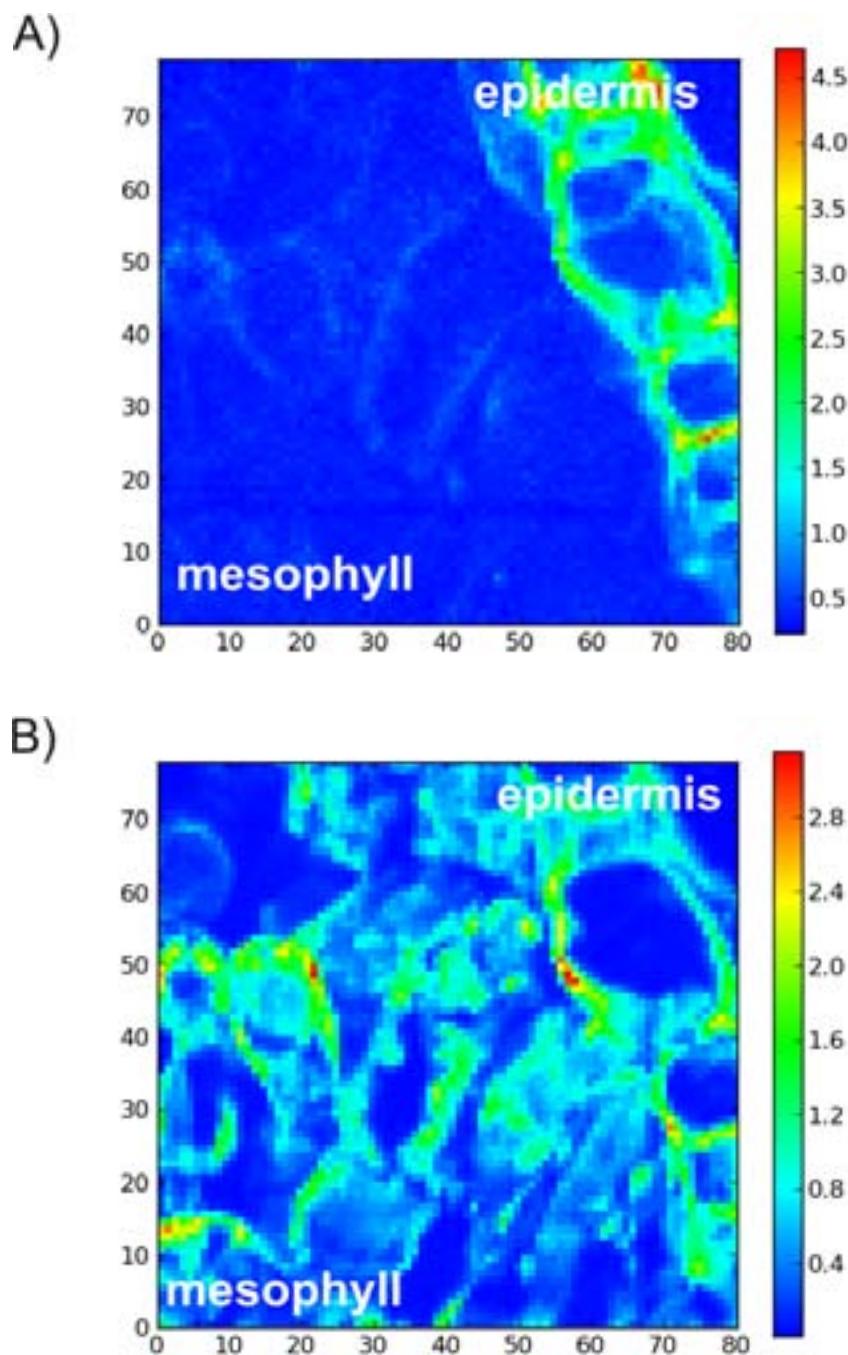


Figure 1. Scan of the representative epidermis-mesophyll region of a tea leaf (size 80 x 80 μm^2 , scan 80 x 80 pixels). A) Aluminium; B) Oxygen. The maps were obtained after scanning with the 1.7 keV beam. The maps were normalized to the intensity of beam current and the time of acquisition (counts $\text{s}^{-1} \text{mA}^{-1}$).

detoxification mechanism that protects photosynthetically active tissues from toxic metals. In addition, strong binding of metals to the cell wall components (Al-oxygen coordination) at the cellular level may fix metal ions and prevents leaking and transport of the metals across plasma membrane to the symplast. This mechanism therefore protects bio-molecules that are crucial for normal cell functioning.

Future research using micro-XANES will reveal Al speciation in tea leaves and confirm Al coordination in the cell walls, giving additional information on availability of accumulated Al for tea consumers.

References

- [1] G. Berthon Coordin, *Chem Rev* **228**, 319-341 (2002).
- [2] C. Poschenrieder, B. Gunesé, I. Corrales, J. Barceló, *Sci Total Environ* **400**, 356-368 (2008).
- [3] V. Frisardi, V. Solfrizzi, C. Capurso, P. G. Kehoe, B. P. Imbimbo, A. Santamato, F. Dellegrazie, D. Seripa, A. Pilotto, A. Capurso, F. Panza, *J. Alzheimer Dis.* **20**, 17-30 (2010).
- [4] R. Tolrà, K. Vogel-Mikuš, R. Hajiboland, P. Kump, P. Pongrac, B. Kaulich, A. Gianoncelli, V. Babin, J. Barceló, M. Regvar, C. Poschenrieder, *J. Plant Res.*, (2010), DOI: 10.1007/s10265-010-0344-3.

VERSATILE LOOPS IN MYCOCYPINS INHIBIT THREE PROTEASE FAMILIES

M. Renko, D. Turk

Department of Biochemistry and Molecular and Structural Biology, Ljubljana, Slovenia

E-mail: dusan.turk@ijs.si



XRD1

Intra and extracellular protein degradation by proteases is a common biological mechanism to enable their normal homeostasis, growth and disassembly. Proteases are however not employed only to act within their own organism, but are also deployed to invade, and feed from, other ones. Therefore inhibition of the exogenous protease activity became a widespread defense mechanism in all species. In plants, protease inhibitors are applied against pests, pathogens and parasites. They are present in a variety of plant tissues. They can be deployed alone or together with a variety of small molecules. In a search for novel classes of protease inhibitors, mycocypins, clitocypins and macrocypins were discovered. They are cysteine protease inhibitors isolated from the mushrooms *Clitocybe nebularis* and *Macrolepiota procera*. Lack of sequence homology to other families of protease inhibitors suggested that mycocypins inhibit their target cysteine protease by a unique mechanism and that a novel fold may be found.

The structure of macrocypin alone was solved from data collected on a crystal soaked in a saturated solution of sodium iodide, using SAD phasing approach and subsequently determined and refined using the native data. In contrast, the crystal structure of cliticypin in the complex with human cathepsin V was solved by the molecular replacement method using cathepsin V structure as the search model and applying the four fold non-crystallographic symmetry averaging to trace the cliticypin structure [1].

The crystal structures revealed that mycocypins possess a β -trefoil fold, the hallmark of a well-known family of the Kunitz type inhibitors. It is a tree-like structure with termini and two loops in the root region, a trunk comprised of a six-stranded antiparallel β -barrel, and two layers of loops in the crown region (Fig 1A and 1B). The crystal structures

of the complex between protease cathepsin V and cliticypin has revealed yet another motif of binding to papain like-cysteine proteases, which in a yet unrevealed way, occludes the catalytic residue. Cliticypin binds into the active site of the target protease in the orientation of a fallen tree, with trunk and roots pointing sideways and up (Fig 1A and 1B). The interaction surface of cliticypin comprises two broad loops positioned at the lower edge of the crown. The first loop binds into the non-primed and the second into the primed substrate-binding site. They occlude the catalytic cysteine in the middle and thereby prevent the approach of substrate molecules (Fig. 1C). The concept of loops occluding the catalytic site has been observed before in proteins with different folds: cystatins, the p41 fragment, and chagasin. In contrast to these proteins, which use three loops for binding, cliticypin uses only two loops. This interaction surface differs from the regions inhibiting serine proteases such as trypsin and legumain, the asparaginyl endopeptidase.

The binding of cliticypin to cathepsin V is unique in yet another way. The binding associated with a peptide-bond flip between Gly24 and Gly25 residues (Fig 2). The peptide bond between the two glycine residues in the free cliticypin appears in two different orientations that are clearly seen in the electron density, both in glycine-preferred regions of the Ramachandran plot. The same peptide both is found in only one orientation in all four cathepsin V - cliticypin complexes in the asymmetric unit, where it forms an additional hydrogen bond with the cathepsin V. To confirm the importance of this finding the flexibility of the main chain was reduced by mutation of Gly 25 to Ala as well as deleted. The resulting cliticypin mutants yielded K_i values to cathepsin V that were 20 times higher than that of the native variant. This

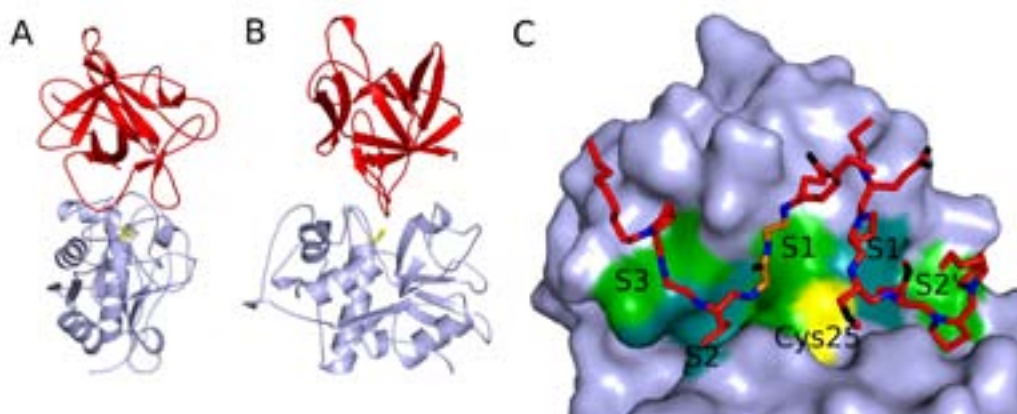


Figure 1.

The cathepsin V - clitocypin complex. A. View along the active site cleft. B. View perpendicular to the active site cleft. The folds of cathepsin V and clitocypin are shown in gray and red. The catalytic cysteine is shown in yellow. Clitocypin binds into the active site of cathepsin V in the orientation of a fallen tree with the trunk and roots pointing sideways and up. The wedge shaped structure fills the active site cleft along its whole length. C. Binding loops of clitocypin in its complex with cathepsin V. The chain of the first binding loop comes down the S3 binding area of cathepsin V, occupies the S2 binding site and continues upwards through the S1 binding site. The second binding loop of clitocypin approaches the S1' and S2' binding sites of cathepsin V from the top.

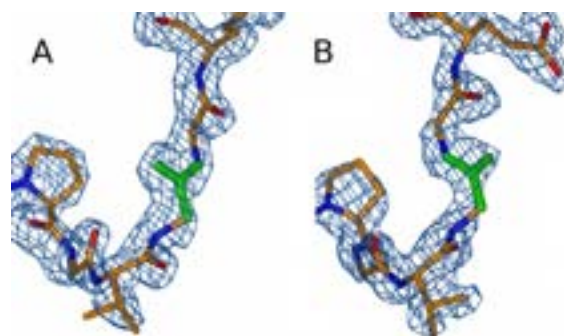


Figure 2.

Orientation of the Gly24-Gly25 peptide bond in the two clitocypin molecules. The $2F_{obs} - F_{calc}$ electron density map is contoured at 1σ . The bonds of glycine 24 are shown in green, while the rest of the chain is shown in red for oxygen, blue for nitrogen and orange for carbon. The Gly24-Gly25 peptide bond is flexible and can exist in either orientation.

suggests a mechanism in which the peptide bond flip occurs prior to, or concurrently with, the inhibitor docking.

This work has revealed the mechanism and the inhibitory potency of mycocypins against the cysteine and serine proteases. The scaffold of the Kunitz type inhibitors with its different binding regions has the potential to target

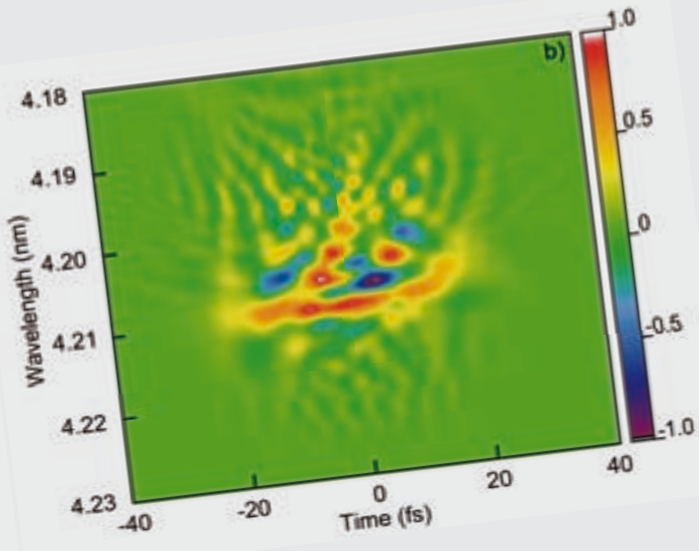
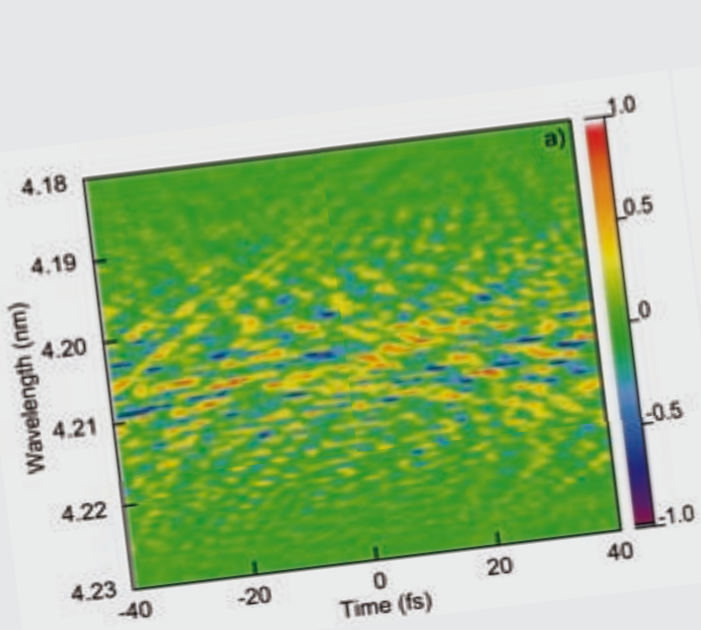
a variety of protease types in plant pests and parasites. Whether the exploitation of these findings for crop protection is feasible needs to be explored.

References

- [1] M. Renko, J. Sabotic, M. Mihelic, J. Brzin, J. Kos & D, *J. Biol. Chem.* **285**, 308 (2010).



FREE ELECTRON LASER AND OTHER COHERENT LIGHT SOURCES



UPDATE ON FERMI@ELETTRA, A NEXT-GENERATION FREE-ELECTRON LASER USER FACILITY

S. V. Milton

Sincrotrone Trieste S.C.p.A., Trieste, Italy

E-mail: stephen.milton@elettra.trieste.it

INTRODUCTION Tremendous progress was made in 2010 on FERMI@Elettra (FERMI), a next-generation synchrotron light source user facility based on a seeded free-electron laser (FEL), and now FERMI is on the cusp of beginning operations for the initial planned experiments and user community. In the following we will provide a brief overview of FERMI, go through the progress that has been made over the last year, and to complete this short report, the broad plans for 2011 leading to the eventual transition to full user operations will be laid out.

OVERVIEW The build up of the FERMI project has its start in a ground-up restoration and expansion of the original Elettra linear accelerator (linac) that was used as the primary injector for the Elettra storage ring. Additional accelerating structures and associated radio frequency (rf) plants were added to bring the nominal energy up to 1.5 GeV, and a high-brightness photocathode-based electron source was installed at the beginning of the linac. Additional specialized equipment such as two electron bunch compressor systems, transverse rf beam deflectors, a laser-driven electron beam heater, and a multitude of beam diagnostics and timing and synchronization systems were added to achieve and ensure control of the electron beam to the levels required.

All this necessitated an equally large modification to the existing conventional facilities. The linac hall was lengthened in both directions and additional laboratory and office space was added along with a local control room. The primary services (electricity, water, etc.) were also upgraded with the addition of a new electrical and mechanical plant building that provides all the power, water and heating, ventilation, and air conditioning services to FERMI.

But this was not the end of the civil construction. Additional space was also needed for the undulator and experimental halls, roughly

100-m and 60-m long respectively. By the end of 2009 most of the civil works for the linac building extension was complete and progress was at about the 40% level on the undulator and experimental halls and the electrical and mechanical plants combined.

We are happy to report that beneficial occupancy of all buildings was granted in early October 2010. Furthermore, through negotiation and planning, co-occupancy of the building during construction was allowed and so we were able to proceed with the technical installation in the buildings simultaneous with the building construction. An aerial view of the new FERMI complex is seen in Figure A.

Once accelerated, compressed and otherwise manipulated to the desired energy and spatial properties the electron beam is transferred to the undulator hall and through the fields of the undulator magnets where it is forced to radiate laser-like light at well defined and chosen wavelengths. This light is split from the electron beam and sent onward through various diagnostics and mirrors where it finally enters the experimental hall and ultimately the experimental chambers of the user programs. A graphical representation of the FERMI linac and undulator systems is shown in Figure B. Figure B also shows a graphical representation of the photon and beam delivery system (PADRES) that is used to diagnose and direct the out coming FEL light pulse to the various user program end stations.

FERMI is designed for a broad user community and thus is capable of being tuned over a wide range of photon wavelengths (100 nm \rightarrow 4 nm on the fundamental). Further flexibility is afforded by the use of variable gap APPLE



Figure A. An aerial view of the Sincrotrone Trieste with the circular storage ring Elettra Laboratory in the background and the roughly 380-m long FERMI@Elettra FEL User Facility in the foreground. The long building in the lower left is the experimental hall.

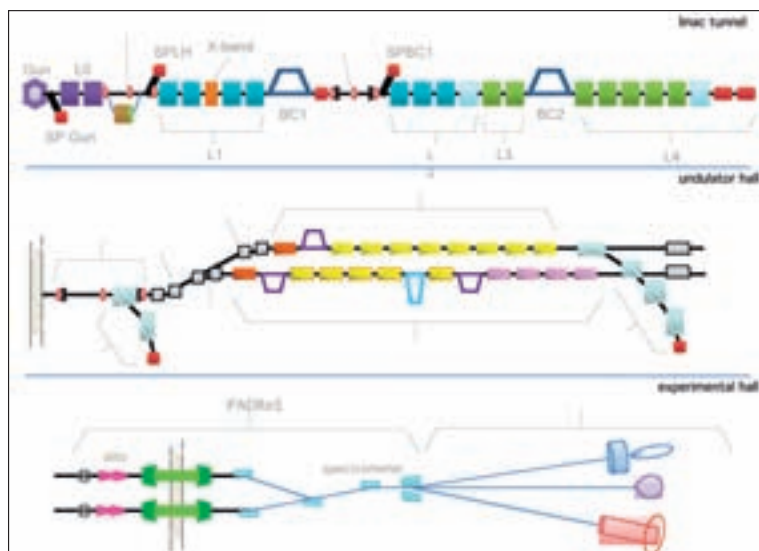


Figure B. Graphical representation of the FERMI@Elettra project. Note: due to space limitations the system has been broken down into three parts, the linac hall, the undulator hall, and the experimental hall; however, in reality they are in series.

II-type undulators that have the ability to provide full control of the output polarization be it planar or circular or anything in between. There will also be two parallel complementary FEL lines with the plan to use one as the primary line while the other is developed in an effort to push to the next level of performance. The expected performance for the two first FEL lines, FEL I and FEL II are shown in Table I and Figure C.

Parameter	FEL -1	FEL -2
HGHG Stages	1	2 ("fresh bunch" in 2nd stage)
Fundamental Wavelength range [nm]	100 to 20	20 to 4.2 (1.4 at 3rd harm.)
Output pulse length (rms) [fs]	< 100	20 – 100 (< 10 future goal)
Bandwidth (rms) [meV]	17 (at 40 nm)	100 (at 4.2 nm)
Polarization	Fully Variable	Fully Variable
Repetition rate [Hz]	50	50
Peak power [GW]	1 to >5	0.5 to 2
Harmonic peak power (% of fundamental)	~2	~0.2 (at 4.2 nm)
Photons per pulse	10^{14} (at 40 nm)	2×10^{14} (at 4.2 nm)
Pulse-to-pulse stability	$\leq 30\%$	~40%
Pointing stability [μ rad]	< 20	< 20
Virtual waist size [μ m]	250 (at 40 nm)	120
Divergence (rms, intensity) [μ rad]	50 (at 40 nm)	10 (at 4.2 nm)

Table I. Expected performance parameters for both FERMI@Elettra FEL I and FEL II systems.

PROGRESS

START OF 2010 By the beginning of 2010 significant progress had been made both in the technical systems and civil construction. As earlier stated, the linac hall was complete and there was a significant amount of technical equipment installed starting from the photocathode rf electron gun through the first 2 accelerating sections and on through the laser heater region, thus giving the commissioning team time to commission the system up through the critical 100 MeV point. (Refer to Figure B to get a general impression of the systems commission. Acronyms are obvious, eg. LH = Laser Heater). Meanwhile, and due in part to a 3-m thick brick wall installed one third of the way down the linac hall (just beyond the 1st bunch compressor spectrometer region SPBC1),

commissioning could progress while installation of technical equipment in the remaining two thirds of the linac continued.

The civil construction works were also well progressed, but there was still a large amount remaining to complete. Work had just started on the undulator hall roof and some of the side walls of the experimental hall were up, but not all. The mechanical and electrical plant building walls and roof were in place, but the equipment installation of the major systems and plumbing had not yet commenced. Needless to say, the construction of the service building that resides on the roof of the undulator hall and is designed to house key equipment such as the FEL seed laser system, controls for the undulators, power supplies for the magnets, processing equipment for diagnostics, et cetera had yet to be started.

11 Months Later: NOVEMBER 2010 A tremendous amount of work was accomplished through 2010, all very notable in the push to achieve first FEL light before the end of calendar year 2010.

As reported earlier the critical civil construction works are complete. There still remain minor items such as landscaping and environmental mitigation of the original construction, but this can be done with no impact on the commissioning and operation of FERMI. Additional civil works enhancements will also be pursued such as the addition of a second tri-generation plant, but again this will have no or very little impact on FERMI.

Equally exciting is the progress made on the technical systems. At this time the entire linac and related systems have been installed and operated up to just above 1.2 GeV. This was done without operating the rf compression cavities. Their operation should allow the system to reach the project goal of 1.5 GeV. Electron beam quality has generally been good with performance figures suitable for initial operation of the FEL at the longer wavelengths. The transfer line leading from the linac, through the FEL I undulator region, and ultimately to the final beam dump in the undulator hall has been completed with the exception of a few diagnostics. And just recently the seven undulators for FEL I have been installed (Figure D) and commissioning of FEL I is proceeding.

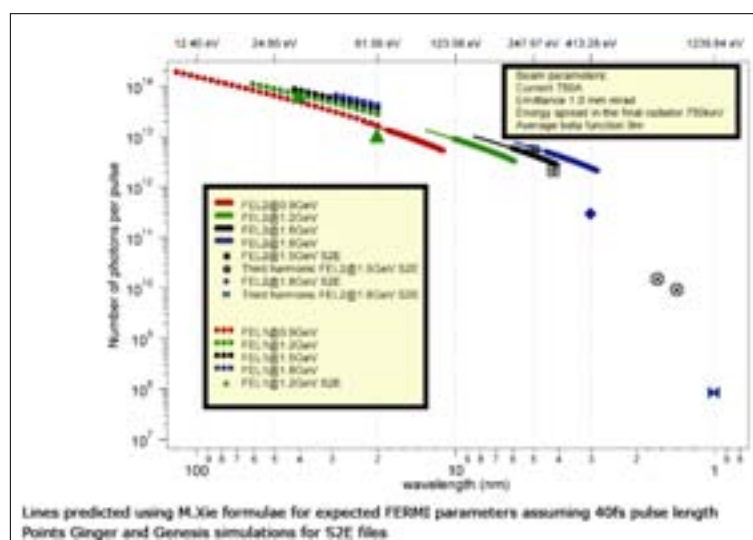
Beyond the electron beam systems lie the photon transport and beamline (PTBL or otherwise referred to as PADReS) system. Installation work has begun on PADReS with a significant fraction of the system linked to FEL I already installed through to the experimental hall. Commissioning of this system will begin along with the commissioning of FEL I.

The experimental program is also proceeding rapidly. Currently there are three approved and funded experimental programs, Low Density Matter (LDM), Elastic and Inelastic Spectroscopy (EIS), and Diffraction and Projection Imaging (DiProI), and one approved but not yet funded experimental program Magnetic Dynamics (MagDyn). All are collaborative efforts with members from Europe and around the world. The status of two of these, EIS and DiProI, is quite advanced with the DiProI system having already been tested using light from the Elettra storage ring, and the EIS system having been tested in the laboratory with an optical laser system. These two will be connected to the output of PADReS and we expect first experiments to begin early in 2011.

PLANS The pace will continue through 2011 with the goal of transitioning to a full user operations program by 2012. Commissioning of the machine and FEL systems will continue; however, interspersed will be days dedicated to servicing the experimental program with high-quality FEL light tuned specifically for their needs. In fact, we are setting a goal of scheduling and providing in 2011 nearly 2000 hours of time to the experimental program. Additionally the beam energy will be slowly raised to 1.5 GeV and consequently the minimal achievable wavelength will decrease. We further expect to install the ten undulators for FEL II in August 2011 and start commissioning of this 2-stage, high-gain harmonic generation (HGHG) FEL shortly after. FEL II will allow us to further extend the wavelength reach to 4 nm on the fundamental.

The buildup of PADReS and the experimental systems will continue through 2011 and will certainly continue to evolve throughout the lifespan of the FERMI facility. It is expected that by the end of 2011 all three funded programs will be installed in their initial configuration and be fed FEL pulses via the PADReS system on a scheduled, agreed upon basis. There is also hope that some portion of the MagDyn system will be funded and installed into the experimental hall.

Early on the need for availability of a high-power ultra short pulse laser system in the experimental hall was recognized. Such a system will enable pump-probe experiments carried out via coupling of these pulses to the femtosecond pulses of the FEL. As laser system technology progresses rapidly, the choice was made to wait until late in the project to procure this item. We are now in this process and will



have this laser system installed and ready for the experimental program by July of 2011.

Additional long range plans for the FERMI facility are also being formulated. On the near term horizon the FERMI project has teamed with the University of Twente in the Netherlands to produce and install a high-harmonic generation (HHG) seed source on FEL I. Provided we can make the HHG source sufficiently powerful we will be able to seed the FEL directly and move away from the more complicated HGHG configuration. We also might be able to push the wavelength range of the FEL I configuration to what will prior be solely the domain of FEL II. If that turns out to be the case then we will be able to service the user base with the upgraded FEL I and use FEL II as a test bed for additional FEL R&D such as echo-enabled harmonic generation.

Thinking further out we are getting involved in the development and use of X-band (12 GHz) rf accelerating systems. Such systems can support very high gradients (80 MV/m) and the addition of a limited amount (20 m) of accelerating structure could greatly extend the operational energy and therefore wavelength reach of FERMI.

Such plans are exciting to not only those who develop the machine and FEL but more importantly to the ultimate end users of the experimental program and they are also designed to place FERMI in a very competitive position in the years to come.

Figure C. Expected performance and tuning ranges of FEL I and FEL II.



Figure D. FEL I undulators installed in the undulator hall.

THE FERMI@ELETTRA FREE-ELECTRON-LASER SOURCE FOR COHERENT X-RAY PHYSICS

E. Allaria¹, C. Callegari¹, D. Cocco¹, W.M. Fawley^{1,2}, M. Kiskinova¹, C. Masciovecchio¹, F. Parmigiani^{1,3}

¹Sincrotrone Trieste S.C.p.A., Trieste, Italy

²Lawrence Berkeley National Laboratory, Berkeley, USA

³Physics Department, University of Trieste, Trieste, Italy

E-mail: enrico.allaria@elettra.trieste.it



The past couple of decades have seen an increasing quest for tools capable of temporally resolving the ultrafast dynamics of photon-matter interactions [1]. Recently built soft and hard x-ray free electron lasers (FELs) such as FLASH [2] and LCLS [3] have produced exciting, groundbreaking scientific results. The FERMI@Elettra FEL project at Sincrotrone Trieste is currently being commissioned and will be operational for user experiments in 2011. FERMI@Elettra will use external laser seeding together with a harmonic upshift scheme to produce transversely and temporally coherent radiation at XUV and soft x-ray wavelengths. This capability, together with the possibilities of temporal synchronization to external lasers and control of the output photon polarization, will open up new opportunities to investigate transient states of condensed, soft and low density matter using a variety of diffraction, scattering, and spectroscopy techniques and temporal correlation modes [4].

FERMI@Elettra will use a 1.5 GeV normal conducting linear accelerator to drive two different FELs that cover different wavelength ranges (Fig.1). Both FERMI FELs employ a harmonic upshifting scheme initiated by a coherent radiation ‘seed’ signal from a tunable, external UV laser together with a single-pass amplifier configuration that employs multiple undulators.

FERMI’s FEL-1 will cover the lower energy photon spectral range (20–100 nm, *i.e.*, 12–60 eV) using a single harmonic upshift stage, while FEL-2 uses two such upshift stages to reach output wavelengths (fundamental) as short as 4 nm (*i.e.*, 300 eV).

Much of the interest in harmonic cascade FELs over the past decade has been motivated by the possibility of producing pulses with a much higher degree of temporal coherence

than is normally possible from self-amplified spontaneous emission (SASE) FELs such as FLASH and LCLS. A series of numerical simulations done for the FERMI FEL-2 case has confirmed this expectation. The comparison has been done for an output wavelength of 4.2 nm that is close to the shortest wavelength of operation for FERMI FEL-2, and thus should be fairly sensitive to non-ideal electron beam properties. To investigate the predicted temporal coherence, we calculated the Wigner transform W of the on-axis far field. With knowledge of the electric field E , W effectively measures the local phase space density of the radiation and is defined as:

$$W(\omega, t) = \int dt' E^*(t - \frac{1}{2}) \cdot E(t + \frac{1}{2}) \cdot e^{i\omega t'}$$

The integration of W over t is proportional to the on-axis power spectrum, while the integration over ω is proportional to instantaneous intensity. Figure 2 shows the false colour image of the W for the SASE output case and the FERMI FEL-2 case. It is important to point out that the SASE calculation used an ideal electron beam pulse with constant properties, while for FEL-2 example we used an (imperfect) electron beam as predicted by detailed ‘start-to-end’ simulations. The disordered structure present in the case of SASE (Fig. 2-a) is indicative of random phase jumps between different intensity spikes. The externally seeded, FEL-2 case has a far smoother and compact W (Fig. 2-b), clearly indicating the advantage of the seeded, harmonic upshift scheme for producing temporal coherence.

We note that the attractiveness of the seeded approach is confirmed by recent proposals, such as the FLASH-2 at DESY and LCLS-2 at SLAC, that use similar (but not identical) approaches to produce highly coherent emission in the x-ray regime.

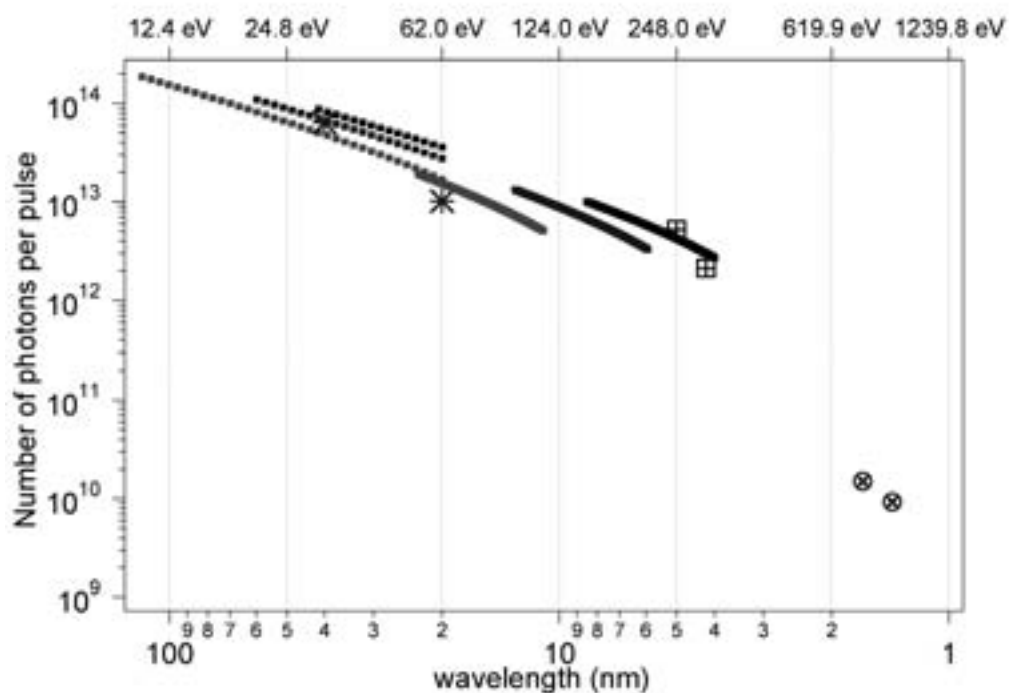
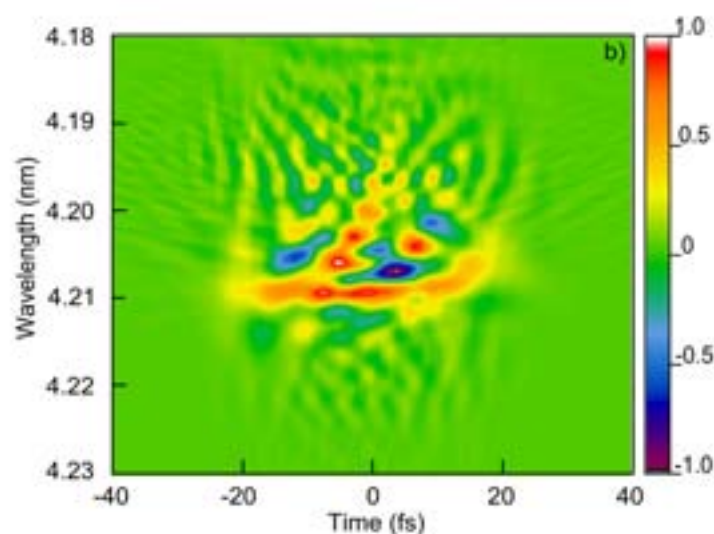
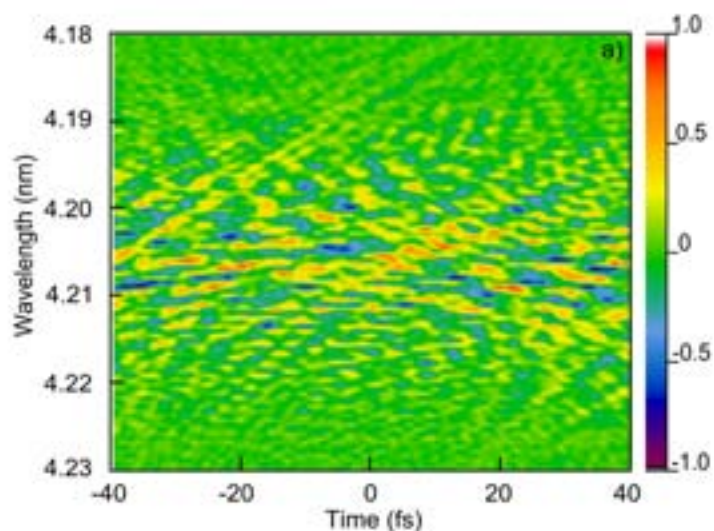


Figure 1. Predicted output from FEL-1 and FEL-2 of FERMI as a function of output wavelength. The lines correspond to a 40 fs pulse reaching saturation (dashed: FEL-1; solid: FEL-2). Each set of three lines corresponds, from left to right, to electron beam energies of 0.9, 1.2 and 1.5 GeV. The isolated markers are the results of detailed 'start-to-end' numerical simulation studies.

Figure 2.

False colour representations of the Wigner transform $W(\omega, t)$ of the predicted, on-axis far-field radiation output for the two cases of (a) SASE with an ideal e-beam; (b) externally seeded using 'start-to-end' e-beam. False colour scale bar in arbitrary units are reported on the right.



References

- [1] A. H. Zewail, *J. Phys. Chem. A* **104**, 5660 (2000).
- [2] J. Feldhaus, *J. Phys. B: At. Mol. Opt. Phys.* **43**, 194002 (2010).
- [3] L. Young *et al.*, *Nature* **466**, 56 (2010).
- [4] E. Allaria *et al.*, *New J. Phys.* **12**, 075002 (2010).

ULTRAFAST INSULATOR-TO-METAL PHASE TRANSITION AS A SWITCH TO MEASURE THE SPECTROGRAM OF A SUPERCONTINUUM LIGHT PULSE

F. Cilento^{1,2}, C. Giannetti³, G. Ferrini³, S. Dal Conte⁴, T. Sala³, G. Coslovich^{1,2}, M. Rini⁵, A. Cavalleri^{6,7}, F. Parmigiani^{1,8}

¹Department of Physics, Università degli Studi di Trieste, Trieste, Italy

²Laboratorio Nazionale TASC IOM-CNR, Trieste, Italy

³Department of Physics, Università Cattolica del Sacro Cuore, Brescia, Italy

⁴Department of Physics A. Volta, Università degli Studi di Pavia, Pavia, Italy

⁵Materials Sciences Division, Lawrence Berkeley National Laboratory, Berkeley, California, USA

⁶Condensed Matter Division, Max Planck Research Department for Structural Dynamics, University of Hamburg, Hamburg, Germany

⁷Department of Physics, Clarendon Laboratory, University of Oxford, Oxford, UK

⁸Sincrotrone Trieste S.C.p.A., Trieste, Italy

E-mail: c.giannetti@dmf.unicatt.it



Lab T-REX

Time-resolved optical spectroscopy is a leading technique to study important topics, such as ultrafast solid-solid phase transitions and strongly correlated systems [1]. The investigation of the physical mechanisms, responsible for the relaxation dynamics of the photoexcited system, is mandatory to understand its electronic and optical properties. The possibility to produce supercontinuum (SC) white light through photonic crystal fibers or through strong focusing on transparent crystals allows at once temporal and spectral resolution. Hence, a true time-resolved spectroscopy (TRS) can be achieved, allowing one to investigate the dynamics of the dielectric function of strongly-correlated systems upon excitation with ultrashort light pulses [2]. We present an experimental setup, in which the standard, monochromatic probe of a conventional pump-probe technique has been replaced with a SC probe pulse, to achieve TRS. The use of a cavity-dumped Ti:Sa oscillator as laser source, chosen for its versatility, severely restricts the options available to generate such a broadband pulse: the preferred method is to use a photonic crystal fiber (PCF), where an infrared laser pulse propagates into the fiber and nonlinear interactions within the silica core generate a broadband non transform-limited pulse with unknown residual spectral chirp. The technique we describe allows one to reveal the spectro-temporal profile of the pulse.

The major modifications in our setup compared to a conventional single colour pump-

probe scheme, stand in the generation of the broadband spectrum, sketched in Fig. 1d, and in the acquisition of the broadband spectrum, performed through a 128 pixel Hamamatsu NMOS linear array sensor. The SC pulse is focused and re-collimated upon reflection from the sample by means of a telescope, and is dispersed onto the linear sensor with a SF11 equilateral prism (Fig. 1a). The probed spectral region extends from 650 to 1050 nm; spectral resolution is determined by the pixel array: it ranges from 2 nm/pixel in the visible to 5 nm/pixel in the near infrared. The use of a double array configuration allows the suppression of the noise due to intensity fluctuations of the probe pulse, by recording the ratio between the reflectivity signal and a reference spectrum, taken before the interaction of the SC pulse with the sample.

Since the temporal structure of a PCF-generated SC pulse is rather involved, a careful pulse characterization is prerequisite, to extract the spectral and temporal structure (spectrogram) of the pulse, and accordingly correct pump-probe measurements. This is the aim of the present work. We demonstrate that this analysis can be done easily and in-situ—in a reflection geometry—if a solid-state optical switch is employed. We employ a VO₂ multilayer, which, when excited by an ultrashort laser pulse, undergoes a simultaneous electronic and structural phase transition which abruptly alters its optical properties [3], allowing its use as an optical switch. Assuming the

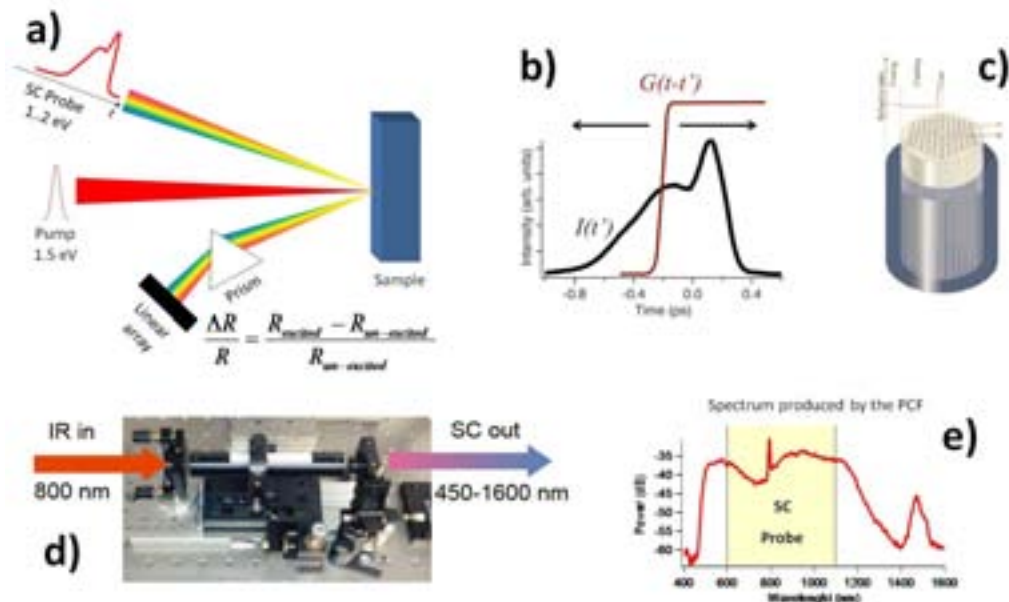


Figure 1.

a) Sketch of the pump–supercontinuum probe experimental configuration. b) Schematic of the switching technique: the VO_2 sample switching response, triggered by the 120-fs pump pulse, is represented by a smeared step function, G , scanned through the SC pulse, I , by changing the pump-probe delay. c) Section of the microstructured PCF. d) PCF assembly: the input radiation is focused into the fiber with an aspheric lens, while the SC output is collimated using an achromatic doublet working in the range 600–1050 nm. e) Full-range SC spectrum produced by the PCF; the region exploited in our setup is highlighted.

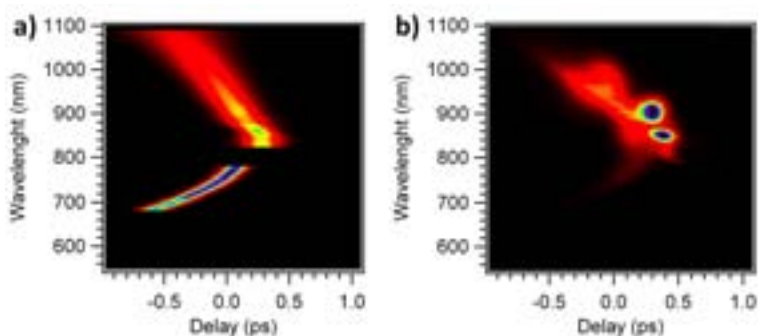


Figure 2. a) Spectrogram of the SC pulse, reconstructed through the VO_2 -based switching technique described in the text. The region around 800 nm cannot be characterized, because of the presence of a postpulse, due to the cavity dumper operation, in the laser output. The VO_2 switching behaviour thus allows for pulse diagnostics. b) Spectrogram of the same pulse, measured through a standard XFROG (angle-dithered) gating technique, shown for comparison.

VO_2 photoinduced reflectivity variation could be described as a step function, we applied a deconvolution procedure to the time-resolved measurement (not shown here, see [4]) and derived the temporal duration and the distribution of the various spectral components of the SC pulse in time, revealing the parabolic dispersion typical of PCF, as can be seen in panel a) of figure 2.

For comparison, the same SC pulse has been characterized with a standard XFROG technique, measuring the sum frequency (of the SC pulse plus a 800 nm gate pulse) generated through a non-linear (NL) BBO crystal. This technique offers a better temporal resolution, since the involved process is purely electronic, but presents some drawbacks: it

is time-consuming, since it requires to angle-dither the NL crystal, it works in transmission, and thus cannot be performed in situ inside a cryostat where other samples are held, and finally, has a non-uniform spectral response which limits the spectral range which can be analyzed.

References

- [1] C. Giannetti et al., *Phys. Rev. B* **79**, 224502 (2009).
- [2] C. Giannetti et al., *Phys. Rev. B* **80**, 235129 (2009).
- [3] M. Rini et al., *Appl. Phys. Lett.* **92**, 181904 (2008).
- [4] F. Cilento et al., *Appl. Phys. Lett.* **96**, 021102 (2010).

BURSTING COHERENT THZ RADIATION AT ELETTRA

E. Karantzoulis¹, G. Penco¹, A. Perucchi¹, S. Lupi^{1,2}

¹Sincrotrone Trieste S.C.p.A., Trieste, Italy

²CNR-INFM Coherentia and Dipartimento di Fisica, University of Rome "La Sapienza", Roma, Italy

E-mail: Emanuel.Karantzoulis@elettra.trieste.it



SISSI
ODAC Accelerator Physics

The last decade has witnessed a huge amount of experimental effort in order to fill the so-called Terahertz (THz) gap. This range of the electromagnetic spectrum, which is located between the microwave region and the infrared (0.1-10 THz, 3 mm – 30 mm), has been indeed scarcely investigated so far, mainly because of the lack of intense and stable THz sources. Much of the recent interest in THz radiation stems from its ability to penetrate deep into many organic materials without the damage associated with ionizing radiation such as X-rays (albeit without the spatial resolution). Tests are under way to determine whether THz tomographic imaging can replace X-ray mammography. Due to the fact that terahertz radiation is readily absorbed by water, it can be used to distinguish between materials with varying water content. Based on this property some have proposed THz imaging as a method of screening passengers at airports. There are many more speculations and applications for fields far apart such as ultrafast time domain and long wave radio astronomy.

An important source of THz radiation is provided by synchrotron light sources and the radiation can be very intense if the length of the electron bunches in the storage ring is within the microwave region. It is known that an accelerated bunch of electrons will emit coherently at wave lengths equal to, or larger than, its length; the emitted power is given as $P = (N(1 - g(\omega)) + N^2g(\omega))P_s$, where P_s is the single electron power, N is the total number of electrons and $g(\omega)$ is the coherence form factor, the squared Fourier transform of the normalized longitudinal charge distribution. One sees that if $g(\omega)$ is different from zero a fraction of the radiated power is proportional to P_s times the number of electrons squared and that when $g(\omega)$ approaches 1 one obtains full coherence which means that the whole emitted power is quadratic with the number of electrons.

However the majority of third generation light sources have bunch lengths of the order of 10 mm, i.e., larger than the microwave region, and the coherence from this length is shielded by the vacuum chamber. To reduce the bunch length down to the microwave region either the optics of the storage ring has to be modified or the energy decreased (both not always possible and certainly non compatible with the other users) or micro bunching introduced that will modulate the bunch length down to the microwave region. To do this one has to make the beam unstable either by reaching the microwave current threshold (i.e., increase the current per bunch) or by exciting the beam externally via a strip-line or a kicker. At present, bursts of Coherent Synchrotron Radiation (CSR) have been detected at several storage-rings (MAX-I, NSLS VUV ring, ALS, MIT South Hall Ring), while steady state CSR has been obtained only at BESSY and, more recently at ANKA, when the ring optics is tuned to the so called low-alpha mode. The poor number of CSR-based THz sources is explained by the strong difficulties experienced in achieving low-alpha mode in most existing storage-rings.

Elettra [1] uses the excitation technique mainly at low energies (0.9 GeV) and the CSR radiation, emitted in bursts, shows a wavelength distribution shorter than the nominal electronic bunch length as expected. Since the emitted power is very significant in this regime, there is a general interest in achieving a better understanding and control over the bursting processes in the prospect of its spectroscopic exploitation through self-normalized experimental set-ups. A profitable spectroscopic use of intense THz light is not only relevant to storage-rings, but shares common issues with IV generation light sources (which also represent very promising sources of coherent THz radiation) such as the FERMI@Elettra free electron laser whose very

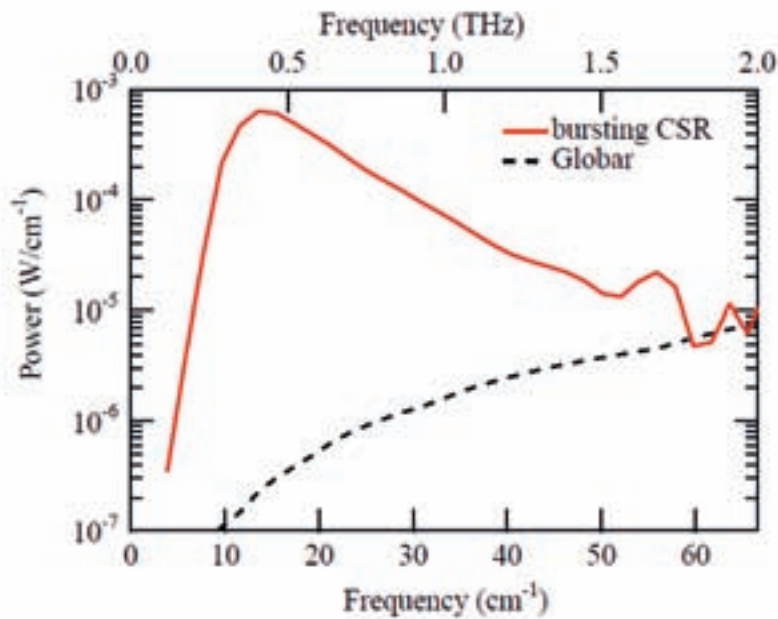


Figure 1.

Power spectrum of THz bursting CSR (solid line) measured at SISSI at 900 MeV, with 260 mA stored in multi-bunch mode and with the injection kickers activated. The absolute power scale is obtained by normalizing to a Globar spectrum (dashed line) measured in the same experimental conditions, using the known characteristics of the Globar source.

short bunch length of the order of 0.3 mm can provide a natural source of intense albeit low-repetition-rate (10-50 Hz) THz radiation.

As mentioned above the CSR emission observed at Elettra is induced either by kickers or driven by instabilities; as the observed CSR radiation is extremely powerful, it can be used for spectroscopic applications. To put this point on a more quantitative ground we compare the signal of an internal Globar source of the spectrometer with the CSR signal produced by a multi-bunch electron beam at 0.9 GeV using the kickers that usually do not disturb the experiment. The resulting spectrum is normalized to the Globar source intensity,

which permits to estimate the CSR power. The ratio of the CSR emission over the Globar is more than 3 orders of magnitude at 0.5 THz (Figure 1) and moreover the integrated emission exceeds 5 mW at THz frequencies. Such a high power level is comparable to that achievable by THz Quantum Cascade Lasers which emit however at one single frequency, and it is orders of magnitude higher than the radiation emitted through lamps (Globar, Hg) or photoconductive antennas.

References

- [1] E. Karantzoulis, G. Penco, A. Perucchi, S. Lupi, *Infrared Phys. Techn.* **53**, 300 (2010).

THE FERMI@Elettra CONTROL SYSTEM

M. Lonza, A. Abrami, F. Asnicar, L. Battistello, A. Bogani, R. Borghes, V. Chenda, S. Cleva, M. De Marco, M. Dos Santos, G. Gaio, F. Giacuzzo, R. Marizza, G. Passos, R. Passuello, L. Pivetta, R. Pugliese, C. Scafuri, G. Scalamera, G. Strangolino, D. Vittor, L. Zambon

Sincrotrone Trieste S.C.p.A., Trieste, Italy

E-mail: marco.lonza@elettra.trieste.it



The FERMI@Elettra free electron laser includes a considerable number of conventional systems and devices to be controlled, requiring standard control system interfaces and functionalities. In addition to them, several special needs and challenges that arise from the complexity of the facility and its required performance have been addressed.

The control system has been designed using commercial hardware components and open standards; a software environment based on GNU/Linux and the Tango package [1] is deployed on all computers. The backbone of the control system is a Gigabit Ethernet network where several types of computers and devices are connected. The main switch is made of two units working in high availability redundant configuration. The interface with the field consists of about 60 VME-based front-end computers (Equipment Controllers) equipped with PowerPC CPU boards running GNU/Linux and the Xenomai real-time extension. Intel based PCs are also used as front-end computers in special cases such as, for example, the five servers employed to acquire a total of 84 CCD cameras; these servers also perform basic online image processing at the bunch repetition frequency. A variety of interfaces are used to control the equipment: direct I/O (ADC, DAC, digital I/O), serial lines (RS 232/485), and Ethernet; the latter is becoming a standard for devices and instrumentation interface. The control room consoles are low consumption quad-core PCs with solid state hard disks each equipped with four monitors (Fig. 1). The control system servers run in a Xen virtualized platform on two physical machines, each equipped with four Intel Xeon quad-core processors, working in a hot backup configuration.

A total of about 26 Programmable Logic Controllers (PLC) are employed for protec-

tion and safety systems, where reliability and robustness are essential. The interlock systems protect magnets, linac RF plants, and the vacuum system, while the machine protection system preserves the undulator permanent magnets from radiation damage. The personnel safety system, which is based on fail-safe PLCs, controls human access to areas potentially subject to radiation such as the linac tunnel, the undulator hall and the safety hutch.

Stepper motors are extensively used in the facility in a wide range of applications; about 340 of them are foreseen. In order to standardize the stepper motor controllers, a new in-house design has been made based on commercial components. It has the flexibility to adapt to any type of motor and to many different applications.

The control room graphical interfaces are based on QTango [2], a C++ library of Tango aware components developed in house, which handles the most common functionalities necessary for building control panels. An online modeling toolkit [3] has been developed to provide machine physicists with tools and methods to easily and quickly develop software applications. Taking advantage of the availability of the Tango bindings, Matlab has been chosen to develop machine physics applications and measurement procedures used during the machine commissioning.

FERMI@Elettra is a pulsed machine generating and accelerating electron bunches at up to 50 Hz repetition rate. The control system implements built-in capabilities to measure, by means of the diagnostic instrumentation, the characteristics of every single laser pulse, electron bunch, and photon pulse, and to link them through a time stamp (bunch number). Moreover, some crucial parameters of the electron and photon beams must be controlled by a number of shot-by-shot feedback loops



Figure 1.
The FERMI@Elettra control room.

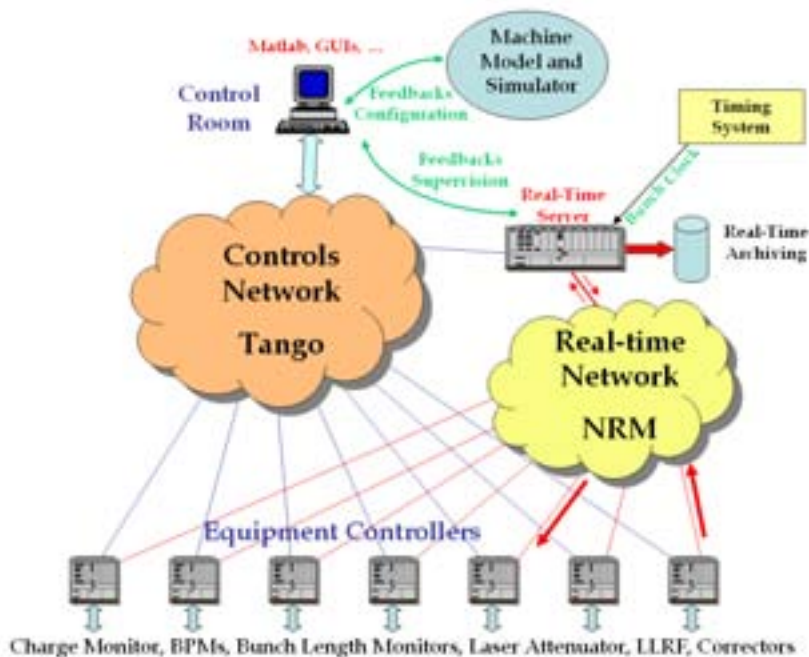


Figure 2.
Architecture of the real-time framework.

[4]. In order to enable the above functionalities a real-time framework (Fig. 2) based on a communication protocol called Network Reflective Memory (NRM) has been developed to efficiently and easily exchange data among the control system computers through a dedicated Ethernet network. A real-time server is in charge of bunch number distribution, data recording/archiving and feedback processing at the linac repetition rate. Multiple feedback loops can run in parallel, reading sensors and setting actuators through the NRM at the bunch repetition frequency.

On the beamline side, the experimental stations will be equipped with efficient data acquisition systems and online processing tools

tightly integrated into the FERMI@Elettra control system. Scientific data storage and grid/cloud computing facilities will be provided to handle the produced data stream.

References

- [1] <http://www.tango-controls.org/>
- [2] G. Strangolino et al., “QTango: a Qt Based Framework for Tango Graphical Control Panels”, ICALEPCS’09, Kobe, October 2009.
- [3] C. Scafuri, “The FERMI@Elettra Online Modeling Toolkit”, ICALEPCS’09, Kobe, October 2009.
- [4] M. Lonza et al., “Beam-based Feedbacks for the FERMI@Elettra Free Electron Laser”, IPAC’10, Kyoto, May 2010.

A METHOD FOR ESTIMATING THE TEMPERATURE IN HIGH ENERGY DENSITY FREE ELECTRON LASER EXPERIMENTS

E. Principi¹, C. Ferrante², A. Filippini², F. Bencivenga³, F. D'Amico³, C. Masciovecchio³, A. Di Cicco^{1,4}

¹CNISM, Università degli Studi di Camerino, Scuola scienze e tecnologie, sez. Fisica, Camerino (MC), Italy

²Dipartimento di Fisica, Università degli Studi dell'Aquila, L'Aquila, Italy

³Sincrotrone Trieste S.C.p.A., Trieste, Italy

⁴IMPMC, Université Paris 6, CNRS, Paris, France

E-mail: emiliano.principi@unicam.it



The “warm dense matter” (WDM) regime is an intriguing state of matter, still largely unexplored, lying between the condensed matter state and the plasma state. WDM is associated with densities ranging from that typical of condensed matter, 1-10 kg m⁻³, down to about 10³-10⁵ kg m⁻³ and temperatures in the 10³-10⁵ K domain. In this intermediate regime the thermal energy is comparable to that of the interatomic bonds thus leading to an exotic state consisting of a dense electron plasma strongly coupled to the lattice ions [1]. Macroscopic amounts of matter under such extreme conditions occur in the interior of large planets and in stars, and can be generated in devices for plasma production and inertial confinement fusion. Experiments aimed at creating and investigating matter in the WDM regime have been recently performed using high-energy-density sub-picosecond beams, based on the free electron laser (FEL) using the fourth-generation light source FLASH (Hamburg) [2], on optical lasers, and on laser-produced protons. The use of FEL radiation for investigating matter under extreme conditions is particularly promising because it embodies some important features of the other techniques, i. e., the high temperatures reachable with optical lasers and the high temperature homogeneity achieved with protons or heavy-ions beams. For this reason, the end-station TIMEX at the forthcoming “FERMI@Elettra” FEL facility has been specifically designed to study the WDM regime [3] by exploiting the unique properties of the FEL radiation.

Ultrafast experiments aiming to generate and probe high energy density matter, such as those devised for TIMEX, require proper diagnostic for estimating basic physical proper-

ties of the target. Measurement of fundamental quantities such as temperature and density is an important prerequisite for carrying out experiments under extreme conditions like those on warm dense matter. An important objective of the TIMEX project is to develop a direct and conceptually simple method (see Fig. 1) to measure the temperature of the lattice ions [4] after absorption of the FEL pulse, associated with the energy released by the heated plasma. This measurement is very important to define the WDM thermodynamical state of the system under investigation. Together with an independent estimate of the density, it could provide the point of the phase diagram reached by the system after the ultrafast heating. We carried out extensive calculations of the time evolution of the sample temperature field (see Fig. 2) by using the heat conduction differential equation opportunely rewritten in polar coordinates:

$$\frac{\partial T(r,t)}{\partial t} = k \frac{1}{r} \frac{\partial}{\partial r} \left(r \frac{\partial T(r,t)}{\partial r} \right) - \gamma (T(r,t)^4 - T_{\text{lat}}^4)$$

Calculations started from a realistic initial temperature profile of the sample and took into account the partial vaporization of the sample after irradiation by a typical FEL pulse [4]. A method to solve the inverse problem, i.e., to retrieve the initial temperature profile $T(r,0)$ from the directly measurable temperature value $T(r^*,t)$ at a distance $r^* \sim 0.5$ mm, was proposed which is based on a Bayesian approach and a Metropolis Monte Carlo algorithm.

Our results demonstrate that simple time-resolved pyrometric temperature measurements acquired with a typical resolution of 10 μ s are able to provide a reliable reconstruction of the sample temperature reached during the WDM

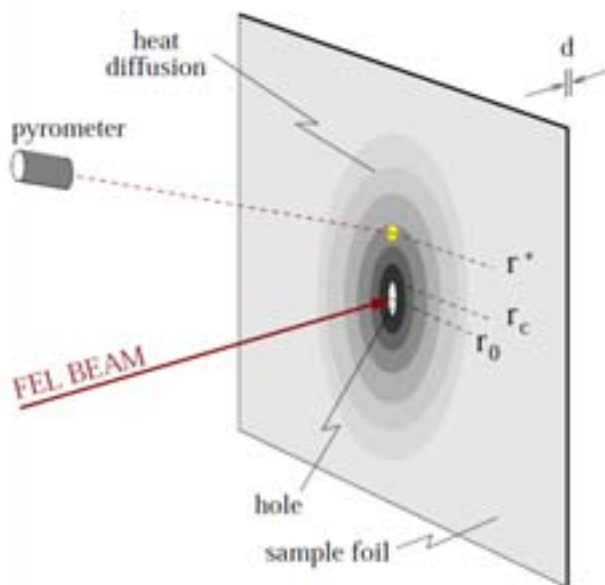


Figure 1. Sketch of the experimental geometry for WDM temperature estimation at the TIMEX end-station (FERMI@Elettra).

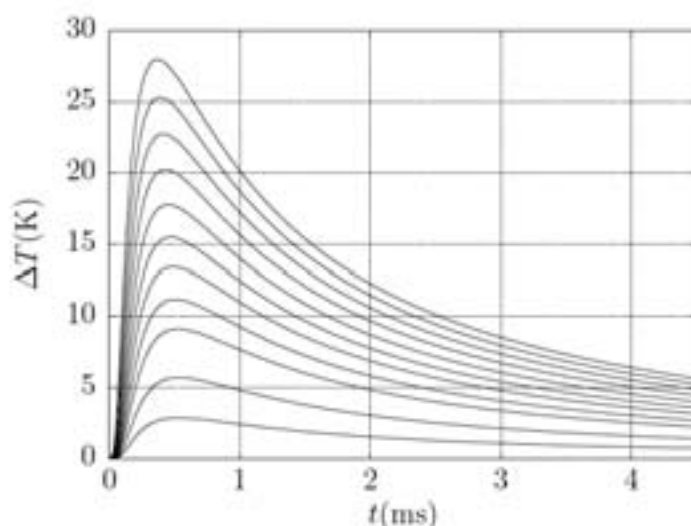


Figure 2. Calculated temporal evolution of the temperature of a thin sample foil at $r^* = 512 \mu\text{m}$ (see Fig. 1) for increasing values of peak temperature T_{max} at r_0 , where $T_{\text{max}} = 1000, 1500, 2250, 3375, 5062, 7593, 11390, 17085, 25628, 38443,$ and 57665 K .

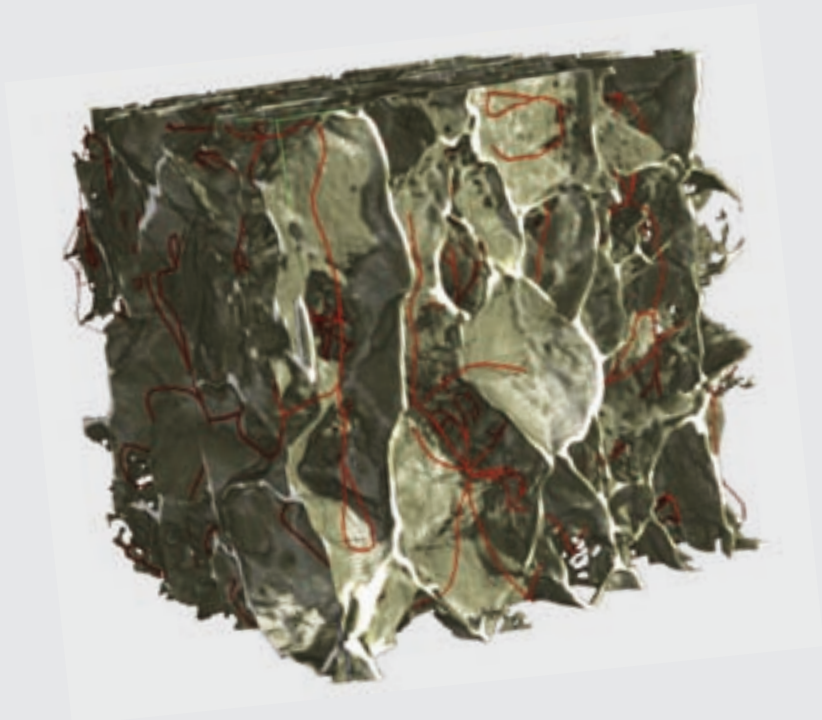
regime ($\sim 1 \text{ ps}$) with a theoretical uncertainty of 100 K on the maximum sample temperature. The calculations presented in our work [4] are thought to provide a solid basis for temperature diagnostics that will be included in the development of the end-station TIMEX at the FERMI@Elettra FEL facility in Trieste.

References

- [1] R. W. Lee et al., *J. Opt. Soc. Am. B* **20**, 770 (2003).
- [2] B. Nagler et al., *Nat. Phys.* **5**, 693 (2009).
- [3] <http://gnxas.unicam.it/TIMEX>.
- [4] E. Principi et al., *Nucl. Instrum. Meth. A* **621**, 643 (2010).



**INSTRUMENTATION DEVELOPMENT
AND SOFTWARE**



PORE3D SOFTWARE-AS-A-SERVICE (SaaS): A TOOL FOR QUANTITATIVE ANALYSIS OF 3D IMAGES

F. Brun^{1,2}, L. Mancini¹, G. Kourousias¹, R. Pugliese¹, D. Dreossi¹, G. Tromba¹

¹Sincrotrone Trieste S.C.p.A., Trieste, Italy

²Department of Electrical, Electronic and Computer Engineering, University of Trieste, Italy

E-mail: lucia.mancini@elettra.trieste.it



SYRMEP
Scientific Computing

In recent years there has been great interest in imaging techniques such as X-ray Computed Tomography (CT) and Magnetic Resonance Imaging (MRI), as well as the related micro-scale techniques μ -CT and μ -MRI because they produce three-dimensional (3D) images of the internal structure of objects in a non-destructive way. A major challenge lies in the quantitative characterization of the object under investigation directly from the acquired images. Pore3D is a package deployed using the Software as a Service (SaaS) paradigm for the analysis of large 3D image datasets. The current release of the package includes several functions tailored for the filtering, segmentation, and analysis of volumetric data; Pore3D is continuously evolving to include new functionalities and algorithms.

Thanks to the recent advances in computer and network technologies, it is possible to introduce the new paradigm of Software as a Service (SaaS), which blurs the classical distinction between hardware and software into the concept of service. Having the feeling of operating on a classical stand-alone environment, Pore3D's users actually exploit the functionalities of a remote high performance clusters. This solution allows to easily process and analyze huge amounts of data (e.g., high resolution μ -CT images), overcoming the bottlenecks and limits of memory size and computational speed normally present in the personal computer available to a typical user.

An interesting field in which μ -CT imaging techniques are widely adopted for different purposes is tissue engineering (TE). The basic concept of tissue engineering is to transplant bio-factors (cells and/or proteins) within a porous degradable material known as a scaffold in order to stimulate tissue regeneration. A scaffold should balance mechanical function with efficient mass transport to aid biological

delivery and tissue regeneration. A quantitative characterization of its microstructure in terms of pore size, pore geometry, spatial distribution of pores, and pore interconnection allows a better understanding of this balance and contributes to the creation of scaffolds with controlled architecture. However, assessing these structural properties is a challenging task. The μ -CT technique with both conventional X-ray sources and synchrotron radiation (SR) seems to be the most promising technique for a further quantitative analysis of porous scaffold microstructures. However, accurate image analysis protocols for a reliable characterization of TE scaffolds have yet to be properly defined. As an example, investigation on alginate/hydroxyapatite bone tissue engineering scaffolds [2] by means of SR μ -CT imaging and Pore3D SaaS analysis is here reported (Fig. 1). Pore size and throat size distribution as well as the degree of interconnectivity are interesting parameters for characterizing the morphology of the scaffold. However there is no standard and model-independent methodology for the assessment of such parameters. An interesting approach is based on skeleton extraction, which roughly represents the "backbone" of the porous network. By determining the thickness along the nodes and the branches of the skeleton it is possible to characterize pore size, throat size and the interconnectivity of the porous space. It is crucial to extract reliable skeletons in order to avoid spurious branches that affect the outcome of such measures. Fig. 1b shows the skeleton of the porous space of the alginate/hydroxyapatite scaffold under consideration, extracted according to a method implemented in Pore3D. From qualitative observations it can be noticed that the skeleton effectively captures the essential topology of the scaffold's pore space. This in turn allows one to compute reliable values for pore and

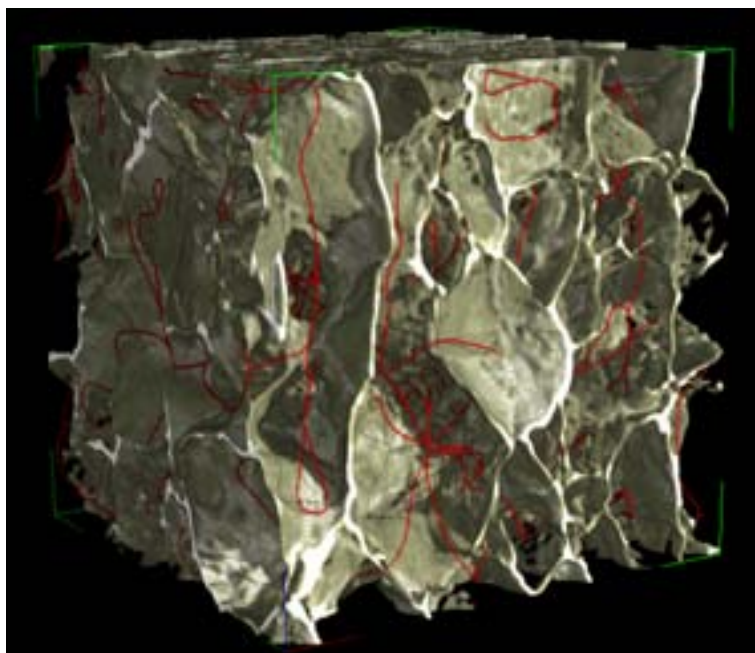
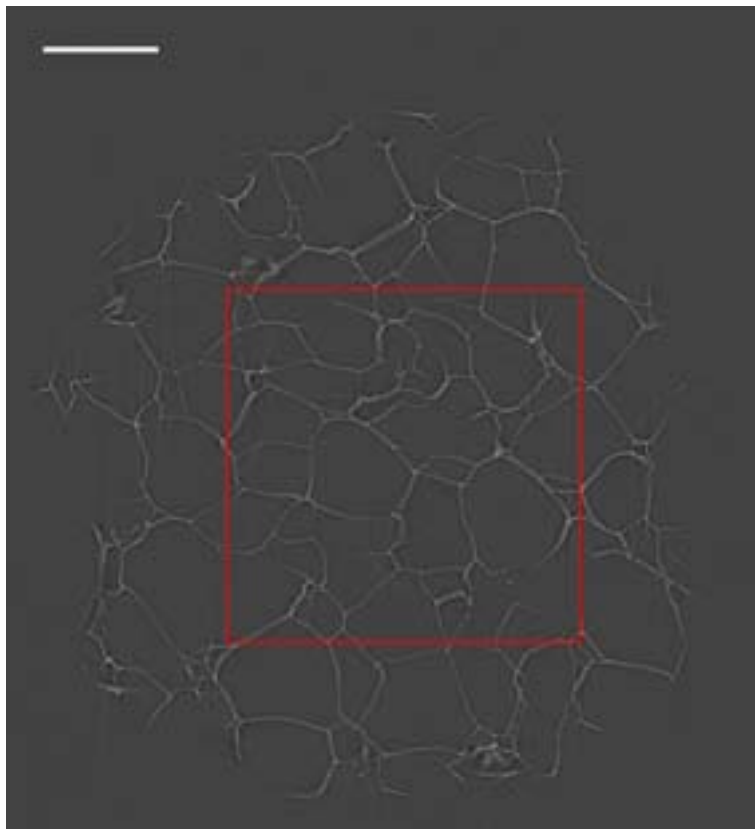


Figure 1. SR μ -CT of an alginate/hydroxyapatite bone tissue engineering scaffold (material courtesy of G. Turco, Department of Life Sciences, University of Trieste, Trieste, Italy). Top: reconstructed slice in which the selection of a Volume of Interest (VOI) is emphasized (the scale bar is 1 mm); bottom: 3D rendering of the extracted $2.7 \times 2.7 \times 2.7 \text{ mm}^3$ VOI with superposition of the skeleton of the porous phase. (Rendering performed using the commercial software VG Studio MAX).

throat size distribution as well as the degree of interconnectivity.

Three-dimensional imaging and quantitative analysis play an important role in the investigation of the internal structure of objects. The produced images require software and hardware tools able to handle and analyze huge image datasets directly in the 3D domain. The Pore3D SaaS is an effective solution for the

analysis of 3D images. More details as well as access policy and news about the evolution of the project can be found at the link <http://ulisse.elettra.trieste.it/uos/pore3d>.

References

- [1] F. Brun et al., *NIMA* **615**, 326 (2010).
- [2] G. Turco et al., *Biomacromolecules* **10**, 1575 (2009).

ELETTRA OPERATES IN TOP-UP MODE

E. Karantzoulis, A. Carniel, K. Casarin, S. Ferry, G. Gaio, F. Giacuzzo, S. Krecic, E. Quai, C. Scafuri, G. Tromba, A. Vascotto, L. Zambon

Sincrotrone Trieste S.C.p.A., Trieste, Italy

E-mail: Emanuel.Karantzoulis@Elettra.trieste.it

ODAC Accelerator Physics

Elettra, the 2/2.4 GeV third generation Italian light source, has successfully joined the synchrotron facilities that operate fully in top-up mode. Elettra has operated for users since 1994, but during the past few years a large upgrade programme has taken place. This has included the construction and start-up operation of a full-energy injector. The new injector chain and the other machine and beam line upgrades, together with the demands for intensity and thermal stability, naturally led to the change to top-up mode, in which frequent beam injections maintain a constant beam current in the storage ring during user operations. This is in contrast with the decay mode, where the stored beam is allowed to decay to some level before refilling occurs (Figure 1).

Elettra was not originally designed for this type of operation (and indeed even operated for many years without a full-energy injector). However, in May 2010, only a year after establishing the stable operations of the new injector, the storage ring began to work successfully with top-up at the two user energies of 2 GeV and 2.4 GeV. Elettra has thus become another example showing how a third-generation synchrotron that previously operated in decay mode can advance to full top-up operation, in this case at multiple energies.

With top-up operation the photon intensity produced at Elettra is stable and the integrated intensity is 60% higher over a time period equal to the beam lifetime. Thermal stability of the optical components of the beam lines also greatly improves, resulting in a higher integrated number of photons and gain in beam time for the experiments. At the same time the intensity-dependent electronics also remain stable, allowing submicron accuracy in the position of the electron beam and hence a higher stability of the photon beam.

Elettra's upgrade to top-up started in 2009 and included the addition of various diagnos-

tic and radiation-safety instruments, modification of the control and interlock software, fine tuning of the timing of the kicker and septa, as well as a revised operation strategy. A great deal of effort in collaboration with the radiation-protection team resulted in a high-level application with a "top-up controller" handling and controlling all aspects of the procedure [2]. Careful radiation measurements at each beam line under various conditions of the injected beam, together with the high injection efficiencies achieved at both energies, meant that no additional shielding was required for the beam lines. Radiation levels in all beam lines remain below 1 $\mu\text{Sv/h}$ for efficiencies higher than 90%.

The project for the full-energy injector started in 2005 and finished by providing beam in March 2008 on time and within budget [1]. The new injection chain consists of a 100 MeV linear accelerator and a 2.5 GeV booster that sends the beam into the storage ring at a rate of up to 3 Hz. The storage ring beam current at 2 GeV is set by the users to 300 mA and top-up occurs every 6 minutes by injecting 1 mA in about 5-8 s, thus keeping the current level constant to 3%. At 2.4 GeV the stored beam current is set to 140 mA and top-up occurs every 20 minutes, injecting 1 mA in about 5-8 s to maintain the current level constant to 7%.

The users have chosen fixed-current interval top-up (1 mA) instead of a fixed time interval. The injection system is perfectly tuned and for the majority of the beam lines does not produce interference with data-acquisition processes. A gating signal is also provided, but up to now only a few, very sensitive beam lines see some interference and therefore are gated.

The change to top-up mode required no transition period and once it began all went exceptionally smoothly, thanks to the very good preparation and the high level of expertise of

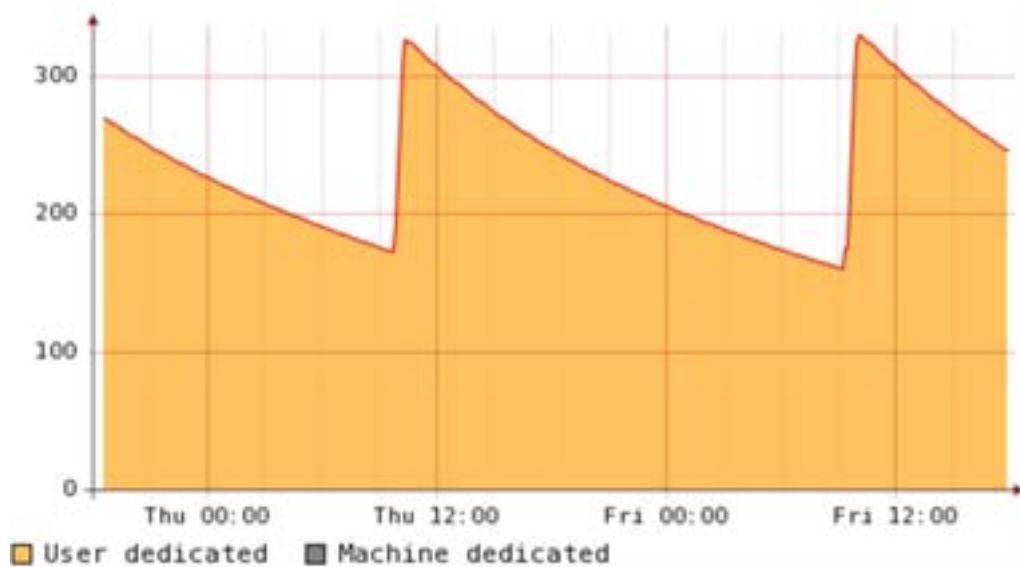
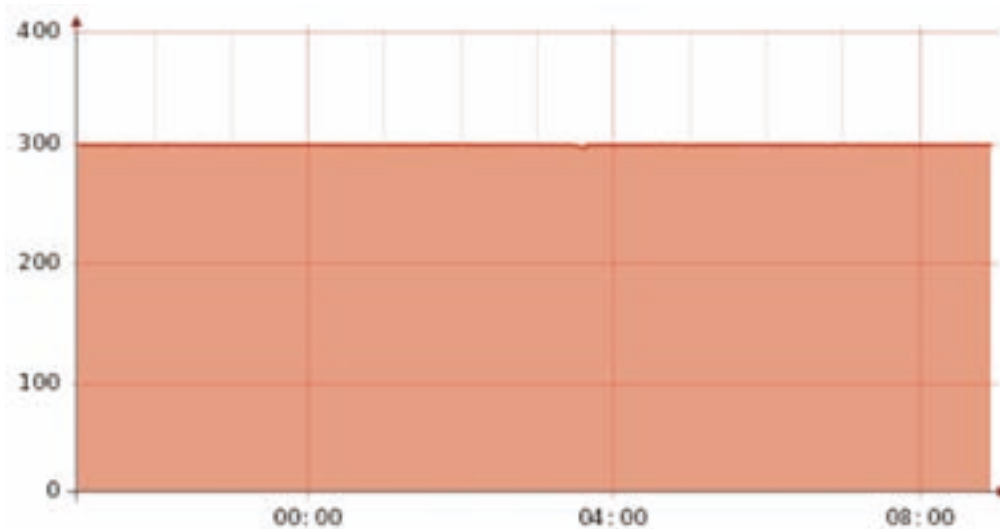


Figure 1. Beam current in decay mode (above) and top-up (below). Vertical axis: current in mA; horizontal axis: time in hours.



the personnel involved. Although at the beginning, the operation in top-up was programmed for 20% of users beam time, it became immediately clear that the users strongly preferred this mode and so Elettra has operated in top-up for 100% of the users-dedicated beam time right from the start, in May 2010.

References

- [1] M. Svandrlik, et al. “*Elettra new full energy injector status report*”, Conf. Proceedings, EPAC 2006, Edinburgh, Scotland.
- [2] E Karantzoulis, et al. “*Top-up Implementation and Operation at Elettra*”, Conf. Proceedings, IPAC 2010, Kyoto, Japan.

A PHOTOELECTRON VELOCITY MAP IMAGING SPECTROMETER FOR EXPERIMENTS COMBINING SYNCHROTRON AND LASER RADIATION

P. O’Keeffe¹, P. Bolognesi¹, M. Coreno¹, A. Moise², R. Richter², G. Cautero², L. Stebel², R. Sergo², L. Pravica³, E. Ovcharenko⁴, L. Avaldi¹

¹CNR-IMIP, Area della Ricerca di Roma 1, Monterotondo Scalo, Italy

²Sincrotrone Trieste S.C.p.A., Trieste, Italy

³The University of Western Australia, Perth, Western Australia

⁴Institute of Electron Physics, Uzghorod, Ukraine

E-mail: patrick.okeeffe@imip.cnr.it



GASPHASE
Instrumentation and Detectors
Laboratory

Photoelectron spectroscopy is one of the most widely used techniques in several fields of science from atomic and molecular physics to material science. Most of the technical developments in photoelectron spectroscopy have focussed on the improvement of energy resolution in both electrostatic analyzers and time of flight spectrometers. However a lot of information on the target and the process under investigation is given by the angular distribution of photoelectrons. Thus there is a need for electron spectrometers that combine high detection efficiency, reasonable resolution, and simultaneous measurement of the whole angular distribution. The velocity map imaging (VMI) technique [1] combined with two-dimensional detectors offers such a possibility. Velocity map imaging is based on the projection of 3D distributions of charged particles onto a position sensitive detector by inhomogeneous electrostatic fields (Fig. 1), which have the property of mapping particles of the same initial velocity to the same point on the detector, independently of the point within the interaction zone at which the particle was born. The original 3D distribution can then be reconstructed from this 2D projection by an inversion procedure, provided the distribution has cylindrical symmetry. An instrument designed specifically for pump-probe experiments combining synchrotron and laser radiation, where a velocity map imaging (VMI) spectrometer and an ion time of flight (TOF) spectrometer are mounted back-to-back, has been built at the Gasphase beamline [2]. The instrument allows photoelectrons to be detected over the entire solid angle with energy and angular resolution using the VMI spectrometer while simultaneously measuring ions with the TOF spectrometer. The VMI spectrometer is

equipped with a position sensitive detector designed and constructed at the Instrumentation and Detectors laboratory of Sincrotrone Trieste [3]. This detector consists of two resistively matched microchannel plates behind which is placed a cross delay line anode with two meander lines. The novelty is that the detector can be operated in two modes: a high spatial resolution mode and a coincidence mode. In the first mode, the data acquisition is internally triggered and the electronics works in multihit mode using the difference in time of arrival of the signals from either end of the delay lines in order to determine the position of arrival of the electron. In the second mode, on the other hand, the data acquisition is triggered by a pick-off pulse from the microchannel plates, and the position is determined by signals from only one end of the delay lines. The advantage of this second method is that electronics channels are freed up allowing the position to be recorded in coincidence with the arrival time of the ions at the TOF detector and with respect to the ring clock. This mode allows significant improvement in the signal to noise ratio for the detection of photoelectrons from two-colour experiments, where the frequency of the laser (83.3 MHz) is such that a laser pulse occurs every six synchrotron light pulses. This is clearly shown in figure 2 where the photoelectron images corresponding to the photoionization of aligned He 1s3p ¹P₁ atoms with laser light are shown. By gating the acquisition in a time bin of 500 ps around the laser pulse it is possible to eliminate 96% of the background.

The set-up, now operational at the beamline, has been successfully used to study the photoionization of polarized He, Ne [4] and Ar atoms as well N₂ molecules near threshold.

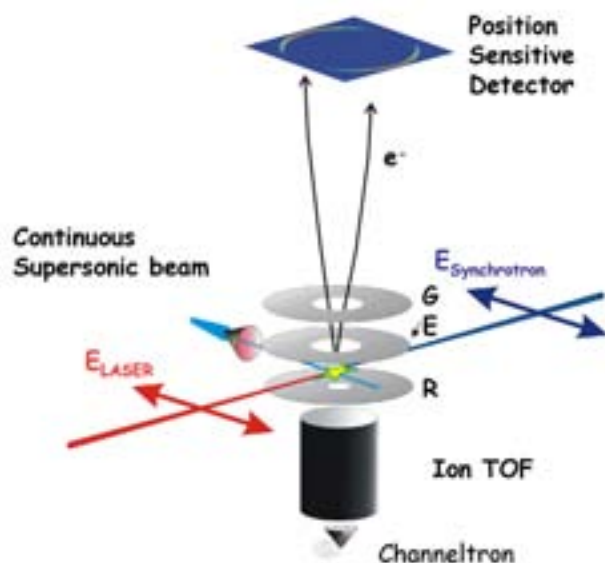


Figure 1. Schematic view of the geometry of the experimental setup. The polarization of the synchrotron light and the polarization of the Ti:Sapphire laser (double arrows) are parallel to each other and the beams are counter-propagating. The electrodes are labelled as follows: R – repeller, E – extractor, G – ground.

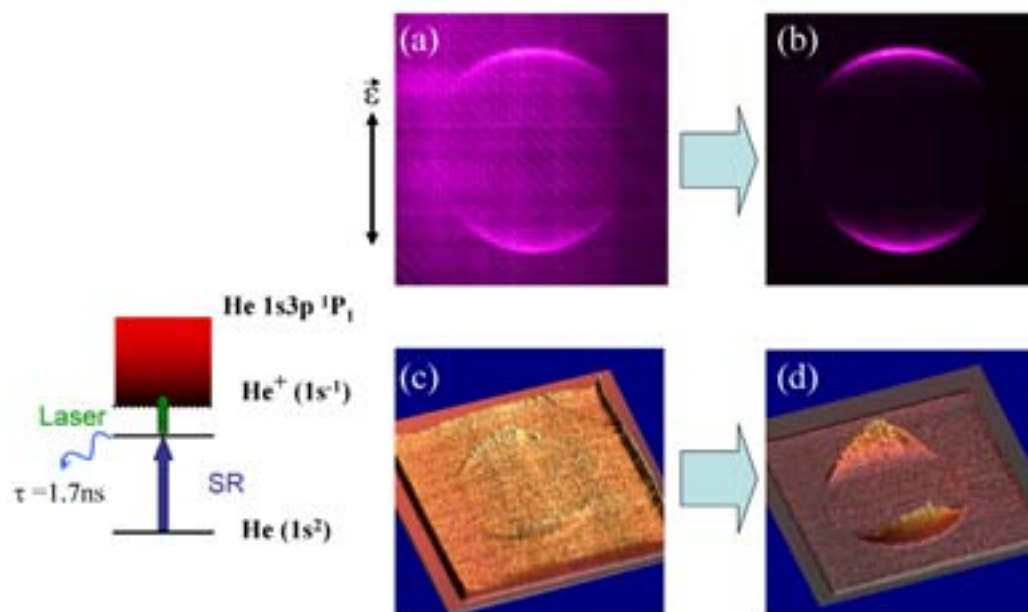


Figure 2. Raw photoelectron images corresponding to the photoionization of aligned He 1s3p 1P_1 atoms with laser light of wavelength 698.5 nm thus producing electrons of 275 meV kinetic energy. The schematic of the process is shown on the left panel. Image (a) is the time integrated image while image (b) is the time-gated image with a laser-on bin of 500ps. Images (c) and (d) are 3D representations of the images. This representation illustrates more clearly the signal to noise ratio of the unfiltered and filtered images.

References

- [1] D.H. Parker and A.T.J.B. Eppink, *J. Chem. Phys.* **107**, 2357 (1997).
- [2] P. O’Keeffe, P. Bolognesi, M. Coreno, A. Moise, R. Richter, G. Cautero, L. Stebel, R. Sergo, L. Pravica, E. Ovcharenko, L. Avaldi, *J. Phys. Conf. Series* **235**, 12006 (2010).
- [3] G. Cautero, R. Sergo, L. Stebel, P. Lacovig, P. Pittana, M. Predonzani and S. Carrato, *Nucl. Instrum. Methods A* **595**, 447 (2008).
- [4] P. O’Keeffe, P. Bolognesi, M. Coreno, A. Moise, R. Richter, G. Cautero, L. Stebel, R. Sergo, L. Pravica, E. Ovcharenko, L. Avaldi, *Phys. Rev A* (2010) accepted for publication.

THE SCIENTIFIC COMPUTING INFRASTRUCTURE OF THE LABORATORY

F. Billè, F. Bonaccorso, R. Borghes, V. Chenda, A. Curri, D. Favretto, G. Kourousias, G. Passos, M. Prica, R. Pugliese, M. Turcinovich

Sincrotrone Trieste S.C.p.A., Trieste, Italy

E-mail: roberto.pugliese@elettra.trieste.it

SCIENTIFIC COMPUTING

Elettra and FERMI@Elettra, with their hosted beamlines, labs, and experimental stations are large scientific data producers. An intelligent e-Infrastructure is required to effectively manage such ever-growing data streams. Its design, presented here, is the result of a tight interdisciplinary collaboration between computer specialists and experimental scientists.

The Scientific Computing team (SciComp) of Sincrotrone Trieste has substantial experience in Grid & Cloud Computing, Imaging, Control Systems, Enterprise Resource Planning (ERP), e-Science, and the so called e-Infrastructure. It has a prominent presence in Regional, National, European and International projects [1,2]. The SciComp team's experience and know-how, together with that of the Information Technology Group, is part of the technological offering of Sincrotrone Trieste SCpA.

The available computing infrastructure (as of November 2010) includes:

- Two state-of-the-art High Performance Computing Clusters equipped with InfiniBand® and over 250 Processor Cores.
- An Interactive computing Cluster with about 40 Processor Cores.
- A Cloud system, with a growing number of cores (presently 30) that can be dedicated to specific tasks. The system is highly available, meaning that it can work even in the event of failure of some nodes.
- A reliable High Speed storage system with about 60TB based on the SAN technology, expandible up to over 1000TB (1PB).
- Various 3D Stereoscopic technologies and hardware equipment, including GPGPU-ready systems.

These resources are easily accessible by the users via a Web portal equipped with advanced technologies: the Virtual Control Room (VCR) and the Instrument Element (IE). The former is a Grid & Cloud access-point with virtual collabora-

tion features and integration tools. The Instrument Element allows the integration of instruments and sensor resources with the computing infrastructure [3] resources (clusters and storage systems).

The team believes that all the complex details and technicalities of the computing infrastructure should be completely hidden, letting the Scientist concentrate only on his/her job: doing science. To achieve that, users and beamline scientists can sign on to one of the available scientific computing gateways simply by using their VUO account (the VUO - Virtual User Office - is a pioneering SciComp development). The portal enables the remote and secure operation of the beamline and of the experimental station, access the raw datasets, and initiate their processing in parallel with their acquisition.

Many applications are currently available and many other can be easily integrated [4]. For example, *GridRingRem* is an online application that performs an advanced post-processing ring artifact filtering on Tomographic reconstructions for SYRMEP and Tomolab. Using the VCR the user can select the dataset to process and the number of worker nodes the application will compute on. *PSGen* is an online application that generates Computerized Tomography Sinograms in parallel with the x-ray CT scan. It has an advanced infrastructure that uses the Instrument Element plus the TANGO Distributed Control System for its steering. *Crudo* is a specialised Data converter and format verifier for the SYRMEP beamline. It implements a fast Lempel-Ziv-Welch compression pipeline and exports a beamline specific unsigned 16bit output.

Current challenges are to use the scientific computing infrastructure to build an effective scientific data infrastructure [5] and to solve the related problems of data format standardisation, automatic metadata association, data management and curation.



Figure 1. Integrating instruments and detectors in the e-Infrastructure.



Figure 2. Applications on the Scientific Computing Gateway.

References

- [1] <http://www.gridcc.org/>
- [2] <http://www.dorii.eu/>
- [3] R. Pugliese, M. Prica, G. Kourousias, A. Del Linz, A. Curri, *Comp. Methods Sci. and Technol.* **15** (2009).
- [4] R. Borghes, R. Pugliese, G. Kourousias, A. Curri, M. Prica, A. Del Linz *The Grid as a Software Application Provider in a Synchrotron Radiation Facility*, Signals and Communication Technology, Springer, 2010.
- [5] <http://www.pandata.eu/>

ANGLE RESOLVED PHOTOEMISSION SPECTROSCOPY AND IMAGING WITH SUB- μM PROBE AT SPECTROMICROSCOPY-3.2L BEAMLINE

P. Dudin, P. Lacovig, C. Fava, E. Nicolini, A. Bianco, G. Cautero, A. Barinov

Sincrotrone Trieste S.C.p.A., Trieste, Italy

E-mail: alexey.barinov@elettra.trieste.it



SPECTROMICROSCOPY

The beamline started its operation in 1999 with the main goal of performing scanning photoelectron microscopy in the vacuum ultra violet range [1]. Here we report on the first results of the implementation of the new experimental end station, which began in 2007. The principal instruments developed for the upgrade are a Schwarzschild objective (SO) for 27 eV photons (designed at *Elettra* and built at the *Fraunhofer Institute for Applied Optics and Precision Engineering*) and an internal hemispherical electron energy analyzer, mounted on a precision goniometer that allows varying of polar and azimuthal acquisition angles (designed at *Elettra* and built by *Elettra* and *Cinel Spa*). An additional feature of the new experimental chamber is the possibility to choose between two objectives, designed for two different photon energies, without breaking vacuum.

We evaluated the performance of three available SO objectives: the original two for 95 eV and 74 eV, together with the new one for 27 eV (see figure 1). One of the principal problems of the previous configuration with the 95 eV SO was coherent enhancement of non-specular reflection from multilayer optics [2] resulting in a few-millimeter halo of scattered light around the focal point. The measured background levels due to such reflection are 50%, 22%, and less than 1% respectively for the 95 eV, 74 eV, and 27 eV SOs. The 74 eV SO has even lower background (12%) if measured with the electron analyzer. Accordingly, the present configuration is composed of 27 eV and 74 eV objectives. The intermediate focus of $\sim 10 \mu\text{m}$ size formed by beamline optics is further demagnified by the SO and the final beam spot size on the sample is $\sim 600 \text{ nm}$. The imaging of the sample is performed with a scanning stage designed and built at *Elettra* and equipped with *Galil inc.* drivers

and *Phytron inc.* stepper motors providing accelerations of up to 5 mm sec^{-2} and ultimate speeds of up to $280 \mu\text{m sec}^{-1}$ in close loop mode realized with *Renishaw plc* linear travel encoders of 100 nm precision.

The electron analyzer operates in two principal regimes: wide acquisition angle (WA) and small angle (SA). WA mode is used for angle-integrated spectroscopy and provides high count rates ($2\text{-}3 \times 10^5 \text{ counts sec}^{-1}$ at Pass Energy=10 V) during the measurements whereas SA is used for angle resolved spectroscopy. Presently, angular resolution in SA is limited to the electrons selected from a small $\pm 0.5^\circ$ cone. The best total energy resolution of 33 meV was measured on the Fermi level of polycrystalline gold at 45 K temperature. The electrons are detected by a bi-dimensional "Z stack" Multi Channel Plate detector with overall 300×300 channels and only four signal cables to obtain a bi-dimensional information via the 'cross delay line technique' [3].

The measurements dedicated to the test of imaging and spectroscopy in angle resolved mode demonstrated the great potential of the instrument. In the first three images of figure 2 the contrast is due to rotation of single crystal flakes of highly oriented pyrolytic graphite. The sequence of three images is obtained from the different channels of the detector acquiring the photoelectrons with different binding energies at the same time. The high contrast level (white) corresponds to flakes in which the electronic band produces electron emission along the acquisition angle and within the energy window selected by the detector channels [4]. The band structure acquired from a single flake of graphite along ΓM and ΓK principal directions is shown in the last two panels.

The upcoming development for next year is a new lens column for the analyzer designed

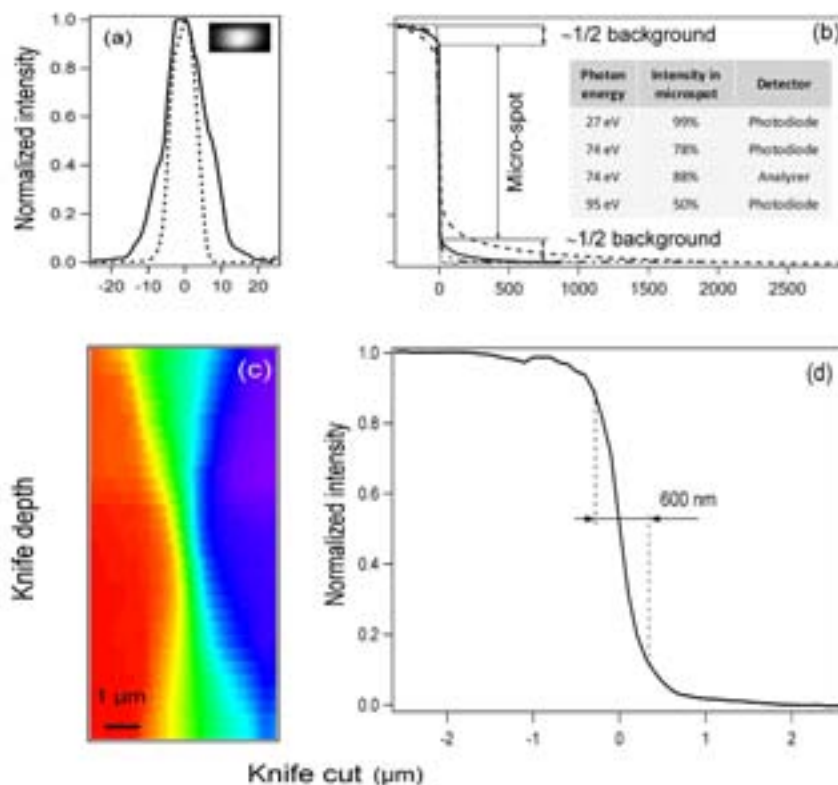


Figure 1. Microprobe characterization: (a) Differentiated horizontal (solid) and vertical (dashed) profiles acquired with moving blade at the intermediate focus position. Inset: micro-image of the spot. (b) Normalized long distance knife-edge profiles at SO focal plane, acquired with photodiode, showing the scattered background for 95 eV (dashed), 74 eV (solid) and 27 eV (dotted) SOs; a profile acquired with photoelectron analyzer, for 74 eV SO, is also shown for comparison (dash-and-dot). The inset table summarizes the percentage of overall intensity within the micro-spot, for different photon energies and acquisition types. (c) Series of knife-edge profiles at various positions along the beam axis near the optimum sample location. (d) Knife edge profile in the best focus. (Reproduced with permission of the International Union of Crystallography [4]).

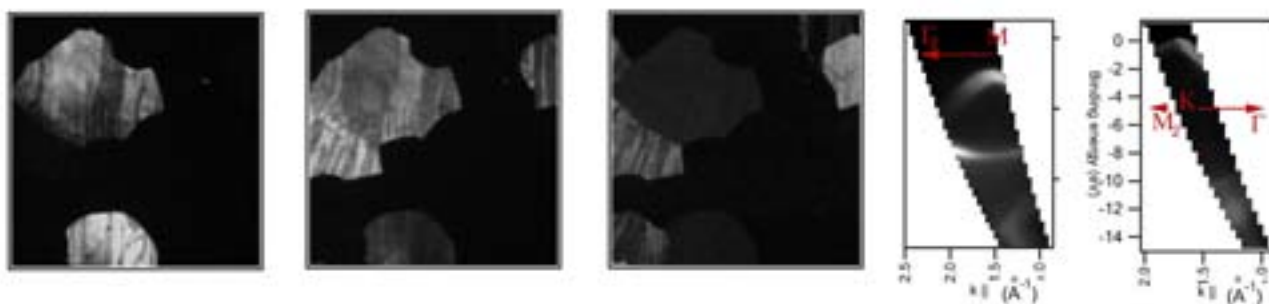


Figure 2. Sequence of three 200x200 μm^2 images obtained from highly oriented pyrolytic graphite, and two band structures. From left to right: photoelectrons with 0, 0.8, and 1.5 eV binding energy, with electron analyzer in SA mode ($h\nu=74$ eV); band structures along the ΓM and ΓK directions measured from a single flake ($h\nu=27$ eV) (Reproduced with permission of the International Union of Crystallography [4]).

for parallel acquisition of electrons originating from various angles so that the information from both dimensions of the analyzer detector (E and θ) will be obtained in a single shot. According to the simulations of the new lens column system the angular- and energy-resolution can be improved to $0.25 \times 0.1^\circ$ and 15 meV respectively.

References

- [1] F. Barbo et al, *Rev. Sci. Instrum.* **71**, 5 (2000).
- [2] S. Singh, H. Solak, F. Cerrina, *Rev. Sci. Instrum.* **67**, 1 (1996).
- [3] G. Cautero et al, *Nucl. Instrum. Methods Phys. Res. A* **595**, 447 (2008).
- [4] P. Dudin et al, *J. Synchrotron Rad.* **17**, 445 (2010).



FACTS & FIGURES

THE COMPANY

Sincrotrone Trieste S.C.p.A. began operations in 1987: it is a **non-profit Share Company** (Società Consortile per Azioni) recognised as being of national interest by a State Law, which manages the **Elettra Laboratory**. Elettra continues to update itself and grow. In addition to significant modernisation projects relating to beamline sources and other components, a new fourth generation light source, **FERMI@Elettra**, is under construction alongside the original one.

Elettra is an Associate Laboratory of the International **Atomic Energy Agency (IAEA)** of Vienna, and forms a key node in the science and technology network of the **Central European Initiative (CEI)**.

It participates in more than twenty projects within the EU Framework Programme for Research and Development, and is the coordinator of the **Integrated Infrastructure Initiative (I3) "ELISA"**, bringing together 17 research infrastructures around Europe. This corresponds to the world's largest network of synchrotrons and FELs facilities, acting as a consortium.

On its site Elettra hosts the **National Laboratory TASC** (IOM-CNR), a facility for micromanufacturing and nanoscience. It has also established enduring working relationships with important Italian and foreign institutions, including various **CNR** (National Research Council) bodies, the **Academies of Science of Austria** and the **Czech Republic**, UNESCO's International Centre of Theoretical Physics (**ICTP**), the International School of Advanced Studies (**SISSA**), and the **Universities** of Milano, Trento, Trieste and Udine. These partners are actively contributing to the construction and operation of beamlines and support laboratories.

Elettra's scientific and technical quality and developments are constantly monitored by board-appointed international Committees which advise on all relevant aspects of the general and development policy, scientific programs, accelerator development, technology transfer and industrial applications.

SHAREHOLDERS

- > AREA Science Park Consortium (51%)
- > Autonomous Region of Friuli Venezia Giulia (40%)
- > IOM-CNR (Istituto per l'Officina dei Materiali of the Italian National Research Council) (5%)
- > The national Agency for inward investment promotion and enterprise development (4%)

ALLIANCES AND PARTNERSHIPS

- > IAEA (International Atomic Energy Agency)
- > CEI (Central European Initiative)
- > IRUVX-EuroFEL (European Consortium for FELs up to the UV/softXray)
- > Austrian Academy of Sciences
- > Academy of Sciences of the Czech Republic
- > CNR (Consiglio Nazionale delle Ricerche – Italian National Research Council)
- > CNRS (Centre National de la Recherche Scientifique – French National Research Council)
- > ICTP - UNESCO (International Centre for Theoretical Physics)
- > Indian Institute of Science, Bangalore
- > Institut für Festkörperforschung Forschungszentrum Jülich
- > INSTM (Consorzio Interuniversitario Nazionale per la Scienza e Tecnologia dei Materiali – National Inter-University Consortium for Materials Science and Technology)
- > INFN (Istituto Nazionale di Fisica Nucleare National Institute of Nuclear Physics)
- > ISAS (International School of Advanced Studies)
- > Charles University, Prague
- > University of Nova Gorica
- > University of Milano – Bicocca
- > University of Trento
- > University of Trieste
- > University of Udine

Sincrotrone Trieste S.C.p.A. is managed by a **Board of Directors**, assisted by a shareholder-appointed **Board of Auditors**, and advised by board-appointed international committees such as the **Council of Partners** for general and development policy, the **Scientific Advisory Council** for scientific programs, the **Machine Advisory Committee** for accelerator development, and the **Industrial Advisory Panel** as far as technology transfer and industrial applications are concerned.

Machine Advisory Committee (MAC)

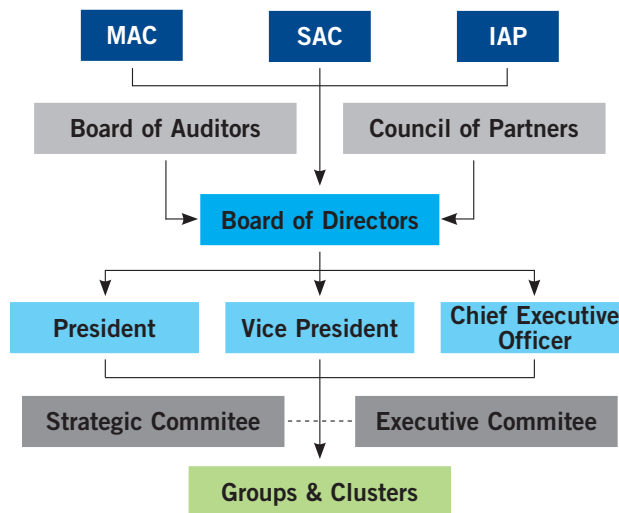
Chairman: Richard P. Walker
 Paul J. Emma
 Mikael Eriksson
 Jerome Hastings
 Carlo Pagani
 Claudio Pellegrini
 Mike Poole
 Robert W. Schoenlein

Scientific Advisory Council (SAC)

Chairman: Ingolf Lindau
 David Attwood
 Gordon Brown
 Charles S. Fadley
 Robert Huber
 Sine Larsen
 Dietrich Menzel
 Charles V. Shank
 Friso van der Veen

Industrial Advisory Panel (IAP)

Chairman: Alberto Sangiovanni-Vincentelli
 Carlo Castellano
 Enrico Albizzati
 Maurizio Arienzo
 Mauro Ferrari

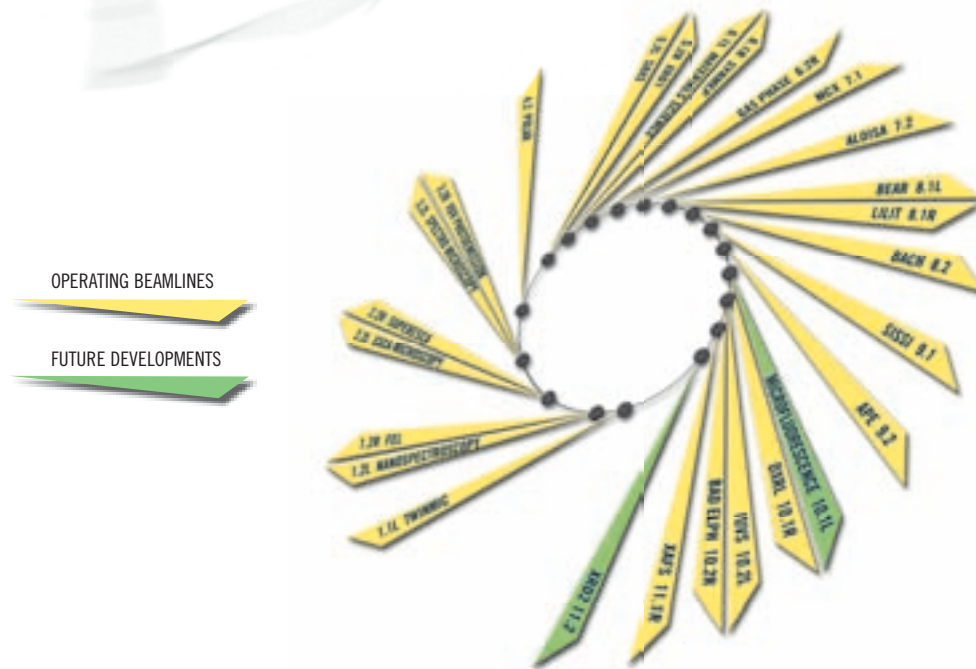


Board of Auditors
Chairman: Fabio Matarazzo
 Nicola Archidiacono
 Claudio Sambri
 Paolo Marchesi
 Ugo Braico

Board of Directors
President: Carlo Rizzuto
Vice President: Giovanni Comelli
Chief Executive Officer: Alfonso Franciosi
 Roberto Della Marina
 Marcello Fontanesi
 Gemma Ravizza
 Giorgio Rossi
 Giorgio Sulligoi
 Alessandro Trovarelli

Council of Partners
President: Carlo Rizzuto
 Fabio Barbone
 Stefano Fantoni
 Alain Fontaine
 Marcello Fontanesi
 Dante Gatteschi
 Peter Laggner
 Vladimir Matolin
 Claudio Tuniz

BEAMLINES AND USERS



BEAMLINES			source *	energy range (eV)	partner institutions
1.1L	TWINMIC	A multipurpose twin X-ray microscopy beamline for improving life conditions and human health	short id	250 - 2000	
1.2L	Nanospectroscopy	SPELEEM and LEEM-PEEM end-station	id	50-1000	IFF Jülich (from 2011)
1.2R	FEL	European Free-Electron Laser project	id	1,8 - 9,5	
2.2L	ESCA Microscopy	Scanning PhotoElectron Microscopy (SPEM)	id	200-1400	
2.2R	SuperESCA	Fast and High Energy Resolution Photoemission and Absorption Spectroscopy	id	85 - 1500	
3.2L	Spectro Microscopy	Angle-Resolved Photoemission microscope	id	27 - 95	
3.2R	VUV Photoemission	Angle-Resolved PhotoElectron Spectroscopy (ARPES) in the VUV range	id	16 - 1000	ISM-CNR
4.2	Circular Polarization	Dichroic measurements on chiral systems	id	5 - 1000	ISM-CNR
5.2L	SAXS	Small Angle X-Ray Scattering	id	8000 - 16000	IBM-ÖAW (A)
5.2R	XRD1	X-ray Diffraction	id	4000 - 22000	IC-CNR
6.1L	Materials science	Photoemission and X-ray absorption	bm	40 - 800	ASCR, Charles University of Prague (CZ)
6.1R	SYRMEP	SYnchrotron Radiation for MEDical Physics	bm	8000 - 35000	UNITS
6.2R	Gas Phase	Research on gaseous systems	id	14 - 1000	IMIP-CNR, IOM-CNR
7.1	MCX	Powder Diffraction Beamline	bm	2100 - 23000	UNITN, INSTM
7.2	ALOISA	Advanced Line for Overlayer, Interface and Surface Analysis	id	120 - 8000	IOM-CNR
8.1L	BEAR	Bending magnet for Emission Absorption and Reflectivity	bm	4 - 1400	IOM-CNR
8.1R	LILIT	Laboratory for Interdisciplinary LITHography	bm	1000 - 5000	IFN-CNR, IOM-CNR
8.2	BACH	Beamline for Advanced DiChroism	id	35 - 1600	IOM-CNR
9.1	SISSI	Source for Imaging and Spectroscopic Studies in the Infrared	bm	0,001 - 3	
9.2	APE	Advanced Photoelectric Effect experiments	id	10-2000	IOM-CNR
10.1L	X-ray microfluorescence	X-ray microfluorescence	bm	4000 - 20000	
10.1R	DXRL	Deep-etch Lithography	bm	2000 - 20000	
10.2L	IUVS	Inelastic Ultra Violet Scattering	id	11-2008	
10.2R	BAD Elph	Low-energy Angle-Resolved PhotoEmission Spectroscopy (ARPES)	id	4 - 25	
11.1R	XAFS	X-ray Absorption Fine Structure	bm	2300 - 25000	ICTP
11.2	XRD2	X-ray Diffraction	id		IIS Bangalore

source* id = Insertion Device (wiggler or undulator)
bm = bending magnet

The **Proposal Review Panel** is a panel composed of senior scientists active in different scientific fields and appointed by the Elettra laboratory management with the aim of evaluating the general User's proposals. The panel is divided into seven subcommittees.

The Proposal Review Panel meets twice a year, gives a written report for each proposal submitted for the ongoing semester and gives suggestions for **beamtime** allocation at the beamlines open to the users.

Atoms, Molecules & Plasmas

Svante Svensson (Chairman)
Vincenzo Aquilanti
Uwe Becker
John M. Dyke

Scattering

Paolo Mariani (Chairman)
Stephanie Finet
Daniele Fioretto
Hermann Franz
Giulio Monaco

Catalytic Material/Surface Science

Carlo Mariani (Chairman)
Maria Carmen Asensio
Karol Hricovini
Adam Fraser Lee
Falko P. Netzer
Michèle Rose Sauvage-Simkin

Hard condensed matter - Structures

Maurizio Benfatto (Chairman)
Robert Joseph Cernik
Paola D'Angelo
Marco Milanesio
Maria Grazia Proietti

Proposal Review Panel

Dipankar Das Sarma
(Chairman)

Condensed matter Electronic & Magnetic Structure

Dipankar Das Sarma (Chairman)
Mark Golden
Giorgio Margaritondo
Danilo Pescia
Maurizio Sacchi

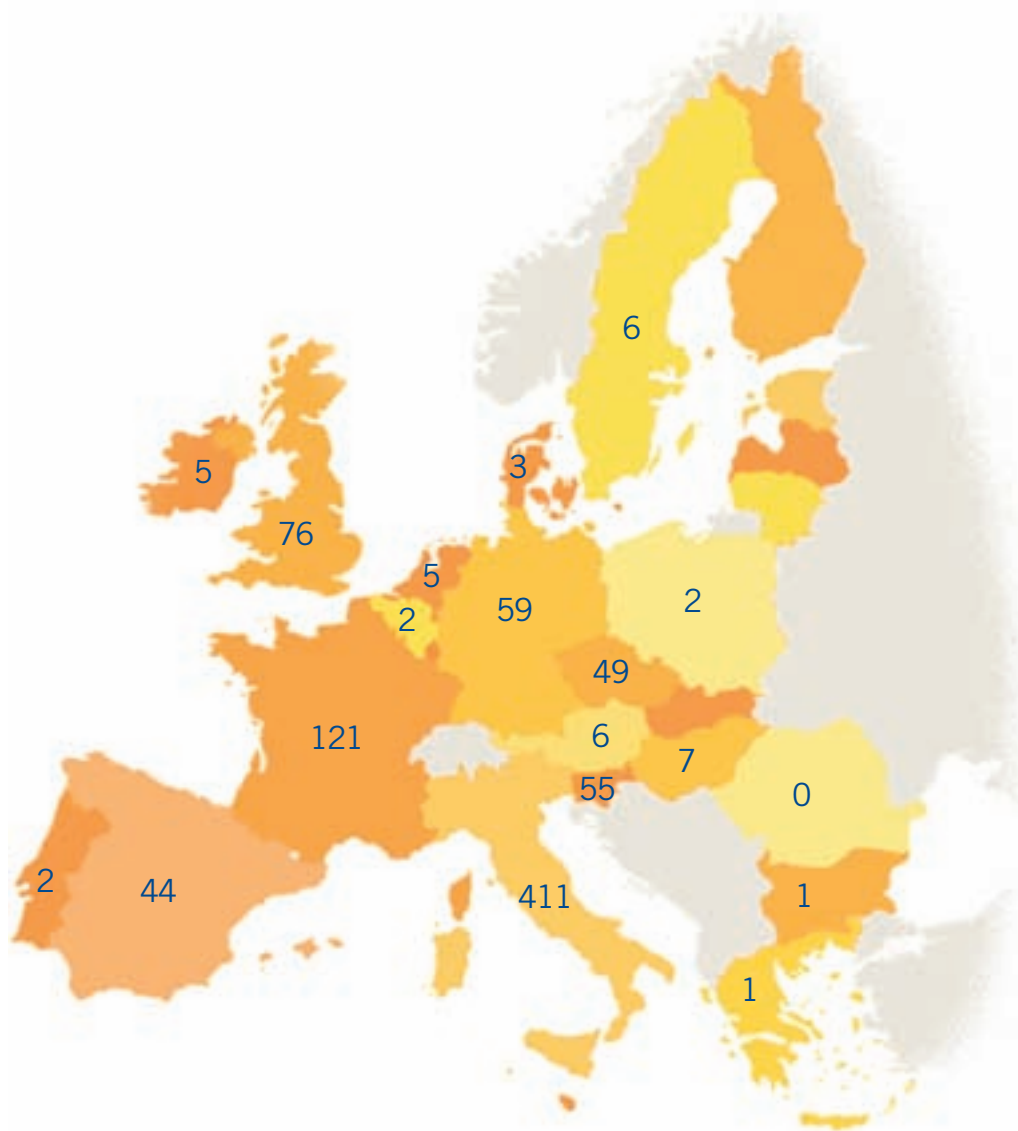
Protein & Macromolecular Crystallography

Giuseppe Zanotti (Chairman)
Peter Brick
Dusan Turk
Luigi Vitagliano

Instrumentation & Technological materials Life and Medical Sciences (excluding Crystallography) Polymers and Soft Matter

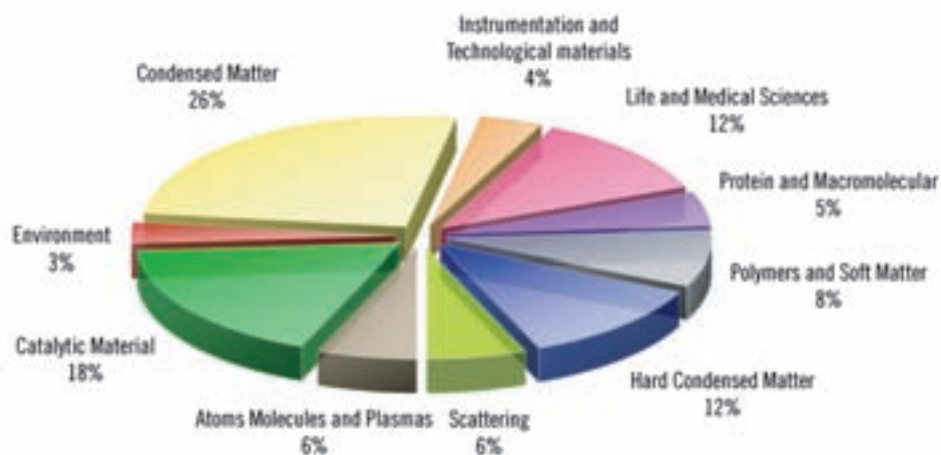
Graeme Morrison (Chairman)
Alberto Bravin
Gianfelice Cinque
Paul Dumas
Christopher Hall
Lisa Miller
Günther Schmahl
Andrew Smith
Stephen William Wilkins

USERS AT ELETTRA: TOTAL = 1052 (July 2009 - June 2010)

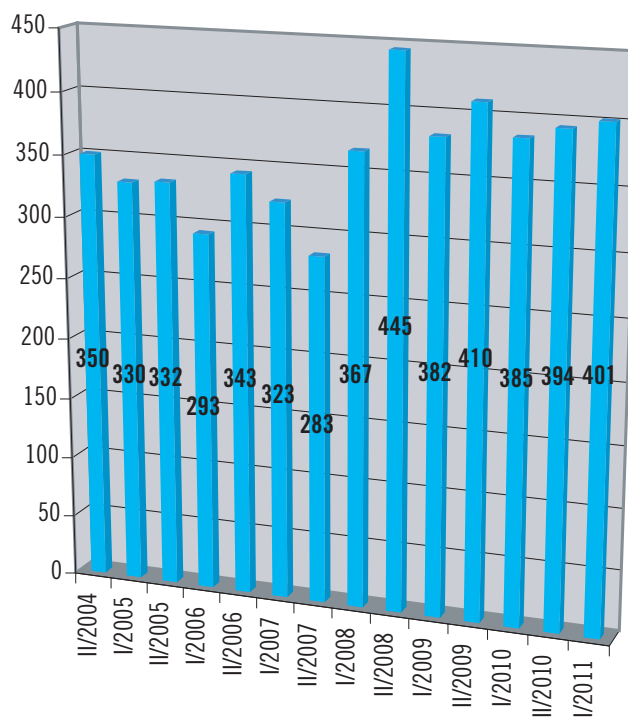


Switzerland 16	Japan 8
Canada 9	China 4
USA 30	Thailand 6
Cuba 2	Sri Lanka 3
Brazil 1	Australia 7
Argentina 1	India 60
Croatia 38	Pakistan 3
Russian Fed. 2	Israel 4
South Africa 3	

ALLOCATED PROPOSALS BY RESEARCH AREA: TOTAL = 438 (July 2009 - June 2010)



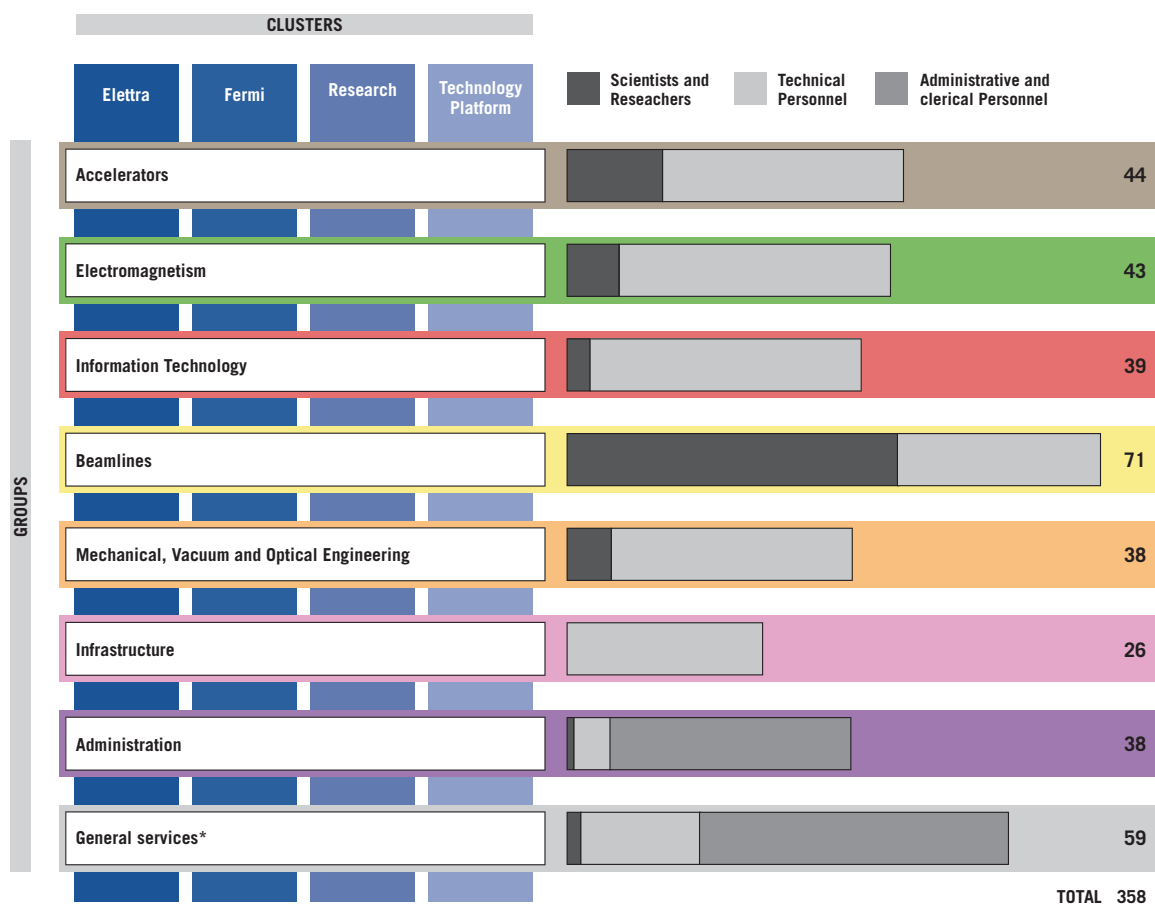
2004 - 2011 PROPOSALS SUBMITTED BY SEMESTER



From October 1st, 2007 to March 2nd, 2008 the Elettra light source was closed due to the booster installation.

STAFF

Sincrotrone Trieste has adopted a matrix-type of organization. The four Strategic Initiatives correspond to and are implemented through four **Clusters** of different **Projects**, grouped together based on the complementarity of the different project goals. The human and instrumental resources required by the different projects are managed within eight **Groups** of staff members with similar or related expertise.



* including personnel, legal, industrial liaison, users offices, etc.

FINANCIAL FIGURES

BUDGET ALLOCATION FOR 2010

Running costs	
General costs	€ 10.067.766
Personnel	€ 10.801.938
Utilities	€ 5.504.115
Accelerator group	€ 92.116
Administration group	€ 249.742
Beamlines group	€ 816.151
Coordination group	€ 1.049.596
Electromagnetism group	€ 138.285
IT group	€ 235.051
Infrastructure group	€ 885.814
Mechanical, Vacuum and Optical engineering	€ 225.982
Industrial Liason Office operation	€ 697.602
Scientific partnerships	€ 350.000
OPAC	€ 790.000
Development projects	€ 3.862.338
Total Ordinary operation	€ 35.766.496
Special projects	
FERMI	€ 26.443.999
Total special projects	€ 26.443.999
GENERAL TOTAL	€ 62.210.495

PROJECTS / SPONSORED RESEARCH

The last two calendar years, 2009 and 2010 (not yet concluded), were extremely successful in attracting resources from external funding institutions: the contributions acquired through research contracts amount to more than 3.6 million Euro in 2009 and more than 2.7 million Euro in the first eight months of 2010.

Among the newly approved initiatives, especially noteworthy is the CITIUS project, supported by the Italy-Slovenia cross-border cooperation programme 2007-2013: the project ranked second out of 27 applications submitted within Priority Axis 2 (Competitiveness and knowledge based society). This cooperation programme is funded under the European Territorial Cooperation Objective of Cohesion Policy 2007-2013: this regional dimension of territorial cooperation is of highest importance in the European Commission agenda as well as in Elettra's plan for the consolidation of international partnerships.

Elettra's solid record as a key player in the landscape of European science policy is further highlighted by its role of coordinator of the presently running ELISA (European Light Sources Activities) I3 (Integrated Infrastructure Initiative) of the European synchrotrons and FELs. As a result of the good management of ELISA, Elettra has been appointed by the project partners to act as coordinator also within the application for the follow-up I3, CECILIA (Coordinated European Centers for Innovative Light Applications), that is in preparation for submission under call FP7-INFRASTRUCTURES-2011-1 at the time of this writing.

During the last 12 months, Elettra participated in 38 research contracts (see table) funded by the following external agencies: European Commission, Italian Ministry of Research, Italian Ministry of Foreign Affairs, Region of Friuli – Venezia - Giulia, International Centre for Theoretical Physics, Indian Department of Science and Technology.

EUROPEAN/INTERNATIONAL RESEARCH CONTRACTS

Name	Short name	Coordinator
Light Source Theory Network	LighTnet	STFC, United Kingdom
ICTP-Elettra Users Programme		Elettra
Transnational access of the Indian scientists to the Elettra beamlines		Elettra
Conservation materials for stained glass windows - assessment of treatments, studies on reversibility, and performance of innovative restoration strategies and products	CONSTGLASS	Fraunhofer-Institut für Silicatiforschung, Germany
Deployment of Remote Instrumentation Infrastructure	DORII	PSNC, Poland
Preparatory Phase of the IRUVX-FEL Consortium	IRUVX-PP	DESY, Germany
TIME-Resolved Spectroscopy of Nanoscale Dynamics in Condensed Matter Physics	TIMER	Elettra
Realising and Managing International Research Infrastructures	RAMIRI	Imperial College of Science, United Kingdom
Research Infrastructures: Foresight and Impact	RIFI	UEFISCSU, Romania
European Light Sources Activities – Synchrotrons and Free Electron Lasers	ELISA	Elettra
Maximizing Synergies for Central European Biotech Research Infrastructures	SynBIOsis	JIC, z.s.p.o., Czech Republic
CEI Research Fellowship Programme	CERES	INCE - Central European Initiative, Italy
Notte dei ricercatori 2009	PROSIT	University of Trieste, Italy
PaN-data Europe Strategic Working Group	PaN-data Europe	STFC, United Kingdom
Science in Trieste And Researchers	STAR	University of Trieste, Italy
Realising and Managing International Research Infrastructures 2	RAMIRI 2	Elettra

NATIONAL RESEARCH CONTRACTS

Post-Genomic Structural Biology: Developing Infrastructures for Protein Crystallography	Structural biology	Elettra
FERMI@Elettra - Phase I		Elettra
High efficiency innovative light sources for solid state illumination devices with civil and automotive applications	LUCI	CNR
FERMI@Elettra - Phase II		Elettra

REGIONAL/CROSS BORDER RESEARCH CONTRACTS

Realization of a technological platform for the crystallographic analysis of biological macromolecules of biomedical interest for the industrial research	DAGEAS	Elettra
Study of hybrid organic/inorganic interfaces for strategic applications in the field of flexible displays and biochips	Nano-BioSOLEd	Elettra
Study and realization of prototype platforms for plane and helical undulators		Elettra
Development and realization of solid state ultrafast laser amplifiers optimized for FEL applications	FEMTOREG	Elettra
Distributed environment monitoring based on Grid	MADBAG	Elettra
Anti Counterfeiting Tags	ACT	Elettra
Development of chemical sensors for environmental and biological diagnosis based on nanowires and nanotubes	AMBIOTEN	Elettra
New conjugated polymers for plastic photovoltaic cells	Plastic photovoltaic cells (Sister II)	Area Science Park
Studies on the decay mechanisms of nanomaterials and their potential dangers in biological systems	NANOTOX	Elettra
Studies and characterization of high power X-band (12 GHz) radiofrequency devices	X-BAND	Elettra
Study of a femtosecond timing system for new synchrotron light sources	SYRATIM@FS	Elettra
Dynamics of macromolecular and biological systems via Raman spectroscopy with ultrashort pulses	MASPERA	Elettra
Study of a photoinjector capable of supplying very high brilliance, 50 Hz pulsed, beam	HiBEGuS	Elettra
Interregional Centre of Ultrafast Photonic Technologies for Spectroscopy	CITIUS	University of Nova Gorica, Slovenia
Definition of protocols for the production of inks based on the technology "Invisible"	Sister LiF	AREA Science Park
Development of a digital Direct Current Current Transformer (DCCT) system for the measurement of direct current with a resolution, accuracy and stability of few parts per million	Sister DCCT	Area Science Park
Imaging - Service Oriented Infrastructure	I-SOI	Elettra
User-friendly domotic systems based on smart lighting devices	EASYHOME	Centro Ricerche Plast-optica S.p.A.

TECHNOLOGY TRANSFER AT ELETTRA

The Industrial Liaison Office (ILO) was started in 2004 to promote the exceptional body of skills and technical expertise resulting from the experience accumulated in the construction and operation of the Elettra facilities over time.

Sincrotrone Trieste S.C.p.A. ILO supplies advanced instrumentation to other Synchrotron Facilities and Research Laboratories, and provides products and services to private companies operating in different fields: mechanics, optics, pharmaceutical, microelectronics, energy, chemistry, agricultural and foodstuff, etc.

Last year, a new web site, specifically dedicated to Sincrotrone Trieste Technological Resources and Services for Industrial Applications, has been launched.

A section is dedicated to four product classes designed in our laboratory:

Accelerator Parts, such as RF resonant cavities and Low Level RF Electronic Units;

Detectors, photon and charged-particle detectors based on centroid finding techniques – such as (cross) delay anode detectors – or based on multi-channel acquisition, employed in several Elettra beamlines; ionization chambers and beam position monitors used to characterise photon and electron beams;

Lab Instruments, picoammeters with high sampling frequency and other devices developed in our Laboratory, such as charge pulse amplifiers and high voltage pulse generators;

Power Supply equipment, such as high voltage bipolar power supply systems especially suited for benders of X-ray bimorph mirrors or bipolar DC/DC current-controlled digital power supplies.

A section dedicated to services presents several analysis and measurements performed in our laboratory. The same examples are also illustrated in the new promotional video, available on our You Tube Channel.

Recently the new **AH-501 picoammeter** has been developed. The device has been designed to achieve very high sensitivity and fast sampling rates, with the best low-noise performance for this class of instruments.

(See next page for a technical description)

A new **advanced four channel time converter** has been developed too. This new device is highly suitable for time-resolved measurements.

(See next page for a technical description)

How to contact us:

Industrial Liaison Office
Sincrotrone Trieste S.C.p.A.
S.S. 14 - km. 163.5 in Area Science Park
34149 Basovizza - Trieste, Italy
Tel. +39 040 3758303 - Fax +39 040 3758623
Web link: ilo.elettra.trieste.it
Profile on linkedin: www.linkedin.com/companies/sincrotrone-trieste-s.c.p.a
YouTube Channel: www.youtube.com/Sincrotronetrieste

AH-501 FAST HIGH RESOLUTION BIPOLAR DIGITAL PICOAMMETER

The AH501 is a compact, fast and high resolution, wide-bandwidth, ultra-wide dynamic range picoammeter, with 4-channel simultaneous sampling inputs.

It consists of a specially designed transimpedance input stage for current sensing combined with several analog-signal-conditioning and -filtering stages that use state-of-the-art electronics.

This device performs bipolar current measurements from ± 2.5 nA (with a resolution of 298 aA) up to ± 10 mA (resolution of 1.35 nA) with sampling frequencies up to 26 kHz (for 1 channel and a 16-bit resolution) and 6.5 kHz (4 channels, 16 bit/sample).



The simultaneous sampling of the 4 independent channels makes this instrument ideal for beam position monitor applications or multichannel acquisition.

The AH501 is housed in a light and extremely compact box that can be placed close to the signal sources, in order to reduce cable lengths and minimize possible noise pick-up.

The picoammeter can be remotely controlled via a communication interface: range, data format, type of acquisition, baudrate and a lot of other parameters can be easily set and checked.

The AH501 picoammeter has a modular communication capability, which gives users the option to freely select among available communication modules: Ethernet (10/100 TCP/IP and UDP), USB 2.0, Wi-Fi, RS232 and RS422/485. This feature extends the communication capabilities to a wide range of protocols and interfaces, allowing instrument control with several programming languages and operating systems.

The AH501 has an external TRIGGER/GATE input signal to synchronize the acquisition of the picoammeter with external events (e.g. laser triggering).

FEATURES	APPLICATIONS
From ± 2.5 nA up to ± 10 mA current range	Fast Feedback applications
Up to 26 kHz sampling frequencies	4-quadrant beam position monitor
24 bit ADC converter	Ion Chamber flux monitoring
Less than 140fA @RNG2 full scale range noise	Photodiode acquisition
4-channel simultaneous sampling	Precision process control
Lightweight and compact design	Multichannel current acquisition
Modular communication interface including Ethernet 10/100 and USB	

THR-02-ST - ADVANCED 4-CHANNEL TIME CONVERTER

The *THR 02 ST 4-Channel time converter* is an instrument highly suitable for time resolved measurements. It consists of 4 independent multihit Time-to-Digital Converters (TDC) and 1 external trigger that can be used for synchronizing multiple events with time resolution up to 27 ps.

Every channel is coupled with a Constant Fraction Discriminator (CFD) that allows very low jitter measurements on a wide range of input pulse heights.

Continuous acquisition on all channels is available up to 10 MCounts/s, while in “burst acquisition” mode it is possible to get up to 400 MCounts/s.

The system can perform a selectable set of hardware elaborations and filters on the acquired data, before sending them to a PC through a fast PCIe connection. It hosts an Ethernet configurable FPGA that controls acquisition operations.

In one of its most popular configurations THR-02-ST is set up for either 1D or 2D delay lines detectors, and provides, for each detected particle, the position as well as the arrival time with respect to any external event.

Alternatively, the system may be connected to any independent signal, for time resolved measurements, such as pump-and-probe or coincidence experiments, as well as time of flight (TOF) acquisitions.

An auxiliary input is available upon request in order to best comply with pump-probe measurements. Control/acquisition LabVIEW drivers are also provided.



FEATURES

- Multihit acquisition during time window
- Configurable time window range (100ns to over 100us, with 25ns step size)
- TDC Bin size: 27ps
- Low deadtime: 5.5ns Input rate: over 100MHz
- 4 independent low jitter CFD input channels with adjustable threshold
- Internal/external trigger supported
- Express processing and preset event filtering, user configurable
- System ready diagnostics
- Reserved Ethernet control interface
- Fast PCIe data acquisition board
- Standard: Rack 19" 2U

APPLICATIONS

- Pump-probe & time-resolved experiments
- Electron/Ion Spectroscopy (2D and 1D time resolved, time-of-flight)
- Diffraction, general imaging
- Multichannel time-resolved acquisition

INSERTION DEVICE DESIGN AND MANUFACTURING@KYMA Srl

Kyma Srl was established in 2007 as a joint venture between Sincrotrone Trieste SCpA and the industrial companies Cosylab d.d. (Ljubljana) and Euromisure SpA (Cremona).

Kyma activities focus on accelerator technology, with specific regard to the development and realization of insertion devices for light sources.

More than twenty years of experience in design, assembling, characterization and operation of insertion devices at Sincrotrone Trieste, has met the manufacturing capabilities of the industrial partners, to build up a world-class company for IDs realization and applications.

Since 2008 a daughter company, Kyma Tehnologija d.o.o., has been established in Sežana, just 10 km from the Elettra site, where all the activities connected with magnetic assembling and characterizations are carried out.

The original purpose of Kyma was the realization of the undulators for the FERMI@Elettra project.

By summer 2010 all the undulators for the FEL-1 free-electron laser have been realized and, subsequently, installed and commissioned. The undulators for the first stage of FEL-2 have been completed and will be delivered by end 2010, while the remaining undulators are scheduled to be delivered by the end of June 2011.

The table below summarizes the undulators for the FERMI@Elettra project.

FUNCTION		TYPE	LENGHT	PERIOD
Laser heater		LPU	540	40.0
FEL1	Modulator	LPU	3220	100.0
	Radiator	6 x EPU	2415	55.0
FEL 2 1 st stage	Modulator	LPU	3220	100.0
	Radiator	2 x EPU	2415	55.0
FEL 2 2 nd stage	Modulator	EPU	2415	55.0
	Radiator	6 x EPU	2400	34.4

Further to the realization of the undulators for FERMI@Elettra, Kyma is now developing its business on the world market. A number of contracts have been already awarded:

- one hybrid wiggler for Canadian Light Source, Saskatoon (Canada);
- one Linearly Polarized Undulator for Raja Ramanna Centre for Advanced Technology, Indore (India);
- two Elliptically Polarized Undulators for Pohang Light Source, Pohang (Korea).



The seven undulators of the FEL-1 chain installed in the FERMI@Elettra tunnel



Undulators under magnetic characterization at the Kyma Tehnologija laboratory in Sežana

How to contact us:

Kyma Srl
 S.S. 14 - km. 163.5 in Area Science Park
 IT-34149 Basovizza - Trieste, Italy
 Tel. +39 040 375 8796 - Fax +39 040 375 8209
 info@kyma-undulators.eu - <http://www.kyma-undulators.eu>

INSTITUTIONAL EVENTS

Mariastella Gelmini - Minister for Education, University and Research

(November 30th 2009)

"A centre of excellence that does credit to Italy and most of all to the Italian researchers, who find opportunities here to express their talent". This is the dedication written in the guest book by Mariastella Gelmini, Minister for Education, University and Research, during her visit to Sincrotrone Trieste. After the Minister's visit to the Elettra experimental room, a ceremony took place to mark the official start up of the beam of electrons of FERMI@Elettra. The start-up of the electronic beam that will enable the new laser source to function was followed live from the "control room" screens in the FERMI Linac building.

ph. Filippo Cianciosi





Ferruccio Fazio - Minister for Health

(March 16th 2010)

A visit by the Minister for Health, Ferruccio Fazio, to Sincrotrone Trieste was the first appointment in a day full of various engagements in Trieste and throughout the Region. The Minister arrived at the Elettra Laboratory accompanied by Vladimir Kosic, Regional Councillor for Health, Social-Health Integration and Social Policy.

His tour of the Laboratory included stop-offs at the research stations that use the synchrotron light source within the field of diagnostics and pharmacology: the Syrmep and TwinMic microscopy lines, which use X-rays to obtain images with an extremely high definition, and the SISSI infra-red ray line.

ph. Filippo Cianciosi



Gregor Golobič - Slovenian Minister for Research

(March 17th 2010)

The Slovenian Minister for Research, Gregor Golobič, visited the Elettra Laboratory in the company of Jana Kolar and Sergej Možina, respectively Director General and Senior Councillor of the Science Directorate. Carlo Rizzuto welcomed the guests as President of Sincrotrone Trieste and Chairman of the European Strategy Forum on Research Infrastructures, along with Giovanni Comelli, Vice President of the Company.

ph. Filippo Cianciosi



Alessandro Giacchetti – Prefect of Trieste

(April 15th 2010)

Dr. Alessandro Giacchetti, the Prefect of Trieste, visited the Elettra Laboratory; Carlo Rizzuto, President of Sincrotrone Trieste welcomed him, along with the Vice President of the company, Giovanni Comelli. The Prefect congratulated them and, as he wrote in the book of institutional visits, he said he was “amazed by this splendid structure that most certainly constitutes one of the excellences of Italian genius. I am certain – he continued in his dedication – that it will constitute an essential reference point for national and European development in the future”.



Ceremony to mark the posting of the new IAEA plaque. The Elettra Laboratory is reconfirmed as a “Collaborating Centre”

(June 16th 2010)

The Elettra Laboratory celebrates an important acknowledgement as it is reconfirmed as a Collaborating Centre for the International Atomic Energy Agency. Werner Burkart, from the General Directorate of the IAEA, participated in the ceremony. The IAEA, which was established in 1957 within the framework of the United Nations, for monitoring and ensuring the peaceful use of nuclear technologies, is now involved in a series of training programmes in various thematic areas: Elettra’s affiliation with the Agency, launched back in 2005, with the use of the synchrotron light sources, can offer effective applicative solutions in various thematic areas and is committed to training young researchers from developing countries.

ph. Filippo Cianciosi





**Sincrotrone Trieste-European Investment Bank:
signature of the financing contract**

(April 29th 2010)

The European Investment Bank (EIB) signed a 20 million euro loan contract with Sincrotrone Trieste, which is destined for the completion and start up of a new FERMI@Elettra light source. Dario Scannapieco was present on behalf of the EIB, he is Vice-President and manager of operations in Italy, Malta

and the Western Balkans; Sincrotrone Trieste was represented by its President Carlo Rizzuto, its Managing Director, Alfonso Franciosi, and its Vice President, Giovanni Comelli. Federica Seganti the Regional Councilor for territorial planning, local autonomies and safety, international and community relations, spoke at the ceremony held to mark the signature of the contract.

ph. Filippo Cianciosi



Inauguration of the Sincrotrone Trieste tri-generation plant

(October 15th 2010)

Alessandro Ortis, chairman of the Authority for electrical energy and gas, and Antonio Costato, vice-president of Confindustria, participated in the event entitled “Energia e sviluppo economico” (Energy and economic development), organised by Confindustria Trieste, Consorzio Energia Trieste and Sincrotrone Trieste.

The day was marked by two important moments: the inauguration of the Sincrotrone Trieste tri-generation plant at the Elettra Laboratory and the conference entitled “I sistemi di approvvigionamento energetico nazionale” (National energy supply systems) at the headquarters of Confindustria.

The plant was established along with the new FERMI@Elettra light source and constitutes a significant improvement in terms of energy efficiency, optimising the maximum degree of calorific value of the primary source (methane). It was created by the Collini Lavori/ Landi temporary consortium, within the framework of the “Main FERMI!” tender and will be managed for ten years by the newly founded Tri-generazione srl (Collini Lavori/ Landi/Sinergie-Acegas-Aps).

The new system will firstly have to ensure the functioning of the entire FERMI@Elettra privileged utility, that is, the electrical circuit reserved for everything that must never be switched off because it keeps control instruments and safety equipment running.

The electrical energy necessary for this purpose will be obtained thanks to three methane-powered engines, having an efficiency level of approximately 40%. The remaining percentage of thermal energy produced, which would otherwise be dispersed in the form of combustion smoke, cooling water and irradiated heat, will be recovered. It will be used for heating buildings, but also for cooling laser plants and entire areas during the summer, given the presence of a powerful refrigeration plant which will “produce cold” at 7°C from the thermal energy through a chemical transformation.

ph. Filippo Cianciosi



WELCOME TO ELETTRA

Open Day 2010

(June 12th 2010)

More than 3500 people gathered at the campuses of Padriciano and Basovizza to participate in the seventh edition of the open day organised by the Area Science Park. As was the case during the past editions, the Sincrotrone Trieste blue route was among the most popular. Elettra was bustling throughout the day: from 10 a.m. to 6 p.m. with departures every 30 minutes for a total of 17 tours, almost 500 visitors entered the laboratory.

The public was given the opportunity to get to know the laboratory through various experiences: from the projection of a video, to the tour and explanation of the functioning of a light line, to the explanation of some research underway with the support of an informative presentation (a new addition this year). Many visitors stayed on after completing the tour, and expert personnel were available to answer questions and satisfy the visitors' curiosity.

ph. Marino Sterle - Filippo Cianciosi





The Researchers' Night

(September 24th 2010)

The enormous success of a year ago in terms of audience was repeated with STAR (Star in Trieste And Researchers) within the suggestive backdrop of Piazza Unità d'Italia and its surroundings, the scientists of the institutes of Trieste, along with other Italian and European cities, gathered to meet with citizens, under the directorship of the European Commission. The throngs of visitors weren't discouraged by the unfavourable weather conditions that compromised the organisation of some appointments this year.

At the Sincrotrone Trieste stand, the Suzuki Piano Music Association held short violin exhibitions during the early afternoon to accompany the explanations on the applications to Elettra, among which the analysis of bowed string instruments.

Given the weather conditions, the visiting Authorities decided to hold the opening speech and cutting of the ribbon near the stand, accompanied by a small orchestra. The first sudden downpour of the afternoon then forced the Mayor Dipiazza, the Chairman of the Provincial Authorities Bassa Poropat, the Chancellor of the University of Trieste Peroni, and the Councillor for Education, University and Research Rossi, to hold the ceremony inside the same stand.

Due to the rain in the evening the "Fisica del Karate" (Karate Physics) event also took place inside the Sincrotrone stand.

Rather than discouraging the public, the persistent rain "carried" many visitors right until the end (11 p.m.)

Apart from the stand, Elettra organised 2 scientific conversations that saw the participation of a very interested public:

- Nanotechnology for the early disease diagnosis;
- Microstructure, what fun!

ph. Filippo Cianciosi - Gabriele Crozzoli







Preview of FERMI@Elettra

(November 9th 2010)

The new Experimental Hall opened its doors to the personnel of Sincrotrone Trieste for the first time.

Carlo Rizzuto, chairman of ST, Stephen Milton (Project Director), Michele Svandrik (Head of Engineering) and Fulvio Parmigiani (Head of Scientific Programs) spoke at the event. The most important moments of the construction of the FEL were documented with the support of a video, then

the speakers moved on to discuss the future prospects of the Laboratory, before thanking all the people who participated both directly and indirectly in the completion of the project. A large aerial photograph with the signatures of the participants in the event will remain as a memoir of the day. Before the toast, all the personnel gathered together for a group photo, taken from the roof of the Safety Hutch of the Experimental Room.

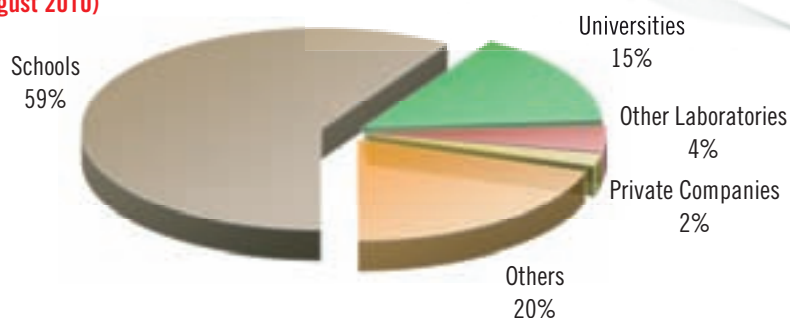
ph. Filippo Cinciosi



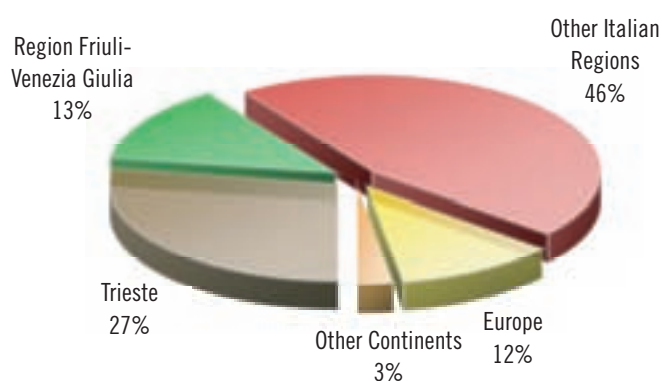
Event	Place / Date	Organisers / Collaborators
Thermodynamically unstable proteins	Trieste, 14-16/12, 2009	ICTP / Sincrotrone Trieste
Users' Assembly	Trieste, 16/12, 2009	Sincrotrone Trieste
Probing Magnetic Dynamics With Ultrashort Coherent X-Ray Pulses	Trieste, 16-18/12, 2009	Sincrotrone Trieste
Photons for Medicine and Materials Science	Melbourne (Australia), 19-21/02, 2010	Australian Gov. / Australian Synchrotron / Embassy of Italy / Sincrotrone Trieste
Let your work flow with Millipore	ST, 30/03, 2010	Millipore / Sincrotrone Trieste
Workshop PyMCA e HDF5	ST, 12-14/04, 2010	Sincrotrone Trieste
International Workshop on Fermentation Technology for Large Scale Protein Production	Trieste, 26-30/04, 2010	CBM / Sincrotrone Trieste / Sissa
School on Synchrotron and Free-Electron-Laser Sources and their Multidisciplinary Applications	Trieste, 26/04-07/05, 2010	ICTP / Sincrotrone Trieste
Frontiers in Water Biophysics	Trieste, 23-26/05, 2010	Univ. TS / Univ. TE / Univ. UD / Sincrotrone Trieste
1st Workshop R3: DNA replication, recombination and repair	S. Miniato (Italy), 30/06-02/07, 2010	CNR PV / CNR NA / FABI / IFON / SNS Pisa / Sincrotrone Trieste / Univ. MI
ESLS RF Workshop	Trieste, 29-30/09, 2010	Sincrotrone Trieste

VISITS

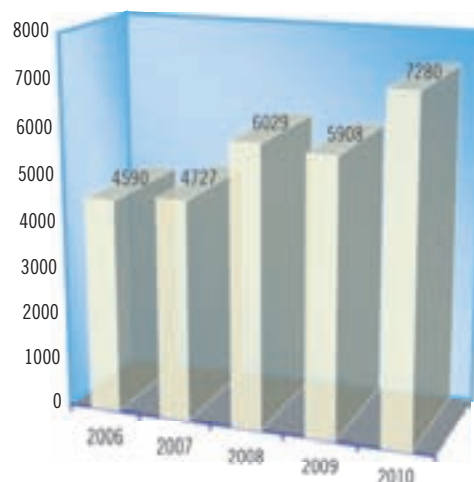
VISITORS DISTRIBUTION: TYPE OF INSTITUTION (September 2009 - August 2010)



VISITORS DISTRIBUTION: GEOGRAPHICAL BREAKDOWN (September 2009 - August 2010)



VISITORS - PERIOD 2006-2010





Sincrotrone Trieste

Elettra Laboratory

PRODUCTS FOR RESEARCH LABS AND SYNCHROTRONS

Power Supplies

New families of intelligent (DSP or PC embedded) power supplies, which cover many types of applications (high voltage/current, four-quadrant, etc.) and configurations are forthcoming. Epics of Tango interface are often already included and custom-built solutions are possible.

Detectors

Photon and charged particle detectors, based on cross delay anodes, multi anodes and centroid finding techniques are continuously developed. 3D information (x, y, time) with spatial and time resolutions in the order of tens of micro- and pico-seconds are available through many custom-built solutions.

Lab Instrumentation

Fast picoammeters, multi-point strain gauges, charge pulse amplifiers, ion chambers, pulse generators, RF filters, etc. Every tool is intelligent and in sole cases Epics/Tango interfaces are already included.

Accelerator Components

Elettra, over the years, has acquired wide experience in developing and realizing accelerators components, such as undulators, resonant cavities, etc. For the production of Insertion Devices a specific spin-off company has been set-up.

Sincrotrone Trieste S.C.p.A.

Industrial Liaison Office

<http://ilo.elettra.trieste.it>

ilo@elettra.trieste.it

Phone: +39 040 375 8303

Fax: +39 040 375 8623



Equipment for Light Sources

Design development of
Permanent Magnet
Undulators

Instrumentation for Magnetic
Measurements

Large Climate Chamber Test
Services



KYMA S.R.L.

S.S. 14 Km 163,5 Km

in Area Science Park

IT-34149 - Trieste - Italy

www.kyma-undulators.eu



AREA Science Park: vision & mission

La vision:

essere riferimento internazionale del trasferimento tecnologico e dell'innovazione organizzativa per la gestione strategica e operativa di ricerca e impresa.

La mission:

accrescere la competitività e l'attrattività dei territori di riferimento mediante:

- la valorizzazione di ricerca e impresa
- la formazione per lo sviluppo d'impresa e per la gestione di ricerca e innovazione
- la promozione, a livello internazionale, di reti di eccellenza scientifiche e imprenditoriali.

Le strategie:

- focalizzazione a livello nazionale e, in particolare, nel Mezzogiorno, sul trasferimento di metodologie relative alla valorizzazione dei risultati della ricerca
- focalizzazione verso l'Est Europeo per il trasferimento delle metodologie di formazione e di governo di nuovi poli scientifici e tecnologici (capacity building)
- accordi extra Unione Europea in caso di ritorni economici e occupazionali significativi.

Gli scenari futuri:

- sviluppo di AREA nel Mezzogiorno, soprattutto con la formazione di broker tecnologici
- selezione e valorizzazione di idee e imprese innovative nel settore dell'energia e del risparmio energetico
- crescita continua e diffusione, anche con partnership qualificate, delle competenze interne trasformate in metodologie distintive a livello internazionale.

The vision:

to be an international reference for technological transfer and organisational innovation for strategic and operative management of research and enterprise.

The mission:

to competitively increase attractiveness in reference areas by means of:

- *the enhancement of research and development*
- *training for company development and for research and innovation management*
- *promotion, on an international level, of a scientific and entrepreneurial excellence network.*

The strategies:

- *focus on a national level, and in particular, in southern Italy, on method transfer in relation to the enhancement of research results*
- *focus on Eastern Europe for the transfer of training and governance methods for new science and technology centres (capacity building)*
- *agreements outside the EU in the case of significant economic and employment returns.*

The future scenarios:

- *development of AREA in the South of Italy, particularly with the creation of technology brokers*
- *selection and enhancement of ideas and innovative enterprise in the energy and energy saving sectors*
- *continuous growth and circulation, with qualified partners as well, for internal proficiency that is transformed into distinct methods at an international level.*

AREA

SciencePark



Sincrotrone Trieste SCpA

S.S. 14 Km. 163,5 in AREA Science Park

34149 Trieste ITALY

www.elettra.trieste.it - info@elettra.trieste.it

